Development and Application of New Numerical Extensions to the Coupled Coherent States Family of Multidimensional Quantum Dynamics Methods

James Alexander Green

Submitted in accordance with the requirements for the degree
of
Doctor of Philosophy

Faculty of Mathematics and Physical Sciences
School of Chemistry
University of Leeds
March 2018

Declaration of Authorship

The candidate confirms that the work submitted is his own, except where work which has formed part of jointly authored publications has been included. The contribution of the candidate and the other authors to this work has been explicitly indicated below. The candidate confirms that appropriate credit has been given within the thesis where reference has been made to the work of others.

The work in Chapter 2 has appeared in publication as follows: Chemical Physics Letters, 2015, Volume 641, Page 173, by J. A. Green and D. V. Shalashilin. The candidate was responsible for writing the program and running the calculations that generated the results, creating figures and writing the majority of the text. The contribution of D. V. Shalashilin was to suggest the idea for the benchmark calculation, along with an edit of the paper.

The work in Chapter 3 has appeared in publication as follows: The Journal of Chemical Physics, 2016, Volume 144, Page 024111, by J. A. Green, A. Grigolo, M. Ronto, and D. V. Shalashilin. The candidate was responsible for writing the program and running the calculations that generated the results, creating figures and performing the final draft of the paper. The other authors were responsible for the 2-layer coupled coherent states idea and formulation of equations, along with prior drafts of the paper, and responses to reviewer comments.

The work in Chapter 5 is currently in preparation to be published, with the manuscript authored by J. A. Green, D. V. Makhov, N. C. Cole-Filipiak, V. G. Stavros, and D. V. Shalashilin. The candidate was responsible for writing the manuscript, producing all figures and tables, and performing the 2-ethylpyrrole calculations. N. C. Cole-Filipiak and V. G. Stavros were responsible for the experimental data, whilst D. V. Makhov conducted the pyrrole calculations and authored the program code that generated the results.

Acknowledgements

My thanks first and foremost go to my supervisor, Prof. Dmitry Shalashilin, for his constant enthusiasm, support and guidance in my work, and without whom I would not be in the position I am today. I am extremely grateful for all he has taught me about quantum mechanics, numerical methods, and science in general, and also for his faith in my ability when I insisted I wanted to go down a more mathematical route for my project.

I am also immensely thankful for all the assistance offered by my colleagues in the Quantum and Classical Molecular Dynamics Group. Dr. Christopher Symonds was a huge help in my first few months in the group, providing aid with all I needed to start and get to grips with my PhD work, and has been a constant source of support in the office ever since. Dr. Dmitry Makhov has also been an ever present point of advice, and I am particularly grateful for all of his help with nonadiabatic calculations. Dr. Miklos Ronto provided a large amount of guidance with my initial work on 2-layer coupled coherent states, and was always much too modest about how much he contributed. I am also highly thankful to everyone else I have shared office 1.53c with, as they have made it a thoroughly enjoyable place to work, particularly in this final year.

I gratefully acknowledge Prof. Ben Whitaker and Dr. Marcelo Miranda for reading my initial reports and providing useful feedback, their advice has certainly helped shape my writing into a much improved form.

I am indebted to my colleagues at The University of Warwick, with Dr. Neil Cole-Filipiak providing many useful insights into my ultrafast nonadiabatic dynamics calculations, and help understanding his experimental work. Prof. Vas Stavros also afforded valuable assessment of these calculations, and was a constant friendly face at our joint group meetings.

My gratitude also goes to Dr. Alexej Streltsov for generously hosting me for a week in Heidelberg, and teaching me about the multiconfigurational time-dependent Hartree for bosons method and program. My discussions with him also greatly helped in the development of the coupled coherent states for indistinguishable bosons method.

I wish to express my thanks to Robert Woodward-Massey for proof reading the final draft of my thesis, and for making these past three and a half years incredibly entertaining.

I am of course greatly indebted to my parents (and not just financially) for supporting me throughout my PhD and life in general, even though I think they still don't know exactly what it is I do.

I am thankful to Dr. Julie Fisher for making me feel very welcome in the department when I arrived, and myself and the rest of the chemistry department miss her greatly. My thanks also go to Dr. Terry Kee and Prof. Malcolm Halcrow in their roles as postgraduate tutors for looking after the welfare of myself and fellow postgraduates.

I would like to acknowledge the funding provided by The University of Leeds University Research Scholarship to permit me to carry out my PhD, as well as funding from the School of Chemistry for the final 6 months.

Finally, I am extremely grateful to have been able to work in such a friendly, social, and vibrant chemistry department. Many lifelong friendships have been formed, and all those within the department, past and present, have made my time here probably the best of my life.

Abstract

The coupled coherent states method has demonstrated itself as an accurate and efficient method of studying the quantum dynamics of various systems. In recent years, its applicability has been extended by incorporating a number of new numerical expansions and modifications to generate a closely related family of methods. In this thesis, two new augmentations are developed to further broaden the scope of problems that are able to be treated. The first of these is a 2-layer extension of coupled coherent states, capable of providing an increased mathematical description of a degree or degrees of freedom within a quantum mechanical system, as well as beneficial numerical and scalability properties. The newly developed method is tested on a model system-bath Hamiltonian consisting of a tunnelling mode governed by an asymmetric double well potential coupled to a harmonic bath. It is found to compare well to previous methods of studying the Hamiltonian, as well as a benchmark calculation on the system conducted in this thesis, and demonstrate the beneficial numerical and scalability properties expected. The second development is to extend coupled coherent states to treat systems of indistinguishable bosons in the second quantisation representation. The method is tested on the same Hamiltonian as the 2-layer coupled coherent states scheme, where the harmonic bath is second quantised as it is comprised of oscillators of the same frequency, so they may be thought of as indistinguishable. Exploiting this symmetry property is found to be extremely advantageous, with remarkable agreement to the benchmark calculation. The method is then tested on a model Hamiltonian consisting of 100 bosons in a shifted harmonic trap, with oscillations in the 1-body density calculated. The results are found to compare favourably with a multiconfigurational time-dependent Hartree for bosons calculation that is equivalent to the Gross-Pitaevskii equation, providing impetus for future studies on systems of Bose-Einstein condensates. The existing *ab initio* multiple cloning extension of coupled coherent states for nonadiabatic dynamics is also used to study the ultrafast photodissociation of 2-ethylpyrrole. The results are compared to experimental data, and a novel insight into the dissociation mechanism is obtained, with it shown to be composed of a two step process. Firstly, molecules that are able to dissociate immediately over the barrier along the N-H coordinate do so in < 50 fs, and this is followed by a second slower dissociation process from molecules that must sample the potential energy surface before finding a way around the barrier. This is not observed experimentally due to the temporal widths of the laser pulses obscuring the dynamics in the < 50 fs window.

Contents

List of Figures

List of Tables

Abbreviations

CCS	**C**oupled **C**oherent **S**tates
2L-CCS	**2**-**L**ayer **C**oupled **C**oherent **S**tates
CCSB	**C**oupled **C**oherent **S**tates for indistinguishable **B**osons
FCCS	**F**ermionic **C**oupled **C**oherent **S**tates
MCE	**M**ulti**C**onfigurational **E**hrenfest
MCEv1	**M**ulti**C**onfigurational **E**hrenfest **v**ersion **1**
MCEv2	**M**ulti**C**onfigurational **E**hrenfest **v**ersion **2**
AI-MCE	***A**b **I**nitio* **M**ulti**C**onfigurational **E**hrenfest
AIMC	***A**b **I**nitio* **M**ultiple **C**loning
MCE-TDDB	**M**ulti**C**onfigurational **E**hrenfest in a **T**ime-**D**ependent **D**iabatic **B**asis
IVR	**I**nitial **V**alue **R**epresentation
VVG	**V**an-**V**leck **G**utzwiller
WKB	**W**entzel-**K**ramers-**B**rillouin
HK	**H**erman-**K**luk
MS	**M**ultiple **S**pawning
FMS	**F**ull **M**ultiple **S**pawning
AIMS	***A**b **I**nitio* **M**ultiple **S**pawning
TDH	**T**ime-**D**ependent **H**artree
MCTDH	**M**ulti**C**onfigurational **T**ime-**D**ependent **H**artree
G-MCTDH	**G**aussian **M**ulti**C**onfigurational **T**ime-**D**ependent **H**artree
MCTDHB	**M**ulti**C**onfigurational **T**ime-**D**ependent **H**artree for **B**osons
MCTDHF	**M**ulti**C**onfigurational **T**ime-**D**ependent **H**artree-**F**ock
vMCG	**v**ariational **M**ulti**C**onfigurational **G**aussian
DD-vMCG	**D**irect **D**ynamics **v**ariational **M**ulti**C**onfigurational **G**aussian
ML-MCTDH	**M**ulti**L**ayer **M**ulti**C**onfigurational **T**ime-**D**ependent **H**artree
SOFT	**S**plit **O**perator **F**ourier **T**ransform
MP/SOFT	**M**atching **P**ursuit **S**plit **O**perator **F**ourier **T**ransform
CI	**C**onfiguration **I**nteraction
sTG	**s**tandard **T**rajectory **G**uided
aTG	**a**daptive **T**rajectory **G**uided
GPE	**G**ross-**P**itaevskii **E**quation

TDSE	**T**ime-**D**ependent **S**chrödinger **E**quation
TDVP	**T**ime-**D**ependent **V**ariational **P**rinciple
PES	**P**otential **E**nergy **S**urface
ACF	**A**uto**C**orrelation **F**unction
CCF	**C**ross**C**orrelation **F**unction
FT	**F**ourier **T**ransform
NACME	**N**on**A**diabatic **C**oupling **M**atrix **E**lement
BAT	**B**ra-ket **A**veraged **T**aylor
CASSCF	**C**omplete **A**ctive **S**pace **S**elf-**C**onsistent **F**ield
2-EP	**2**-**E**thyl**P**yrrole
HRA-PTS	**H**ydrogen (**R**ydberg) **A**tom **P**hotofragment **T**ranslational **S**pectroscopy
VMI	**V**elocity **M**ap **I**mage
TR-VMI	**T**ime-**R**esolved **V**elocity **M**ap **I**maging
TR-IY	**T**ime-**R**esolved **I**on **Y**ield
REMPI	**R**esonance **E**nhanced **M**ulti**P**hoton **I**onisation
KIE	**K**inetic **I**sotope **E**ffect
TKER	**T**otal **K**inetic **E**nergy **R**elease
IRF	**I**nstrument **R**esponse **F**unction
OMP/OpenMP	**O**pen **M**ulti-**P**rocessing
MPI	**M**essage **P**assing **I**nterface
GPU	**G**raphics **P**rocessing **U**nit
LAPACK	**L**inear **A**lgebra **PACK**age
RK4	**R**unge-**K**utta 4th order

Notation

Throughout this thesis, the following conventions are used:

i, j, k, l	Basis function index, given as subscript, i.e. $\mathbf{z}_k$
m, n	Dimensional/degree of freedom index, given as superscript in parentheses, i.e. $z^{(m)}$
$\alpha, \beta, \gamma, \zeta$	Quantum state index, given as superscript in parenthesis, i.e. $z^{(\alpha)}$
s,b	System and bath degrees of freedom label, given in Roman as superscript in parenthesis, i.e. $\Psi^{(\mathrm{s})}$
z	Refers to a single dimensional coherent state
$\mathbf{z}$	Refers to a multidimensional coherent state, where $\|\mathbf{z}\rangle = \prod_m \|z^{(m)}\rangle$ in CCS and 2L-CCS and $\|\mathbf{z}\rangle = \prod_\alpha \|z^{(\alpha)}\rangle$ in CCSB

Any other notation convention used is specified in the text.

Chapter 1

Background and Theory

Since the inception of computational chemistry, a central aim has been to develop methods that are capable of treating chemical systems with ever increasing complexity or dimensionality. New methodologies, combined with the growth of computing power in the previous few decades has allowed the simulation of chemical interactions to become a valuable tool to understand processes on an atomic scale, predict bulk properties, and examine the relationship between the two. In the classical regime, molecular dynamics has been used extensively in modelling large biomolecules due to the relatively inexpensive solution of Newton's equations required for a simulation to progress, alongside modern parallelisation techniques, GPU processing, and the development of solvent and coarse graining models [1].

In the quantum regime the most common way of approaching a problem is to solve the Schrödinger equation. This is a considerably more challenging task than calculating the solution of Newton's equations, and places a greater limit on the size of system that can be studied. The Schrödinger equation may be cast into a time-independent picture, where the wavefunction and Hamiltonian form an eigenvalue problem requiring diagonalisation, or a time-dependent picture where the wavefunction is propagated according to the Hamiltonian. In either case, the wavefunction is traditionally represented as a basis set expansion of orthonormal time-independent basis functions and associated amplitudes. This representation requires exponentially more basis functions for every degree of freedom in the system studied, and solution of the equations generated rapidly becomes intractable for current computational hardware to deal with. In the time-dependent picture, which is the focus of this thesis, powerful integrators such as the split-operator [2, 3], Chebyshev expansion [4] and short iterative Lanczos [5] methods have been developed for propagation of the wavefunction, however they are limited to low dimensionality problems with not more than a few degrees of freedom.

Attempts to find some middle ground between the speed of classical simulations and the accuracy of quantum ones has been offered by semiclassical theory, in particular with work by Heller, Herman and Kluk, and Miller and Marcus [6–14]. Heller developed the time-dependent "thawed" and subsequent "frozen" Gaussian approaches [6, 7], whilst Herman and Kluk [8, 9] reconciled this frozen Gaussian approach with earlier work by Miller and

Marcus on initial value representations (IVR) [10–14]. Miller and Marcus' IVR work was for scattering calculations, although Herman and Kluk applied the IVR treatment to the semiclassical van Vleck-Gutzwiller propagator [15, 16]. These approaches were seminal in the development of time-dependent semiclassical methods that are capable of studying the dynamics of atoms and molecules, and were an important stepping stone to time-dependent fully quantum approaches. Fully quantum approaches are desirable, because semiclassical methods — as their name suggests — do not completely take into account quantum effects. The multiconfigurational time-dependent Hartree (MCTDH) method [17–19] has emerged as a very accurate method of wavepacket propagation, capable of treating higher dimensional problems than the integrators mentioned above [20–23]. However MCTDH still suffers from exponential scaling, albeit with a smaller base to be exponentiated, limiting the size of the system that can be studied to tens of degrees of freedom.

Fully quantum methods capable of scaling more favourably with system size utilise Gaussian basis sets in the spirit of Heller's work. Examples of these include Gaussian-based multiconfigurational time-dependent Hartree (G-MCTDH) [24], variational multiconfigurational Gaussians (vMCG) [25, 26], full multiple spawning (FMS) [27], and matching pursuit split-operator Fourier transform (MP/SOFT) [28], as well as the coupled coherent states (CCS) family of methods that are the subject of this thesis [29–35]. The Gaussian functions are used as time-dependent basis functions, as opposed to the time-independent basis functions used traditionally, and evolve as the wavefunction evolves. Extensive grid-based sampling of the Gaussian basis functions is not required, instead they are guided by trajectories (with the exception of MP/SOFT), mininising basis set size and ensuring the methods do not scale exponentially with system size. The downside of this non-grid-based sampling approach is that noise and slow convergence can become apparent in calculations. However, all methods mentioned above have been successfully applied to a number of multidimensional quantum problems [36–49].

Whilst CCS has been applied to a number of problems [42–49], it is desirable to develop new numerical extensions to the method to further extend its applicability, and provide a toolkit of options for studying a particular quantum mechanical problem. The aim is that these extensions may exploit certain properties of a problem, such as different dynamical descriptions for different degrees of freedom, symmetries arising from indistinguishabilities, or nonadiabatic effects, to provide a calculation with increased accuracy, numerical efficiency, or combination thereof. By exploiting these properties, the extensions will be particularly suited to certain classes of quantum problems, such as system-bath, Bose-Einstein condensates, and ultrafast photochemical reactions, respectively. This thesis will develop two new extensions to treat the former two class of problems, and a recent third extension [34] will be applied to the latter.

As this thesis aims to develop and apply new approaches to the CCS family of quantum dynamics methods, in the following introductory chapter it is beneficial to present the historical origins of CCS. CCS may be considered a quantum initial value representa-

tion method, using trajectory guided frozen Gaussian basis functions, and each of these components that make up the method will be reviewed in turn. Firstly, a brief overview of classical Lagrangian and Hamiltonian mechanics will be presented in Sec. 1.1.1 and 1.1.2, as well as their quantum analogues in Feynmans's path integral approach to quantum mechanics, and Schrödinger's approach to quantum mechanics in Sec. 1.1.3 and 1.1.4. The classical mechanics formulations are used in the description of trajectories in CCS, and Schrödinger mechanics sets the foundation for the quantum solution of the CCS working equations. Feynman's path integral approach can be used to evaluate the semiclassical propagator in terms of trajectories, as shown in Sec. 1.1.5, which leads on to the initial value representation of the propagator in Sec. 1.2.1. Gaussians were first used for dynamics by Heller, and this will subsequently be reviewed in Sec. 1.2.2. Initially the thawed formalism will be presented [6], followed by the frozen formalism [7] that is used in CCS. The Herman-Kluk (HK) method will then be covered in Sec. 1.2.3, which reconciles the semiclassical propagator and frozen Gaussian methods. The HK method is one of the most popular semiclassical time-dependent approaches, and can serve as a comparison to CCS. After this background theory has been shown, the derivation and working equations of CCS will be presented, and applications of the method will be reviewed in Sec. 1.3. The generalisation of CCS to the multiconfigurational Ehrenfest (MCE) method [31–33] for nonadiabatic dynamics will also be derived and reviewed in Sec. 1.4. The methodology used in the derivation of MCE is used in the development of a 2-layer extension of CCS (2L-CCS) in Chapter 3, as well as providing the foundation for "on-the-fly" nonadiabatic dynamics in the *ab initio* multiple cloning (AIMC) method, which is used in Chapter 5. The final aspect of the introductory review will be a comparison between CCS and alternative quantum dynamics methods in Sec. 1.5. A summary, conclusions, and an outline of the thesis will then be given in Sec. 1.6.

Following this introductory chapter, in Chapter 2 a model double well tunnelling problem will be presented that has previously been studied by CCS, as well as other quantum dynamics methods, and a benchmark calculation will be carried out for it. This enables the newly developed 2L-CCS method to be tested against it in Chapter 3, as well as CCS for indistinguishable bosons (CCSB) that is developed in Chapter 4. For the latter method, a model Bose-Einstein condensate problem is also considered, as the aim of CCSB is to be used to study such systems. The derivation of working equations for both new methods will be presented, and suitable further applications of these numerical extensions of CCS will be suggested. In the penultimate chapter, Chapter 5, the extension of the MCE method to on-the-fly nonadiabatic dynamics with AIMC will be briefly reviewed, and then applied to study the ultrafast photodissociation of 2-ethylpyrrole. In the final chapter, Chapter 6, the methods developed and applied in this thesis will be summarised, conclusions drawn, and future applications discussed. In the appendices, the program code developed to conduct the calculations in this thesis will be described in Appendix A, and additional calculations performed by the CCSB method on the double well tunnelling problem will be presented in Appendix B.

1.1 Classical Lagrangian and Hamiltonian Mechanics, Path Integral Formulation and the Semiclassical Propagator

The foundation of the CCS method, and indeed much of quantum mechanics, can be found in classical Lagrangian and Hamiltonian mechanics. The working equations and trajectories guiding basis functions in CCS incorporate elements of both Lagrangian and Hamiltonian mechanics, and more generally Feynman's path integral approach stems from Lagrangian mechanics, and Schrödinger's approach stems from Hamiltonian mechanics.

1.1.1 Classical Lagrangian Mechanics

Beginning chronologically, Lagrangian mechanics was first introduced by the eponymous Joseph-Louis Lagrange in 1788 as an alternative to the classical Newtonian mechanics that had preceded it. Lagrangian mechanics possesses two main advantages over Newtonian mechanics: the first is that any forces of constraint in a system (which may not be known) are explicitly needed in Newtonian mechanics but may be bypassed in Lagrangian mechanics. The second is that the equations for Lagrangian mechanics take the same form in different coordinate systems (invariant under canonical transformation in coordinate space), whereas representation of the force in Newtonian mechanics is different in different coordinate systems, and is suited primarily to Cartesian coordinates.

Defining the main features of the approach, the Lagrangian function $\mathcal{L}$ (simply referred to as the Lagrangian) is given by

$$\mathcal{L}(\dot{q}, q, t) = T(q, \dot{q}) - V(q, t), \tag{1.1.1}$$

where T is the kinetic and V the potential energy. The Lagrangian is a function of "generalised coordinates" q, "generalised velocities" $\dot{q}$, and time if the potential is time-dependent (although it will be assumed not to be below). The kinetic energy may depend on coordinates q, as well as the usual $\dot{q}^2$ factor depending on the system studied. For a particle that follows a trajectory connecting q' and q'' in a time interval from t' to t'' (i.e. $q(t') = q'$ and $q(t'') = q''$), a quantity known as the action S may be computed

$$S = \int_{t'}^{t''} \mathcal{L}(\dot{q}, q)\, \mathrm{d}t. \tag{1.1.2}$$

The classical trajectory the particle follows is one for which S is an extremum,

$$\delta S = S(q + \delta q) - S(q) = 0, \tag{1.1.3}$$

where δq is some small variation in q that leaves S unchanged to a first order approximation. This is known as the principle of least action, or more accurately stationary action — the reason for which will be discussed below. Using the definition of the action given

in the integral in Eq. (1.1.2) alongside a first order Taylor expansion gives

$$\begin{aligned} S(q+\delta q) &= \int_{t'}^{t''} \mathcal{L}(\dot{q}+\delta\dot{q}, q+\delta q)\,\mathrm{d}t \\ &= \int_{t'}^{t''} \left[\mathcal{L}(\dot{q},q) + \delta\dot{q}\frac{\partial\mathcal{L}}{\partial\dot{q}} + \delta q\frac{\partial\mathcal{L}}{\partial q}\right]\,\mathrm{d}t \\ &= S(q) + \int_{t'}^{t''} \left(\delta\dot{q}\frac{\partial\mathcal{L}}{\partial\dot{q}} + \delta q\frac{\partial\mathcal{L}}{\partial q}\right)\,\mathrm{d}t. \end{aligned} \tag{1.1.4}$$

Rearranging the above so it is equivalent to Eq. (1.1.3), and integrating the first term in the integrand using integration by parts yields

$$\delta S = \left[\delta q\frac{\partial\mathcal{L}}{\partial\dot{q}}\right]_{t'}^{t''} - \int_{t'}^{t''} \delta q\left[\frac{\mathrm{d}}{\mathrm{d}t}\left(\frac{\partial\mathcal{L}}{\partial\dot{q}}\right) - \frac{\partial\mathcal{L}}{\partial q}\right]\,\mathrm{d}t. \tag{1.1.5}$$

Since the value of δq is zero at the end points, the first term on the right hand side of the above equation is zero. Between the end points δq can take any value, therefore the condition that satisfies S as an extremum is

$$\frac{\mathrm{d}}{\mathrm{d}t}\left(\frac{\partial\mathcal{L}}{\partial\dot{q}}\right) - \frac{\partial\mathcal{L}}{\partial q} = 0, \tag{1.1.6}$$

which is the classical Lagrangian equation of motion, or Euler-Lagrange equation. For kinetic energy $T = \frac{1}{2}m\dot{q}^2$ and some time-independent potential $V = V(q)$, evaluation of the Euler-Lagrange equation gives

$$\frac{\mathrm{d}}{\mathrm{d}t}(m\dot{q}) = -\frac{\partial V(q)}{\partial q}, \tag{1.1.7}$$

which is simply Newton's second law. As such, the derivative $\frac{\partial\mathcal{L}}{\partial\dot{q}}$ can be thought of as a generalised momentum, and $\frac{\partial\mathcal{L}}{\partial q}$ as a generalised force.

The principle of stationary action is occasionally referred to as the principle of least action, however to determine whether the extremum is a maximum, minimum, or saddle point, the second variation must be determined

$$\delta^2 S = \delta S(q+\delta q) - \delta S(q). \tag{1.1.8}$$

This isn't strictly relevant to classical mechanics, as the Euler-Lagrange equation of motion remains the same whether the action is maximum, minimum or a saddle point. However, the second variation becomes important when discussing the path integral derivation of the semiclassical propagator in Sec. 1.1.5.

Using the definition of the first variation in the action δS from Eq. (1.1.5), remembering that the first term in that expression is equal to zero, substituting in a general Lagrangian

$\mathcal{L} = \frac{1}{2}m\dot{q}^2 - V(q)$, and using a Taylor expansion gives

$$\begin{aligned}\delta^2 S &= \int_{t'}^{t''} \delta q \left[-m(\ddot{q} + \delta\ddot{q}) - \frac{\partial V(q+\delta q)}{\partial q}\right] \mathrm{d}t - \int_{t'}^{t''} \delta q \left[-m\ddot{q} - \frac{\partial V(q)}{\partial q}\right] \mathrm{d}t \\ &= \int_{t'}^{t''} \delta q \left[-m\delta\ddot{q} - \frac{\partial^2 V(q)}{\partial q^2}\delta q\right] \mathrm{d}t \\ &= \int_{t'}^{t''} \delta q \left[-m\frac{\mathrm{d}^2}{\mathrm{d}t^2} - \frac{\partial^2 V(q)}{\partial q^2}\right] \delta q \, \mathrm{d}t.\end{aligned} \tag{1.1.9}$$

At this point, it is useful to expand δq in an orthonormal basis of eigenfunctions u_n of the operator $\Lambda = -m\frac{\mathrm{d}^2}{\mathrm{d}t^2} - \frac{\partial^2 V(q)}{\partial q^2}$, such that

$$\Lambda u_n(t) = \lambda_n u_n(t) \tag{1.1.10}$$

and

$$\delta q(t) = \sum_n a_n u_n(t) \tag{1.1.11}$$

where $u_n(t') = u_n(t'') = 0$. It then follows that

$$\delta^2 S = \sum_n \lambda_n a_n^2 \tag{1.1.12}$$

and there are an infinite number of eigenvalues.

For a short time ($\tau = t'' - t'$) the potential does not change much, the motion is free particle-like, the eigenvalues λ_n are all positive, and $\delta^2 S$ is positive. Therefore, the extremum of the action is a minimum. As τ increases the influence of the potential is greater, and one or more of the eigenvalues may become negative and will not return to being positive. For these longer time periods the paths of extreme action become saddle points, heading closer to the character of a maximum as τ increases. The number of negative eigenvalues ν is known as the Morse index, and this will appear in Sec. 1.1.5.

In all the discussion thus far equations have been presented in a 1-dimensional form, however the Lagrangian formalism can be readily extended to M-dimensions

$$\frac{\mathrm{d}}{\mathrm{d}t}\left(\frac{\partial \mathcal{L}}{\partial \dot{q}^{(m)}}\right) = \frac{\partial \mathcal{L}}{\partial q^{(m)}} \qquad [m = 1, 2, \ldots, M]. \tag{1.1.13}$$

If the Lagrangian is independent of a particular coordinate $q^{(m)}$ then it can be said that the coordinate is ignorable or cyclic. The derivative of $\mathcal{L}$ with respect to that coordinate, i.e. the right hand side of Eq. (1.1.13) for given m, will be equal to zero. Therefore, the time derivative of $\frac{\partial \mathcal{L}}{\partial \dot{q}^{(m)}}$, i.e. generalised momentum $p^{(m)}$, will also be equal to zero meaning it is conserved. This is an example of Noether's theorem which states that whenever there is a continuous symmetry in the Lagrangian (transformation of the generalised coordinates, velocities or time that leaves the Lagrangian unaffected), there is an associated conservation law. The above was an example of conservation of momentum, whilst another important example is independence of time that leads to conservation of energy.

The time derivative of the Lagrangian, taking into account the time-dependence of

$q^{(m)}$ and $\dot{q}^{(m)}$, can be given as

$$\begin{aligned}\frac{\mathrm{d}}{\mathrm{d}t}\mathcal{L} &= \sum_{m=1}^{M}\frac{\partial\mathcal{L}}{\partial q^{(m)}}\dot{q}^{(m)} + \sum_{m=1}^{M}\frac{\partial\mathcal{L}}{\partial\dot{q}^{(m)}}\ddot{q}^{(m)} + \frac{\partial\mathcal{L}}{\partial t} \\ &= \sum_{m=1}^{M}\frac{\mathrm{d}}{\mathrm{d}t}\left(\frac{\partial\mathcal{L}}{\partial\dot{q}^{(m)}}\right)\dot{q}^{(m)} + \sum_{m=1}^{M}p^{(m)}\ddot{q}^{(m)} + \frac{\partial\mathcal{L}}{\partial t} \\ &= \frac{\mathrm{d}}{\mathrm{d}t}\sum_{m=1}^{M}\left(p^{(m)}\dot{q}^{(m)}\right) + \frac{\partial\mathcal{L}}{\partial t}.\end{aligned} \tag{1.1.14}$$

In the case that $\frac{\partial\mathcal{L}}{\partial t} = 0$,

$$\frac{\mathrm{d}}{\mathrm{d}t}\left[\sum_{m=1}^{M}\left(p^{(m)}\dot{q}^{(m)}\right) - \mathcal{L}\right] = 0. \tag{1.1.15}$$

The portion of the above equation inside the time derivative is the classical Hamiltonian

$$\mathcal{H} = \sum_{m=1}^{M}\left(p^{(m)}\dot{q}^{(m)}\right) - \mathcal{L}. \tag{1.1.16}$$

Therefore, when $\mathcal{L}$ does not depend explicitly on time, the Hamiltonian and hence total energy is conserved.

1.1.2 Classical Hamiltonian Mechanics

The Hamiltonian serves as the main function used in a further development of classical mechanics in 1834 by William Hamilton, named Hamiltonian mechanics. In most cases $\mathcal{H}$ corresponds to the total energy, which as mentioned above is conserved in time-independent potentials

$$\mathcal{H}(q,p) = T(q,p) + V(q). \tag{1.1.17}$$

Note that $\mathcal{H}$ depends on generalised coordinates and momenta (q,p) rather than generalised coordinates and velocities $(q,\dot{q})$ like in Lagrangian mechanics. The Hamiltonian approach therefore defines points in phase space as opposed to state space in the Lagrangian approach, and $\mathcal{H}$ is invariant under canonical transformation in phase space. Using this phase space formulation a more explicit relation of $\mathcal{H}$ to $\mathcal{L}$ than Eq. (1.1.16) may be provided by using a Legendre transformation with dependency of all variables explicitly stated

$$\mathcal{H}(q,p) = p\dot{q}(q,p) - \mathcal{L}(q,\dot{q}(q,p)). \tag{1.1.18}$$

The equations of motion for the Hamiltonian approach to classical mechanics may be obtained via the derivatives of $\mathcal{H}(q,p)$ in this Legendre transformation form with respect to q and p, which are known as Hamilton's equations. Firstly, the derivative with respect

to q is

$$\begin{aligned}\frac{\partial \mathcal{H}}{\partial q} &= p\frac{\partial \dot{q}}{\partial q} - \left[\frac{\partial \mathcal{L}}{\partial q} + \frac{\partial \mathcal{L}}{\partial \dot{q}}\frac{\partial \dot{q}}{\partial q}\right] \\ &= p\frac{\partial \dot{q}}{\partial q} - \left[\frac{\mathrm{d}}{\mathrm{d}t}\left(\frac{\partial \mathcal{L}}{\partial \dot{q}}\right) + p\frac{\partial \dot{q}}{\partial q}\right] \\ &= -\frac{\mathrm{d}}{\mathrm{d}t}p \\ &= -\dot{p}.\end{aligned} \tag{1.1.19}$$

Secondly, the derivative with respect to p is

$$\begin{aligned}\frac{\partial \mathcal{H}}{\partial p} &= \left[\dot{q} + p\frac{\partial \dot{q}}{\partial p}\right] - \frac{\partial \mathcal{L}}{\partial \dot{q}}\frac{\partial \dot{q}}{\partial p} \\ &= \left[\dot{q} + p\frac{\partial \dot{q}}{\partial p}\right] - p\frac{\partial \dot{q}}{\partial p} \\ &= \dot{q}.\end{aligned} \tag{1.1.20}$$

As with the Lagrangian formalism, this may be readily extended to M-dimensions

$$\frac{\partial \mathcal{H}}{\partial q^{(m)}} = -\dot{p^{(m)}} \quad [m = 1, 2, \ldots, M] \tag{1.1.21a}$$

$$\frac{\partial \mathcal{H}}{\partial p^{(m)}} = \dot{q^{(m)}} \quad [m = 1, 2, \ldots, M]. \tag{1.1.21b}$$

An important advantage Hamiltonian mechanics possesses over Lagrangian mechanics can be found in Liouville's theorem. This states that the volume occupied by a "cloud" of trajectories moving through phase space under the influence of Hamilton's equations does not change from an initial time to some time later. There is no corresponding theorem for Lagrangian mechanics in state space.

1.1.3 Schrödinger's Approach to Quantum Mechanics

Turning to quantum mechanics, the Hamiltonian is also a central feature in Schrödinger's approach where it describes time evolution and total energy. However, rather than a function like in classical mechanics, the Hamiltonian appears as an operator $\mathcal{H} \to \hat{H}$

$$\begin{aligned}\hat{H} &= \hat{T} + \hat{V} \\ &= \frac{\hat{p}^2}{2m} + V(\hat{q}).\end{aligned} \tag{1.1.22}$$

Kinetic and potential energies also appear as operators, which are in turn dependent on coordinate and momentum operators $(\hat{q}, \hat{p})$. The time-dependent Schrödinger equation (TDSE) describes how the state of a system, represented by the wavefunction $|\Psi(t)\rangle$, evolves in time

$$i\hbar\frac{\mathrm{d}\,|\Psi(t)\rangle}{\mathrm{d}t} = \hat{H}\,|\Psi(t)\rangle\,. \tag{1.1.23}$$

The TDSE is often solved in position space, using a basis set expansion of orthonormal time-independent basis functions χ, and associated time-dependent amplitudes $C(t)$ to

represent the M-dimensional wavefunction. The TDSE in position space is given by

$$i\hbar\frac{\mathrm{d}\Psi(\mathbf{q},t)}{\mathrm{d}t} = \left[-\frac{\hbar^2}{2\mu}\nabla^2 + V(\mathbf{q})\right]\Psi(\mathbf{q},t), \tag{1.1.24}$$

where $\Psi(\mathbf{q},t) = \langle\mathbf{q}|\Psi(t)\rangle$, μ is the reduced mass, and ∇ is the differential operator. The basis set expansion is given by

$$\Psi(\mathbf{q},t) = \Psi(q^{(1)},\ldots,q^{(M)},t) = \sum_{i^{(1)}=1}^{N^{(1)}}\cdots\sum_{i^{(M)}=1}^{N^{(M)}} C_{i^{(1)}\ldots i^{(M)}}(t)\prod_{m=1}^{M}\chi_{i^{(m)}}^{(m)}\left(q^{(m)}\right), \tag{1.1.25}$$

where $N^{(m)}$ are the number of basis functions for the mth degree of freedom. When substituted into the TDSE, multiplied by the conjugate of the orthonormal basis functions χ^*, and integrated over all space, the time-dependence of the amplitudes are obtained

$$\begin{aligned} i\dot{C}_{i^{(1)}\ldots i^{(M)}}(t) = &\sum_{j^{(1)}=1}^{N^{(1)}}\cdots\sum_{j^{(M)}=1}^{N^{(M)}} C_{j^{(1)}\ldots j^{(M)}}(t) \\ &\times\int \mathrm{d}\mathbf{q}\prod_{m=1}^{M}\chi_{i^{(m)}}^{(m)*}\left(q^{(m)}\right)\left[-\frac{\hbar^2}{2\mu}\nabla^2 + V(\mathbf{q})\right]\prod_{n=1}^{M}\chi_{j^{(n)}}^{(n)}\left(q^{(n)}\right), \end{aligned} \tag{1.1.26}$$

which forms a set of linear equations to be solved. The amount of these equations that are necessary to be solved rises exponentially with number of degrees of freedom M, rapidly becoming impossible to compute and providing motivation for alternative methods.

Another way of finding the time-dependence of the wavefunction is in terms of the time evolution operator, also known as the propagator $\hat{U}(t'',t')$. The propagator describes the transformation from an initial state of the system studied $|\Psi(t')\rangle$ to some later state $|\Psi(t'')\rangle$

$$|\Psi(t'')\rangle = \hat{U}(t'',t')\,|\Psi(t')\rangle\,. \tag{1.1.27}$$

To determine the form of the propagator, a number of properties it possesses must be defined. Firstly, the propagator is unitary

$$\hat{U}^*\hat{U} = \hat{I}, \tag{1.1.28}$$

where $\hat{I}$ is the identity operator. Secondly, it has the composition property such that

$$\hat{U}(t_2,t_0) = \hat{U}(t_2,t_1)\hat{U}(t_1,t_0). \tag{1.1.29}$$

Finally, it is continuous in time

$$\hat{U}(t,t) = 1. \tag{1.1.30}$$

The final property allows the following to be written for an infinitesimal time evolution

$$\lim_{\mathrm{d}t\to 0}\hat{U}(t'+\mathrm{d}t,t') = 1. \tag{1.1.31}$$

Assuming that the difference between $\hat{U}(t' + \mathrm{d}t, t')$ and 1 is first order in $\mathrm{d}t$ gives

$$\hat{U}(t' + \mathrm{d}t, t') = 1 - i\Omega\,\mathrm{d}t, \tag{1.1.32}$$

where $\hat{\Omega}$ is some Hermitian operator and i is included to satisfy unitarity. The operator $\hat{\Omega}$ has units of inverse time (frequency), and as energy is related to angular frequency by $E = \hbar\omega$, it can be written that

$$\hat{\Omega} = \frac{\hat{H}}{\hbar}. \tag{1.1.33}$$

Therefore, the infinitesimal time evolution operator is written as

$$\hat{U}(t' + \mathrm{d}t, t') = 1 - \frac{i\hat{H}\,\mathrm{d}t}{\hbar}. \tag{1.1.34}$$

Using the composition property,

$$\hat{U}(t'' + \mathrm{d}t, t') = \hat{U}(t'' + \mathrm{d}t, t'')\hat{U}(t'', t') = \left(1 - \frac{i\hat{H}\,\mathrm{d}t}{\hbar}\right)\hat{U}(t'', t'), \tag{1.1.35}$$

where $t'' - t'$ is not infinitesimal. This can be rearranged and given in differential equation form

$$i\hbar\frac{\partial}{\partial t}\hat{U}(t'', t') = \hat{H}\hat{U}(t'', t'). \tag{1.1.36}$$

For a time-independent Hamiltonian the solution to this equation is

$$\hat{U}(t'', t') = \mathrm{e}^{i\hat{H}(t''-t')/\hbar}, \tag{1.1.37}$$

which gives a mathematical form for the propagator based on its properties. The propagator may also be written as

$$K(q'', t''; q', t') = \langle q''|\mathrm{e}^{i\hat{H}(t''-t')/\hbar}|q'\rangle\,, \tag{1.1.38}$$

which can be interpreted as the propagator of a particle or wavefunction initially localised at point q' at time t' going to some point q'' at time t''. If the initial wavefunction is delocalised at time t' then K acts as the kernel of an integration over q' to go to q''

$$\Psi(q'', t'') = \int_{-\infty}^{\infty} K(q'', t''; q', t')\Psi(q', t')\,\mathrm{d}q'. \tag{1.1.39}$$

For this reason it is given the symbol K to distinguish it from the unitary time evolution operator $\hat{U}$.

The propagator K is also the Green's function for the TDSE

$$\left(\hat{H}(q'') - i\hbar\frac{\partial}{\partial t}\right)\Theta(t'' - t')K(q'', t''; q', t') = -i\hbar\delta(q'' - q')\delta(t'' - t') \tag{1.1.40}$$

where $\Theta(t'' - t')$ is the Heaviside unit step function and $\delta(q'' - q')$ and $\delta(t'' - t')$ are Dirac delta functions.

A final representation of the propagator, is in terms of a transition or probability amplitude for a particle or wavefunction to go from point q' at time t' to q'' and time t''

$$K(q'', t''; q', t') = \langle q'', t''|q', t'\rangle \,. \tag{1.1.41}$$

This representation becomes relevant in the following section, with discussion of Feynman's path integral approach to quantum mechanics.

1.1.4 Feynman's Path Integral Approach

Whilst Schrödinger's approach to quantum mechanics incorporates elements of classical Hamiltonian mechanics, Feynman's path integral approach incorporates elements of classical Lagrangian mechanics. Considering a particle that travels from point q' at time t' to q'' at time t'', in classical Lagrangian mechanics the path this particle takes is one that has stationary action. Feynman stated that rather than a particle taking a single path of stationary action, all the paths (including those that are classically forbidden) contribute with equal magnitudes but different phases to the transition amplitude $K(q'', t''; q', t')$. This is represented approximately as

$$K(q'', t''; q', t') = \langle q'', t''|q', t'\rangle \sim \sum_{\text{all paths}} \mathrm{e}^{iS/\hbar}. \tag{1.1.42}$$

The exponential factor $\mathrm{e}^{iS/\hbar}$ is the phase, and the action S is discretised in units of $\hbar$.

Before proceeding with a more complete definition of the above, it is worth considering what happens in the classical limit to ensure classical Lagrangian mechanics emerges from this quantum picture. In the classical limit S will be much larger than $\hbar$, and the phase will be highly oscillatory as small changes in S will be large in comparison to $\hbar$. This means that nearby paths will tend to cancel each other out, as one path with a positive phase will destructively interfere with a nearby one with a negative phase. However, for paths near to the path of extreme action there will be no change in S to a first order approximation, and they will constructively interfere. Therefore, only those paths near to the extremum contribute and the classical trajectory emerges from Feynman's quantum approach.

Now that the emergence of classical dynamics is confirmed qualitatively, a more quantitative definition of the path integral approach may be considered. In the quantum picture, the action will be comparable to $\hbar$ and all trajectories will contribute to the amplitude $K(q'', t''; q', t')$. The sum in Eq. (1.1.42) is therefore over an infinite number of trajectories, and a definition involving integrals is more appropriate. The approach used involves time-slicing, where the interval between t' and t'' is split into a set of N gaps that are some small amount ϵ apart, with $t_0 = t'$, $t_n = t_0 + n\epsilon$, and $t_N = t''$. At each time there are also a set of coordinates, with $q(t_0) = q_0 = q'$, $q(t_n) = q_n$ and $q(t_N) = q_N = q''$. Integrating over all q_n in the region between q' and q'' yields all possible paths connecting the two in

the limit of $N \to \infty$ or $\epsilon \to 0$

$$K(q'', t''; q', t') = \lim_{\substack{N\to\infty \\ \epsilon\to 0}} A \int_{-\infty}^{+\infty} \int_{-\infty}^{+\infty} \dots \int_{-\infty}^{+\infty} \mathrm{e}^{iS/\hbar}\, \mathrm{d}q_1\, \mathrm{d}q_2\, \dots\, \mathrm{d}q_{N-1}. \tag{1.1.43}$$

Note that the integration is not over q_0 or q_N as these points are fixed at q' and q'', and the limits for q_n in the region between are $[-\infty : \infty]$ as all paths connecting q_0 and q_N are included. In order for a limit of this integral to exist, an appropriate normalisation factor A must be evaluated. As the time interval is so small, the path between $q_i(t_i)$ and $q_{i+1}(t_{i+1})$ may be approximated as a straight line. The action for each of these slices may then be evaluated as follows

$$\begin{aligned} S &= \int_{t_i}^{t_{i+1}} L(\dot{q}, q)\, \mathrm{d}t = \int_{t_i}^{t_{i+1}} \frac{m\dot{q}^2}{2} - V(q)\, \mathrm{d}t \\ &= \epsilon \left[\frac{m}{2} \left(\frac{q_{i+1} - q_i}{\epsilon} \right)^2 - V\left(\frac{q_{i+1} + q_i}{2} \right) \right]. \end{aligned} \tag{1.1.44}$$

Considering the simplest possible case of a free particle where $V = 0$ (other examples may be found in Ref. [50]), Eq. (1.1.43) now becomes

$$K(q'', t''; q', t') = \lim_{\substack{N\to\infty \\ \epsilon\to 0}} A \int_{-\infty}^{+\infty} \int_{-\infty}^{+\infty} \dots \int_{-\infty}^{+\infty} \exp\left(\frac{im}{2\hbar\epsilon} \sum_{i=0}^{N-1} (q_{i+1} - q_i)^2 \right) \mathrm{d}q_1\, \mathrm{d}q_2\, \dots\, \mathrm{d}q_{N-1}. \tag{1.1.45}$$

Carrying out the integration of each of these Gaussian functions in turn gives

$$K(q'', t''; q', t') = \lim_{\substack{N\to\infty \\ \epsilon\to 0}} A \left(\frac{2\pi\hbar\epsilon i}{m} \right)^{N/2} \left(\frac{m}{2\pi\hbar i N\epsilon} \right)^{1/2} \exp\left(\frac{im}{2\hbar N\epsilon} (q_N - q_0)^2 \right). \tag{1.1.46}$$

For the limit of $N \to \infty$, $\epsilon \to 0$ and $N\epsilon \to (t_N - t_0)$ to exist, it is clear the normalisation factor must be

$$A = \left(\frac{2\pi\hbar\epsilon i}{m} \right)^{-N/2}. \tag{1.1.47}$$

Feynman's path integral approach is then commonly written as

$$K(q'', t''; q', t') = \int \mathcal{D}[q(t)] \mathrm{e}^{iS/\hbar} \tag{1.1.48}$$

where

$$\int \mathcal{D}[q(t)] = \lim_{\substack{N\to\infty \\ \epsilon\to 0}} \left(\frac{2\pi\hbar\epsilon i}{m} \right)^{-N/2} \int_{-\infty}^{+\infty} \int_{-\infty}^{+\infty} \dots \int_{-\infty}^{+\infty} \mathrm{d}q_1\, \mathrm{d}q_2\, \dots\, \mathrm{d}q_{N-1}. \tag{1.1.49}$$

The path integral approach is mathematically equivalent to the Schrödinger formulation of quantum mechanics, however the path integral approach is global and determines what occurs over an entire time period, whereas Schrödinger mechanics determines what occurs in the next infinitesimal time period. As the path integral approach is simply an alternative viewpoint on quantum mechanics to the Schrödinger equation, applying it still suffers from exponential scaling, and finding the correct path integral can be difficult. However,

conceptually the ideas it presents can be used to develop other methods, and the following section uses the path integral approach to derive the semiclassical propagator.

1.1.5 The Semiclassical (van Vleck-Gutzwiller) Propagator

A semiclassical approximation to the propagator, known as the van Vleck propagator, was originally derived based on WKB theory [15]. However, it can also be obtained via path integrals by considering all classical paths plus second order corrections from functional variations around the classical paths

$$K_{\mathrm{SC}}(q'',t'';q',t') = \left(\frac{m}{2\pi i\hbar(t''-t')}\right)^{1/2} \sum_{\substack{\text{classical}\\ \text{paths}}} \int \mathcal{D}[q(t)] \mathrm{e}^{i(S+\delta S+\frac{\delta^2 S}{2})/\hbar}. \tag{1.1.50}$$

For classical paths $\delta S = 0$, and using the expansion of $\delta^2 S$ given in Eq. (1.1.12), a series of Gaussian integrals may be obtained for the above expression that can be evaluated to give

$$K_{\mathrm{SC}}(q'',t'';q',t') = \sum_{\substack{\text{classical}\\ \text{paths}}} \left(\frac{1}{2\pi i\hbar}\right)^{1/2} \left(\frac{\partial^2 S}{\partial q''\partial q'}\right)^{1/2} \mathrm{e}^{iS/\hbar}. \tag{1.1.51}$$

The phase and magnitude of this expression can be factored out explicitly by taking into account the number of negative eigenvalues (i.e. the Morse index ν) in the expansion of $\delta^2 S$

$$K_{\mathrm{SC}}(q'',t'';q',t') = \sum_{\substack{\text{classical}\\ \text{paths}}} \left(\frac{1}{2\pi i\hbar}\right)^{1/2} \left|\frac{\partial^2 S}{\partial q''\partial q'}\right|^{1/2} \mathrm{e}^{\frac{iS}{\hbar}-\frac{i\nu\pi}{2}}. \tag{1.1.52}$$

The above is known as the van Vleck-Gutzwiller (VVG) propagator, as the factoring of the van Vleck propagator to include the Morse index was first proposed by Gutzwiller [16].

The VVG propagator is an important semiclassical result, showing that quantum interference can be incorporated to the sum over classical paths via the phase. However, it is not without its numerical difficulties that must be resolved before it can be put to practical use. Considering the following equalities governing the $\frac{\partial^2 S}{\partial q''\partial q'}$ prefactor, derived from the position space derivatives of the action with the Lagrangian in the form of Eq. (1.1.18),

$$-\frac{\partial^2 S}{\partial q''\partial q'} = -\frac{\partial p''}{\partial q'} = \frac{\partial p'}{\partial q''} = \left(\frac{\partial q''}{\partial p'}\right)^{-1}, \tag{1.1.53}$$

it can be seen that it is equal to the inverse of the sensitivity of the final position to the initial momentum. When trajectories that have a broad range of initial momenta lead to the same final position, the value of $\frac{\partial q''}{\partial p'}$ goes to zero, and the VVG propagator explodes to infinity as it is proportional to the inverse of this quantity. These points where trajectories intersect are known as conjugate points or caustics, and the value of the Morse index increases by 1 at them. As well as counting the number of negative eigenvalues in the expansion of $\delta^2 S$, the Morse index therefore also counts the number of times a caustic is encountered. This can be demonstrated clearly with the following identity from Levit

and Smilansky [51, 52]

$$\prod_{n=1}^{\infty} \frac{\lambda_n}{\lambda_n^0} = \frac{M_{qp}}{M_{qp}^0}, \tag{1.1.54}$$

where $M_{qp} = \frac{\partial q''}{\partial p'}$, and λ_n^0 and M_{qp}^0 are eigenvalues and partial derivatives for free particle dynamics, respectively. From this relationship, it can be seen that when M_{qp} goes to zero at a caustic, the product of eigenvalues will also. As the eigenvalues start positive and once they become negative they never return to being positive, it follows that at a caustic one of the eigenvalues becomes zero, and immediately following the caustic it is negative such that the Morse index increases by one.

The M_{qp} partial derivative is also known as an element of the monodromy or stability matrix $\mathbf{M}$, which includes the partial derivatives of final positions and momenta with respect to initial positions and momenta

$$\mathbf{M} = \begin{pmatrix} M_{pp} & M_{pq} \\ M_{qp} & M_{qq} \end{pmatrix} = \begin{pmatrix} \frac{\partial p''}{\partial p'} & \frac{\partial p''}{\partial q'} \\ \frac{\partial q''}{\partial p'} & \frac{\partial q''}{\partial q'} \end{pmatrix}. \tag{1.1.55}$$

This matrix, or elements of it, enters into almost all semiclassical propagators, and another example will be seen in Sec. 1.2.3.

Returning to the VVG propagator, there are further problems with the form given in Eq. (1.1.52), in addition to the caustic issue. Firstly, there are an unspecified number of non-unique trajectories connecting the boundary conditions of points q' and q''. Obtaining these trajectories is a numerically difficult root search problem due to multiple possible values of initial momentum p'. Furthermore, if there are nearby root trajectories, adding their contributions is no longer accurate as a "uniformising" procedure is required that goes beyond the second order correction from functional variations around the classical path [53]. A final problem is that the Morse indices are non-trivial to calculate. Fortunately, these issues may be addressed by the initial value representation (IVR) method, and changing the propagator from coordinate to coherent state or "frozen" Gaussian representation. These alterations permit a useful, tractable semiclassical formulation to be used and are discussed in the following section.

1.2 Initial Value Representations and Frozen Gaussians

The IVR method was first introduced by Miller [10–13] and Marcus [14] with their work on calculating classical S-matrix elements. The S-matrix (or scattering matrix) is a probability amplitude in quantum scattering theory, relating initial and final states of atoms and/or molecules undergoing a collision process. Miller and Marcus demonstrated that a semiclassical approach to the S-matrix, known as the classical S-matrix, can be obtained by considering classical trajectories originating from the initial state, ending at the final state, and carrying an associated phase that incorporates quantum mechanical effects. This is analogous to the semiclassical approximation to the propagator described in the previous section. The additional step they took however, was to negate the numerically difficult root search for final conditions and compute the classical S-matrix as an integral over initial conditions. The following section describes this initial value representation as it pertains to the semiclassical propagator, rather than the classical S-matrix, however the principle applied is the same.

1.2.1 Initial Value Representation of the Semiclassical Propagator

A matrix element of the propagator between some initial state $\psi(q')$ and a final state $\psi(q'')$ can be given as

$$\langle\psi(q'')|\mathrm{e}^{-i\hat{H}(t''-t')/\hbar}|\psi(q')\rangle = \int \mathrm{d}q' \int \mathrm{d}q''\, \psi^*(q'')\, \langle q''|\mathrm{e}^{-i\hat{H}(t''-t')/\hbar}|q'\rangle\, \psi(q'). \tag{1.2.1}$$

Inserting the VVG expression for the propagator into the above gives

$$\langle\psi(q'')|\mathrm{e}^{-i\hat{H}(t''-t')/\hbar}|\psi(q')\rangle = \sum_{\substack{\text{classical}\\ \text{paths}}} \int \mathrm{d}q' \int \mathrm{d}q''\, \psi^*(q'') \left(\frac{1}{2\pi i\hbar}\right)^{\frac{1}{2}} \left|\frac{\partial^2 S}{\partial q''\partial q'}\right|^{\frac{1}{2}} \mathrm{e}^{\frac{iS}{\hbar}-\frac{i\nu\pi}{2}} \psi(q') \tag{1.2.2}$$

where the summation is over all classical trajectories starting at q' and finishing at q'', with multiple possible values of initial momentum p' requiring a root search. The key result of the IVR approach that avoids this root search is to use the following integration relationship

$$\sum_{\substack{\text{classical}\\ \text{paths}}} \mathrm{d}q'' = \mathrm{d}p' \frac{\partial q''(q',p')}{\partial p'}, \tag{1.2.3}$$

which is possible because q'' may be determined from initial positions and momenta, and q' is constant inside the q'' integral. Substitution of this relationship into Eq. (1.2.2) gives

$$\langle\psi(q'')|\mathrm{e}^{-i\hat{H}(t''-t')/\hbar}|\psi(q')\rangle = \int \mathrm{d}q' \int \mathrm{d}p'\, \psi^*(q'') \left(\frac{1}{2\pi i\hbar}\right)^{1/2} \left|\frac{\partial q''}{\partial p'}\right|^{1/2} \mathrm{e}^{\frac{iS}{\hbar}-\frac{i\nu\pi}{2}} \psi(q'). \tag{1.2.4}$$

The above expression is now an integration over only initial conditions (q', p'), hence no difficult root search is required. Furthermore, the partial derivative $\frac{\partial q''}{\partial p'}$ now appears

in the numerator rather than the denominator of the expression meaning that there are no singularities at caustics, the propagator simply equals zero. A number of studies have been performed on this IVR of the VVG propagator, see Refs. [54–63] for further details. Although the IVR of the VVG propagator does overcome some of the difficulties associated with it in its original form, there is another that remains — the evaluation of the Morse indices. This final difficulty is overcome by switching from a coordinate to coherent state basis, which will be described in the following sections with Heller's frozen Gaussian approach, and the subsequent HK method.

1.2.2 Thawed and Frozen Gaussians

Following Miller's work on the classical S-matrix, Heller considered treating dynamics using a Gaussian form for the wavepacket [6,7,64,65]. Initially a formalism was used where the Gaussian was allowed to spread in time [6, 64], retrospectively called the "thawed" Gaussian approach [65], with the wavefunction represented as

$$\Psi(x,t) = \exp\left(\frac{i}{\hbar}\alpha(t)(x-q(t))^2 + \frac{i}{\hbar}p(t)(x-q(t)) + \frac{i}{\hbar}\beta(t)\right). \tag{1.2.5}$$

The parameters α and β are complex and time-dependent, with α representative of the width of the Gaussian and β the phase. The position and momentum centres q and p are real and time-dependent. The evolution of these parameters is found via expansion of the potential in a Taylor series with up to quadratic terms kept

$$V(x) \simeq V(q) + \left.\frac{\mathrm{d}V}{\mathrm{d}x}\right|_{x=q}(x-q) + \frac{1}{2}\left.\frac{\mathrm{d}^2V}{\mathrm{d}x^2}\right|_{x=q}(x-q)^2. \tag{1.2.6}$$

Substitution into the Schrödinger equation, comparison of like powers of $(x-q)$, and defining the energy as $E = p^2/2m + V(q)$ gives

$$\dot{q} = \frac{\partial H}{\partial p} = \frac{p}{m} \tag{1.2.7a}$$

$$\dot{p} = -\frac{\partial H}{\partial q} = -\left.\frac{\mathrm{d}V}{\mathrm{d}x}\right|_{x=q} \tag{1.2.7b}$$

$$\dot{\alpha} = -\frac{1}{2}\left.\frac{\mathrm{d}^2V}{\mathrm{d}x^2}\right|_{x=q} - \frac{2\alpha^2}{m} \tag{1.2.7c}$$

$$\dot{\beta} = \frac{i\hbar\alpha}{m} + p\dot{q} - E = \frac{i\hbar\alpha}{m} + \mathcal{L} \tag{1.2.7d}$$

where $\mathcal{L}$ is the Lagrangian. The Eqs. (1.2.7a) and (1.2.7b) are simply the classical Hamilton's equations of motion as seen in Eqs. (1.1.19) and (1.1.20), and as Eq. (1.2.7d) involves the Lagrangian it can be seen that β will include the action. The motivation behind this approach was given by a quote from Dirac: *"for any dynamical system with a classical analogue, a state for which the classical description is valid as an approximation is represented in quantum mechanics by a wavepacket ... Schrödinger's wave equation fixes how such a wavepacket varies with time, so in order that the classical description may remain*

valid, the wavepacket should remain a wavepacket and should move according to the laws of classical dynamics" [66]. This statement, coupled with the fact that a Gaussian in a harmonic potential remains a Gaussian, and the equations of motion for its position and momentum centres are classical, provided justification for the method. However, a number of deficiencies immediately became apparent: due to the quadratic approximation to the potential, there are naturally errors associated with any potential that is not locally quadratic which grow as the wavepacket spreads [60]. Furthermore, if the potential causes bifurcation of the wavepacket a single Gaussian function cannot represent this.

To remedy these issues, Heller heuristically proposed to use a wavepacket representation consisting of a swarm of Gaussian functions instead, which for mathematical ease had a fixed or "frozen" width parameter. This was then known as the frozen Gaussian approach, with wavefunction representation [7]

$$\Psi(x,t) = \sum_{n=1}^{N} c_n g_n(x, q_n(t), p_n(t)) \tag{1.2.8}$$

where

$$g_n(x, q_n(t), p_n(t)) = \langle x | q_n, p_n \rangle = \left(\frac{\gamma}{\pi}\right)^{1/4} \exp\left(-\frac{\gamma}{2}(x - q_n(t))^2 + \frac{i}{\hbar} p_n(t)(x - q_n(t))\right), \tag{1.2.9}$$

and the c_n carry the initial phase and amplitude of the wavepacket. The centres of each Gaussian function are guided by classical trajectories, as with the thawed Gaussian approach, with the overall motion following a "guiding" trajectory. The phase of the wavepacket is the classical action along the path of the guiding trajectory. The collective motion of the frozen Gaussians was found to provide an accurate description of wavepacket motion, able to account for spreading and contraction, as well as the bifurcation that was not possible with a single Gaussian function. It should be noted that the width parameter is time-independent, and if it is set to $\gamma = m\omega/\hbar$ then the frozen Gaussian is a minimum uncertainty wavepacket, $\Delta q \Delta p = \hbar/2$, also known as a coherent state. The concept of coherent states was first proposed in 1926 by Schrödinger, with their dynamics most closely resembling that of a classical harmonic oscillator [67]. They were subsequently popularised with seminal work by Glauber on the description of photon statistics in 1963 [68–70].

The numerical propagation in Heller's methods depends only on the initial trajectories, similar to the IVR method, so no difficult root search is required. A closer link to the IVR method incorporating the semiclassical propagator was proposed a few years after Heller's work by Herman and Kluk [8, 9].

1.2.3 Herman-Kluk Method

Starting with the VVG propagator (without the explicit dependence on the Morse index), Herman and Kluk twice inserted the resolution of the identity in a basis of frozen Gaussians

$$\hat{I} = \frac{1}{2\pi\hbar} \int \mathrm{d}q \int \mathrm{d}p \; |q,p\rangle \langle q,p| \tag{1.2.10}$$

and carried out stationary phase integrals to obtain

$$K_{\mathrm{HK}}(x',x'') = \frac{1}{2\pi\hbar}\int \mathrm{d}q' \int \mathrm{d}p'\, C(q',p')\mathrm{e}^{iS/\hbar}\,\langle x''|q'',p''\rangle\,\langle q',p'|x'\rangle\,. \tag{1.2.11}$$

The prefactor $C(q',p')$ was missing from Heller's frozen Gaussian method, and is equal to

$$C(q',p') = \left|\frac{1}{2}\left(\frac{\partial p''}{\partial p'} + \frac{\partial q''}{\partial q'} - i\gamma\hbar\frac{\partial q''}{\partial p'} + \frac{i}{\hbar\gamma}\frac{\partial p''}{\partial q'}\right)\right|^{1/2}. \tag{1.2.12}$$

This prefactor ensures theoretical semiclassical rigour in the method, as it is derived from the VVG propagator as opposed to heuristically, leading to an improvement in accuracy over the frozen Gaussian method [63]. It also contains all elements of the monodromy matrix, shown in Eq. (1.1.55). Furthermore, despite not using the form of the VVG propagator with explicit dependence on the Morse index, Kay showed that if the phase of the prefactor is chosen such that it is continuous in time, the Morse index is automatically taken into account [54]. This resolves the final problem with the semiclassical propagator that the initial value representation on its own did not. Finally, the HK method permits better norm conservation than the frozen Gaussian approach (basis sets consisting of a superposition of coherent states do not conserve the norm by default). These factors have lead to the HK method being one of the most popular time-dependent semiclassical treatments.

Further extensive reviews of semiclassical initial value representation methods can be found in Refs. [53, 60–63] and [71]. Whilst semiclassical methods have proven to be very popular, they are not without their drawbacks, as by their very nature they only permit partial treatment of many quantum problems. Subsequent developments have been made from the standpoint of exact quantum mechanics including, but not limited to, the coupled coherent states method.

1.3 Coupled Coherent States (CCS)

The coupled coherent states method of quantum dynamics was first proposed by Shalashilin and Child in 2000 [29], following on from the work by Heller, and Herman and Kluk mentioned in the previous section, along with subsequent research involving Gaussian wavepackets by Metiu *et al.* [72,73], and Shalashilin and Jackson [74]. In the original paper [29] an approach for propagating the wavefunction exactly in a coherent state representation was presented, as opposed to semiclassically in the frozen Gaussian and HK methods. In CCS the time-dependent coherent state basis set is guided by classical trajectories, similar to the frozen Gaussian and HK methods. However, unlike those methods the coherent states are paired with fully quantum amplitudes. It is these amplitudes that ensure CCS is a fully quantum technique, whilst the guiding trajectories keep the basis in the dynamically important region and economise basis set size. CCS depends only on the initial choice of coherent state basis and amplitudes, therefore it may be thought of as a fully quantum initial value representation method.

1.3.1 Properties of Coherent States

Before proceeding any further to describe the CCS method, it is worth briefly reviewing some properties of coherent states that will be useful in determining the CCS working equations. In CCS so called $|z\rangle$ notation is used, rather than the $|q,p\rangle$ notation used in the frozen Gaussian approach. A coherent state in $|z\rangle$ notation is represented as

$$\langle x|z\rangle = \left(\frac{\gamma}{\pi}\right)^{1/4} \exp\left(-\frac{\gamma}{2}(x-q)^2 + \frac{i}{\hbar}p(x-q) + \frac{ipq}{2\hbar}\right), \tag{1.3.1}$$

where an additional phase factor $\exp\left(\frac{ipq}{2\hbar}\right)$ has appeared compared to Eq. (1.2.9) due to the change of notation. The width parameter $\gamma = m\omega/\hbar$. Coherent states are eigenfunctions of the creation and annihilation operators, respectively

$$\langle z|\,\hat{a}^\dagger = \langle z|\,z^* \tag{1.3.2a}$$

$$\hat{a}\,|z\rangle = z\,|z\rangle\,, \tag{1.3.2b}$$

where the creation and annihilation operators are given by

$$\hat{a}^\dagger = \sqrt{\frac{\gamma}{2}}\hat{q} - \frac{i}{\hbar}\sqrt{\frac{1}{2\gamma}}\hat{p} \tag{1.3.3a}$$

$$\hat{a} = \sqrt{\frac{\gamma}{2}}\hat{q} + \frac{i}{\hbar}\sqrt{\frac{1}{2\gamma}}\hat{p}. \tag{1.3.3b}$$

In the context of the quantum harmonic oscillator, the creation and annihilation operators are also known as the raising and lowering operators, and they act on eigenfunctions of the harmonic oscillator to generate another eigenfunction with an eigenvalue 1 larger or smaller, respectively. The eigenvalues of the creation and annihilation operators them-

selves z and z^* can be used to label a coherent state, and from Eqs. (1.3.3a) and (1.3.3b) it can be seen they are given by

$$z^* = \sqrt{\frac{\gamma}{2}}q - \frac{i}{\hbar}\sqrt{\frac{1}{2\gamma}}p \tag{1.3.4a}$$

$$z = \sqrt{\frac{\gamma}{2}}q + \frac{i}{\hbar}\sqrt{\frac{1}{2\gamma}}p. \tag{1.3.4b}$$

An important consequence of the above is that one may write a Hamiltonian in terms of creation and annihilation operators rather than position and momentum operators. A normal ordered Hamiltonian may then be obtained when the creation operators precede the annihilation ones

$$\hat{H}(\hat{q},\hat{p}) = \hat{H}(\hat{a},\hat{a}^\dagger) = H^{\text{ord}}(\hat{a}^\dagger,\hat{a}). \tag{1.3.5}$$

From this, matrix elements of the Hamiltonian are simple to calculate in a coherent state basis

$$\langle z'|H^{\text{ord}}(\hat{a}^\dagger,\hat{a})|z\rangle = \langle z'|z\rangle\, H^{\text{ord}}(z'^*,z). \tag{1.3.6}$$

Coherent states form a non-orthogonal basis set, so the overlap $\langle z'|z\rangle$ in Eq. (1.3.6) is not the Dirac delta function, but instead is given by

$$\langle z'|z\rangle = \exp\left(z'^*z - \frac{1}{2}(z'^*z' + z^*z)\right). \tag{1.3.7}$$

Another important property is that coherent states form an overcomplete basis set, meaning that any coherent state can be expressed as a superposition of all others (completeness), even if a basis vector is removed (overcompleteness). This is represented by

$$|z'\rangle = \frac{1}{\pi}\int \mathrm{d}^2z\, |z\rangle\,\langle z|z'\rangle\,, \tag{1.3.8}$$

where $\mathrm{d}^2z = \frac{\mathrm{d}q\mathrm{d}p}{2\hbar}$. An expression for the identity operator in the coherent state basis then follows straightforwardly

$$\hat{I} = \frac{1}{\pi}\int \mathrm{d}^2z\, |z\rangle\,\langle z|\,. \tag{1.3.9}$$

The identity operator can then be used to express the wavefunction $|\Psi\rangle$ in a coherent state representation

$$|\Psi\rangle = \hat{I}\,|\Psi\rangle = \frac{1}{\pi}\int \mathrm{d}^2z\, |z\rangle\,\langle z|\Psi\rangle\,. \tag{1.3.10}$$

A final useful relationship is that M-dimensional coherent states may be generated from the product of 1-dimensional coherent states for multidimensional problems

$$|\mathbf{z}\rangle = \prod_{m=1}^{M} |z^{(m)}\rangle\,. \tag{1.3.11}$$

Note that in the multidimensional representation, singular powers of π will be changed to π^M. Henceforth, the multidimensional representation shall be utilised.

1.3.2 Development of Working Equations for CCS

As mentioned in the introduction to this section, the premise of the CCS method of multidimensional quantum dynamics is that a time-dependent basis set of coherent states is guided by classical trajectories, whilst being paired with fully quantum mechanical time-dependent amplitudes. As with Heller's frozen Gaussian method, the centre of each coherent state is guided by a classical trajectory, and this classical trajectory may be found by applying the principle of stationary action. The Lagrangian in $\mathbf{z}$ notation can be written as

$$\mathcal{L}[\mathbf{z}(t)] = \frac{i\hbar}{2}(\mathbf{z}^*\dot{\mathbf{z}} - \dot{\mathbf{z}}^*\mathbf{z}) - H^{\mathrm{ord}}(\mathbf{z}^*, \mathbf{z}). \tag{1.3.12}$$

Applying the principle of stationary action, Eq. (1.1.3), to $\mathbf{z}$ and $\mathbf{z}^*$ in turn, a pair of Euler-Lagrange equations may be obtained

$$\frac{\partial \mathcal{L}}{\partial \mathbf{z}^*} - \frac{\mathrm{d}}{\mathrm{d}t}\frac{\partial \mathcal{L}}{\partial \dot{\mathbf{z}}^*} = 0 \tag{1.3.13a}$$

$$\frac{\partial \mathcal{L}}{\partial \mathbf{z}} - \frac{\mathrm{d}}{\mathrm{d}t}\frac{\partial \mathcal{L}}{\partial \dot{\mathbf{z}}} = 0. \tag{1.3.13b}$$

These may each be solved to arrive at the trajectories for the basis functions

$$\dot{\mathbf{z}} = -\frac{i}{\hbar}\frac{\partial H^{\mathrm{ord}}(\mathbf{z}^*, \mathbf{z})}{\partial \mathbf{z}^*} \tag{1.3.14a}$$

$$\dot{\mathbf{z}}^* = \frac{i}{\hbar}\frac{\partial H^{\mathrm{ord}}(\mathbf{z}^*, \mathbf{z})}{\partial \mathbf{z}}, \tag{1.3.14b}$$

which are simply Hamilton's equations, a $\mathbf{z}$ notation analogue of Eqs. (1.2.7a) and (1.2.7b). However, it should be noted that the ordered Hamiltonian is subtly different to the classical Hamiltonian, due to terms arising from the commutator between powers of $\hat{a}'$ and $\hat{a}$, with $H^{\mathrm{ord}} = H^{\mathrm{cl}} + H^{\mathrm{comm}}$. These terms add small quantum corrections to the classical Hamiltonian, influencing the trajectories due to the average over the ordered Hamiltonian.

The TDSE may be cast into a coherent state integro-differential form via substitution of the wavefunction in coherent state representation, Eq. (1.3.10), closing with a basis bra $\langle \mathbf{z}|$ and accounting for the time-dependence of the basis

$$\begin{aligned}\frac{\mathrm{d}\langle \mathbf{z}|\Psi\rangle}{\mathrm{d}t} &= \langle \dot{\mathbf{z}}|\Psi\rangle + \langle \mathbf{z}|\dot{\Psi}\rangle \\ &= \int \left[\langle \dot{\mathbf{z}}|\mathbf{z}'\rangle - \frac{i}{\hbar}\langle \mathbf{z}|\hat{H}|\mathbf{z}'\rangle\right]\langle \mathbf{z}'|\Psi\rangle \,\frac{\mathrm{d}^2\mathbf{z}'}{\pi^M}.\end{aligned} \tag{1.3.15}$$

The term $\langle \dot{\mathbf{z}}|\mathbf{z}'\rangle$ is given by

$$\langle \dot{\mathbf{z}}|\mathbf{z}'\rangle = \langle \mathbf{z}|\mathbf{z}'\rangle\left(\dot{\mathbf{z}}^*\mathbf{z}' - \frac{1}{2}\left(\mathbf{z}\dot{\mathbf{z}}^* + \dot{\mathbf{z}}\mathbf{z}^*\right)\right). \tag{1.3.16}$$

It then follows from Eqs. (1.3.6), (1.3.12), (1.3.14) and (1.3.16) that Eq. (1.3.15) can be written as

$$\frac{\mathrm{d}\langle \mathbf{z}|\Psi\rangle}{\mathrm{d}t} = \int \langle \mathbf{z}|\mathbf{z}'\rangle\left(\frac{i}{\hbar}\mathcal{L}[\mathbf{z}(t)] - \frac{i}{\hbar}\delta^2 H^{\mathrm{ord}}(\mathbf{z}^*, \mathbf{z}')\right)\langle \mathbf{z}'|\Psi\rangle \,\frac{\mathrm{d}^2\mathbf{z}'}{\pi^M}, \tag{1.3.17}$$

where $\delta^2 H^{\text{ord}}(\mathbf{z}^*, \mathbf{z}')$ is given by

$$\begin{aligned}\delta^2 H^{\text{ord}}(\mathbf{z}^*, \mathbf{z}') &= H^{\text{ord}}(\mathbf{z}^*, \mathbf{z}') - H^{\text{ord}}(\mathbf{z}^*, \mathbf{z}) + i\hbar\dot{\mathbf{z}}^*(\mathbf{z}' - \mathbf{z}) \\ &= H^{\text{ord}}(\mathbf{z}^*, \mathbf{z}') - H^{\text{ord}}(\mathbf{z}^*, \mathbf{z}) - \frac{\partial H^{\text{ord}}(\mathbf{z}^*, \mathbf{z})}{\partial \mathbf{z}}(\mathbf{z}' - \mathbf{z}).\end{aligned} \tag{1.3.18}$$

If the following coherent state wavefunction representation is used

$$\langle \mathbf{z}|\Psi\rangle = C[\mathbf{z}(t)]\mathrm{e}^{iS[\mathbf{z}(t)]/\hbar}, \tag{1.3.19}$$

where $S[\mathbf{z}(t)]$ is the action in $\mathbf{z}$ notation given by virtue of the Lagrangian in Eq. (1.3.12) as

$$S[\mathbf{z}(t)] = \int \left[\frac{i\hbar}{2}\left(\mathbf{z}^*\dot{\mathbf{z}} - \dot{\mathbf{z}}^*\mathbf{z}\right) - H^{\text{ord}}(\mathbf{z}^*, \mathbf{z})\right] \mathrm{d}t, \tag{1.3.20}$$

then the time-dependence of the amplitudes $C[\mathbf{z}(t)]$ is given as

$$\frac{\mathrm{d}C[\mathbf{z}(t)]}{\mathrm{d}t} = -\frac{i}{\hbar}\int \langle \mathbf{z}|\mathbf{z}'\rangle\, \delta^2 H^{\text{ord}}(\mathbf{z}^*, \mathbf{z}')C[\mathbf{z}'(t)]\mathrm{e}^{i(S[\mathbf{z}'(t)]-S[\mathbf{z}(t)])/\hbar}\frac{\mathrm{d}^2\mathbf{z}'}{\pi^M}. \tag{1.3.21}$$

This allows the amplitudes coupled to the coherent state basis set to be propagated in a fully quantum manner, and is one of the main working equations of the CCS method, along with Eq. (1.3.14) that guides the trajectories. This result was the nascent methodology behind CCS published in the initial paper [29].

In practice, the integral given in Eq. (1.3.21) should be evaluated by a finite sum. The simplest initial idea was to replace the integral over $\mathrm{d}^2\mathbf{z}$ with a Riemann sum over small volumes of phase space

$$\frac{\mathrm{d}C_k}{\mathrm{d}t} = -\frac{i}{\hbar}\sum_{l=1}^{K} \langle \mathbf{z}_k|\mathbf{z}_l\rangle\, \delta^2 H^{\text{ord}}(\mathbf{z}_k^*, \mathbf{z}_l)C_l\mathrm{e}^{i(S_l-S_k)/\hbar}\frac{\Delta^2\mathbf{z}_l}{\pi^M}. \tag{1.3.22}$$

The sum is over K configurations, with $\Delta^2\mathbf{z} = \Delta\mathbf{q}\Delta\mathbf{p}/(2\hbar)$ the average phase space volume for each coherent state.

This discretisation was employed for the first few studies with CCS [29, 42, 43, 75], however it is non-unitary, and subsequently a unitary representation was proposed [30]. The unitary discretisation represents the identity operator as

$$\hat{I} = \sum_{k,l=1}^{K} |\mathbf{z}_k\rangle\, (\mathbf{\Omega}^{-1})_{kl}\, \langle \mathbf{z}_l|\,, \tag{1.3.23}$$

where $(\mathbf{\Omega}^{-1})_{kl}$ is an element of the inverse of the overlap matrix, $\mathbf{\Omega}_{kl} = \langle \mathbf{z}_k|\mathbf{z}_l\rangle$. When acting on $|\Psi\rangle$, this produces a discretised version of the wavefunction as

$$|\Psi\rangle = \sum_{k,l=1}^{K} |\mathbf{z}_k\rangle\, (\mathbf{\Omega}^{-1})_{kl}\, \langle \mathbf{z}_l|\Psi\rangle = \sum_{k,l=1}^{K} |\mathbf{z}_k\rangle\, (\mathbf{\Omega}^{-1})_{kl}C_l\mathrm{e}^{iS_l/\hbar}, \tag{1.3.24}$$

and discretised version of the coherent state integro-differential equation, Eq. (1.3.15), as

$$\frac{\mathrm{d}\langle \mathbf{z}_j|\Psi\rangle}{\mathrm{d}t} = \sum_{k,l=1}^{K}\left[\langle \dot{\mathbf{z}}_j|\mathbf{z}_k\rangle - \frac{i}{\hbar}\langle \mathbf{z}_j|\mathbf{z}_k\rangle\langle \mathbf{z}_j|\hat{H}|\mathbf{z}_k\rangle\right](\Omega^{-1})_{kl}\langle \mathbf{z}_l|\Psi\rangle\,. \tag{1.3.25}$$

Repeating the derivation of Eq. (1.3.21) in this discrete form yields

$$\frac{\mathrm{d}C_j}{\mathrm{d}t} = -\frac{i}{\hbar}\sum_{k,l=1}^{K}\langle \mathbf{z}_j|\mathbf{z}_k\rangle\,\delta^2 H^{\mathrm{ord}}(\mathbf{z}_j^*,\mathbf{z}_k)(\boldsymbol{\Omega}^{-1})_{kl}C_l\mathrm{e}^{i(S_l-S_j)/\hbar}. \tag{1.3.26}$$

This approach was used until a paper in 2008 [76] used a slightly modified representation of the wavefunction that had been suggested previously in a 2004 review [30]. This in turn was based on work by Miller in 2002 comparing the HK method to an exact expansion of the wavefunction in coherent states [77]. The modified representation of the wavefunction gives an integral expression of it as

$$|\Psi\rangle = \int D[\mathbf{z}'(t)]\mathrm{e}^{iS[\mathbf{z}'(t)]/\hbar}\,|\mathbf{z}'\rangle\,\frac{\mathrm{d}^2\mathbf{z}'}{\pi^M}. \tag{1.3.27}$$

Substituting this into the Schrödinger equation, closing with a basis bra $\langle\mathbf{z}|$ and performing various substitutions, as with the derivation for $C[\mathbf{z}(t)]$, yields

$$\int\langle \mathbf{z}|\mathbf{z}'\rangle\,\frac{\mathrm{d}D[\mathbf{z}'(t)]}{\mathrm{d}t}\mathrm{e}^{iS[\mathbf{z}'(t)]/\hbar}\,\frac{\mathrm{d}^2\mathbf{z}'}{\pi^M} = -\frac{i}{\hbar}\int\langle \mathbf{z}|\mathbf{z}'\rangle\,\delta^2 H^{\mathrm{ord}*}(\mathbf{z}^*,\mathbf{z}')D[\mathbf{z}'(t)]\mathrm{e}^{iS[\mathbf{z}'(t)]/\hbar}\,\frac{\mathrm{d}^2\mathbf{z}'}{\pi^M}, \tag{1.3.28}$$

where

$$\begin{aligned}\delta^2 H^{\mathrm{ord}*}(\mathbf{z}^*,\mathbf{z}') &= H^{\mathrm{ord}}(\mathbf{z}^*,\mathbf{z}') - H^{\mathrm{ord}}(\mathbf{z}'^*,\mathbf{z}') - i\hbar\dot{\mathbf{z}}'(\mathbf{z}^*-\mathbf{z}'^*)\\ &= H^{\mathrm{ord}}(\mathbf{z}^*,\mathbf{z}') - H^{\mathrm{ord}}(\mathbf{z}'^*,\mathbf{z}') - \frac{\partial H^{\mathrm{ord}}(\mathbf{z}'^*,\mathbf{z}')}{\partial\mathbf{z}'^*}(\mathbf{z}^*-\mathbf{z}'^*).\end{aligned} \tag{1.3.29}$$

To discretise this form of the CCS equation, rather than perform an identity operation, the following discrete wavefunction ansatz for Eq. (1.3.27) may be given

$$|\Psi\rangle = \sum_{k=1}^{K} D_k\mathrm{e}^{iS_k/\hbar}\,|\mathbf{z}_k\rangle\,. \tag{1.3.30}$$

Repeating the derivation of Eq. (1.3.28) in this discrete form yields

$$\sum_{l=1}^{K}\langle \mathbf{z}_k|\mathbf{z}_l\rangle\,\mathrm{e}^{iS_l/\hbar}\frac{\mathrm{d}D_l}{\mathrm{d}t} = -\frac{i}{\hbar}\sum_{l=1}^{K}\langle \mathbf{z}_k|\mathbf{z}_l\rangle\,\delta^2 H^{\mathrm{ord}*}(\mathbf{z}_k^*,\mathbf{z}_l)\mathrm{e}^{iS_l/\hbar}D_l. \tag{1.3.31}$$

This set of linear equations for D obviates the need to calculate the inverse of the overlap matrix like for C in Eq. (1.3.26), which could potentially be problematic if the overlap matrix is large and sparse. It can also be seen that the relationship between the C and D amplitudes is given by

$$D_k\mathrm{e}^{iS_k/\hbar} = \sum_{l=1}^{K}(\boldsymbol{\Omega}^{-1})_{kl}C_l\mathrm{e}^{iS_l/\hbar}. \tag{1.3.32}$$

The latter form of the discrete CCS equations involving D amplitudes have been used from 2008 onwards, are a foundation for the multiconfigurational Ehrenfest method that will be reviewed in Sec. 1.4, and is the form of the equations used in this work.

Several attractive features of the CCS formalism presented have been noted previously [29, 30, 42], such as the C and D amplitudes having a smooth time-dependence due to being paired with the phase factor $\mathrm{e}^{iS/\hbar}$. Also, the expressions for $\delta^2 H^{\mathrm{ord}}(\mathbf{z}^*, \mathbf{z}')$ and $\delta^2 H^{\mathrm{ord}*}(\mathbf{z}^*, \mathbf{z}')$ vanish for $\mathbf{z}' = \mathbf{z}$, are small for close lying coherent states, and the overlap $\langle \mathbf{z} | \mathbf{z}' \rangle$ vanishes for remote coherent states. The coupling is therefore almost always small and sparse. Finally, by virtue of the Liouville theorem mentioned in Sec. 1.1.2, as the trajectories are guided by Hamiltonian mechanics the volume occupied by them does not change from an initial time to some time later $\mathrm{d}^2\mathbf{z}(t) = \mathrm{d}^2\mathbf{z}(0)$. This means the integrals in Eqs. (1.3.21) and (1.3.28) may be performed over the initial phase space and biased to the peak of the initial propagating wavefunction, yielding a distribution for the initial coherent states. This permits importance and Monte Carlo sampling to allow the initial basis to best represent the wavefunction. This basis set sampling is a key feature of CCS, permitting accuracy of the calculation and reduction in basis set size as long as it is performed correctly. Many different methods to approach this initial sampling have been suggested over the years, and the following section will review them, alongside a brief introduction to Monte Carlo and importance sampling.

1.3.3 Basis Set Sampling in CCS

A significant proportion of the accuracy of a CCS calculation depends upon an appropriate choice of sampling for the initial coherent state basis functions in phase space. A good initial sample means that the initial wavefunction is well represented, the number of basis functions required are minimised, and thereafter the trajectories will keep the basis in the dynamically important region. A number of different approaches for doing this have been developed over the years.

In the paper that introduced the CCS formalism [29], a static uniform rectangular grid was used where the phase space volume of each of the basis functions was used to carry out the Riemann sum in Eq. (1.3.22). A moving grid was also tested, guided by an average over each of the basis functions trajectories. The possibility of using Monte Carlo and importance sampling to evaluate the integral in Eq. (1.3.21) was also mentioned here. The Monte Carlo method relies on random sampling of points to approximate an integral, and importance sampling samples the random points from a probability distribution that aims to place more points where the contribution from the integrand is high or "important". As a straightforward example, the integral

$$I = \int_a^b f(x)\,\mathrm{d}x \tag{1.3.33}$$

may be evaluated in a Monte Carlo fashion by using a set of N uniform randomly dis-

tributed variables $X_i \in [a, b]$ to give

$$I \approx (b-a)\frac{1}{N}\sum_{i=1}^{N} f(X_i). \tag{1.3.34}$$

Importance sampling may be incorporated by noting that the integral may be written as

$$I = \int_a^b \frac{f(x)}{P(x)} P(x)\,\mathrm{d}x, \tag{1.3.35}$$

where $P(x)$ is a probability distribution that can be used to generate the random variables X_i to approximate the integral as

$$I \approx (b-a)\frac{1}{N}\sum_{i=1}^{N} \frac{f(X_i)}{P(X_i)}. \tag{1.3.36}$$

As long as an appropriate probability distribution is chosen to bias the random points to the important parts of the integral, the accuracy of the Monte Carlo integration will be improved for a given number of samples N.

Returning to initial CCS paper [29], it was shown that Eq. (1.3.21) can be replaced by

$$\frac{\mathrm{d}C[\mathbf{z}(t)]}{\mathrm{d}t} = -\frac{i}{\hbar}\int \langle \mathbf{z}(t)|\mathbf{z}'(t)\rangle\, \delta^2 H^{\mathrm{ord}}(\mathbf{z}^*(t), \mathbf{z}'(t)) \mathrm{e}^{i(S[\mathbf{z}'(t)]-S[\mathbf{z}(t)])/\hbar} \frac{C[\mathbf{z}'(t)]}{f[\mathbf{z}'(0)]} f[\mathbf{z}'(0)]\, \frac{\mathrm{d}^2\mathbf{z}'(0)}{\pi^M}, \tag{1.3.37}$$

where the Liouville theorem has been utilised to perform the integration over the initial phase space $\mathrm{d}^2\mathbf{z}(0)$, and $f[\mathbf{z}'(0)]$ is a distribution function from which the initial coherent state basis functions may be sampled in a Monte Carlo fashion, biased to the initial wavefunction. The integral can then be computed by

$$\frac{\mathrm{d}C_k[\mathbf{z}_k(t)]}{\mathrm{d}t} = -\frac{i}{\hbar}\sum_{l=1}^{K} \langle \mathbf{z}_k(t)|\mathbf{z}_l(t)\rangle\, \delta^2 H^{\mathrm{ord}}(\mathbf{z}_k^*(t), \mathbf{z}_l(t)) \mathrm{e}^{i(S_l[\mathbf{z}_l(t)]-S_k[\mathbf{z}_k(t)])/\hbar} \frac{C_l[\mathbf{z}_l(t)]}{f[\mathbf{z}_l(0)]\pi^M}. \tag{1.3.38}$$

Quite often the initial wavefunction is a Gaussian, so a common choice for the distribution function in CCS is a Gaussian distribution centred around initial coordinates and momenta $\mathbf{z}(0)$

$$f(\mathbf{z}) \propto \exp\left(-\sigma|\mathbf{z}-\mathbf{z}(0)|^2\right). \tag{1.3.39}$$

The parameter σ is a compression factor determining the width of the distribution. Although an initial wavefunction that is Gaussian is being represented by Gaussians, the basis must be sampled sufficiently to allow proper spreading in time. When the initial wavefunction is not Gaussian, a distribution function can be obtained from $|\langle z|\Psi\rangle|^2$. The coherent state derivative of this function may be obtained to find its maximum and allow the distribution to be centred around it.

Fig. 1.1 demonstrates the economisation of basis set size that may be obtained by this biased random sampling combined with the trajectory guided basis functions, compared

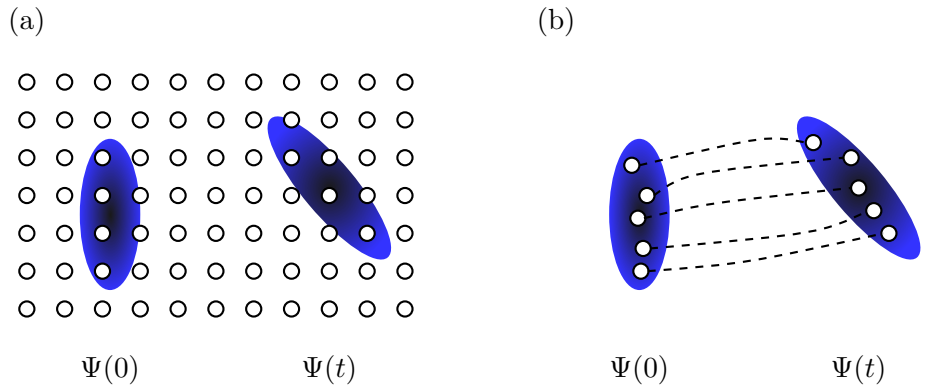

Figure 1.1: Representation and propagation of a wavefunction via (a) grid-based sampling and (b) trajectory guided methods with biased random sampling.

to traditional grid-based sampling. In the grid-based sampling method each basis function enters into the calculation at all times, even when not dynamically relevant, whereas CCS seeks to only contain basis functions that are dynamically relevant at all times. This allows a CCS calculation with random sampling to scale in principle quadratically with respect to basis set size, compared to exponentially with grid-based sampling.

A 2008 paper by Shalashilin and Child provided an account of basis set sampling techniques in CCS, covering two that had been used in previous applications and a third new technique [76]. One of the two previous techniques was that of the random sampling mentioned above (also known as a "swarm"), whilst another previously used but unnamed technique was dubbed "pancake" sampling. Pancake sampling is used when there are two (or more) different types of mode in a particular system that require different distributions for accurate representation of the initial wavefunction, such as in a system-bath problem. In the example presented of a Henon-Heiles potential, a Gaussian distribution was used for both the system and bath, but with different compression parameters for each. More generally, different distributions may be used for different modes to qualify as pancake sampling. The third sampling technique, which had not been utilised before, was that of a "train" basis. In this sampling technique batches of coherent state basis functions are initiated on the same trajectory but with successive time delays, producing "carriages" of coherent state basis functions that together form a "train". The idea behind this methodology was to to combine the beneficial properties of random sampling and regular grids (good scaling with dimensionality and fast convergence, respectively), whilst minimising the undesired properties of each (slow convergence and poor scaling, respectively). Also, for systems where the coherent state basis spreads rapidly over phase space and loses coupling, the trains will remain coupled to one another.

An additional technique proposed to tackle the issue of the basis spreading rapidly over phase space and uncoupling is that of adaptive reprojection [78]. In this approach the basis is initially sampled in a usual way by a regular grid, random swarm, or other distribution, then during the propagation when the basis functions are beginning to run away from one another any trajectories not significantly contributing to the propagation are discarded, and the basis is reprojected back onto the initial distribution. The time

for reprojection is user defined, whilst a quantity C'_j is calculated to determine which trajectories should be discarded

$$C'_j = \sum_{k=1}^{K} \langle \mathbf{z}_j^{\text{init}} | \mathbf{z}_k \rangle \, D_k \mathrm{e}^{iS_k/\hbar}. \tag{1.3.40}$$

Any values of C'_j that do not satisfy the condition

$$|C'_j| \geq \zeta \tag{1.3.41}$$

correspond to trajectories $\mathbf{z}_j$ that should be discarded, where ζ is a user defined parameter that controls how much of the basis is to be discarded. Once those trajectories are discarded K' trajectories remain, and the wavefunction is reprojected back onto the initial distribution

$$\begin{aligned} |\Psi\rangle &= \sum_{i,j=1}^{K'} \sum_{k=1}^{K} |\mathbf{z}_i^{\text{init}}\rangle \, (\mathbf{\Omega}_{\text{init}}^{-1})_{ij} \, \langle \mathbf{z}_j^{\text{init}} | \mathbf{z}_k \rangle \, D_k \mathrm{e}^{iS_k/\hbar} \\ &= \sum_{i=1}^{K'} D'_i \, |\mathbf{z}_i^{\text{init}}\rangle \, . \end{aligned} \tag{1.3.42}$$

The new amplitude D'_i ensures that the wavefunction remains unchanged, and is calculated from the set of linear equations

$$C'_j = \langle \mathbf{z}_i^{\text{init}} | \mathbf{z}_j^{\text{init}} \rangle \, D'_i, \tag{1.3.43}$$

where the action is set to 0.

All of these sampling techniques have been used with CCS for a variety of applications that are reviewed in the following section.

1.3.4 Applications of CCS

The first application of CCS, in the paper that introduced the formalism, was simply to a Morse oscillator in 1D [29]. The probability distribution of the wavefunction at the end of the calculation was compared to the exact split-operator Fourier transform (SOFT) method [3]. It was also compared to the HK method where it was noted that an advantage CCS possessed (aside from being fully quantum) was that there are no problems arising from exponentially growing prefactors.

A second application proved the effectiveness of CCS in combating a fully quantum problem, and the advantage it possessed over semiclassical methods [75]. A 1D tunneling problem was considered, and characteristic beatings in the autocorrelation function were observed. This allowed tunneling splittings to be calculated that were seen to be in good agreement with the SOFT method. Contrastingly, no beating pattern was observed in the autocorrelation function when using the HK method [79]. A 2D problem was also considered, but convergence could only be achieved for times much shorter than the beating

period. However, the number of trajectories needed for this was an order of magnitude less than the HK method.

A following paper in the same year introduced multidimensional equations for CCS that were presented in Sec. 1.3.2 [42]. This allowed the full potential of CCS to be realised, as the ability to sample the initial coherent states in a Monte Carlo fashion and benefit from the improved mathematical scaling mentioned in the previous section could be exploited. The Henon-Heiles potential was investigated in 2D, 6D, 10D and 14D; with the latter dimensions being out of reach for traditional grid sampling methods. To illustrate this point, the 2D problem was found to be propagated accurately using sampling from a grid, whilst the 6D, 10D and 14D problems could not and required importance sampling for convergence. However, it was observed that the use of importance sampling resulted in the initially compact sample spreading over a large phase volume and uncoupling, imposing a long time limit on the technique. Note that this does not imply a breakdown of Liouville's theorem, because as the trajectories uncouple they spread out into "filaments" that occupy small volumes of phase space that in total are the same as the initial compact distribution. The filaments themselves are simply well spread in phase space. The results from the Henon-Heiles potential were compared to the HK method, where close agreement was found [80]. A subsequent thorough comparison of CCS with the HK method, and Heller's frozen and thawed Gaussians displayed how they can be derived as approximate analytic solutions of the CCS integro-differential Schrödinger equation [81].

The first application of CCS to a real molecule, simulating Fermi-resonance and intramolecular vibrational energy redistribution of CHD_3, illustrated the capability to provide real quantum mechanical molecular models [43]. All 9 vibrational modes were taken into account for this simulation, and the advantages CCS possesses with respect to scaling with dimensionality were demonstrated once more. Furthermore, due to appropriate initial conditions a narrow part of the spectrum corresponding to the Fermi-resonance was able to be focussed on. However, the long time limit of the technique was observed once more with the autocorrelation function exhibiting decay due to noise from the Monte Carlo sampling. Despite this, it was observed that noise could be reduced to a level sufficient for obtaining eigenvalues from the autocorrelation function.

Further real molecular systems were then tested, with CCS being applied to the far infrared absorption spectrum of a water trimer [44], and the absorption spectrum of pyrazine [45]. In the former application, to produce the infrared absorption spectrum of a water trimer the dipole moment autocorrelation function was calculated which required propagation in imaginary time. A couple of issues arose whilst doing this, firstly, in complex time the coordinates $\mathbf{q}$ and momenta $\mathbf{p}$ are imaginary so $\mathbf{z}^*$ must be replaced by $\mathbf{z}^\dagger$ in all CCS working equations as it is no longer conjugate to $\mathbf{z}$. Secondly, classical trajectories are unstable when propagated in imaginary time, so after a short time step they were re-projected back onto their initial distribution. The latter application to pyrazine is a common benchmark for testing multidimensional quantum mechanical techniques, and a number of methods have previously attempted to treat the problem [20, 82–84]. Prop-

agation over two electronic potential energy surfaces (PESs) is required, unlike one in all previous CCS applications. This was achieved by the mapping Hamiltonian approach [85] that combines the 24 vibrational modes with the 2 electronic modes to create a 26D problem. The results were shown to compare reasonably well with experiment [86] and the HK method [84], however the spectrum was missing some of the features that appeared in the MCTDH calculation [20, 82].

Following this, the first application of CCS to electron dynamics was published [87,88], as previously only nuclear dynamics had been considered, and potential energy curves for the two lowest electronic levels of H_2 were generated via the propagation of two electrons in a field of two fixed protons. The same CCS working equations as employed previously for nuclear dynamics were used, the only difference was that the Coulombic potential terms in the Hamiltonian had to be evaluated by integration rather than the usual normal-ordering. The evaluation of these integrals included the error function that resulted in the removal of Coulombic singularities at the nuclei. This ensured the system remained bound, rather than one electron falling into the Coulombic well and the other escaping to infinity. Additionally, the use of trajectory guided coherent states ensured that electron correlation was included. This resulted in potential energy curves being within good chemical accuracy (10^{-3} a.u./1 kcal mol^{-1}) of the most accurate *ab initio* calculations.

A second application of CCS to electron dynamics followed a few years later, simulating the strong laser field double ionisation of a He atom and providing physical insight into the mechanism [89]. Once more integrals over the Coulombic potential were required, which included the error function and lead to the averaged Hamiltonian remaining bound. It was noted that this provided an advantage over another trajectory guided method, Full Multiple Spawning [27], whose integrals over the Coulombic potential would not include the error function, and hence would lead to autoionisation.

The success of these applications lead to the development of a specialised adaptation of CCS to treat electron dynamics, known as fermionic CCS (FCCS) [90]. This adaptation takes the exchange symmetry of fermions into account, and uses fermion molecular dynamics to propagate trajectories. It was applied to the double ionisation of He once again, with FCCS providing double ionisation yields in much closer agreement to experiment than standard CCS. The calculation was run over a great many laser periods, a feat that would be extremely difficult with standard quantum dynamics methods. A second version of FCCS was proposed by Eidi *et. al.* that provides an alternative symmetrisation of the spatial wavefunction [91].

Standard CCS has also been used for other strong field phenomena in recent years: firstly to model the dynamics of an electronic wave packet in a strong laser field [92], and subsequently to high harmonic generation [78]. In the former application, CCS accurately identified signatures of over-the-barrier and tunnelling ionisation, reproducing the results of an exact TDSE solver and providing an improved result over the HK method. In the latter application, high harmonic generation is a phenomenon where extreme ultraviolet to soft x-ray wavelengths of light may be produced from an input near-infrared field. This

occurs via a three step process: firstly, an electron tunnels through the barrier formed by the Coulomb potential and the near-infrared laser field; secondly, it oscillates and gains kinetic energy under the influence of the laser field; and thirdly, it recombines with its parent ion when the laser field inverts direction resulting in a harmonic photon being emitted. CCS was used to simulate this high harmonic generation phenomenon for a single electron interacting with a strong laser field, where an adaptive reprojection of the basis set (discussed in Sec. 1.3.3) was utilised. The adaptive reprojection technique had to be used because the trajectories were rapidly being led away from the initial position of the wavefunction by the dynamics of the system, causing them to be uncoupled. By reprojecting onto the initial basis, this issue was remedied. Also, the initial basis had to be placed on a exponentially scaling regular grid, rather than a random sample, so the adaptive size reduced the cost of the calculation when trajectories weren't contributing significantly. The high harmonic spectra produced by CCS were found to be in very good agreement with that produced by an exact TDSE solver.

Returning to nuclear dynamics, CCS has also been used to simulate tunnelling through a symmetric and an asymmetric double well potential [46]. The symmetric double well was calculated in 2D and 10D, and showed good agreement to the SOFT method in 2D, and MP/SOFT in 10D. The asymmetric double well was calculated in 2D and 20D, with the 2D calculation showing good agreement to the SOFT method. However, the 20D calculation was not as successful and did not compare as well to the MP/SOFT method. This system will be the subject of Chapters 2 to 4 in this thesis, and more on this will be discussed there. Other molecular applications of CCS include intramolecular vibrational energy redistribution and dissociation of $HO{-}SO_2$ [47,48], and predissociation of Ne_nBr_2 [49,93]. In the latter CCS was implemented in a Cartesian frame, similar to classical molecular dynamics, allowing simulations to be performed on large molecules without requiring the identification of appropriate normal modes to describe the molecule.

A generalisation of CCS for nonadiabatic dynamics occurring on two or more potential energy surfaces known as the multiconfigurational Ehrenfest (MCE) method was presented a number of years after CCS was initially proposed [31–33], and is reviewed in the following section.

1.4 Multiconfigurational Ehrenfest (MCE)

The MCE method can be viewed as a generalisation of CCS for nonadiabatic processes occurring on two or more PESs. It was first proposed by Shalashilin in 2009 [31], with modifications to the working equations presented in 2010 [32]. These will both be reviewed below, with derivation of the working equations and subsequent applications and developments, alongside the relevant background theory to the Ehrenfest approximation.

1.4.1 Ehrenfest Theorem and Approximation

The main crux of the MCE method relies on the Ehrenfest approximation introduced by Meyer and Miller [94], and Billing [95], which in turn relies on Ehrenfest's theorem. The Ehrenfest theorem relates the time derivative of the expectation value of the momentum operator to the expectation of the position operator derivative of the potential. The expectation value of the momentum operator is in turn related to the time derivative of the expectation value of the position operator. This is derived as follows: consider the expectation value of a generic operator $\hat{A}$

$$\langle\Psi|\hat{A}|\Psi\rangle = \langle\hat{A}\rangle = \int \Psi^* \hat{A}\Psi \,\mathrm{d}\tau, \tag{1.4.1}$$

where $\mathrm{d}\tau$ implies an integration over all space. The time derivative of this expectation is given as

$$\begin{aligned}\frac{\mathrm{d}}{\mathrm{d}t}\langle\hat{A}\rangle &= \left\langle \frac{\mathrm{d}\Psi}{\mathrm{d}t} \middle| \hat{A}\Psi \right\rangle + \left\langle \Psi \middle| \hat{A}\frac{\mathrm{d}\Psi}{\mathrm{d}t} \right\rangle + \left\langle \Psi \middle| \frac{\mathrm{d}\hat{A}}{\mathrm{d}t}\Psi \right\rangle \\ &= \frac{1}{i\hbar}\langle -\hat{H}\Psi|\hat{A}\Psi\rangle + \frac{1}{i\hbar}\langle\Psi\hat{A}|\hat{H}\Psi\rangle + \left\langle \Psi \middle| \frac{\mathrm{d}\hat{A}}{\mathrm{d}t}\Psi \right\rangle\end{aligned} \tag{1.4.2}$$

where the derivation from lines 1 to 2 proceeds via the TDSE. If $\hat{A}$ has no explicit time-dependence then

$$\frac{\mathrm{d}}{\mathrm{d}t}\langle\hat{A}\rangle = \frac{1}{i\hbar}\langle\Psi|[\hat{A},\hat{H}]|\Psi\rangle\,. \tag{1.4.3}$$

If $\hat{A}$ is either the position or momentum operator, then for Hamiltonians of the form $\hat{H} = \hat{\mathbf{p}}^2/(2m) + V(\hat{\mathbf{q}})$ the following may be evaluated

$$\frac{\mathrm{d}}{\mathrm{d}t}\langle\hat{\mathbf{q}}\rangle = \frac{1}{i\hbar}\langle\Psi|[\hat{\mathbf{q}},\hat{H}]|\Psi\rangle = \frac{\langle\hat{\mathbf{p}}\rangle}{m} \tag{1.4.4a}$$

$$\frac{\mathrm{d}}{\mathrm{d}t}\langle\hat{\mathbf{p}}\rangle = \frac{1}{i\hbar}\langle\Psi|[\hat{\mathbf{p}},\hat{H}]|\Psi\rangle = \left\langle -\frac{\partial V}{\partial\hat{\mathbf{q}}} \right\rangle. \tag{1.4.4b}$$

The above is the mathematical representation of Ehrenfest's theorem, and from these relationships it can (loosely) be said that the expectation values of quantum mechanical operators obey Newtonian mechanics.

Turning to the Ehrenfest approximation, the assumption made here is that certain problems can be split into the sum of quantum and classical parts, for example light electrons being quantum and heavy nuclei being classical. The total Hamiltonian can

then be written as

$$\hat{H}(\hat{\mathbf{q}},\hat{\mathbf{p}},\mathbf{Q},\mathbf{P}) = \hat{H}^{\mathrm{q}}(\hat{\mathbf{q}},\hat{\mathbf{p}}) + \hat{H}^{\mathrm{cl}}(\mathbf{Q},\mathbf{P}) + \hat{V}^{\mathrm{int}}(\hat{\mathbf{q}},\hat{\mathbf{p}},\mathbf{Q},\mathbf{P}), \tag{1.4.5}$$

where $\hat{H}^{\mathrm{q}}(\hat{\mathbf{q}},\hat{\mathbf{p}})$ is the Hamiltonian of the quantum subsystem, $\hat{H}^{\mathrm{cl}}(\mathbf{Q},\mathbf{P})$ is the Hamiltonian of the classical subsystem and $\hat{V}^{\mathrm{int}}(\hat{\mathbf{q}},\hat{\mathbf{p}},\mathbf{Q},\mathbf{P})$ is their interaction. The operators $(\hat{\mathbf{q}},\hat{\mathbf{p}})$ are position and momenta operators for the quantum part, and $(\mathbf{Q},\mathbf{P})$ are vectors of position and momentum for the classical part. The equations of motion for the classical part can be determined by the Ehrenfest average over the Hamiltonian, and the following Hamilton equations may be given

$$\dot{\mathbf{Q}} = \frac{\partial H^{\mathrm{Ehr}}}{\partial \mathbf{P}} \tag{1.4.6a}$$

$$\dot{\mathbf{P}} = \frac{\partial H^{\mathrm{Ehr}}}{\partial \mathbf{Q}}. \tag{1.4.6b}$$

The Ehrenfest Hamiltonian, H^{Ehr} is the Hamiltonian averaged over the quantum wavefunction

$$H^{\mathrm{Ehr}} = \langle \Psi^{\mathrm{q}} | \hat{H}(\hat{\mathbf{q}},\hat{\mathbf{p}},\mathbf{Q},\mathbf{P}) | \Psi^{\mathrm{q}} \rangle \,, \tag{1.4.7}$$

with the quantum wavefunction represented on a suitable basis,

$$|\Psi^{\mathrm{q}}\rangle = a_1 \,|\phi_1\rangle + a_2 \,|\phi_2\rangle + \dots \,. \tag{1.4.8}$$

The evolution of the quantum system is then found through the time-dependence of the coefficients

$$\frac{\mathrm{d}a_i}{\mathrm{d}t} = -\frac{i}{\hbar} \sum_{j=1}^{J} \langle \phi_i | \hat{H}(\hat{\mathbf{q}},\hat{\mathbf{p}},\mathbf{Q},\mathbf{P}) | \phi_j \rangle \, a_j. \tag{1.4.9}$$

The accuracy of the Ehrenfest approximation is dependent on how good the treatment of the classical part is (in the example of nuclei being classical, the obvious downfall will be when quantum effects such as tunnelling occur), in addition to how well the interaction between classical and quantum subsystems is evaluated. The MCE method aims to remedy these deficiencies by using an ensemble of trajectories for the classical part rather than a single one, and treating it in a fully quantum manner to take into account any small amounts of quantum behaviour.

1.4.2 MCE Working Equations

1.4.2.1 MCE v1

The derivation of MCE working equations begins with the Ehrenfest approximation that the Hamiltonian can be split into the sum of quantum and classical parts, and hence the wavefunction can be split into quantum and classical parts (although the classical part is treated in a fully quantum manner). For simplicity it will be assumed that the quantum part consists of orthogonal states $|\phi_i\rangle$ as above (which could for example represent

electronic states), whilst coherent state basis functions are used to represent the classical part. In the first version of MCE the wavefunction ansatz was given as

$$\begin{aligned} |\Psi\rangle &= \sum_{k=1}^{K} |\varphi_k\rangle \\ &= \sum_{k=1}^{K} \left[\sum_{i=1}^{J} a_{ik} \, |\phi_i\rangle \right] |\mathbf{z}_k\rangle \\ &= \sum_{k=1}^{K} \left[\sum_{i=1}^{J} d_{ik} \mathrm{e}^{is_{ik}/\hbar} \, |\phi_i\rangle \right] |\mathbf{z}_k\rangle \,, \end{aligned} \tag{1.4.10}$$

where a discretised version was employed from the outset [31]. The amplitudes a_{ik} are factored into the product of d_{ik} amplitude and phase factor $\mathrm{e}^{is_{ik}/\hbar}$ like in CCS. The action in this representation is given as

$$s_{ik} = \int \left[\frac{i\hbar}{2} \left(\mathbf{z}_k^* \dot{\mathbf{z}}_k - \dot{\mathbf{z}_k}^* \mathbf{z}_k \right) - H_{ii}^{\mathrm{ord}}(\mathbf{z}_k^*, \mathbf{z}_k) \right] \mathrm{d}t \tag{1.4.11}$$

where $H_{ii}^{\mathrm{ord}}(\mathbf{z}_k^*, \mathbf{z}_k) = \langle \mathbf{z}_k | \hat{H}_{ii} | \mathbf{z}_k \rangle = \langle \mathbf{z}_k | \, \langle \phi_i | \hat{H} | \phi_i \rangle \, | \mathbf{z}_k \rangle$. The evolution of the wavefunction is determined by the time-dependence of the a amplitudes, or equivalently the smoothed d amplitudes and action like with CCS, and the trajectories of the coherent states. The time-dependence of the action follows straightforwardly from its definition in Eq. (1.4.11), whilst the time-dependence of the amplitudes and trajectories may be obtained by applying the time-dependent variational principle (TDVP) [96],

$$\delta \int L \, \mathrm{d}t = 0, \tag{1.4.12}$$

which is the quantum equivalent of the principle of stationary action. The quantum Lagrangian is given as

$$L = \langle \Psi | i\hbar \frac{\hat{\partial}}{\partial t} - \hat{H} | \Psi \rangle \,. \tag{1.4.13}$$

The time-dependence of the d amplitudes is then given as

$$\begin{aligned} \sum_{l=1}^{K} \langle \mathbf{z}_k | \mathbf{z}_l \rangle \, \mathrm{e}^{is_{il}/\hbar} \frac{\mathrm{d}d_{il}}{\mathrm{d}t} = -\frac{i}{\hbar} \Bigg[& \sum_{l=1}^{K} \langle \mathbf{z}_k | \mathbf{z}_l \rangle \, \delta^2 H_{ii}^{\mathrm{ord}*}(\mathbf{z}_k^*, \mathbf{z}_l) \mathrm{e}^{is_{il}/\hbar} d_{il} \\ & + \sum_{l=1}^{K} \sum_{j \neq i} \langle \mathbf{z}_k | \mathbf{z}_l \rangle \, H_{ij}^{\mathrm{ord}}(\mathbf{z}_k^*, \mathbf{z}_l) \mathrm{e}^{is_{jl}/\hbar} d_{jl} \Bigg] \end{aligned} \tag{1.4.14}$$

where

$$\delta^2 H_{ii}^{\mathrm{ord}*}(\mathbf{z}_k^*, \mathbf{z}_l) = H_{ii}^{\mathrm{ord}}(\mathbf{z}_k^*, \mathbf{z}_l) - H_{ii}^{\mathrm{ord}}(\mathbf{z}_l^*, \mathbf{z}_l) - i\hbar(\mathbf{z}_k^* - \mathbf{z}_l^*)\dot{\mathbf{z}}_l, \tag{1.4.15}$$

analogous to CCS Eq. (1.3.29), and $\langle \mathbf{z}_k|\mathbf{z}_l\rangle\, H_{ij}^{\mathrm{ord}}(\mathbf{z}_k^*, \mathbf{z}_l) = \langle \mathbf{z}_k|\hat{H}_{ij}|\mathbf{z}_l\rangle = \langle \mathbf{z}_k|\,\langle\phi_i|\hat{H}|\phi_j\rangle\,|\mathbf{z}_l\rangle$. The time-dependence of the trajectories is given as

$$\dot{\mathbf{z}_k} = -\frac{i}{\hbar}\frac{\partial H^{\mathrm{Ehr}}(\mathbf{z}_k^*, \mathbf{z}_k)}{\partial \mathbf{z}_k^*} \tag{1.4.16a}$$

$$\dot{\mathbf{z}_k}^* = \frac{i}{\hbar}\frac{\partial H^{\mathrm{Ehr}}(\mathbf{z}_k^*, \mathbf{z}_k)}{\partial \mathbf{z}_k}, \tag{1.4.16b}$$

where the Ehrenfest Hamiltonian H^{Ehr} is averaged over the quantum subsystem

$$H^{\mathrm{Ehr}}(\mathbf{z}_k^*, \mathbf{z}_k) = \frac{\sum_{i,j=1}^{J} H_{ij}^{\mathrm{ord}}(\mathbf{z}_k^*, \mathbf{z}_k) a_{ik}^* a_{jk}}{\sum_{i,j=1}^{J} \delta_{ij} a_{ik}^* a_{jk}}, \tag{1.4.17}$$

and δ_{ij} is the Kronecker delta. The Eqs. (1.4.11), (1.4.14) and (1.4.16) comprise the working equations of the initial version of MCE.

1.4.2.2 MCE v2

A second version was proposed a year later [32], where the wavefunction ansatz was given as

$$\begin{aligned} |\Psi\rangle &= \sum_{k=1}^{K} D_k\,|\varphi_k\rangle \\ &= \sum_{k=1}^{K} D_k \left[\sum_{i=1}^{J} a_{ik}\,|\phi_i\rangle\right] |\mathbf{z}_k\rangle \\ &= \sum_{k=1}^{K} D_k \left[\sum_{i=1}^{J} d_{ik} \mathrm{e}^{is_{ik}/\hbar}\,|\phi_i\rangle\right] |\mathbf{z}_k\rangle\,. \end{aligned} \tag{1.4.18}$$

The difference here is the multiconfigurational amplitude D_k that was not included in the first version given in Eq. (1.4.10). In the first version, the amplitudes d_{ik} are coupled within the same configuration (same k) and across different configurations (different k) which makes the $\mathbf{z}_k$ effectively coupled also. In the second version the d_{ik} amplitudes and $\mathbf{z}_k$ trajectories are no longer interacting with other configurations, as the D_k amplitude is responsible for that. Trajectories can therefore be run individually for each configuration before coupling them together with the D_k amplitudes. This makes the second version convenient for future use with on-the-fly dynamics, where expensive electronic structure calculations are required for each trajectory. It is much more efficient to calculate the electronic structure for each trajectory individually rather than all simultaneously. The uncoupling of configurations also adds stability to the Ehrenfest trajectories, as well as flexibility to the wavefunction representation due to the additional time-dependent parameter.

The time-dependence of the trajectories are the same as for the first version, given by Eq. (1.4.16), whilst the time-dependence of the d_{ik} amplitudes is now given by

$$\frac{\mathrm{d}d_{ik}}{\mathrm{d}t} = -\frac{i}{\hbar}\sum_{j\neq i}^{J} H_{ij}^{\mathrm{ord}*}(\mathbf{z}_k^*, \mathbf{z}_k)\mathrm{e}^{i(s_{jk}-s_{ik})/\hbar} d_{jk}. \tag{1.4.19}$$

This was calculated by applying the TDVP to a single configuration $|\varphi_k\rangle$ so the amplitudes are no longer coupled across configurations. The action and its time-dependence is still given by Eq. (1.4.11). The time-dependence of the D amplitudes is found via substitution of the wavefunction into the TDSE

$$\sum_{l=1}^{K} \langle\varphi_k|\varphi_l\rangle \frac{\mathrm{d}D_l}{\mathrm{d}t} = -\frac{i}{\hbar} \sum_{l=1}^{K} \langle\mathbf{z}_k|\mathbf{z}_l\rangle \, \Delta^2 H_{ij}^{\mathrm{ord}*}(\mathbf{z}_k^*, \mathbf{z}_l) D_l \tag{1.4.20}$$

where

$$\langle\varphi_k|\varphi_l\rangle = \langle\mathbf{z}_k|\mathbf{z}_l\rangle \sum_{i,j=1}^{J} \left[\delta_{ij} d_{ik}^* d_{jl} \mathrm{e}^{i(s_{jl}-s_{ik})/\hbar}\right] \tag{1.4.21}$$

and

$$\Delta^2 H_{ij}^{\mathrm{ord}*}(\mathbf{z}_k^*, \mathbf{z}_l) = \sum_{i,j=1}^{J} d_{ik}^* d_{jl} \mathrm{e}^{i(s_{jl}-s_{ik})/\hbar} \left[H_{ij}^{\mathrm{ord}}(\mathbf{z}_k^*, \mathbf{z}_l) - H_{ij}^{\mathrm{ord}}(\mathbf{z}_l^*, \mathbf{z}_l) - i\hbar\delta_{ij}(\mathbf{z}_k^* - \mathbf{z}_l^*)\dot{\mathbf{z}}_l\right] \tag{1.4.22}$$

with δ_{ij} being the Kronecker delta. The Eqs. (1.4.11), (1.4.16), (1.4.19) and (1.4.20) make up the working equations for the second version of MCE.

1.4.3 Applications of MCE

The paper that presented the first version of MCE applied it to simulate the spin-boson model [31], a system-bath problem consisting of a two-level system coupled to a bath of oscillators. It is used in physics to describe things such as light-harvesting complexes, quantum dots and decoherence. This problem had already been tackled with up to a few thousand degrees of freedom with the multilayer MCTDH (ML-MCTDH) method by Wang and Thoss with great success [97,98]. Using basis sets of only 50–300 coherent states, the ML-MCTDH results at short times were reproduced for tens, hundreds and thousands of degrees of freedom. Prior to MCE no other simulation technique could achieve this level of accuracy for the spin-boson model on that scale, and it is much more algorithmically straightforward than ML-MCTDH. However, a long time limit on the technique — as with CCS — was observed, with some deviation from ML-MCTDH as the simulation progressed. Due to the success of this first version of MCE to treat the spin-boson model, a number of years later it was utilised to model quantum information processing in an entangling quantum gate that had spin-boson like couplings [99]. At present, the above two papers are the only ones that have used the MCE equations in their first form.

The paper that reformulated the MCE equations into the second version [32] applied the method to study the nonadiabatic dynamics of pyrazine on two coupled electronic states, enabling the absorption spectrum to be simulated. As mentioned in Sec. 1.3.4, this is a common benchmark test for multidimensional quantum mechanical techniques, and MCE performed much better than the prior CCS application [45]. It was also in good agreement with MCTDH [20], something that the CCS calculation could not manage, whilst requiring only 500 configurations for the converged calculation.

The following year this figure was reduced down to 290 configurations by introducing

some regularity in the initial sampling of the coherent states, ensuring the more important modes were well represented [33]. A separate calculation utilising a mere 34 configurations also managed to produce the main features of the spectrum. Another application presented in this paper was the sticking of a hydrogen atom to a surface [33]. A system-bath model can represent this process, where the interaction of hydrogen with the surface is given by a Morse oscillator coupled to a harmonic bath of phonons. The sticking probability followed the MCTDH result [23] at a range of incident energies of the hydrogen atom wavepacket, although it was uniformly 15% lower. A final remark made in this paper was that MCE could be paired with electronic structure theory to calculate PESs as the simulation was running, or on-the-fly, for fully quantum nonadiabatic dynamics calculations. This is in contrast to MCTDH, which requires determination of the PES before the simulation is started. The use of Gaussians in MCE requires only information about the potential in the region where the functions are, and typically the potential and its derivatives at the centre of each Gaussian wavepacket are used to approximately evaluate the electronic integrals required as the calculation proceeds.

In the following year Saita [100] implemented this on-the-fly dynamics approach, formulating a technique known as the *ab initio* multiconfigurational Ehrenfest (AI-MCE) method that uses the MOLPRO [101, 102] electronic structure program to calculate PESs. To be able to interface with MOLPRO, the MCE working equations presented in Sec. 1.4.2.2 had to be modified as they are in diabatic representation and MOLPRO calculates adiabatic electronic states. This modification is presented in Chapter 5, when nonadiabatic calculations are performed using an extension of AI-MCE mentioned below.

AI-MCE was applied to the excited state $\pi\pi^*$ dynamics of ethylene, previously studied by *ab initio* multiple spawning (AIMS) [103, 104]. The AIMS technique also uses Gaussian basis functions to treat nonadiabatic quantum dynamics, with electronic structure calculations on-the-fly [104, 105]. The results of AI-MCE and AIMS were comparable, despite the trajectories used by AI-MCE being different to those of AIMS. It should be noted that in AI-MCE when a small number of trajectories are used they run away from one another quickly, the D amplitude becomes constant and the simulation is essentially a semiclassical one. In an example given, 16 trajectories were found to be uncoupled after 10 fs, although AI-MCE can still produce good results in the semiclassical limit as information about the quantum phases is retained. In a subsequent paper [106], a significantly increased number of trajectories (1000) was used to simulate the ultrafast x-ray scattering from ethylene and provide aid to analysis of recent experiments on the process [107]. This was then compared to simulation of ultrafast electron diffraction from ethylene [108]. Both diffraction techniques were found to be qualitatively similar for short times, demonstrating carbon-carbon dynamics due to oscillations of the C-C bond length, pyrimidisation and twisting around the bond, and dispersion of the carbon-carbon wavepacket. However for longer times, when the carbon-carbon wavepacket is dispersed, dynamics due to motion of the hydrogen atoms becomes prominent and ultrafast electron diffraction was observed to be more sensitive to this than ultrafast x-ray diffraction.

AI-MCE has also been applied to study the photodynamics of pyrrole, looking at N−H bond fission and subsequent radical formation [109]. Experimental results for this process by way of hydrogen (Rydberg) atom photofragment translational spectroscopy (HRA-PTS) were available [110], and AI-MCE provided evidence for the correct assignment of the spectra. The simulations were once again not fully quantum, with uncoupling of trajectories occurring at 50 fs. To address this problem, recently Makhov *et al.* [34] proposed adding a "multiple cloning" scheme to AI-MCE where the basis set is expanded at longer time periods, analogous to the spawning procedure of FMS/AIMS. The *ab initio* multiple cloning (AIMC) method is the subject of Chapter 5 and a thorough review will be presented there, alongside the conversion of MCE working equations from diabatic to adiabatic representation.

Very recently a couple of alternative methods to carry out nonadiabatic calculations that use the CCS/MCE formalism have been proposed: surface hopping CCS [111], and MCE in a time-dependent diabatic basis (MCE-TDDB) [112]. In the former, CCS was combined with Tully's fewest switches surface hopping algorithm [113, 114] to describe nonadiabatic transitions between electronic states. It was posited that this method will allow a more intuitive description of a trajectory as it will be assigned to a specific electronic state, as opposed to an Ehrenfest trajectory that has contributions from many. However, the working equations are given in diabatic form, which means that the method cannot be paired with electronic structure software in its current guise, and instead model potentials must be used. The example application given in the paper is of a 2 state 2D model potential for a conical intersection. The method reproduced state probabilities compared to a numerically exact solution of the Schrödinger equation, as well as interference effects of the nuclear wavepacket between the two states.

The latter development offers a variation on the AI-MCE method, where the overlap between electronic states on different trajectories is explicitly taken into account rather than assumed to be Kronecker delta. The premise behind this modification is to allow MCE-TDDB to better model large conjugated systems where electronic states can change character significantly along the width of a Gaussian. The dynamics of electronic and vibrational energy transfer in a phenylene ethynylene dendrimer was simulated via this method [112]. The absorption spectrum was produced (which had not been directly measured previously), illustrating the contributions of different electronic states on different portions on the molecule due to localisation within the conjugated system. It should be noted that the name "time-dependent diabatic basis" does not imply the electronic states are calculated in a diabatic basis, they are calculated in a adiabatic basis by electronic structure software the same as AI-MCE and AIMC. The difference is that each trajectory carries its own time-dependent diabatic electronic basis that coincides with the adiabatic basis at the centre of each Gaussian. A further review of the MCE method and its developments may be found in Ref. [115].

1.5 Other Quantum Dynamics Methods

1.5.1 MCTDH

Of all the quantum dynamics approaches that have been developed in the past few decades, the most widely used are those of the MCTDH family. The original scheme was first proposed in 1990 by H.-D. Meyer, U. Manthe and L. S. Cederbaum [17] as a multiconfigurational extension of the earlier time-dependent Hartree (TDH) method [116, 117]. The wavefunction is represented as a linear combination of Hartree products of time-dependent orthonormal single particle functions φ with expansion coefficients A

$$\begin{aligned}\Psi(q^{(1)},\ldots,q^{(M)},t) &= \sum_{k^{(1)}=1}^{K^{(1)}} \cdots \sum_{k^{(M)}=1}^{K^{(M)}} A_{k^{(1)},\ldots,k^{(M)}}(t) \prod_{m=1}^{M} \varphi_{k^{(m)}}^{(m)}(q^{(m)},t) \\ &= \sum_{\mathbf{k}} A_{\mathbf{k}} \Phi_{\mathbf{k}}.\end{aligned} \tag{1.5.1}$$

The second line defines the composite index for the configurations $\mathbf{k} = k^{(1)},\ldots,k^{(M)}$ and the Hartree product $\Phi_{\mathbf{k}}$. The single particle functions are usually expanded on a set of primitive time-independent basis functions that are chosen dependent on the problem studied

$$\varphi_{k^{(m)}}^{(m)}(q^{(m)},t) = \sum_{i^{(m)}=1}^{I^{(m)}} a_{i^{(m)},k^{(m)}}^{(m)}(t)\chi_{i^{(m)}}^{(m)}(q^{(m)}). \tag{1.5.2}$$

Applying the Dirac-Frenkel variational principle [116] to the MCTDH wavefunction representation yields a set of equations for the time-dependence of the single particle functions and expansion coefficients. Note that the Dirac-Frenkel variational principle is subtly different to the TDVP presented in Eq. (1.4.12), being given by

$$\langle \delta\Psi | i\hbar \frac{\partial}{\partial t} - \hat{H}|\Psi\rangle = 0. \tag{1.5.3}$$

Both variational principles can give equivalent solutions, but differ in their application. Further information on the equivalence of these variational principles and the as yet unmentioned McLachlan variational principle [117] may be found in Ref. [118].

Returning to MCTDH, the time-dependence of single particle functions and expansion coefficients permit a fully quantum propagation of the wavefunction to occur, and as such MCTDH is highly numerically accurate [18]. This high numeric accuracy has some drawback however, as the method scales exponentially with dimensionality, albeit with a smaller base to be exponentiated than the traditional method of quantum dynamics as presented in Eq. (1.1.25). This is generally due to requiring fewer time-dependent single particle functions in MCTDH than the time-independent basis functions in the traditional method. The exponential scaling makes MCTDH particularly suited to problems of four to twelve degrees of freedom, although mode combination can be utilised to increase this value. In mode combination, degrees of freedom are grouped together in the single particle functions to generate multimode single particle functions. As long as appropriate mode

combinations are chosen the method may treat higher dimensionality problems, such as the dynamics of pyrazine with 24 degrees of freedom studied in Ref. [82].

Another modification of the single particle functions to allow higher dimensionality problems to be treated is offered by ML-MCTDH [97, 119]. In this approach the single particle functions are built in several layers, where the single particle functions of a particular layer are multiconfigurational expansions of further single particle functions

$$\begin{aligned} \varphi^{(m)}_{k^{(m)}}(t) &= \sum_{l^{(1)}}^{L^{(1)}} \cdots \sum_{l^{(N)}=1}^{L^{(N)}} B_{l^{(1)},\ldots,l^{(N)}}(t) \prod_{n=1}^{N} \zeta^{(m,n)}_{l^{(n)}}(t) \\ \zeta^{(m,n)}_{l^{(n)}}(t) &= \sum_{j^{(1)}}^{J^{(1)}} \cdots \sum_{j^{(R)}=1}^{J^{(R)}} C_{j^{(1)},\ldots,j^{(R)}}(t) \prod_{r=1}^{R} \xi^{(m,n,r)}_{j^{(r)}}(t) \\ &\cdots . \end{aligned} \tag{1.5.4}$$

This allows the top layer to contain many more degrees of freedom than standard MCTDH, and is capable of simulations of a few hundred to a few thousand degrees of freedom. As a representative example, Ref. [120] simulated the Henon-Heiles Hamiltonian in 1458D using a 7-layer MCTDH scheme. The multilayer extension of MCTDH serves as inspiration for a 2-layer extension of CCS, which is developed in Chapter 3.

Other extensions of the MCTDH approach include taking account of exchange symmetry to treat systems of indistinguishable bosons and fermions with MCTDHB [121,122] and MCTDHF [123–125], respectively, and the unification thereof [126]. In these approaches, rather than the single particle functions consisting of a Hartree product, they are symmetrised permanents for bosons and antisymmetrised Slater determinants for fermions. They have both also been extended into multilayer formalism by Wang and Thoss [127]. The MCTDH extension to indistinguishable bosons serves as inspiration for a CCS extension to indistinguishable bosons developed in Chapter 4. As such, the theory behind indistinguishable particles will be discussed in greater detail there.

MCTDH has also been modified to include Gaussian basis functions in G-MCTDH [24]. In this approach the configurations in the wavefunction ansatz of Eq. (1.5.1) are given as

$$\Phi_{\mathbf{k}}(q^{(1)},\ldots,q^{(M)},t) = \prod_{m=1}^{\mu} \varphi^{(m)}_{k^{(m)}}(q^{(m)},t) \prod_{m=\mu+1}^{M} G^{(m)}_{k^{(m)}}(q^{(m)},t), \tag{1.5.5}$$

where the first μ degrees of freedom are described by the single particle functions as before, whilst the remaining degrees of freedom are described by Gaussian wavepackets. In the limit that only Gaussians are used to describe the wavefunction, the method is termed variational multiconfigurational Gaussians (vMCG) [25]. VMCG was first formulated in 2003, and subsequently reformulated in the style of CCS equations in 2013 by Ronto and Shalashilin [26]. Like MCE, in vMCG the Gaussian basis functions may be paired with electronic structure theory to perform on-the-fly dynamics, and this has been implemented in the direct dynamics variational multiconfigurational Gaussians (DD-vMCG) method [128].

1.5.2 Multiple Spawning

Another set of methods that utilise Gaussian basis functions and are capable of performing on-the-fly dynamics calculations is the multiple spawning family. Full multiple spawning (FMS) was first proposed in 1996 by Martínez, Ben-Nun and Levine as a way to simultaneously solve nuclear dynamics and electronic structure problems in a fully quantum manner, whilst retaining some classical flavour in the spirit of Heller's frozen Gaussian approach [27]. The wavefunction ansatz in FMS is given as

$$\begin{aligned}\Psi(\mathbf{R},\mathbf{r},t) &= \sum_{i=1}^{J}\phi_i(\mathbf{r};\mathbf{R})G_i(\mathbf{R},t) \\ &= \sum_{i=1}^{J}\phi_i(\mathbf{r};\mathbf{R})\left[\sum_{k=1}^{K}C_{ik}(t)\mathrm{e}^{iS_{ik}/\hbar}g_{ik}(\mathbf{R},\mathbf{Q}_{ik}(t),\mathbf{P}_{ik}(t),\gamma_{ik})\right],\end{aligned} \tag{1.5.6}$$

where $\mathbf{R}$ is the set of nuclear coordinates, $\mathbf{r}$ are the electronic coordinates, the sum is over J electronic states, ϕ_i is the electronic wavefunction for state i, G_i is a superposition of time-dependent frozen Gaussian basis functions g_{ik} with associated coefficients C_{ik}, $\mathrm{e}^{iS_{ik}/\hbar}$ is the usual phase factor, and γ_{ik} a time-independent width parameter that takes different values for different atoms. The time-dependence of the coefficients is found via substitution of the wavefunction representation into the TDSE, much like CCS and MCE. The time-dependence of the position and momentum centres of the Gaussians are given by Hamiltons equations evolving on a single electronic state

$$\frac{\partial\mathbf{Q}_{ik}}{\partial t} = \frac{\mathbf{P}_{ik}}{\mathbf{m}} \tag{1.5.7a}$$

$$\frac{\partial\mathbf{P}_{ik}}{\partial t} = -\left.\frac{\partial V_{ii}(\mathbf{R})}{\partial\mathbf{R}}\right|_{\mathbf{R}=\mathbf{Q}_{ik}}. \tag{1.5.7b}$$

In the original formulation, the potential energy surface was assumed to be known *a priori*. In a subsequent modification FMS was paired with electronic structure theory (and is included in the MOLPRO software [101, 102]) to calculate these potential energy surfaces on-the-fly. This development was named *ab initio* multiple spawning (AIMS) [104, 105, 129].

For both FMS and its generalisation to on-the-fly dynamics with AIMS, a key feature in the propagation of the wavefunction is a "spawning" procedure. This procedure adaptively expands the basis set size in a physically motivated way, describing quantum mechanical effects associated with electronic nonadiabaticity. When an existing basis function passes through a region of significant electronic coupling from one state to another, an additional "child" basis function may be "spawned" on a different electronic state to the "parent" basis function that generates it. This permits modelling of wavepacket splitting, and allows parent and child to be coupled together for a period of time to model nonadiabatic effects due to the superposition of states. This is in contrast to Tully's surface hopping technique where a trajectory only evolves on a single electronic state at a time, and so does not include these superposition effects [113, 114].

As the nuclear dynamics are computed in a similar way to CCS and MCE, they are relatively inexpensive. However, often high level electronic structure calculations are required that limits the method to small molecule systems, such as ethylene and cyclobutene [103, 129]. Recently, electronic structure calculations on graphical processing units (GPUs) have been developed [130–133], that allow much faster computation of electronic integrals. This has been paired with AIMS to allow nonadiabatic simulations of much larger molecules to be conducted, such as provitamin D_3 [134] and 4-(N,N-dimethylamino)benzonitrile (DMABN) [135].

1.5.3 Others

Whilst the MCTDH and MS methods of quantum dynamics have been the chief alternatives to CCS and MCE in the literature, two additional methods are reviewed here as they have been applied to the problem studied in Chapters 2 to 4. The first of these is matching-pursuit split-operator Fourier transform (MP/SOFT) [28]. The essence of this method is that it extends the exponentially scaling grid-based SOFT method into a dynamically adaptive coherent state representation to scale more favourably with system size. Firstly, a wavefunction representation is generated via the matching pursuit algorithm applied to a basis set expansion of coherent states. Then the wavefunction is propagated according to the SOFT scheme, with an approximation of the short time-propagator to second order (known as the Trotter expansion) applied. This requires Fourier transforms of the wavefunction representation between position and momentum space to apply the potential and kinetic energy components of the propagator. The coherent states in the wavefunction representation allow analytical Fourier transforms to be carried out straightforwardly, and is the reason the method does not scale exponentially with system size. After the wavefunction is propagated forward in time, it is re-expressed in terms of coherent states to adaptively adjust the size of the basis in accordance with the needs of the wavefunction. MP/SOFT has been extended to study nonadiabatic dynamics [41, 136, 137], however parameterised model Hamiltonians are required as the method does not incorporate on-the-fly dynamics.

The second method, or more accurately class of methods, developed by Habershon and Saller uses trajectories in an alternative way to that discussed previously. Rather than utilising them to guide time-dependent basis functions, they are used to sample a potential energy surface to determine appropriate places to use time-independent basis functions. The first implementation of this was authored by Habershon in 2012 for dynamics on a single potential energy surface, and was named a trajectory guided configuration interaction (CI) expansion [138]. The prescription for the method proceeds in three steps: firstly, trajectory simulations are used to generate dynamically relevant configurations on a potential energy surface; secondly, these configurations are used to construct a representation of the potential energy surface using an algorithm similar to matching pursuit; and thirdly, a CI expansion of the wavefunction using time-independent basis functions that are eigenfunctions of this approximate potential energy surface is performed, and the

wavefunction is propagated forward in time. The CI expansion of the approximate potential energy surface requires many fewer basis functions than the exact potential energy surface, and is the reason the method does not scale exponentially with system size.

The second implementation of this approach was given by Saller and Habershon is 2015 [139]. In this development, rather than using the trajectories to generate an approximate potential energy surface, they are used to generate probabilities that basis functions would be found at coordinates on the actual potential energy surface. This allows a non-uniform grid of time-independent Gaussian wavepackets to be sampled, the wavefunction expanded in terms of them and propagated via coefficients. Unlike the previous trajectory guided approach, this method incorporates nonadiabatic effects. It was retrospectively named a standard trajectory guided (sTG) scheme, to differentiate it from the modified approach that followed.

The modified approach incorporates an adaptive basis set to mininise the size of the calculation, and was named adaptive trajectory guided (aTG) [140]. This is achieved by splitting the propagation time into repetitions of short "bursts" of trajectory sampling and basis set propagation, as opposed to performing trajectory sampling for the entire propagation time and then basis set propagation for the entire propagation time. As before, the wavefunction representation is given via time-independent Gaussian wavepackets and time-dependent coefficients, with the Gaussians placed on a nonuniform grid defined by the trajectory sampling. The difference is that the coefficients are only propagated for a certain number of steps before minimisation of the basis occurs via a matching pursuit algorithm. Following this, the potential energy surface is sampled for the next few propagation steps, additional Gaussian basis functions are placed according to the probabilites generated, and the coefficients are propagated again before matching pursuit mininisation.

1.5.4 Comparisons to CCS and MCE

When comparing quantum dynamical methods, the two main factors are accuracy and speed. As MCTDH implements a fully variational solution to the TDSE it is highly accurate, however CCS and MCE have demonstrated comparable accuracy at a lower computational cost providing appropriate basis set sampling is chosen [31, 32, 45]. The lower computational cost of CCS/MCE arises due to random, rather than grid-based, sampling of the basis functions so that scaling with basis set size is in principle quadratic as opposed to exponential. Furthermore, for nonadiabatic dynamics MCTDH needs an analytical form of the PES that is known *a priori* due to the nonlocal nature of the basis functions used. In contrast, MCE — due to its use of local Gaussian basis functions — can compute PESs on-the-fly for direct dynamics. The generalisation of MCTDH to vMCG is capable of direct dynamics however, due to its exclusive use of Gaussian basis functions. Variational trajectories can follow the evolution of a wavefunction more closely than classical trajectories, especially in regions with large quantum effects such as tunnelling. However, they can also run into numerical instabilities [141].

FMS and AIMS are more directly related to MCE (and its on-the-fly extensions in AI-

MCE and AIMC) than MCTDH, due to their use of time-dependent frozen Gaussian basis functions guided by classical trajectories. The main difference arises in the trajectories themselves. FMS and AIMS evolve based on the potential and derivative of the current electronic state the trajectory finds itself on, and nonadiabatic effects are only incorporated in the region of a spawning process occuring at a conical intersection. However, as MCE and its extensions use Ehrenfest trajectories that incorporate effects from multiple potential energy surfaces, they include nonadiabatic effects at all times and not just in the region of a conical intersection. Ehrenfest trajectories also do not separate as quickly as purely classical trajectories, which can aid convergence in the short time period.

A review of the AIMC method and further comparison to AIMS will be offered in Chapter 5, as the technique is used there for simulation of ultrafast photodissociation. Numerical comparison to the MP/SOFT and trajectory guided sampling approaches will be offered in Chapters 2 to 4, as they have been applied to the same problem as CCS, and the CCS extensions developed in this thesis. Further extensive comparison between quantum dynamics methods may also be found in the recent review articles in Refs. [142, 143]

A summary of the quantum dynamics methods mentioned in this section in shown in Fig. 1.2. Each method is shown in a box with coloured stripes, with different coloured stripes representing different properties of each method. The first stripe indicates the method incorporates trajectories, with different colours representing different kinds of trajectories. The second stripe indicates the method incorporates nonadiabatic dynamics, either on-the-fly or with an *a priori* PES. The third stripe indicates the method uses Gaussian basis functions. The fourth stripe indicates the method adapts its basis set size, either by expanding or contracting. Uncoloured stripes indicates the method does not incorporate that property.

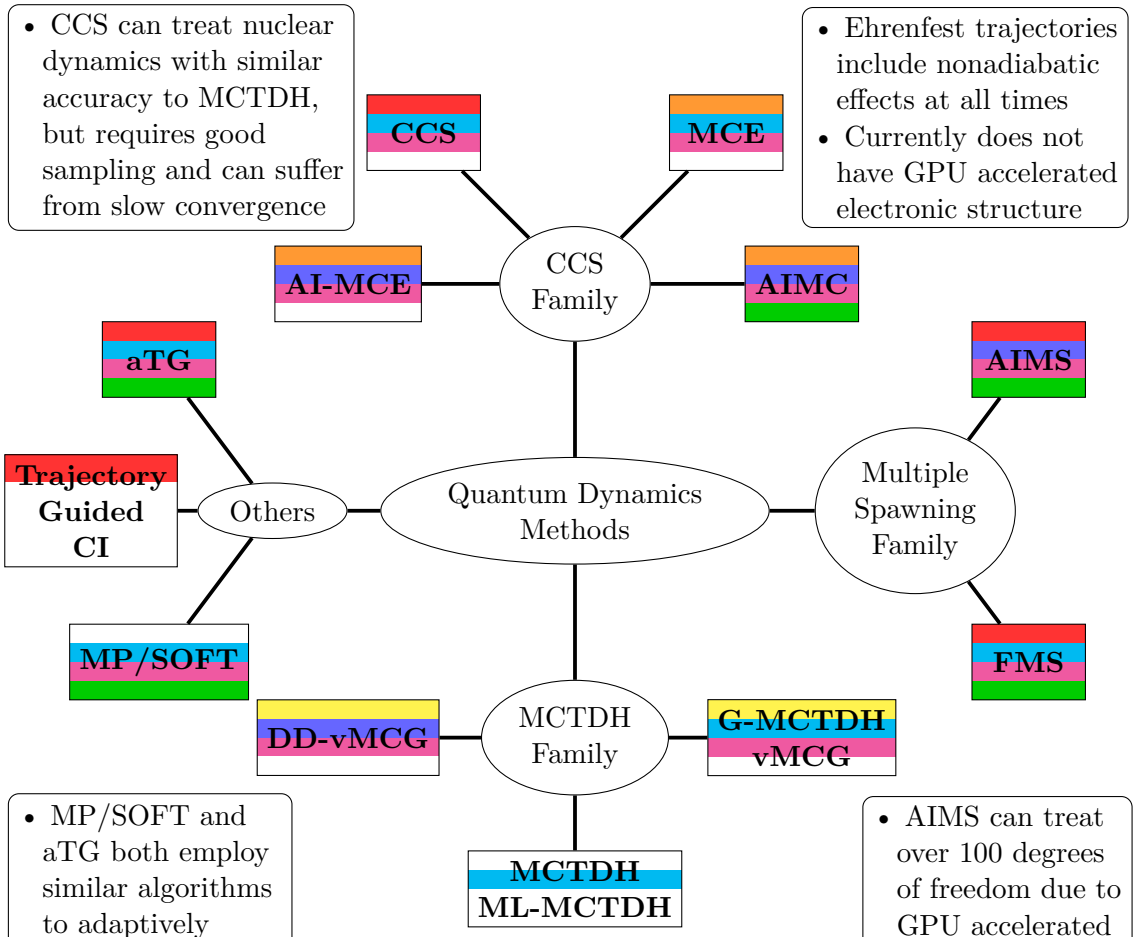

Figure 1.2: Summary of comparison between different quantum dynamics methods, with different coloured stripes representing different properties of each method. Uncoloured stripes indicate the method does not incorporate that property. Brief summary of salient information for each method is given in the bullet points surrounding.

1.6 Concluding Remarks and Thesis Outline

This chapter has provided a review of the historical basis of CCS, with origins in Heller's frozen Gaussian approach, Miller's IVR treatment, the semiclassical VVG propagator, and the HK method. The theoretical foundation of these methods in classical Lagrangian and Hamiltonian mechanics has also been presented, as well as their quantum analogues in Feynmans's path integral and Schrödinger's wavefunction approaches to quantum mechanics. The derivation of working equations for CCS has been shown, and applications of the method reviewed. The generalisation of CCS to the MCE method for nonadiabatic dynamics has been presented, and the combination with electronic structure theory for on-the-fly dynamics mentioned. This latter development is the subject of an application in a later chapter in this thesis, however first two new formulations of the CCS method are developed and applied to a model tunnelling problem in the following chapters. A full outline of the rest of the thesis is as follows:

- **Chapter 2**: A fully converged result for a model system-bath asymmetric double well tunnelling problem is obtained. This problem has been studied by quantum dynamics methods previously, however it has never been converged properly, and as such no standard benchmark result has been obtained. The benchmark result is obtained in this chapter, compared to the previous methods of studying the problem, and used to provide a reference test for the CCS extensions developed subsequently.
- **Chapter 3**: CCS is extended into 2-layer formalism (2L-CCS), providing a more flexible wavefunction representation than standard CCS, and increased mathematical treatment for a degree or degrees of freedom where necessary. After presentation of the working equations, the method is applied to the double well tunnelling problem and compared to the reference result obtained by the benchmark calculation.
- **Chapter 4**: CCS is extended to treating systems of indistinguishable bosons (CCSB) in the second quantisation formalism. It is applied to the double well tunnelling problem, where the bath may be second quantised, and the results are compared to the benchmark calculation. CCSB is also applied to a model Bose-Einstein condensate problem, as the ultimate aim of the method is to be used to study such systems.
- **Chapter 5**: The extension of CCS to nonadiabatic on-the-fly dynamics in AIMC is applied to the ultrafast photodissociation of 2-ethylpyrrole. The results are compared to experimental data, demonstrating the ability of the method to reproduce observable quantites whilst providing novel insight into the dissociation mechanism.
- **Chapter 6**: The results obtained in the previous chapters are summarised, conclusions drawn, and future areas of research discussed.
- **Appendix A**: Program code used to calculate the results in the thesis is described.
- **Appendix B**: Additional calculations for the CCSB method applied to the double well tunnelling problem are shown.

Chapter 2

Benchmark Calculation for the Double Well Tunnelling Problem

2.1 Introduction

Tunnelling is a fundamentally quantum feature, absent from classical dynamics calculations and only partially treated by semiclassical ones. Tunnelling events are vital for many processes in biology, chemistry and physics, including hydrogen tunnelling in enzyme catalysis [144,145], proton transfer in proteins [146], tunnelling through a reaction barrier [147], and atomic tunnelling of a Bose-Einstein condensate in a double well trap [148, 149]. In order to correctly treat the dynamics of such problems, fully quantum techniques must be used. Whilst CCS is fully quantum, tunnelling can pose difficulties if the basis set is initially sampled naively, as the classical trajectories that guide it thereafter may not sample sufficient regions of phase space.

A model Hamiltonian exhibiting tunnelling dynamics through a multidimensional asymmetric double well potential therefore presents an appropriate challenge for the CCS methods developed in this thesis, testing initial sampling of the basis set and ability to deal with a multidimensional problem that exhibits quantum behaviour. The Hamiltonian consists of a 1-dimensional tunnelling mode coupled to an $(M-1)$-dimensional harmonic bath, and has previously been studied with $M = 20$ by the matching pursuit split-operator Fourier transform (MP/SOFT) method [28,39], standard CCS [46], trajectory guided configuration interaction (CI) [138], and the adaptive trajectory guided (aTG) scheme [140]. It is a system-bath problem that bears some similarity to the Caldeira-Leggett model of tunnelling in a dissipative system [150, 151]. However, unlike the Caldeira-Leggett model this Hamiltonian has a finite bath, and the harmonic modes all have the same frequency. System-bath models play an important role in physics, and an example of their use is to describe superconductivity at a Josephson junction in a superconducting quantum interface device [152], for which the Caldeira-Leggett model provides a theoretical basis. Quantum dissipation is also of great interest, describing irreversible energy transfer to the environment (relaxation) and decoherence effects. System-bath problems with finite harmonic baths containing tens of degrees of freedom can be important for short time

dynamics, and examples of these have been investigated previously [36, 153].

Whilst the model Hamiltonian has been studied previously, it has never been converged properly. As such, no standard reference result has thus far been proposed, and instead comparison to other methods and indication of tunnelling taking place has been used to evaluate the effectiveness of the methods used to study it. Therefore, in this chapter a benchmark result will be proposed for this problem to permit comparison to previous methods, and provide a reference result for the methods developed in this thesis. Details of the model Hamiltonian, alongside a description of the method used to provide a benchmark result for it are described in Sec. 2.2; results of the benchmark calculation and comparisons to previous methods are given in Sec. 2.3; and conclusions are offered in Sec. 2.4. The results from this chapter have been published in Ref. [154].

2.2 Numerical Details

2.2.1 Hamiltonian

The model Hamiltonian consists of a 1-dimensional system tunnelling mode coupled to an $(M-1)$-dimensional harmonic bath. It is given by

$$\hat{H} = \frac{\hat{p}^{(1)^2}}{2} - \frac{\hat{q}^{(1)^2}}{2} + \frac{\hat{q}^{(1)^4}}{16\eta} + \frac{\hat{\mathbf{P}}^2}{2} + \frac{\left(1+\lambda\hat{q}^{(1)}\right)\hat{\mathbf{Q}}^2}{2} \tag{2.2.1}$$

where $(\hat{q}^{(1)}, \hat{p}^{(1)})$ are the position and momentum operators of the 1-dimensional system tunnelling mode, and $(\hat{\mathbf{Q}}, \hat{\mathbf{P}})$ are the position and momentum operators of the $(M-1)$-dimensional harmonic bath modes, with $\hat{\mathbf{Q}} = \sum_{m=2}^{M} \hat{q}^{(m)}$ and $\hat{\mathbf{P}} = \sum_{m=2}^{M} \hat{p}^{(m)}$. The coupling between system and bath is given by the constant λ, whilst η determines the well depth. The system is governed by an asymmetric double well potential, which when coupled quadratically to the bath decreases the well depth for $q^{(1)} < 0$ and increases it for $q^{(1)} > 0$. As the coupling between the system and bath increases or the number of bath modes increases, the separation of the two wells increases. As the initial position of the system wavefunction $\Psi^{(s)}(0)$ is in the lower left hand well, the separation of the two wells is the effective tunnelling barrier. This is illustrated in Fig. 2.1, where the 1D $\lambda = 0.0$ case is the pure or uncoupled tunnelling potential.

Previous studies [39,46,138,140] have considered the case of a 19-dimensional bath, so in total a 20-dimensional problem, $M = 20$, with system-bath coupling constant $\lambda = 0.1$.

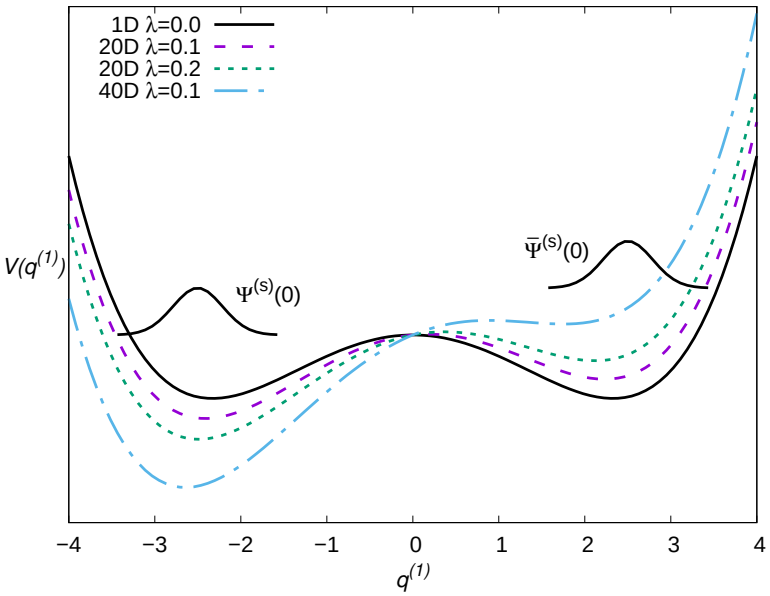

Figure 2.1: Tunnelling potential $V(q^{(1)})$ with different couplings of the system and bath and different dimensionalities of the bath. The 1D $\lambda = 0.0$ case represents the pure or uncoupled tunnelling potential. The initial position of the system wavepacket $\Psi^{(s)}(0)$ is shown in the lower well, with its mirror image $\bar{\Psi}^{(s)}(0)$ in the upper well.

These parameters will also be used initially to provide comparison to existing methods, before providing a benchmark for more challenging cases of higher dimensionality bath ($M = 40$ and $M = 80$, $\lambda = 0.1$) and stronger system-bath coupling ($M = 20$, $\lambda = 0.2$). The well depth parameter $\eta = 1.3544$ for all dimensions and coupling constants. Atomic units are used throughout, with $\hbar = 1$.

2.2.2 Quantum Dynamics

The wavefunction is represented as a basis set expansion

$$|\Psi(t)\rangle = \sum_{j=1}^{N_{\text{bth}}} \sum_{l=1}^{N_{\text{sys}}} c_{jl}(t)\, |\psi_j^{(\text{b})}\rangle\, |\psi_l^{(\text{s})}\rangle\,, \tag{2.2.2}$$

where $c_{jl}(t)$ are complex, time-dependent amplitudes, $|\psi_j^{(\text{b})}\rangle$ is a time-independent basis function for the bath modes and $|\psi_l^{(\text{s})}\rangle$ is a time-independent basis function for the system mode. The number of bath and system basis functions are given by N_{bth} and N_{sys}, respectively. Substitution into the TDSE leads to an equation for the time-dependence of the amplitudes

$$\frac{\mathrm{d}c_{ik}(t)}{\mathrm{d}t} = -i \sum_{j=1}^{N_{\text{bth}}} \sum_{l=1}^{N_{\text{sys}}} H_{ikjl} c_{jl}(t), \tag{2.2.3}$$

where H_{ikjl} is the Hamiltonian matrix

$$\begin{aligned} H_{ikjl} &= \langle \psi_i^{(\text{b})} \psi_k^{(\text{s})} | \hat{H} | \psi_j^{(\text{b})} \psi_l^{(\text{s})} \rangle \\ &= \langle \psi_k^{(\text{s})} | \frac{\hat{p}^{(1)^2}}{2} - \frac{\hat{q}^{(1)^2}}{2} + \frac{\hat{q}^{(1)^4}}{16\eta} | \psi_l^{(\text{s})} \rangle\, \delta_{ij} + \langle \psi_i^{(\text{b})} | \frac{\hat{\mathbf{P}}^2}{2} + \frac{\hat{\mathbf{Q}}^2}{2} | \psi_j^{(\text{b})} \rangle\, \delta_{kl} \\ &\quad + \frac{\lambda}{2} \langle \psi_i^{(\text{b})} | \hat{\mathbf{Q}}^2 | \psi_j^{(\text{b})} \rangle \langle \psi_k^{(\text{s})} | \hat{q}^{(1)} | \psi_l^{(\text{s})} \rangle\,. \end{aligned} \tag{2.2.4}$$

The bath and system basis functions are orthonormal (see below), a fact that has been exploited in the above.

The basis functions for the system are those of a particle in a rectangular box

$$\langle q^{(1)} | \psi_l^{(\text{s})} \rangle = \sqrt{\frac{2}{L}} \sin\left(\frac{l\pi}{L} (q^{(1)} - q_{\text{box}}) \right), \tag{2.2.5}$$

where L is the size and q_{box} the lower coordinate of the box. Both these values may be adjusted to ensure a large enough area of coordinate space is sampled by the system basis functions to properly account for the double well potential.

The bath modes are harmonic, therefore they can be represented by harmonic oscillator basis functions. A complete description of the bath would involve all excited state harmonic oscillator configurations, however in practice configurations can simply be added on until a converged result is achieved. For an $(M-1)$-dimensional bath, an excited state is comprised of the product of $(M-1)$ single particle harmonic oscillator functions $\prod_{m=2}^{M} |\alpha^{(m)}\rangle$, with different permutations of this product yielding different configurations, and $\alpha^{(m)}$ is the number of harmonic oscillator quanta in a particular bath mode m. As the

coupling of system and bath modes is proportional to $\hat{\mathbf{Q}}^2$ and all bath modes are initially in the ground state, only excitations with an even number of quanta are involved.

The size of the bath basis can be reduced further by exploiting the effective indistinguishability of the bath modes. The amplitudes of the harmonic oscillator excited state configurations, which correspond to similar vibrational excitations but differ only by the bath modes involved, will be identical for a given excited state. This means that configurations corresponding to these similar excitations can be grouped together and associated with a single amplitude. This simplification reflects the permutational symmetry of the Hamiltonian in Eq. (2.2.1), with the harmonic bath modes all having the same frequency. For example, including all even excitations up to a total quanta of 8 (the reasons for this choice will become apparent later), the bath basis functions obtained by grouping configurations are:

$$
\begin{aligned}
|\psi_1^{(\mathrm{b})}\rangle &= && |0000\ldots0000\rangle \\
|\psi_2^{(\mathrm{b})}\rangle &= 1/\sqrt{M-1} && (|2000\ldots0000\rangle + \cdots + |0000\ldots0002\rangle) \\
|\psi_3^{(\mathrm{b})}\rangle &= 1/\sqrt{M-1} && (|4000\ldots0000\rangle + \cdots + |0000\ldots0004\rangle) \\
|\psi_4^{(\mathrm{b})}\rangle &= \sqrt{2!}/\sqrt{(M-1)(M-2)} && (|2200\ldots0000\rangle + \cdots + |0000\ldots0022\rangle) \\
|\psi_5^{(\mathrm{b})}\rangle &= 1/\sqrt{M-1} && (|6000\ldots0000\rangle + \cdots + |0000\ldots0006\rangle) \\
|\psi_6^{(\mathrm{b})}\rangle &= 1/\sqrt{(M-1)(M-2)} && (|4200\ldots0000\rangle + \cdots + |0000\ldots0024\rangle) \\
|\psi_7^{(\mathrm{b})}\rangle &= \sqrt{3!}/\sqrt{(M-1)(M-2)(M-3)} && (|2220\ldots0000\rangle + \cdots + |0000\ldots0222\rangle) \\
|\psi_8^{(\mathrm{b})}\rangle &= 1/\sqrt{M-1} && (|8000\ldots0000\rangle + \cdots + |0000\ldots0008\rangle) \\
|\psi_9^{(\mathrm{b})}\rangle &= 1/\sqrt{(M-1)(M-2)} && (|6200\ldots0000\rangle + \cdots + |0000\ldots0026\rangle) \\
|\psi_{10}^{(\mathrm{b})}\rangle &= \sqrt{2!}/\sqrt{(M-1)(M-2)} && (|4400\ldots0000\rangle + \cdots + |0000\ldots0044\rangle) \\
|\psi_{11}^{(\mathrm{b})}\rangle &= \sqrt{2!}/\sqrt{(M-1)(M-2)(M-3)} && (|4220\ldots0000\rangle + \cdots + |0000\ldots0224\rangle) \\
|\psi_{12}^{(\mathrm{b})}\rangle &= \sqrt{4!}/\sqrt{(M-1)(M-2)(M-3)(M-4)} && (|2222\ldots0000\rangle + \cdots + |0000\ldots2222\rangle)
\end{aligned}
\tag{2.2.6}
$$

with relevant normalisation factors included. The square of the normalisation factors is simply equal to the number of configurations grouped; in the case of $M = 20$ there are 8855 bath configurations governed by only 12 distinct bath basis functions, and hence 12 distinct amplitudes. This reduction of parameters due to indistinguishability of modes or particles and permutational symmetry of the Hamiltonian is well known and exploited by the second quantisation approach, which will be covered in more detail in Chapter 4. Here the idea is used in a more straightforward fashion. The basis functions take explicit account of excitations with degenerate energy, for example $|\psi_3^{(\mathrm{b})}\rangle$ and $|\psi_4^{(\mathrm{b})}\rangle$.

2.2.3 Matrix Elements

Now the basis functions have been defined, the matrix elements of the Hamiltonian may be evaluated. The system elements

$$\begin{aligned}\langle\psi_k^{(\mathrm{s})}|\frac{\hat{p}^{(1)^2}}{2}-\frac{\hat{q}^{(1)^2}}{2}+\frac{\hat{q}^{(1)^4}}{16\eta}|\psi_l^{(\mathrm{s})}\rangle =&\frac{l^2\pi^2}{2L^2}\delta_{kl} \quad +\frac{2}{L}\int_{q_{\mathrm{box}}}^{q_{\mathrm{box}}+L}\sin\left(\frac{k\pi}{L}(q^{(1)}-q_{\mathrm{box}})\right)\\ &\times\sin\left(\frac{l\pi}{L}(q^{(1)}-q_{\mathrm{box}})\right)\left(\frac{q^{(1)^4}}{16\eta}-\frac{q^{(1)^2}}{2}\right)\mathrm{d}q^{(1)},\end{aligned} \tag{2.2.7}$$

are the particle in a box energy levels, plus an additional potential term. This integral may be evaluated analytically for $l \neq k$, however for $l = k$ a division by zero appears in the analytic solution, so the integral must be evaluated numerically. The composite Simpson's rule is used for this, due to the highly oscillatory nature of the integrand for large values of l and k. For a function $f(y)$ integrated on a region $[a, b]$, the composite Simpson's rule is [155]

$$\int_a^b f(y)\,\mathrm{d}y \approx \frac{c}{3}\left[f(y_0)+2\sum_{s=1}^{R/2-1}f(y_{2s})+4\sum_{s=1}^{R/2}f(y_{2s-1})+f(y_R)\right], \tag{2.2.8}$$

where R is the number of subintervals the interval $[a, b]$ is split up into by Simpson's rule, c is the "step length" given by $c = (b - a)/R$ and $y_s = a + sc$ for $s = 0, 1, \ldots, (R - 1), R$. Evaluating Eq. (2.2.8) for the integral in Eq. (2.2.7) when $l = k$ gives

$$\begin{aligned}&\langle\psi_k^{(\mathrm{s})}|\frac{\hat{p}^{(1)^2}}{2}-\frac{\hat{q}^{(1)^2}}{2}+\frac{\hat{q}^{(1)^4}}{16\eta}|\psi_l^{(\mathrm{s})}\rangle \approx\\ &\approx\frac{k^2\pi^2}{2L^2}+\frac{L}{3R}\left[\frac{4}{L}\sum_{s=1}^{R/2-1}\sin^2\left(\frac{2sk\pi}{R}\right)\left(\frac{[(q_{\mathrm{box}}+2sL)/R]^4}{16\eta}-\frac{[(q_{\mathrm{box}}+2sL)/R]^2}{2}\right)\right.\\ &\left.+\frac{8}{L}\sum_{s=1}^{R/2}\sin^2\left(\frac{(2s-1)k\pi}{R}\right)\left(\frac{[(q_{\mathrm{box}}+(2s-1)L)/R]^4}{16\eta}-\frac{[(q_{\mathrm{box}}+(2s-1)L)/R]^2}{2}\right)\right].\end{aligned} \tag{2.2.9}$$

The maximum error bound of the composite Simpson's rule approximation is [155]

$$\frac{c^4}{180}(b-a)\left|\frac{\mathrm{d}^4 f(\xi)}{\mathrm{d}y^4}\right|_{\max}, \tag{2.2.10}$$

for some $\xi \in [a, b]$. The number of subintervals was chosen to be $R = k \times 10^4$ to give an error on the order of 10^{-14} for a matrix element on the order of 1. The number of subintervals was related to k, because an increase in k leads to increased oscillation of the integrand and a larger value of $\left|\frac{\mathrm{d}^4 f(\xi)}{\mathrm{d}y^4}\right|_{\max}$.

The bath elements

$$\langle\psi_i^{(\mathrm{b})}|\frac{\hat{\mathbf{P}}^2}{2}+\frac{\hat{\mathbf{Q}}^2}{2}|\psi_j^{(\mathrm{b})}\rangle=\delta_{ij}\left(\sum_{m=2}^{M}\alpha_i^{(m)}+\frac{M-1}{2}\right) \tag{2.2.11}$$

are simply the harmonic oscillator eigenvalues, where $\alpha_i^{(m)}$ is the number of quanta in one mode.

The system-bath interaction elements are comprised of a bath term multiplied by a system term. The bath term is given by

$$\langle\psi_i^{(\mathrm{b})}|\hat{\mathbf{Q}}^2|\psi_j^{(\mathrm{b})}\rangle=\begin{cases}\dfrac{A_{ij}}{2}\sqrt{(\alpha_i^{(m)}+2)(\alpha_i^{(m)}+1)} & \text{if } \alpha_i^{(m)}=\alpha_j^{(m)}-2 \text{ in only one mode}\\ & \text{and } \alpha_i^{(m)}=\alpha_j^{(m)} \text{ in all other modes}\\ \dfrac{A_{ij}}{2}\sqrt{\alpha_i^{(m)}(\alpha_i^{(m)}-1)} & \text{if } \alpha_i^{(m)}=\alpha_j^{(m)}+2 \text{ in only one mode}\\ & \text{and } \alpha_i^{(m)}=\alpha_j^{(m)} \text{ in all other modes}\\ \displaystyle\sum_{m=2}^{M}\alpha_i^{(m)}+\frac{M-1}{2} & \text{if } \alpha_i^{(m)}=\alpha_j^{(m)} \text{ in all modes}\\ 0 & \text{if states differ by more than two}\\ & \text{quanta in one mode, or two}\\ & \text{quanta in more than one mode}\end{cases} \tag{2.2.12}$$

where A_{ij} is a constant that depends upon the normalisation factors and the number of configurations that differ by only two quanta in one mode. Returning to the example of including all harmonic oscillator excited states with even quanta up to and including a total quanta of 8, the $\langle\psi_i^{(\mathrm{b})}|\hat{\mathbf{Q}}^2|\psi_j^{(\mathrm{b})}\rangle$ matrix elements may be evaluated for clarity:

$$\begin{array}{c|cccccccccccc}
 & |\psi_1^{(\mathrm{b})}\rangle & |\psi_2^{(\mathrm{b})}\rangle & |\psi_3^{(\mathrm{b})}\rangle & |\psi_4^{(\mathrm{b})}\rangle & |\psi_5^{(\mathrm{b})}\rangle & |\psi_6^{(\mathrm{b})}\rangle & |\psi_7^{(\mathrm{b})}\rangle & |\psi_8^{(\mathrm{b})}\rangle & |\psi_9^{(\mathrm{b})}\rangle & |\psi_{10}^{(\mathrm{b})}\rangle & |\psi_{11}^{(\mathrm{b})}\rangle & |\psi_{12}^{(\mathrm{b})}\rangle \\
\hline
\langle\psi_1^{(\mathrm{b})}| & \frac{M-1}{2} & \frac{\sqrt{2(M-1)}}{2} & 0 & 0 & 0 & 0 & 0 & 0 & 0 & 0 & 0 & 0 \\
\langle\psi_2^{(\mathrm{b})}| & \frac{\sqrt{2(M-1)}}{2} & 2+\frac{M-1}{2} & \sqrt{3} & \sqrt{M-2} & 0 & 0 & 0 & 0 & 0 & 0 & 0 & 0 \\
\langle\psi_3^{(\mathrm{b})}| & 0 & \sqrt{3} & 4+\frac{M-1}{2} & 0 & \frac{1}{2}\sqrt{30} & \frac{\sqrt{2(M-2)}}{2} & 0 & 0 & 0 & 0 & 0 & 0 \\
\langle\psi_4^{(\mathrm{b})}| & 0 & \sqrt{M-2} & 0 & 4+\frac{M-1}{2} & 0 & \sqrt{6} & \frac{\sqrt{6(M-3)}}{2} & 0 & 0 & 0 & 0 & 0 \\
\langle\psi_5^{(\mathrm{b})}| & 0 & 0 & \frac{1}{2}\sqrt{30} & 0 & 6+\frac{M-1}{2} & 0 & 0 & \frac{1}{2}\sqrt{56} & \frac{\sqrt{2(M-2)}}{2} & 0 & 0 & 0 \\
\langle\psi_6^{(\mathrm{b})}| & 0 & 0 & \frac{\sqrt{2(M-2)}}{2} & \sqrt{6} & 0 & 6+\frac{M-1}{2} & 0 & 0 & \frac{1}{2}\sqrt{30} & \frac{1}{2}\sqrt{24} & \sqrt{M-3} & 0 \\
\langle\psi_7^{(\mathrm{b})}| & 0 & 0 & 0 & \frac{\sqrt{6(M-3)}}{2} & 0 & 0 & 6+\frac{M-1}{2} & 0 & 0 & 0 & \frac{1}{2}\sqrt{36} & \sqrt{2(M-4)} \\
\langle\psi_8^{(\mathrm{b})}| & 0 & 0 & 0 & 0 & \frac{1}{2}\sqrt{56} & 0 & 0 & 8+\frac{M-1}{2} & 0 & 0 & 0 & 0 \\
\langle\psi_9^{(\mathrm{b})}| & 0 & 0 & 0 & 0 & \frac{\sqrt{2(M-2)}}{2} & \frac{1}{2}\sqrt{30} & 0 & 0 & 8+\frac{M-1}{2} & 0 & 0 & 0 \\
\langle\psi_{10}^{(\mathrm{b})}| & 0 & 0 & 0 & 0 & 0 & \frac{1}{2}\sqrt{24} & 0 & 0 & 0 & 8+\frac{M-1}{2} & 0 & 0 \\
\langle\psi_{11}^{(\mathrm{b})}| & 0 & 0 & 0 & 0 & 0 & \sqrt{M-3} & \frac{1}{2}\sqrt{36} & 0 & 0 & 0 & 8+\frac{M-1}{2} & 0 \\
\langle\psi_{12}^{(\mathrm{b})}| & 0 & 0 & 0 & 0 & 0 & 0 & \sqrt{2(M-4)} & 0 & 0 & 0 & 0 & 8+\frac{M-1}{2}
\end{array} \tag{2.2.13}$$

Of course, this can be easily extended to take into account additional excitations as necessary for the calculation to converge. For the system term

$$\langle\psi_k^{(\mathrm{s})}|\hat{q}^{(1)}|\psi_l^{(\mathrm{s})}\rangle=\frac{2}{L}\int_{q_{\mathrm{box}}}^{q_{\mathrm{box}}+L}\sin\left(\frac{k\pi}{L}(q^{(1)}-q_{\mathrm{box}})\right)\sin\left(\frac{l\pi}{L}(q^{(1)}-q_{\mathrm{box}})\right)q^{(1)}\,\mathrm{d}q^{(1)}. \tag{2.2.14}$$

This may be evaluated analytically, with the value of the integral equal to zero when $k=l$

because the integrand is symmetric as long as the box is symmetric around the origin.

2.2.4 Initial Values

As with previous studies [39, 46, 138, 140], the initial wavepacket is defined by

$$\langle \mathbf{q}|\Psi(0)\rangle = \left(\frac{1}{\pi}\right)^{\frac{M}{4}} \prod_{m=1}^{M} \exp\left(-\frac{1}{2}\left(q^{(m)} - q^{(m)}(0)\right)^2\right), \tag{2.2.15}$$

where the initial tunnelling coordinate $q^{(1)}(0) = -2.5$ is located in the lower well, and initial bath coordinates $q^{(m)}(0) = 0.0$ for $m > 1$. The initial momenta for all modes is $p^{(m)}(0) = 0.0$. Thus, the initial conditions for all bath modes are identical, which along with their identical Hamiltonian parameters makes them indistinguishable.

The initial amplitudes are calculated via projection onto the initial wavepacket, with all bath modes in the ground state at $t = 0$

$$\begin{aligned} c_{ik}(0) =& \langle \psi_i^{(\mathrm{b})} \psi_k^{(\mathrm{s})} | \Psi(0)\rangle = \delta_{1k} \langle \psi_k^{(\mathrm{s})} | \Psi^{(\mathrm{s})}(0)\rangle \\ =& \delta_{1k} \sqrt{\frac{2}{L}} \int_{q_{\mathrm{box}}}^{q_{\mathrm{box}}+L} \sin\left(\frac{k\pi}{L}(q^{(1)} - q_{\mathrm{box}})\right) \left(\frac{1}{\pi}\right)^{\frac{1}{4}} \exp\left(-\frac{1}{2}\left(q^{(1)} - q^{(1)}(0)\right)^2\right) \mathrm{d}q^{(1)}. \end{aligned} \tag{2.2.16}$$

The above integral may be evaluated numerically using the composite Simpson's rule once more, and substitution of Eq. (2.2.16) into Eq. (2.2.8) gives

$$\begin{aligned} c_{ik}(0) \approx& \delta_{1k} \frac{2\sqrt{2L}}{3R} \left(\frac{1}{\pi}\right)^{1/4} \left[\sum_{s=1}^{R/2-1} \sin\left(\frac{2sk\pi}{R}\right) \exp\left(-\frac{1}{2}\left(\frac{q_{\mathrm{box}} + 2sL}{R} - q^{(1)}(0)\right)^2\right) \right. \\ & \left. + 2 \sum_{s=1}^{R/2} \sin\left(\frac{(2s-1)k\pi}{R}\right) \exp\left(-\frac{1}{2}\left(\frac{q_{\mathrm{box}} + (2s-1)L}{R} - q^{(1)}(0)\right)^2\right) \right]. \end{aligned} \tag{2.2.17}$$

As with the evaluation of the system matrix elements, Eq. (2.2.9), a value of $R = k \times 10^4$ was chosen to give an error on the order 10^{-14} for an initial amplitude in the range $[10^{-3}, 10]$.

2.3 Results

The quantity of interest is the cross-correlation function (CCF) between the wavefunction at time t and the mirror image of the initial wavepacket, $|\bar{\Psi}(0)\rangle$. The mirror image of the initial state is located in the upper well of the asymmetric potential (as indicated on Fig. 2.1), therefore non-zero values of the CCF are indicative of tunnelling. Rather than express $|\bar{\Psi}(0)\rangle$ as a Gaussian wavepacket in the CCF, it is simpler to represent it as the basis set expansion instead, with initial amplitudes $\bar{c}$ calculated according to Eq. (2.2.16) using the mirror image coordinates (i.e. $\bar{q}^{(1)}(0) = +2.5$)

$$\begin{aligned}
\mathrm{CCF}(t) &= \langle \bar{\Psi}(0) | \Psi(t) \rangle \\
&= \sum_{i,j=1}^{N_{\mathrm{bth}}} \sum_{k,l=1}^{N_{\mathrm{sys}}} \bar{c}^{*}_{ik}(0) c_{jl}(t) \, \langle \psi_i^{(\mathrm{b})} \psi_k^{(\mathrm{s})} | \psi_j^{(\mathrm{b})} \psi_l^{(\mathrm{s})} \rangle \\
&= \sum_{i,j=1}^{N_{\mathrm{bth}}} \sum_{k,l=1}^{N_{\mathrm{sys}}} \bar{c}^{*}_{ik}(0) c_{jl}(t) \delta_{ij} \delta_{kl} \\
&= \sum_{i=1}^{N_{\mathrm{bth}}} \sum_{k=1}^{N_{\mathrm{sys}}} \bar{c}^{*}_{ik}(0) c_{ik}(t).
\end{aligned} \tag{2.3.1}$$

The spectra of the real component of the CCFs are also presented via a Fourier transform (FT):

$$I(\omega) = \int_0^T \mathrm{Re}(\mathrm{CCF}(t)) \exp(-i\omega t) \, \mathrm{d}t. \tag{2.3.2}$$

The FT makes it simpler to identify the long-time propagation accuracy of a quantum dynamical method, due to a small number of sharp peaks as opposed to the highly oscillatory nature of the CCF. Total propagation time is $T = 120$ a.u for all results that follow, with step size $\delta t = 0.001$ a.u.

2.3.1 20D

2.3.1.1 $\lambda = 0.1$

The first set of parameters used are those that have been previously studied [39, 46, 138, 140], with a 19-dimensional bath, 1-dimensional tunnelling mode, and system-bath cou-

M	λ	N_{sys}	N_{bth}	L	q_{box}
20	0.1	50	12	12	-6
20	0.2	50	45	12	-6
40	0.1	50	30	12	-6
80	0.1	50	45	14	-7

Table 2.1: Parameters for the fully converged benchmark calculations: number of degrees of freedom M, system-bath coupling constant λ, number of system basis functions N_{sys}, number of bath basis functions N_{bth}, size of box for system basis functions L, and lower box coordinate q_{box}.

pling constant $\lambda = 0.1$. The calculation can be converged with respect to the system box length L to ensure sufficient coordinate space sampling of the tunnelling mode and allow correct representation of the initial wavepacket. The calculation can also be converged with respect to the number of system basis functions N_{sys} and number of bath basis functions N_{bth} to ensure sufficient basis functions, and hence amplitudes, are included to represent the system and bath modes and their time-dependence over the timeframe of the calculation. Each of these parameters may be increased until the CCF and FT show no observable change, and this is illustrated in Figs. 2.2 to 2.4 to establish that the method performs correctly. When the calculation is converged with respect to one parameter, the other two are held fixed at their fully converged value. The fully converged values of the parameters are shown in the figure captions, and also Table 2.1. As well as visual inspection, a quantitative illustration of convergence is shown in the bottom panel of the CCFs in Figs. 2.2 to 2.4. This quantitative measure is given via the cumulative error of the difference between the absolute value of the CCF for the fully converged benchmark calculation, and unconverged benchmark calculations

$$\chi_{\text{bench}} = \int \left| \text{Abs}(\langle \bar{\Psi}(0) | \Psi(t) \rangle)_{\text{bench}_{\text{conv}}} - \text{Abs}(\langle \bar{\Psi}(0) | \Psi(t) \rangle)_{\text{bench}_{\text{unconv}}} \right| \, \mathrm{d}t. \tag{2.3.3}$$

Firstly, the change in the calculation with respect to system box length L is illustrated in Fig. 2.2. A box symmetric around the origin is chosen for all values of L, therefore the lower coordinate of the box $q_{\text{box}} = -L/2$. A box size of $L = 6$ is clearly inadequate as seen in the (a) panes of Fig. 2.2, with $L = 8$ an improvement in (b), and $L = 10$ being very close to being converged in (c). The $L = 12$ case is fully converged in (d), with small differences from the $L = 10$ case seen in the CCF at $t > 90$ a.u, which are very subtly manifested in the FT at the peaks of $\omega = 12.5$ and $\omega = 13.5$. The $L = 14$ case exhibits no difference from the $L = 12$ case (not shown here). This is quantitatively shown in panel (e) on the left hand side of the figure, with the error term χ_{bench} decreasing upon increasing L and q_{box}. Therefore the initial system wavefunction and system wavefunction at time t until $t = 120$ a.u. samples coordinate space in the region $[-6 : 6]$.

The change in the benchmark calculation with respect to the number of system basis functions N_{sys} is illustrated in Fig. 2.3. The calculation converges rapidly with respect to N_{sys}, with virtually no difference between $N_{\text{sys}} = 30$ and $N_{\text{sys}} = 50$, as shown in the (b) and (c) panes of the figure. This is quantitatively shown in panel (d) on the left hand side of the figure, with the error term χ_{bench} decreasing upon increasing N_{sys}, with the $N_{\text{sys}} = 30$ line lying virtually on top of the time axis. Although this is a relatively small number of basis functions, only a single mode is being treated by them and they cover a large amount of coordinate space. This indicates a significant amount of delocalisation, as may be expected from a tunnelling mode, hence accurate treatment of the system by other methods may not be as trivial as for this benchmark calculation. The range of momentum values needed to be sampled by other methods can be estimated based on the wavelengths of the particle in a box basis functions and the De Broglie relationship. The basis function with longest wavelength occurs when $n = 1$ in Eq. (2.2.5) and smallest when $n = N_{\text{sys}}$.

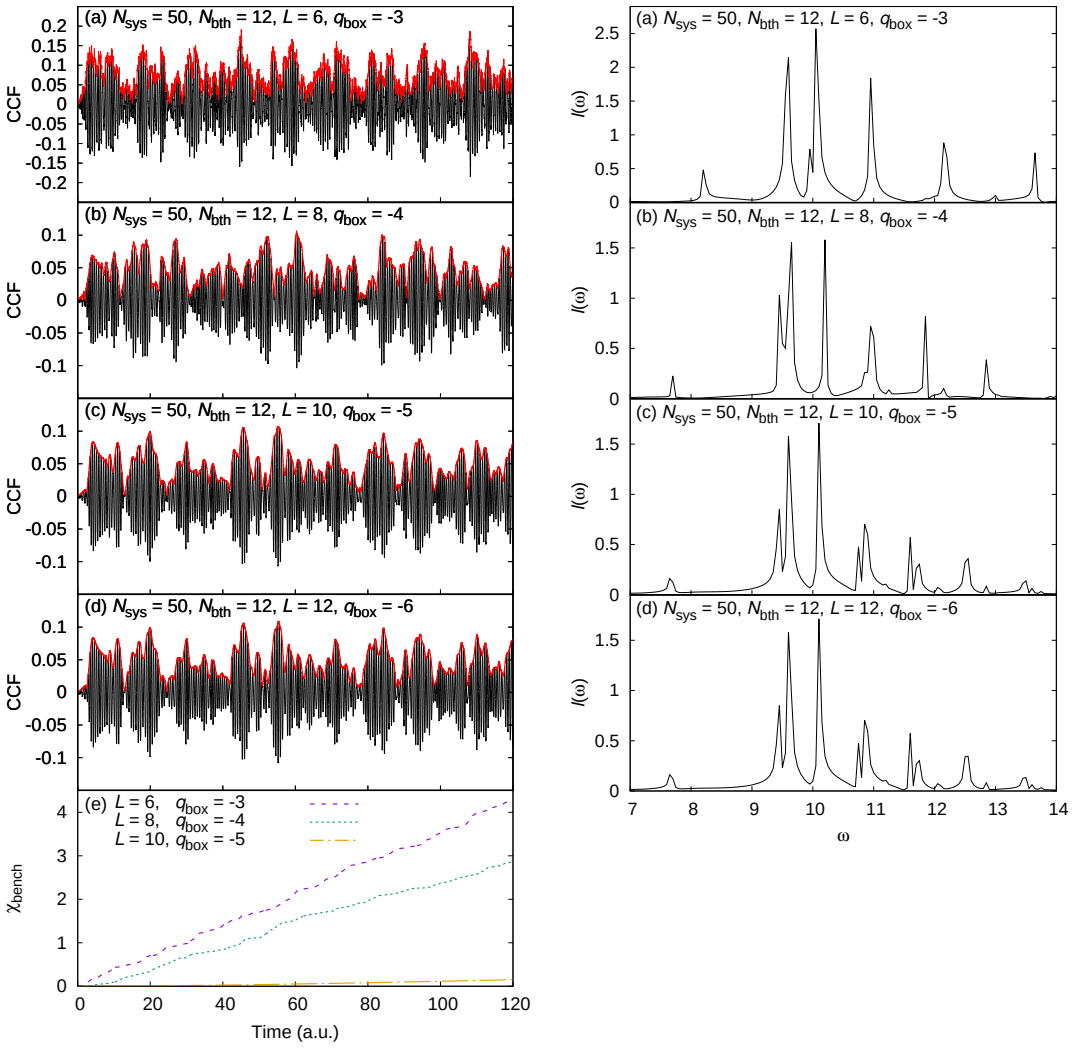

Figure 2.2: Convergence of the cross-correlation function (left, real part in black and absolute value in red), and the Fourier transform of the real part of the CCF (right) with increasing system box length L and lower box coordinate q_{box}: (a) $L = 6$, $q_{\text{box}} = -3$, (b) $L = 8$, $q_{\text{box}} = -4$, (c) $L = 10$, $q_{\text{box}} = -5$, (d) $L = 12$, $q_{\text{box}} = -6$. Panel (e) on the left hand side shows the cumulative error χ_{bench} between the converged benchmark calculation and unconverged benchmark calculations obtained via Eq. (2.3.3).

This gives a range of wavelengths from $\lambda = 2L$ and $\lambda = 2L/N_{\text{sys}}$, leading to momenta of $p = \pi/L$ and $p = \pi N_{\text{sys}}/L$. Therefore, as well as a significant amount of coordinate space, a large amount of momentum space must also be sampled.

The change in the benchmark calculation with respect to the number of bath basis functions N_{bth} is illustrated in Fig. 2.4. The different number of bath basis functions used in each panel of the figure corresponds to including excited harmonic oscillator energy states with increasing even numbers of quanta, i.e. $N_{\text{bth}} = 1$ corresponds to 0 quanta (only the harmonic oscillator ground state), $N_{\text{bth}} = 2$ corresponds to including 2 quanta (ground state and first excited state with even quanta), $N_{\text{bth}} = 4$ corresponds to including 4 quanta (ground state, first excited state with even quanta, and next two degenerate twice excited states with even quanta), etc. The benchmark is fully converged by $N_{\text{bth}} = 12$,

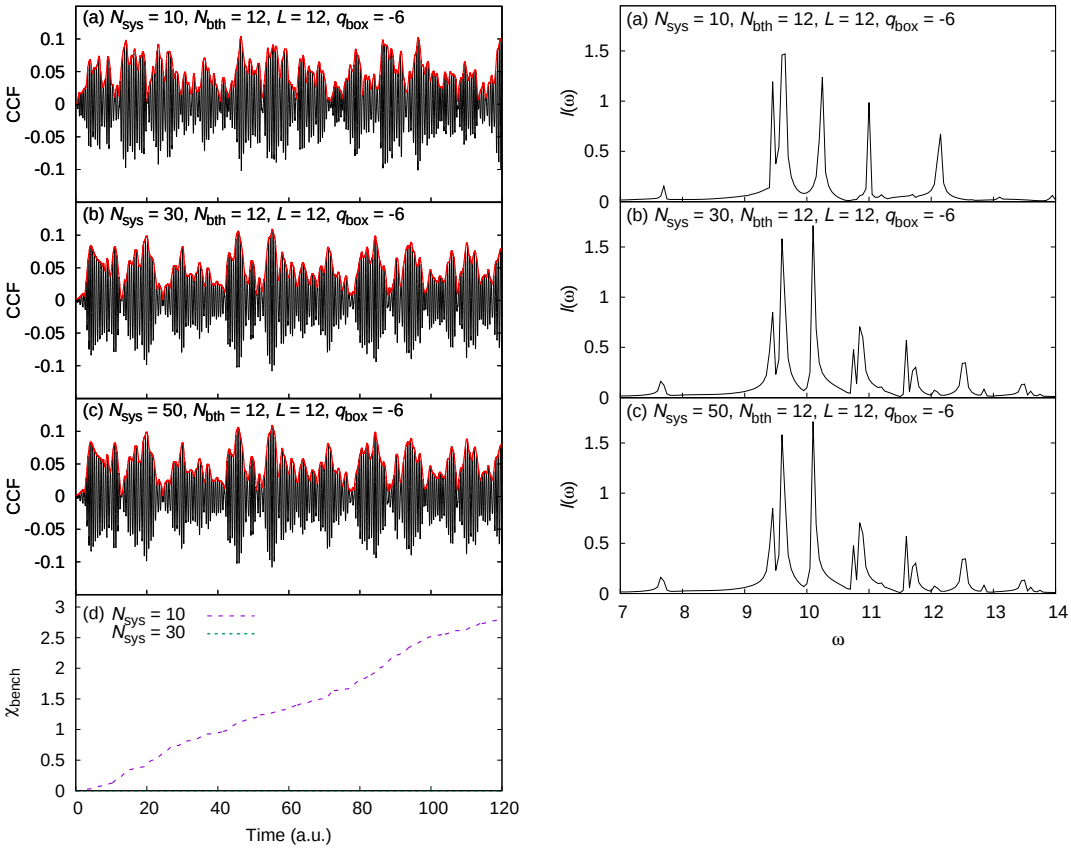

Figure 2.3: Convergence of the cross-correlation function (left, real part in black and absolute value in red), and the Fourier transform of the real part of the CCF (right) with an increasing number of system basis functions N_{sys}: (a) $N_{\text{sys}} = 10$, (b) $N_{\text{sys}} = 30$, (c) $N_{\text{sys}} = 50$. Panel (d) on the left hand side shows the cumulative error χ_{bench} between the converged benchmark calculation and unconverged benchmark calculations obtained via Eq. (2.3.3). The $N_{\text{sys}} = 30$ line lies virtually on top of the time axis.

when even excited harmonic oscillator states up to and including 8 quanta are present, as shown visually in panels (a)-(e), and quantitatively in panel (f) on the left hand side. The explicit form of these basis functions has been demonstrated in Eq. (2.2.6). Whilst this may not seem like a very large amount, the simplification made earlier may be recalled: all configurations for a particular state with similar vibrational excitations are governed by the same amplitude. So for the fully converged calculation there are 8855 configurations governed by only 12 bath basis functions, a significant reduction. Taking into account that the number of system basis functions $N_{\text{sys}} = 50$, the total wavefunction is a superposition of 50×8855 configurations, described only by 50×12 amplitudes that evolve according to Eq. (2.2.3). For calculations where this trick is not possible, a large amount of basis functions may be required for accurate modelling of the wavefunction, requiring a large amount of phase space to be sampled for the system and bath.

A comparison of the fully converged benchmark calculation (with $L = 12$, $N_{\text{sys}} = 50$ and $N_{\text{bth}} = 12$) to previous methods of studying this problem [39, 46, 138, 140] is shown in Fig. 2.5. Evaluating each of the methods in turn, MP/SOFT [39] in panel (a) compares well to the benchmark for short time propagation, although there is a loss of structure

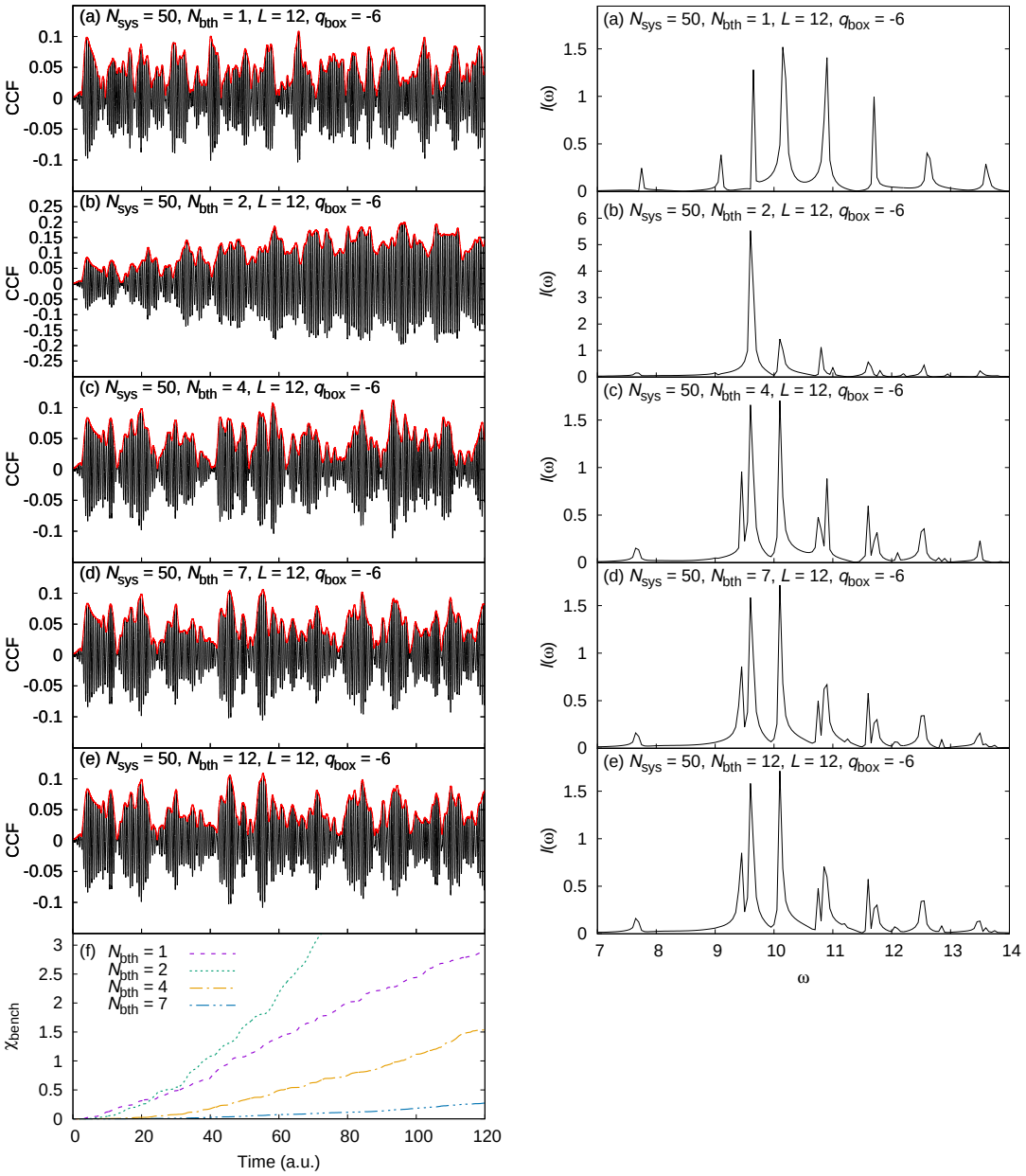

Figure 2.4: Convergence of the cross-correlation function (left, real part in black and absolute value in red), and the Fourier transform of the real part of the CCF (right) with an increasing number of bath basis functions N_{bth}: (a) $N_{\mathrm{bth}} = 1$, (b) $N_{\mathrm{bth}} = 2$, (c) $N_{\mathrm{bth}} = 4$, (d) $N_{\mathrm{bth}} = 7$, (e) $N_{\mathrm{bth}} = 12$. Panel (f) on the left hand side shows the cumulative error χ_{bench} between the converged benchmark calculation and unconverged benchmark calculations obtained via Eq. (2.3.3).

and amplitude in the CCF at $t > 25$ a.u. This suggests that the calculation is less able to treat tunnelling as the propagation progresses, and is affected by noise due to the matching pursuit algorithm. In panel (b) the CCS calculation from Ref. [46] does not reproduce the converged result, with the CCF deviating from the benchmark after ~ 5 a.u. Furthermore, the large peak splitting in the FT is missing at $\omega = 9.5$, as well as the smaller splittings at $\omega = 10.8$ and $\omega = 11.6$. There is also a peak at $\omega = 9.0$ that does not

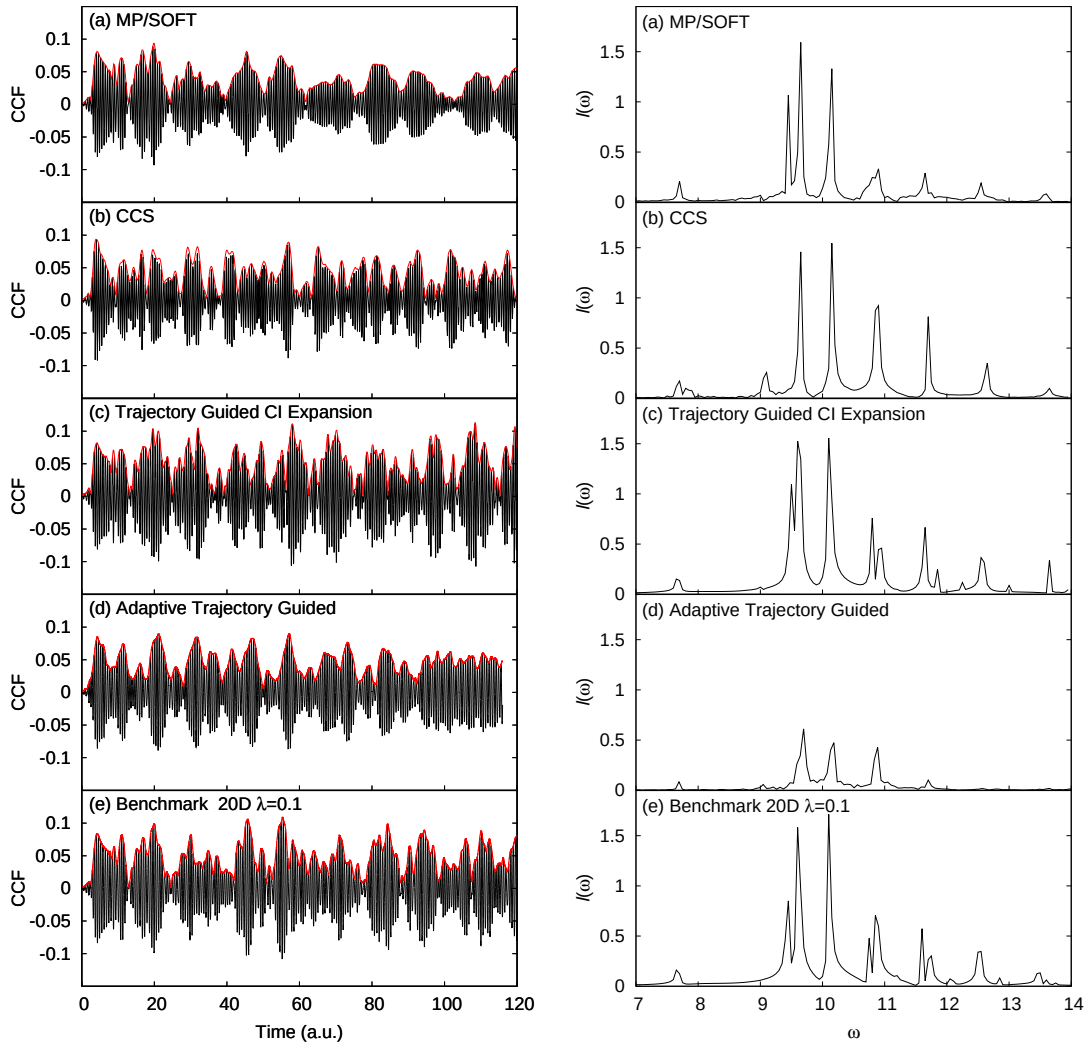

Figure 2.5: Comparison of the cross-correlation functions (left, real parts in black and absolute values in red) and the Fourier transforms of the real part of the CCF (right) for different methods that have studied the Hamiltonian Eq. (2.2.1): (a) MP/SOFT [39], (b) CCS [46], (c) trajectory guided CI expansion [138], (d) aTG [140], (e) Benchmark.

appear in the fully converged benchmark calculation. The CCS calculation does however resemble an unconverged benchmark result in panel (a) of Fig. 2.4 when $N_{\text{bth}} = 1$ (only ground harmonic oscillator state included in basis). An indication for this resemblance may be found in Ref. [46]: when the sampling procedure for the bath basis functions in the CCS calculation is discussed it was noted that they are sampled from a narrow distribution. This indicates that an insufficient area of phase space is sampled by the CCS basis functions for the bath, and a broader distribution may be required to accurately model the contributions from the excited harmonic oscillator states. The trajectory guided CI expansion [138] performs best out of all methods in panel (c), with a CCF that is accurate with respect to the benchmark for a longer time than MP/SOFT and CCS, leading to a FT spectrum that is also more accurate. This is to be expected as the CI expansion is similar to the benchmark calculation through the use of a regular time-independent basis set. The small differences arise with the choice of this basis set expansion: the trajectory

guided CI expansion initially samples the potential energy surface to determine the most important configurations for the expansion, and so may miss some small features. However, the present calculation exploits symmetry properties in the Hamiltonian to include all configurations at a reduced cost of calculation, and so does not need to make any approximation. The aTG method in panel (d) reproduces the CCF well for the first ~ 5 a.u., and thereafter the absolute value of the CCF is broadly similar to the benchmark until $t \sim 85$ a.u. However, there is a significant loss of structure in the oscillations of the real part of the CCF, which leads to a FT spectrum that does not reproduce the benchmark result well, as the peaks in the $\omega = 9.5$–11.6 region are significantly less intense and not split, and the peaks at $\omega > 11.6$ do not appear.

2.3.1.2 $\lambda = 0.2$

The $\lambda = 0.2$, $M = 20$ case has not been explored by any previous work, but it presents a more stringent test as the increase in coupling between system and bath will cause greater perturbation of the bath by the system. One would therefore expect an increased number of bath basis functions required for convergence in the calculation. The fully converged result is shown in Fig. 2.6, with the CCF on the top of the figure, and the FT on the bottom. Figures illustrating how this calculation converges are not included for brevity, as the same procedure as the 20D $\lambda = 0.1$ case was followed. The fully converged calculation parameters are shown in Table 2.1.

The system box size L is the same as for the $\lambda = 0.1$ case, and the number of system basis functions required is also the same. Therefore, the tunnelling mode appears to be as delocalised as for the $\lambda = 0.1$ case, requiring no further sampling of phase space over the timeframe of the calculation. The increase in complexity arises with the modelling of the bath, as a much greater number of bath basis functions are required with $N_{\text{bth}} = 45$. This corresponds to involving even harmonic oscillator excited energy states up to and including 14 quanta. Without exploiting the indistinguishability of the excited state configurations, an extremely large number of basis functions would be required; in this result there are 657800 bath configurations governed by only 45 basis functions. The total wavefunction is a superposition of the 50×657800 configurations, which can be described by only 50×45 independent amplitudes. As expected, this strongly coupled system and bath illustrates the significant perturbation of the bath by the system due to the large number of bath configurations required for convergence. The amplitude of the CCF is slightly smaller than the $\lambda = 0.1$ case, indicating that there is a small decrease in the amplitude of tunnelling. This is because, as shown in Fig. 2.1, increasing the coupling between system and bath causes an increase in the separation of the two wells.

2.3.2 40D & 80D

Calculations have also been performed for 40D and 80D cases, i.e. with 39 and 79 bath modes. There is no obvious computational scaling with dimensionality for the benchmark calculation as the bath basis functions represent harmonic oscillator excited states of the

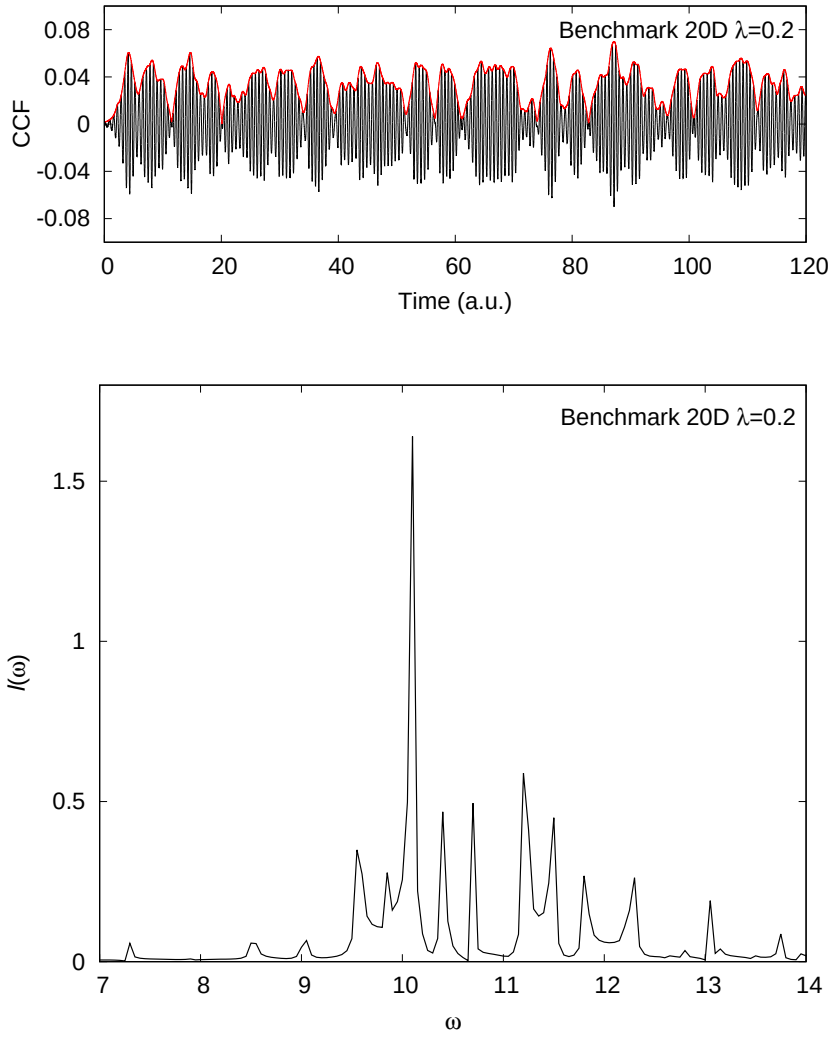

Figure 2.6: Fully converged benchmark calculation for the 20D, $\lambda = 0.2$ case. Top: real part (black line) and absolute value (red line) of the cross-correlation function. Bottom: Fourier transform of the real part of the cross-correlation function.

entire bath rather than individual modes. However, a greater number of excited states may be required due to the increase in dimensionality of the bath. The weak coupling case of $\lambda = 0.1$ is reverted to for this reason, as an increase in the number of bath modes and their coupling may result in a calculation that is prohibitively expensive to converge, even when exploiting mode indistinguishabilities. Furthermore, both increasing the coupling and increasing the dimensionality of the bath causes the wells to separate in the double well potential, and eventually the upper well becomes unbound.

The fully converged result for the 40D case is shown in Fig. 2.7, with the CCF on the top of the figure, and the FT on the bottom. The fully converged calculation parameters are shown in Table 2.1. It can be seen that the CCF oscillates at a higher frequency than the 20D, $\lambda = 0.1$ case, which is demonstrated in the FT with a shift to higher frequencies. The greater frequency of tunnelling for 40D compared to 20D is due to the greater number of bath modes the tunnelling coordinate $q^{(1)}$ is coupled to. As the dimensionality increases,

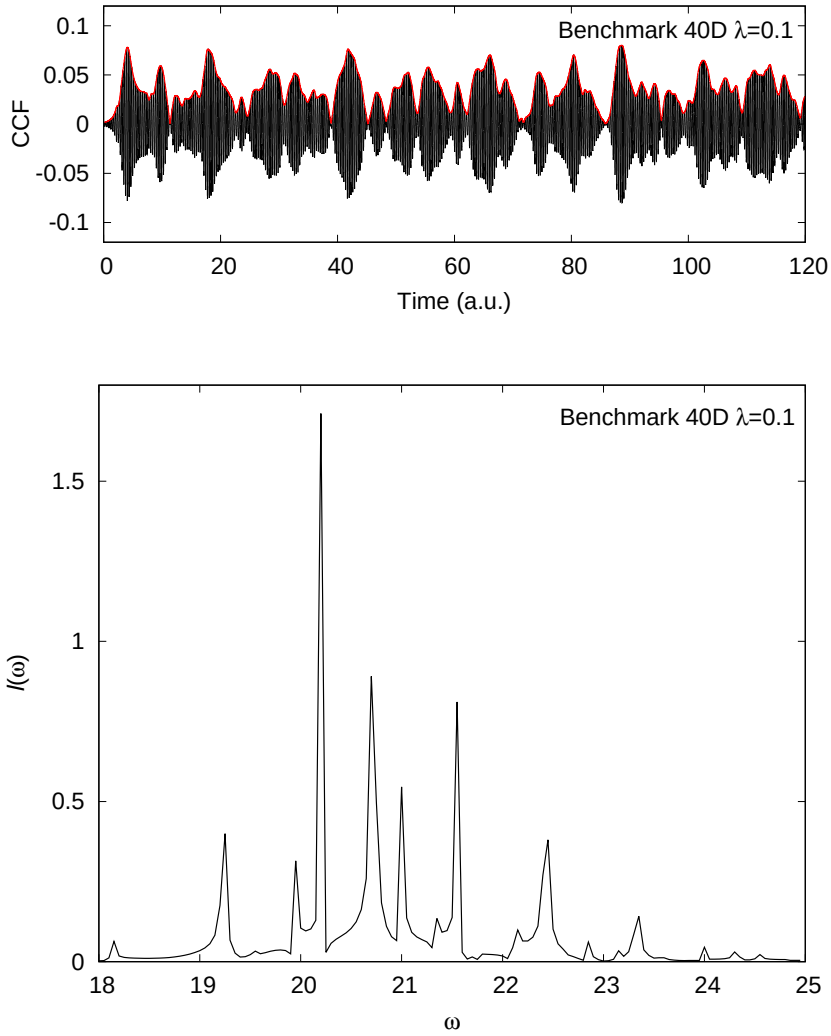

Figure 2.7: Fully converged benchmark calculation for the 40D, $\lambda = 0.1$ case Top: real part (black line) and absolute value (red line) of the cross-correlation function. Bottom: Fourier transform of the real part of the cross-correlation function.

so does the separation between the two wells, therefore one would expect a decrease in the amplitude of tunnelling. By comparison of the CCF's for the 20D and 40D case it can be seen that there is a small decrease in the amplitude for the 40D case, indicative of a small decrease in the amplitude of tunnelling.

For the 80D case, the fully converged result is shown in Fig. 2.8, with the CCF on the top of the figure, and the FT on the bottom. The fully converged calculation parameters are shown in Table 2.1. There is a large decrease in the amplitude of the CCF compared to the 20D and 40D cases, indicating a large decrease in the amplitude of tunnelling due to the increase in separation of the wells. As with the 40D case, the frequency of tunnelling increases because of coupling to a larger number of bath modes.

For both the 40D and 80D cases, the number of system basis functions required for convergence does not increase from the 20D case. Therefore, even though the tunnelling mode is coupled to more bath modes, more system basis functions are not required. The

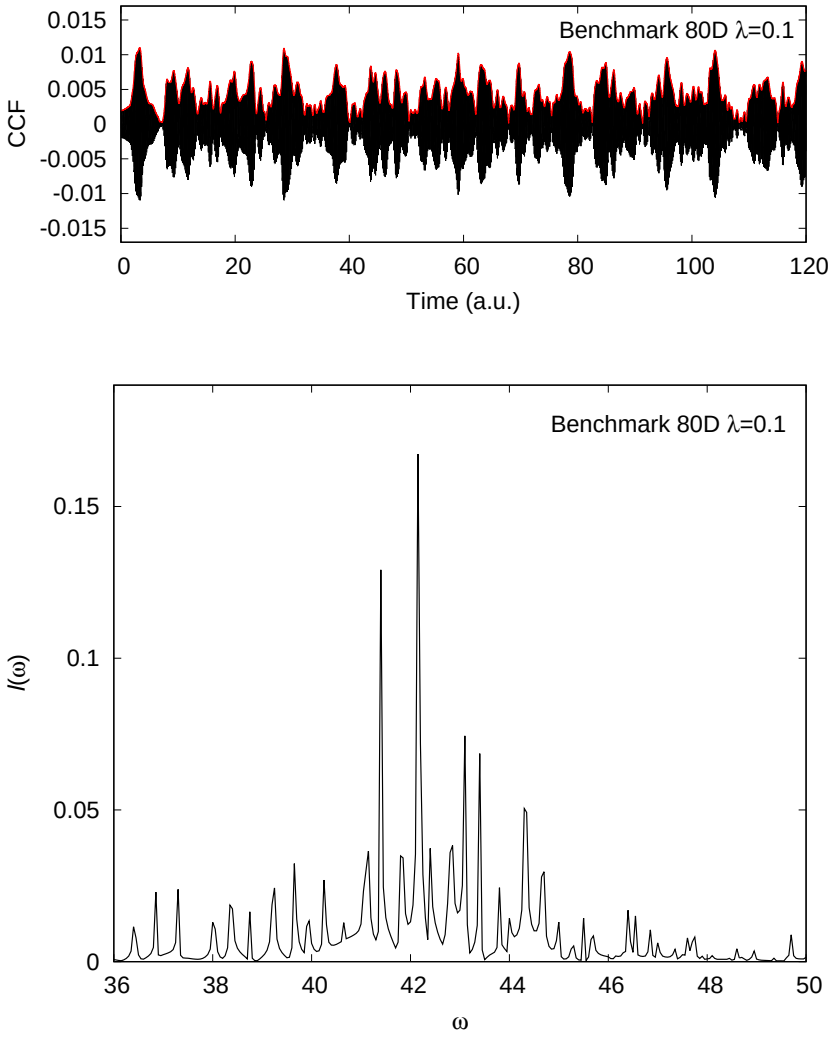

Figure 2.8: Fully converged benchmark calculation for the 80D, $\lambda = 0.1$ case Top: real part (black line) and absolute value (red line) of the cross-correlation function. Bottom: Fourier transform of the real part of the cross-correlation function.

size of the box required for the system basis functions does not increase for the 40D case relative to 20D; however, there is a small increase for the 80D case, meaning a small increase in the region of coordinate space required to be sampled by the tunnelling mode. As the increased dimensionality will result in bath modes that cover a larger region of coordinate space, and the fact that the tunnelling mode is coupled to all of them, this can be explained. The most significant change for both the 40D and 80D cases when compared to the 20D case is the number of bath basis functions required. For the 40D case $N_{\text{bth}} = 30$, corresponding to the bath basis functions involving even harmonic oscillator excited states up to and including 12 quanta. For the 80D case $N_{\text{bth}} = 45$, corresponding to the bath basis functions involving even harmonic oscillator excited states up to and including 14 quanta, the same as required for 20D, $\lambda = 0.2$. As expected, the increased dimensionality of the bath has required more harmonic oscillator excited states to converge. The total wavefunction is a superposition of the 50×8145060 and 50×5373200880 configurations for

the 40D and 80D cases respectively, which is described by sets of only 50×30 and 50×45 independent amplitudes. The much larger number of bath configurations for the 40D and 80D cases compared to 20D is due to the increased number of bath modes. Note that in Ref. [154] these configuration totals were miscalculated, and they have been corrected here.

2.4 Conclusions

In this chapter a benchmark calculation has been presented for tunnelling through a multidimensional asymmetric double well potential. The model Hamiltonian, previously used by the MP/SOFT [39], CCS [46], trajectory guided CI expansion [138], and aTG methods [140] consists of a 1-dimensional system tunnelling mode coupled via a constant λ to an $(M-1)$-dimensional harmonic bath — a system-bath problem. The dynamics were computed via a basis set expansion of the wavefunction, comprising of separate time-independent basis functions for the system and bath, and associated time-dependent amplitudes. The basis functions for the system were those of a particle in a box, and those for the bath were harmonic oscillator basis functions. The number of bath basis functions required to converge the calculation was reduced by noting two useful properties of this problem. Firstly, the coupling of bath and system is proportional to the square of the bath coordinate; therefore, as initially all modes are in the ground state, only excited state harmonic oscillator configurations with even numbers of quanta were required. Secondly, and more significantly, the indistinguishability of the harmonic oscillator excited state configurations was exploited so that only one amplitude was required to be associated to each set of indistinguishable configurations, rather than one amplitude per configuration.

A fully converged result for the 20D, $\lambda = 0.1$ problem has been presented, with comparison to the methods that have previously studied this Hamiltonian. The MP/SOFT and CI expansion methods compared well to the benchmark, whereas the aTG [140] and CCS calculations [46] did not perform as well. For the latter, it was suggested this it is due to insufficient sampling of the bath. Guidance for sampling this problem has also been presented, with the tunnelling mode being delocalised and requiring a considerable amount of phase space to be sampled, as may be expected. Ranges for sampling the coordinates and momenta of the system have been given in Sec. 2.3.1.1. The bath required a large number of configurations for convergence, although it greatly benefited from the exploitation of indistinguishability to reduce the number of basis functions required in this calculation.

A stronger system-bath coupling case, not previously studied, using $\lambda = 0.2$ was computed and it was observed that the system did not need additional basis functions to accurately represent it, although the bath did due to increased perturbation by the system. Higher dimensional cases of 40D and 80D have also been presented, in the $\lambda = 0.1$ regime once more. As with the stronger coupling case additional basis functions were required for the bath, but no additional basis functions for the system were required. However, a larger box size in the 80D case for the system particle in a box basis functions was necessary.

The fully converged CCFs and FTs for each of these calculations has been presented, providing a point of comparison for future tests on tunnelling/system-bath problems using this model Hamiltonian, including the new CCS methods that are developed in the following chapters.

Chapter 3

2-Layer Coupled Coherent States (2L-CCS)

3.1 Introduction

Multilayer formulations of numerical methods in multidimensional quantum dynamics can offer a flexible representation of the wavefunction and improved scaling with dimensionality without any loss of theoretical rigour. The MCTDH method has been extended into multilayer formalism (ML-MCTDH) [97, 119], and has been shown to be able to treat a Henon-Heiles Hamiltonian in over a thousand degrees of freedom [120]. Gaussian-based MCTDH has also been extended into a 2-layer formalism, expected to improve performance and convergence properties of the G-MCTDH method [156]. Motivated by these multilayer approaches, in this chapter CCS will be extended into a 2-layer formalism, dubbed 2-layer CCS (2L-CCS), and tested on the model Hamiltonian presented in the previous chapter.

The numerical details, including wavefunction ansatz and working equations are presented in Sec. 3.2, the application to the double well problem is in Sec. 3.3, and conclusions and possible future applications of the method are offered in Sec. 3.4. The application to the double well model includes derivation of the normal ordered form of the Hamiltonian, initial calculation parameters, and comparison of the results to the benchmark calculation and previous methods of studying the problem. The numerical efficiency and parallel scalability of the method when applied to this model is also investigated in this section, and compared to standard CCS.

The results from this chapter have been published in Ref. [35].

3.2 Numerical Details

The proposal for the 2L-CCS method is that it takes a similar form to MCE v2, reviewed in Sec. 1.4.2.2, where a quantum mechanical problem may be split into quantum and classical subsystems — although both are treated in a fully quantum manner. However, unlike MCE where the quantum part consists of regular time-independent basis functions such as electronic states $|\phi_i\rangle$, in 2L-CCS both the quantum and classical parts will be represented on a basis of coherent states. The wavefunction ansatz for 2L-CCS is then given by

$$\begin{aligned} |\Psi\rangle &= \sum_{k=1}^{K} D_k \, |\varphi_k\rangle \\ &= \sum_{k=1}^{K} D_k \left[\sum_{i=1}^{J} a_{ik} \, |\mathbf{z}_{ik}^{(\mathrm{q})}\rangle \right] |\mathbf{z}_{k}^{(\mathrm{c})}\rangle \\ &= \sum_{k=1}^{K} D_k \left[\sum_{i=1}^{J} d_{ik} \mathrm{e}^{is_{ik}/\hbar} \, |\mathbf{z}_{ik}^{(\mathrm{q})}\rangle \right] |\mathbf{z}_{k}^{(\mathrm{c})}\rangle \\ &= \sum_{k=1}^{K} D_k \left[\sum_{i=1}^{J} d_{ik} \mathrm{e}^{is_{ik}/\hbar} \, |\mathbf{z}_{ik}\rangle \right], \end{aligned} \tag{3.2.1}$$

where $|\mathbf{z}_{ik}^{(\mathrm{q})}\rangle$ are the coherent states describing the quantum part, whilst $|\mathbf{z}_{k}^{(\mathrm{c})}\rangle$ describe the classical part.

The sums are over K "outer layer" configurations and J "inner layer" quantum basis functions per configuration. When $J = 1$ the 2L-CCS ansatz is equivalent to the CCS ansatz with K configurations. When $J > 1$ the additional summation gives 2L-CCS its 2-layer nature, and permits more accurate treatment of the degree(s) of freedom represented by $|\mathbf{z}_{ik}^{(\mathrm{q})}\rangle$. The amplitude a_{ik} is factorised into the product of oscillating action exponent $\mathrm{e}^{is_{ik}/\hbar}$ and smooth pre-exponential factor d_{ik}, as with CCS and MCE. In the last line of Eq. (3.2.1), the separate basis coherent states describing the quantum and classical subsystems have been combined for simplicity. For a given configuration k all $|\mathbf{z}_{ik}\rangle$ with different i differ by only the $|\mathbf{z}_{ik}^{(\mathrm{q})}\rangle$ part.

The time-dependence of the coherent state basis functions may be determined "layer by layer". Initially, considering only the inner layer with basis functions $|\mathbf{z}_{ik}^{(\mathrm{q})}\rangle$, amplitudes d_{ik} and action exponent $\mathrm{e}^{is_{ik}/\hbar}$, it can be observed that it resembles the CCS ansatz given in Eq. (1.3.30) but with an extra index i. Therefore the time-dependence of $|\mathbf{z}_{ik}^{(\mathrm{q})}\rangle$ can be intuitively assigned to be the same as for CCS, i.e. Hamilton's equations

$$\dot{\mathbf{z}}_{ik}^{(\mathrm{q})} = -\frac{i}{\hbar} \frac{\partial H^{\mathrm{ord}}(\mathbf{z}_{ik}^{*}, \mathbf{z}_{ik})}{\partial \mathbf{z}_{ik}^{(\mathrm{q})*}} \tag{3.2.2a}$$

$$\dot{\mathbf{z}}_{ik}^{(\mathrm{q})*} = \frac{i}{\hbar} \frac{\partial H^{\mathrm{ord}}(\mathbf{z}_{ik}, \mathbf{z}_{ik})}{\partial \mathbf{z}_{ik}^{(\mathrm{q})}}. \tag{3.2.2b}$$

This can be justified by application of the principle of stationary action to the inner layer coherent states $|\mathbf{z}_{ik}^{(\mathrm{q})}\rangle$, like with CCS at the start of Sec. 1.3.2.

The outer layer of D_k amplitudes and $|\mathbf{z}_k^{(\mathrm{c})}\rangle$ basis functions closely resembles that of MCE (Eq. (1.4.18)), therefore the time-dependence of $|\mathbf{z}_k^{(\mathrm{c})}\rangle$ can be assigned to be governed by Ehrenfest trajectories

$$\begin{aligned}\dot{\mathbf{z}}_k^{(\mathrm{c})} &= -\frac{i}{\hbar}\frac{\partial \langle\varphi_k|\hat{H}|\varphi_k\rangle}{\partial \mathbf{z}_k^{(\mathrm{c})*}} \\ &= -\frac{i}{\hbar}\sum_{i,j=1}^{J} d_{ik}^* d_{jk} \langle \mathbf{z}_{ik}|\mathbf{z}_{jk}\rangle \frac{\partial H^{\mathrm{ord}}(\mathbf{z}_{ik}^*, \mathbf{z}_{jk})}{\partial \mathbf{z}_k^{(\mathrm{c})*}} \mathrm{e}^{i(s_{jk}-s_{ik})/\hbar}\end{aligned} \tag{3.2.3a}$$

$$\begin{aligned}\dot{\mathbf{z}}_k^{(\mathrm{c})*} &= -\frac{i}{\hbar}\frac{\partial \langle\varphi_k|\hat{H}|\varphi_k\rangle}{\partial \mathbf{z}_k^{(\mathrm{c})}} \\ &= -\frac{i}{\hbar}\sum_{i,j=1}^{J} d_{ik}^* d_{jk} \langle \mathbf{z}_{ik}|\mathbf{z}_{jk}\rangle \frac{\partial H^{\mathrm{ord}}(\mathbf{z}_{ik}^*, \mathbf{z}_{jk})}{\partial \mathbf{z}_k^{(\mathrm{c})}} \mathrm{e}^{i(s_{jk}-s_{ik})/\hbar}.\end{aligned} \tag{3.2.3b}$$

As with Eq. (3.2.2), the above may also be justified by application of the principle of stationary action. This time however, the Lagrangian is written in terms of φ_k as

$$\begin{aligned}\mathcal{L}[\varphi_k] &= i\hbar \langle\varphi_k|\dot{\varphi}_k\rangle - \langle\varphi_k|\hat{H}|\varphi_k\rangle \\ &= i\hbar \sum_{i,j=1}^{J} \left(a_{ik}^* \langle \mathbf{z}_{ik}^{(\mathrm{q})}|\mathbf{z}_{jk}^{(\mathrm{q})}\rangle \dot{a}_{jk} + a_{ik}^* \langle \mathbf{z}_{ik}^{(\mathrm{q})}|\dot{\mathbf{z}}_{jk}^{(\mathrm{q})}\rangle a_{jk} \right) \\ &\quad + \frac{i\hbar}{2}\left(\mathbf{z}_k^{(\mathrm{c})*}\dot{\mathbf{z}}_k^{(\mathrm{c})} - \dot{\mathbf{z}}_k^{(\mathrm{c})*}\mathbf{z}_k^{(\mathrm{c})} \right) - \langle\varphi_k|\hat{H}|\varphi_k\rangle\,.\end{aligned} \tag{3.2.4}$$

Applying the principle of stationary action to the variation in $\mathbf{z}_k^{(\mathrm{c})}$, the following Euler-Lagrange equations are obtained

$$\frac{\partial \mathcal{L}}{\partial \mathbf{z}_k^{(\mathrm{c})*}} - \frac{\mathrm{d}}{\mathrm{d}t}\frac{\partial \mathcal{L}}{\partial \dot{\mathbf{z}}_k^{(\mathrm{c})*}} = 0 \tag{3.2.5a}$$

$$\frac{\partial \mathcal{L}}{\partial \mathbf{z}_k^{(\mathrm{c})}} - \frac{\mathrm{d}}{\mathrm{d}t}\frac{\partial \mathcal{L}}{\partial \dot{\mathbf{z}}_k^{(\mathrm{c})}} = 0, \tag{3.2.5b}$$

which may each be solved to yield Eqs. (3.2.3a) and (3.2.3b).

It can seen from Eq. (3.2.3) that the trajectories for $\mathbf{z}_k^{(\mathrm{c})}$ are averaged over $\mathbf{z}_{ik}^{(\mathrm{q})}$, just as the Ehrenfest trajectories in the MCE method (Eq. (1.4.16)) were averaged over the quantum subsystem. The only difference is that for 2L-CCS the $|\mathbf{z}_{ik}^{(\mathrm{q})}\rangle$ are non-orthogonal, as opposed to the orthogonal $|\phi_i\rangle$ in MCE, meaning there is an overlap term $\langle \mathbf{z}_{ik}|\mathbf{z}_{jk}\rangle$ rather than the Kronecker delta.

The time-dependence of the amplitudes may also proceed layer by layer, as with the trajectories. The equations of motion for d_{ik} can be calculated via substitution of $|\varphi_k\rangle$ into the TDSE and closing with a basis bra $\langle \mathbf{z}_{ik}|$, which yields

$$\sum_{j=1}^{J} \langle \mathbf{z}_{ik}|\mathbf{z}_{jk}\rangle\, \mathrm{e}^{is_{jk}/\hbar}\dot{d}_{jk} = -\frac{i}{\hbar}\sum_{j=1}^{J} \langle \mathbf{z}_{ik}|\mathbf{z}_{jk}\rangle\, \mathrm{e}^{is_{jk}/\hbar} d_{jk}\delta^2 H^{\mathrm{ord}*}(\mathbf{z}_{ik}^*, \mathbf{z}_{jk}). \tag{3.2.6}$$

This is exactly analogous to CCS in Eq. (1.3.31), which should be expected as $|\varphi_k\rangle$ has exactly the same form as the wavefunction ansatz for CCS. However, the equality on

the second line of Eq. (1.3.29) cannot be applied for $\delta^2 H^{\mathrm{ord}*}(\mathbf{z}^*_{ik}, \mathbf{z}_{jk})$ in 2L-CCS because $i\hbar\dot{\mathbf{z}}_{jk}$ does not equal $\frac{\partial H^{\mathrm{ord}}(\mathbf{z}^*_{jk}, \mathbf{z}_{jk})}{\partial \mathbf{z}^*_{jk}}$, as the time-dependence of $\mathbf{z}_{jk}$ are governed by separate equations for $\mathbf{z}^{(\mathrm{c})}_k$ and $\mathbf{z}^{(\mathrm{q})}_{jk}$.

The time-dependence of the D_k amplitudes may be calculated by substitution of the entire wavefunction into the TDSE and closing with $\langle\varphi_k|$

$$\langle\varphi_k|\dot{\Psi}\rangle = \sum_{l=1}^{K} \langle\varphi_k|\varphi_l\rangle\, \dot{D}_l + \langle\varphi_k|\dot{\varphi}_l\rangle\, D_l = -\frac{i}{\hbar} \sum_{l=1}^{K} \langle\varphi_k|\hat{H}|\varphi_l\rangle\, D_l. \tag{3.2.7}$$

After taking into account the time-dependence of all elements of the basis set and following considerable substitution and rearrangement, the following is obtained:

$$\begin{aligned} &\sum_{l=1}^{K} \sum_{i,j=1}^{J} d^*_{ik} d_{jl}\, \langle \mathbf{z}_{ik}|\mathbf{z}_{jl}\rangle\, \mathrm{e}^{i(s_{jl}-s_{ik})/\hbar} \dot{D}_l \\ &= -\sum_{l=1}^{K} \sum_{i,j=1}^{J} \langle \mathbf{z}_{ik}|\mathbf{z}_{jl}\rangle\, d^*_{ik} \left(\dot{d}_{jl} + \frac{i}{\hbar} d_{jl} \delta^2 H^{\mathrm{ord}*}(\mathbf{z}^*_{ik}, \mathbf{z}_{jl}) \right) \mathrm{e}^{i(s_{jl}-s_{ik})/\hbar} D_l. \end{aligned} \tag{3.2.8}$$

The trajectories Eqs. (3.2.2) and (3.2.3), and time-dependence of the amplitudes Eqs. (3.2.6) and (3.2.8) therefore comprise the working equations of the 2L-CCS method, and they are applied in the following section to the model Hamiltonian of Eq. (2.2.1).

3.3 Application to the Double Well Tunnelling Problem

The double well tunnelling problem as described in Chapter 2 is a system-bath problem, where the tunnelling mode is the system coupled to a harmonic bath. The wavefunction ansatz of 2L-CCS makes it appropriate for application to such a system-bath problem, as it is conveniently split to represent two kinds of mode. The 1-dimensional tunnelling mode will be represented by the inner layer of $z_{ik}^{(\mathrm{q})}$, as its delocalised nature may require a large number of basis functions to model accurately. The bath is represented by the outer layer of $\mathbf{z}_k^{(\mathrm{c})}$, benefitting from trajectories that are averaged over the tunnelling mode. The bath basis functions are also initially sampled in an improved manner compared to Ref. [46], explained in the following section. The 2L-CCS calculations are therefore capable of improving both the system and bath description compared to the previous CCS calculation. The coherent state basis functions for 2L-CCS may be defined as $z_{ik}^{(\mathrm{q})} = (q_{ik}^{(1)} + ip_{ik}^{(1)})/\sqrt{2}$ and $\mathbf{z}_k^{(\mathrm{c})} = (\mathbf{Q}_k + i\mathbf{P}_k)/\sqrt{2} = \sum_{m=2}^{M}(q_k^{(m)} + ip_k^{(m)})/\sqrt{2}$ to follow the nomenclature of the Hamiltonian Eq. (2.2.1).

To be able to be used in 2L-CCS, like with CCS, the Hamiltonian must be in normal ordered form. Therefore, the position and momentum operators $\hat{q}$ and $\hat{p}$ must be replaced by creation and annihilation operators $\hat{a}^\dagger$ and $\hat{a}$, with the creation operators preceding the annihilation ones. This allows matrix elements of the Hamiltonian in the coherent state basis to be straightforwardly evaluated, as given by Eq. (1.3.6). To convert the Hamiltonian of Eq. (2.2.1) into normal ordered form and obtain the matrix elements, the operator identities in Eq. (1.3.3) and coherent state relationships in Eq. (1.3.2) may be applied to obtain

$$\begin{aligned} H^{\mathrm{ord}}(\mathbf{z}_{ik}^*, \mathbf{z}_{jl}) = &-\frac{1}{2}\left(z_{ik}^{(1)*^2} + z_{jl}^{(1)^2}\right) \\ &+\frac{1}{64\eta}\Big(z_{ik}^{(1)*^4} + z_{jl}^{(1)^4} + 4z_{ik}^{(1)*^3}z_{jl}^{(1)} + 4z_{ik}^{(1)*}z_{jl}^{(1)^3} \\ &+6z_{ik}^{(1)*^2}z_{jl}^{(1)^2} + 12z_{ik}^{(1)*}z_{jl}^{(1)} + 6z_{ik}^{(1)*^2} + 6z_{jl}^{(1)^2} + 3\Big) \\ &+\sum_{m=2}^{M} z_{ik}^{(m)*}z_{jl}^{(m)} + \frac{1}{2} + \frac{\lambda}{4\sqrt{2}}\left(z_{ik}^{(m)*^2} + z_{jl}^{(m)^2} + 2z_{ik}^{(m)*}z_{jl}^{(m)} + 1\right) \\ &\times\left(z_{ik}^{(1)*} + z_{jl}^{(1)}\right). \end{aligned} \tag{3.3.1}$$

The simplest case treated by the benchmark calculation (although still a challenging problem) of 19-dimensional bath ($M = 20$), with system-bath coupling constant $\lambda = 0.1$ is studied in the following by 2L-CCS (and nominally CCS when $J = 1$). The initial wavepacket is a multidimensional Gaussian, as with the benchmark calculation shown in Eq. (2.2.15), with initial tunnelling coordinate $q^{(1)}(0) = -2.5$ located in the lower left hand well, and initial bath coordinates $q^{(m)}(0) = 0.0$ for $m > 1$. The initial momenta for all modes is $p^{(m)}(0) = 0.0$. This is used to define the initial amplitudes and basis set sampling procedure employed for 2L-CCS, described in the following section.

J	K	$J \times K$	$\sigma^{(\mathrm{b})}$	$\sigma^{(\mathrm{s})}$	Rel. t 1 proc.	Rel. t 16 proc.
1	2000	2000	0.8	1.0	1.0	1.0
2	2000	4000	0.8	1.0	3.2	2.6
4	2000	8000	0.8	1.0	11.5	8.3
4	100	400	5.0	1.0	0.028	0.023
4	500	2000	1.2	1.0	0.69	0.52

Table 3.1: Sampling parameters for the 2L-CCS calculations: number of inner layer basis functions per configuration J, number of configurations K, compression for the distribution sampling the bath modes $\sigma^{(\mathrm{b})}$, compression for the distribution sampling the system tunnelling mode $\sigma^{(\mathrm{s})}$, relative execution time t for a single propagation step on 1 and 16 processors, where a single 2L-CCS step with $K = 2000$, $J = 1$ is taken as unity.

3.3.1 Initial Values

The initial coherent state basis functions are sampled from a "pancake" distribution, as mentioned in Sec. 1.3.3 and introduced in Ref. [76], where different distributions are used for the system and bath modes. For this Hamiltonian, a Gaussian distribution is used for both the system and bath mode coherent states, but with different compression parameters for each. The system tunnelling mode uses a compression parameter $\sigma^{(\mathrm{s})} = 1.0$ with the distribution centered around the initial tunnelling mode coordinates like in the previous CCS study [46]. Other compression parameters were tested, however this gave the best results as it permits the basis to be sufficiently compact to allow accurate representation of the initial wavepacket, whilst at the same time being sufficiently broad to model the subsequent spreading and delocalisation.

For the bath modes, it was noted in Sec. 2.3.1.1 that the previous CCS study sampled them from a distribution that was too narrow, therefore in the present work it is desirable to sample from a broader distribution. However, it is not possible to sample all bath modes from a broad distribution, as this results in coherent states that are coupled inadequately and an initial distribution that does not represent the initial wavefunction, leading to a norm far away from unity. Therefore, drawing on inspiration from the benchmark calculation in which a number of individual bath modes are "excited", a random two bath modes per configuration k are sampled from a broad distribution ("excited") with compression parameter $\sigma^{(\mathrm{b})}$, whilst all others are sampled with an infinite compression parameter. This allows the value of $\sigma^{(\mathrm{b})}$ to be smaller than if all bath modes had the same compression parameter, permitting a greater range of phase space to be sampled. The other modes being sampled with an infinite compression parameter also allows better representation of the initial wavefunction, as the initial conditions are $q^{(m)}(0) = 0.0$ and $p^{(m)}(0) = 0.0$ for $m > 1$. Choosing two modes to be decompressed rather than any other number was found to lead to an appropriate balance of ample bath sampling and well conserved norm near unity; though admittedly this is quite an *ad hoc* approach. The values of $\sigma^{(\mathrm{b})}$ for the 2L-CCS calculations performed in this chapter are shown in Table 3.1, along with other calculation parameters. As the number of configurations K increases, the value

of $\sigma^{(\mathrm{b})}$ decreases, as a broader distribution is able to be obtained whilst still conserving the norm. The relationship between basis set size, compression parameter and conservation of the norm has been demonstrated in Ref. [76] for CCS, and the same principle applies for 2L-CCS.

The initial amplitudes are calculated in two stages. Firstly, the initial set of J d_{ik} amplitudes for configuration k are calculated by projecting the coherent state distribution for the tunnelling mode $|z_{ik}^{(\mathrm{q})}(0)\rangle$ onto the initial wavefunction for the tunnelling mode $|\Psi^{(\mathrm{s})}(0)\rangle$

$$\langle z_{jk}^{(\mathrm{q})}(0)|\Psi^{(\mathrm{s})}(0)\rangle = \sum_{i=1}^{J} d_{ik}(0)\,\langle z_{jk}^{(\mathrm{q})}(0)|z_{ik}^{(\mathrm{q})}(0)\rangle\,. \tag{3.3.2}$$

The overlap $\langle z_{jk}^{(\mathrm{q})}(0)|\Psi^{(\mathrm{s})}(0)\rangle$ can be calculated using the overlap of Gaussians, Eq. (1.3.7), as $|\Psi^{(\mathrm{s})}(0)\rangle$ is a Gaussian.

Once the initial d_{ik} amplitudes have been calculated for K configurations, the initial D_k amplitudes may be determined by projection of the entire initial coherent state distribution $|\mathbf{z}_{ik}(0)\rangle$ with d_{ik} amplitudes onto the entire initial wavepacket $|\Psi(0)\rangle$

$$\langle \mathbf{z}_{jl}(0)|\Psi(0)\rangle = \sum_{k=1}^{K} D_k(0) \sum_{i=1}^{J} d_{ik}(0)\,\langle \mathbf{z}_{jl}(0)|\mathbf{z}_{ik}(0)\rangle\,. \tag{3.3.3}$$

Once more, the overlap $\langle \mathbf{z}_{jl}(0)|\Psi(0)\rangle$ can be calculated using the overlap of Gaussians. The action s_{ik} is initially set to zero. The coherent state width parameter is set to $\gamma = m\omega/\hbar = 1$.

3.3.2 Results

As with the benchmark calculation, the quantity of interest is the CCF between the wavefunction at time t and mirror image of the initial wavepacket. This is calculated via the overlap of the 2L-CCS wavefunction representation with the mirror image of the initial wavepacket, which can be written as

$$\begin{aligned}\langle \bar{\Psi}(0)|\Psi(t)\rangle = \sum_{k=1}^{K}\sum_{i=1}^{J} D_k(t) d_{ik}(t) \mathrm{e}^{is_{ik}(t)/\hbar} \prod_{m=1}^{M} \exp\Bigg[\frac{1}{\sqrt{2}}\left(\bar{q}^{(m)}(0) - i\bar{p}^{(m)}(0)\right) z_{ik}^{(m)}(t) \\ -\frac{1}{2}\left(\frac{1}{2}\left(\bar{q}^{(m)}(0) - i\bar{p}^{(m)}(0)\right)\left(\bar{q}^{(m)}(0) + i\bar{p}^{(m)}(0)\right) + z_{ik}^{(m)*}(t) z_{ik}^{(m)}(t)\right)\Bigg],\end{aligned} \tag{3.3.4}$$

where $(\bar{q}^{(m)}(0), \bar{p}^{(m)}(0))$ are the mirror image coordinates and momenta of the initial wavepacket. The spectra are also presented via the FT of the real part of the CCF to assess the long time propagation accuracy of the method. Total propagation time $T = 120$ a.u. and step size for the calculations is $\delta t = 0.1$ a.u.

Initially, the convergence of 2L-CCS with respect to the benchmark calculation in the short and long time regimes will be tested by varying the number of configurations K and inner layer tunnelling mode basis functions per configuration J. As 2L-CCS, like CCS, is based on random sampling of basis functions it is expected to be affected by noise as

the calculation progresses. Therefore, it will perform best for short times, which is why convergence with respect to the benchmark in this regime will be illustrated. For this short timescale, the CCF obtained from 2L-CCS will be qualitatively compared to that of the benchmark in the first 25 a.u. of the calculation, as well as the quantitative measure introduced in Eq. (2.3.3), describing the cumulative error of the difference between the absolute value of the CCF for 2L-CCS and the benchmark. It will be labelled $\chi_{\text{2L-CCS}}$ to differentiate it from χ_{bench} in Eq. (2.3.3)

$$\chi_{\text{2L-CCS}} = \int \left| \text{Abs}(\langle \bar{\Psi}(0)|\Psi(t)\rangle)_{\text{bench}} - \text{Abs}(\langle \bar{\Psi}(0)|\Psi(t)\rangle)_{\text{2L-CCS}} \right| \, \mathrm{d}t. \tag{3.3.5}$$

The long time accuracy can be assessed via the FT, and how it compares to the benchmark result. Following this, the method will be compared to others that have studied the Hamiltonian, as presented in Sec. 2.3.1.1, and the numerical efficiency of the method in comparison to CCS (i.e. when $J = 1$) will be demonstrated.

3.3.2.1 Convergence of 2L-CCS

The quality of short time propagation with respect to the number of configurations K and number of inner layer tunnelling mode basis functions per configuration J is shown in Fig. 3.1, with the former in the left panel and the latter on the right. The calculation with $K = 2000$ and $J = 1$ can be regarded as a CCS calculation with $K = 2000$. It can be seen qualitatively in panels (a)-(c) that both increasing K and J improves the quality of the calculation, with the phase and amplitude of the 2L-CCS CCF more closely matching the benchmark. In the (d) panels the quantitative improvement of the calculation with respect to K and J is demonstrated, with the error term $\chi_{\text{2L-CCS}}$ (defined in Eq. (3.3.5)) decreasing upon increasing these parameters.

The quality of long time propagation with respect to the number of configurations K and number of inner layer tunnelling mode basis functions per configuration J is shown in Fig. 3.2, with the former in the left panel and the latter on the right. Increasing the value of K appears to have a significant effect on the FT spectrum, with an anomalous peak at $\omega = 9$ for $K = 100$ and $K = 500$ that disappears by $K = 2000$. There is also no splitting of the peak at $\omega = 9.5$ for $K = 100$ and $K = 500$, although it appears by $K = 2000$. Increasing the value of J appears to have a more modest effect on the FT spectrum, with no anomalous peak at $\omega = 9.0$ for $J = 1$, $J = 2$ and $J = 4$, and some degree of peak splitting at $\omega = 9.5$ for each. The main difference is the correct reproduction of the relative intensities of the peaks at $\omega = 9.5$ and $\omega = 10.2$ by $J = 4$. The intensity of the peak at $\omega = 10.8$ is also more closely matched to the benchmark by this point, despite not reproducing the peak splitting.

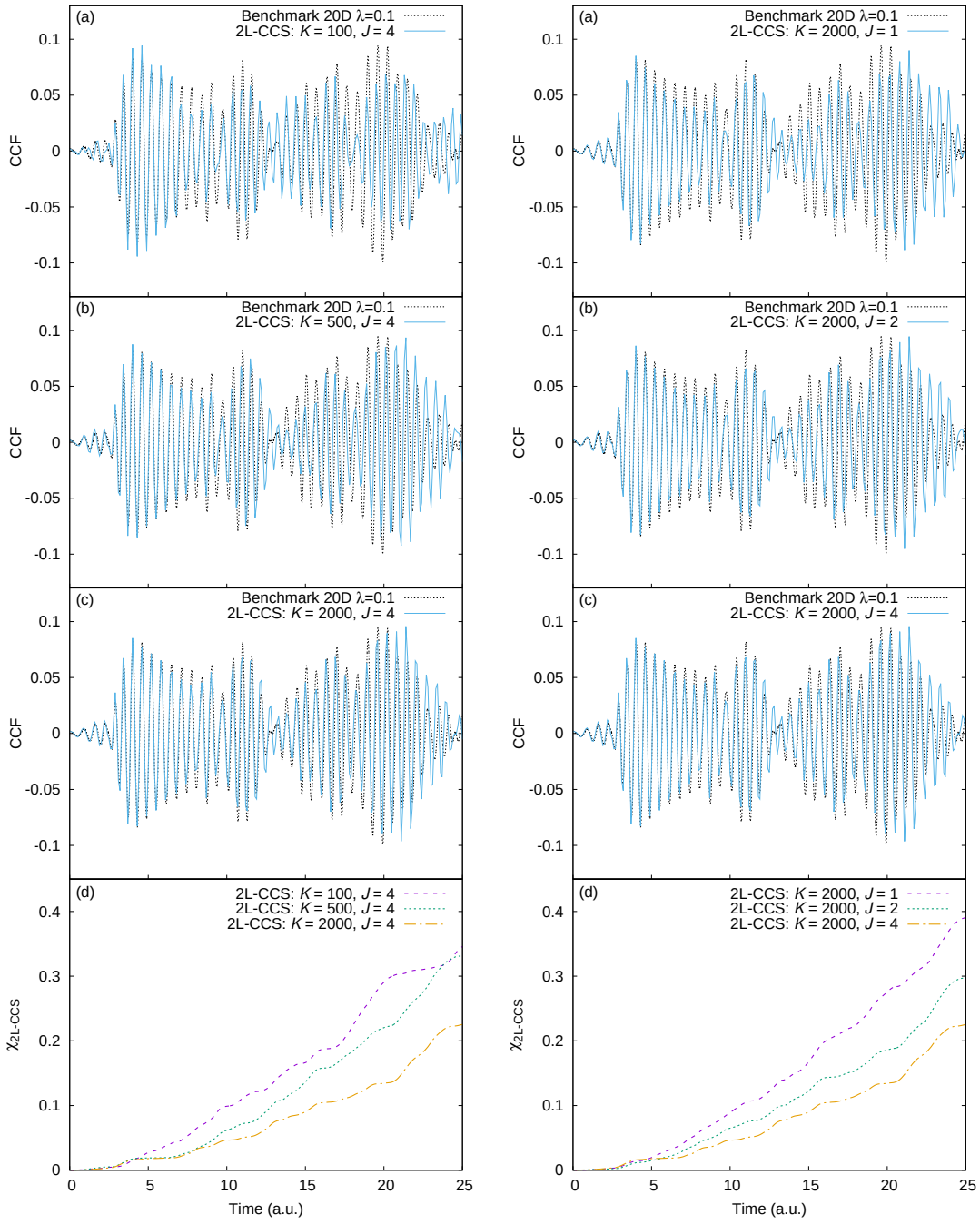

Figure 3.1: Convergence of 2L-CCS method with respect to the benchmark in the short time regime by varying number of configurations K (left) and number of tunnelling mode basis functions per configuration J (right). Panels (a)-(c) show how the calculated 2L-CCS CCFs compare to the benchmark calculation for increasing K and J. Panel (d) shows the cumulative error $\chi_{\text{2L-CCS}}$ between the 2L-CCS calculation and benchmark obtained via Eq. (3.3.5).

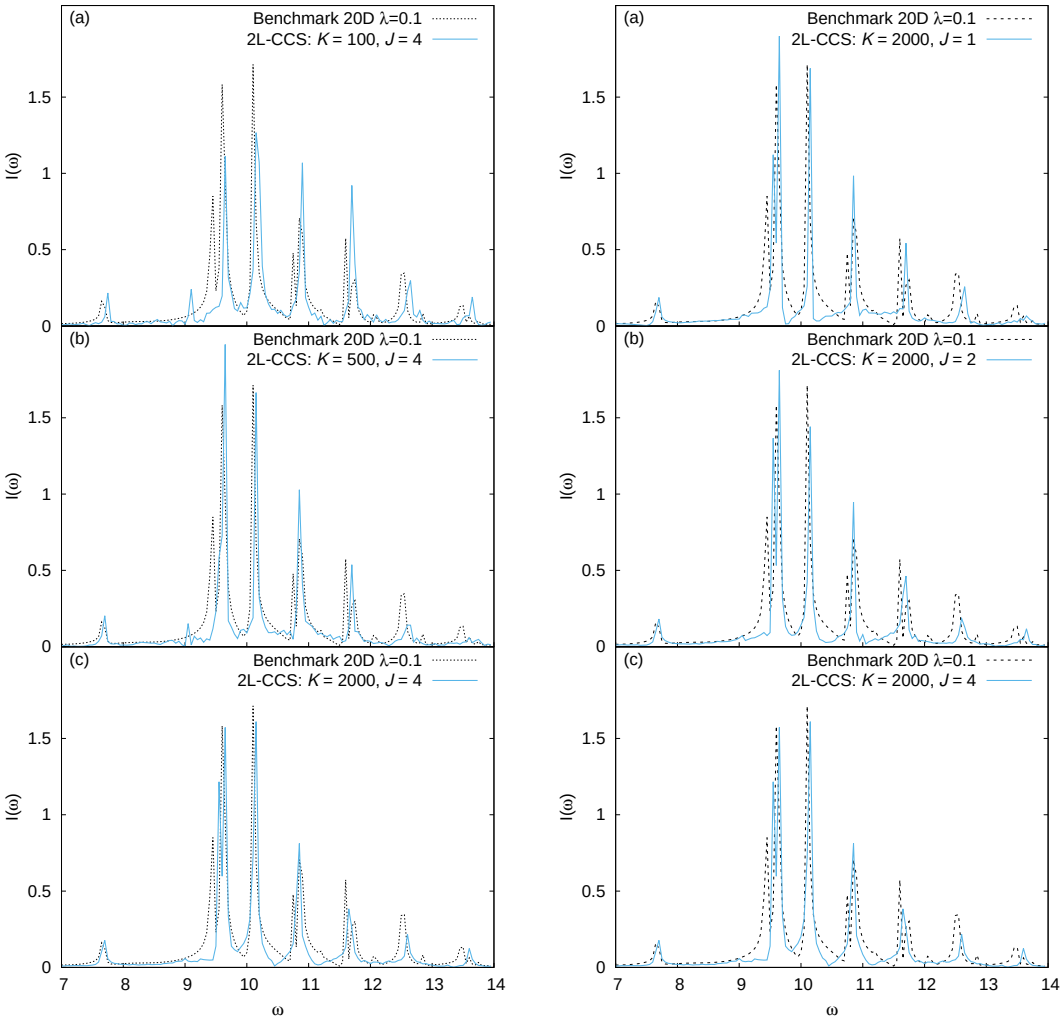

Figure 3.2: Convergence of 2L-CCS method with respect to the benchmark in the long time regime by varying number of configurations K (left) and number of tunnelling mode basis functions per configuration J (right). Panels (a)-(c) show how the calculated 2L-CCS FTs compare to the benchmark calculation for increasing K and J.

3.3.2.2 Comparison to Benchmark and Other Methods

The 2L-CCS calculation can be compared to the previous methods of studying this Hamiltonian and the benchmark calculation shown in Sec. 2.3.1.1. This comparison is demonstrated in Fig. 3.3, with CCFs on the left hand side of the figure, and FT spectra on the right hand side. The 2L-CCS calculation is that presented in the previous section with $K = 2000$ and $J = 4$. It can be seen that the 2L-CCS calculation is a vast improvement on the previous CCS calculation, with the CCF remaining accurate with respect to the benchmark and other methods up to $t = 25$ a.u. as opposed to ~ 5 a.u. The FT is also an improvement over the previous CCS calculation, with peak splitting beginning to appear at $\omega = 9.5$, and the anomalous peak at $\omega = 9$ disappearing. It should be noted that this is largely due to the improved sampling of the bath however, as it was shown in Fig. 3.2 that the 2L-CCS calculation with $K = 2000$ and $J = 1$ (hence equivalent to a CCS calculation) produced a similar FT spectrum. Further sampling of the bath was attempted, and 2L-

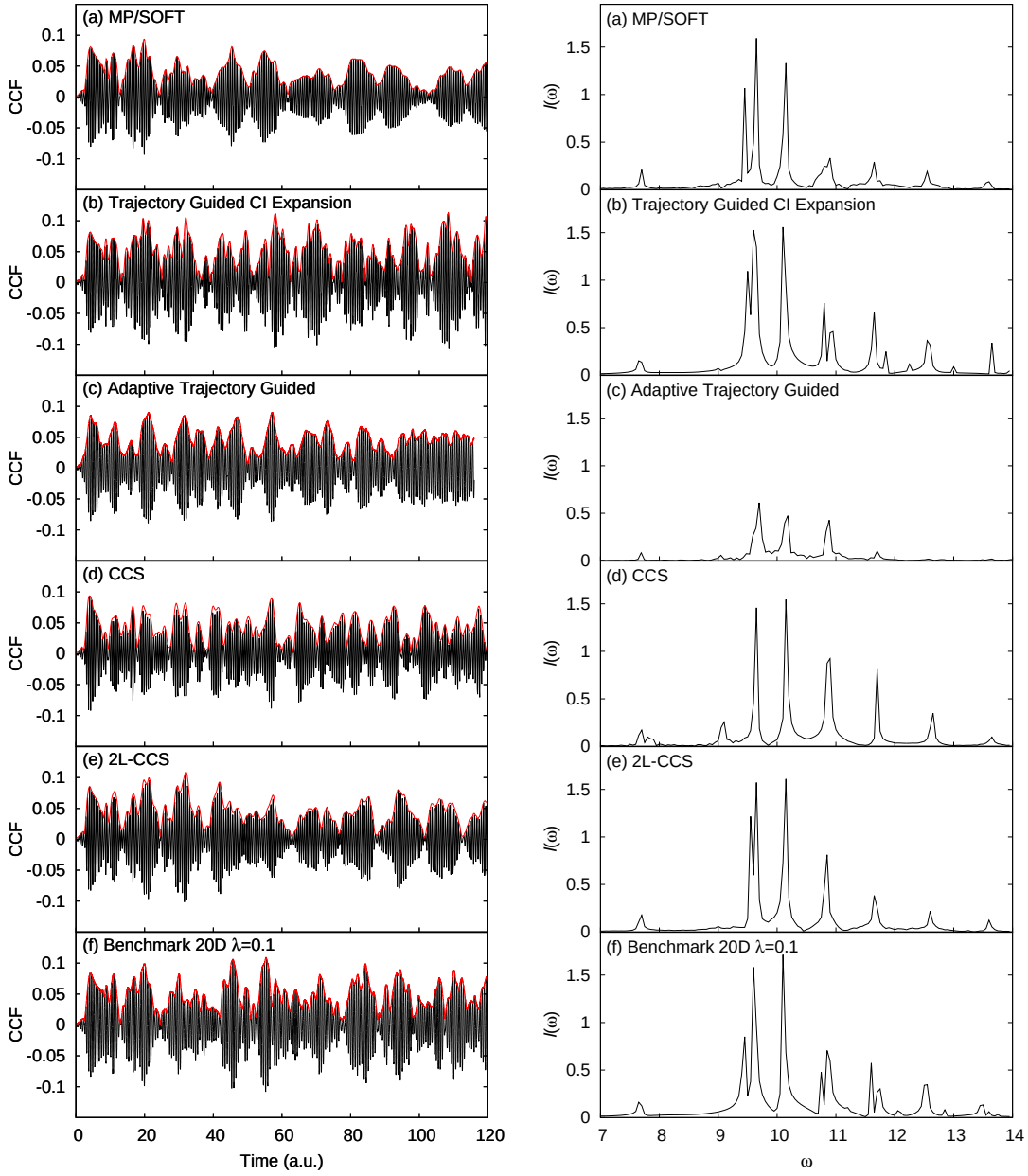

Figure 3.3: Comparison of the 2L-CCS cross-correlation functions (left, real parts in black and absolute values in red) and Fourier transforms of the real part of the CCF (right) to other methods that have studied the Hamiltonian Eq. (2.2.1): (a) MP/SOFT [39], (b) Trajectory Guided CI Expansion [138], (c) Adaptive Trajectory Guided [140], (d) CCS [46], (e) 2L-CCS, (f) Benchmark.

CCS calculations were run with the inner and outer layer modes switched (i.e. tunnelling mode represented by the outer layer $\mathbf{z}_k^{(c)}$ and bath modes represented by $\mathbf{z}_{ik}^{(q)}$), however no further improvement of the CCF beyond 25 a.u. or the FT spectrum was observed. The peak splitting at $\omega = 9.5$ also only begins to appear in the benchmark calculation beyond 50 a.u., which is the reason it is not more pronounced in the 2L-CCS calculation. Furthermore, the peak splitting at higher frequencies are not reproduced as the basis is not able to cover the high energy region effectively. A similar effect was noted in Ref. [44] when CCS was applied to the far infrared absorption spectrum of a water trimer.

The only method capable of reproducing the high frequency peak splitting is the trajectory guided CI expansion, which as mentioned in Sec. 2.3.1.1 is due to its similarity to the benchmark calculation. Aside from this point, the CCF from the 2L-CCS calculation is comparable to that from the trajectory guided CI expansion for the first 40 a.u., and the splitting of the main peak at $\omega = 9.5$ in the FT spectrum is reproduced as well as in the CI expansion. Comparing to MP/SOFT, it can be seen that the structure of oscillations and amplitude of the 2L-CCS CCF does not decay as quickly, and the higher frequency peaks in the FT spectrum are better resolved (despite neither method reproducing the splitting). The 2L-CCS method also performs better than the aTG method, with the CCF and FT spectrum much more closely matching the benchmark.

3.3.2.3 Numerical Performance of 2L-CCS

Numerically, the 2-layer method scales with the number of inner layer basis functions per configuration J and the number of configurations K, but its performance — similar to CCS — does not depend explicitly on the number of degrees of freedom. This is due to the fact that none of the working equations (Eqs. (3.2.2), (3.2.3), (3.2.6) and (3.2.8)) scale directly with dimensionality.

For the standard CCS method with K configurations, a $K \times K$ linear system has to be solved at each time step (Eq. (1.3.31)). For 2L-CCS a $K \times K$ linear system must also be solved at each time step (Eq. (3.2.8)), in addition to a $J \times J$ linear system (Eq. (3.2.6)) that must be solved K times. Solving K linear systems of size $J \times J$ and one linear system of size $K \times K$ is more efficient than solving a single $[J \times K] \times [J \times K]$ linear system, as long as J and K are balanced adequately. This is the essential idea of improved numerical performance in multilayer formulations, and means that 2L-CCS will be numerically favourable to a CCS calculation that has $J \times K$ configurations. A comparison of the numerical performance of the 2L-CCS calculations in this work can be seen in Table 3.1, where the relative times shown are for a propagation step. Basis set generation is not included in the relative times, however it is rapid in comparison to propagation. The calculation with $K = 2000$ and $J = 1$, which is equivalent to a CCS calculation with $K = 2000$, and the calculation with $K = 500$ and $J = 4$ illustrates the point made above, solving K linear systems of size $J \times J$ and one linear system of size $K \times K$ is more efficient than solving a single $[J \times K] \times [J \times K]$ linear system. On 1 processor the $K = 500$, $J = 4$ calculation is approximately 1.5× as fast, and on 16 processors it is approximately 2× as fast. For problems where K and

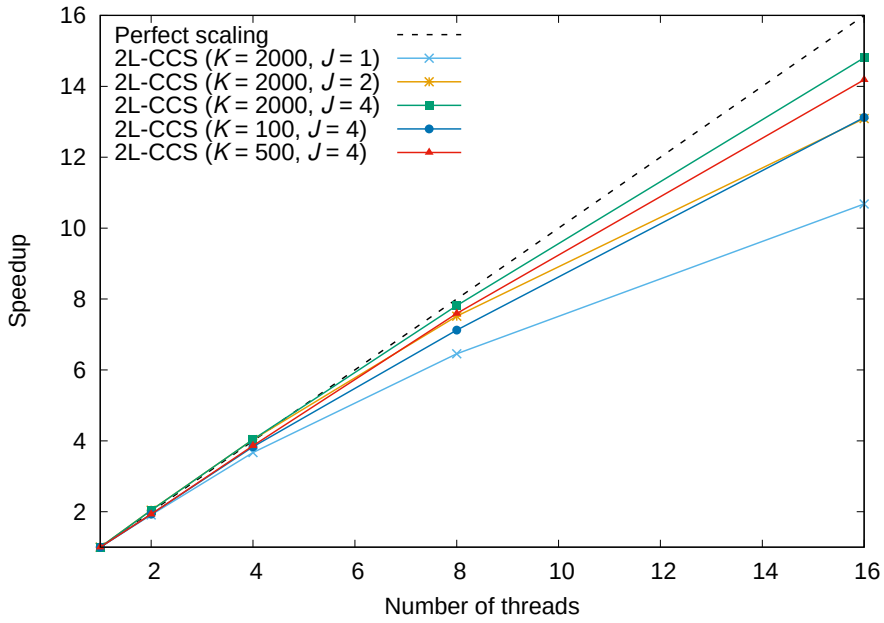

Figure 3.4: Parallel speedup for the 2L-CCS calculations studied in this chapter.

J can be even more evenly balanced, this numerical efficiency is expected to be further improved.

The 2L-CCS calculation also benefits from parallelisation to a greater extent as J is increased, and this is partially demonstrated in Table 3.1 and more profoundly shown in Fig. 3.4. The bottleneck of the calculation is the solution of the $K \times K$ linear system, however as J is increased and the number of processors is increased, the rest of the propagation can be sped up around the parallel solution of K linear systems of size $J \times J$, leading to greater parallel efficiency. This is particularly significant for the $K = 2000$, $J = 4$ calculation compared to $K = 2000$, $J = 1$, where both have the same $K \times K$ linear system to solve. On 1 processor a propagation step is 11.5× slower for the former compared to the latter, whilst for 16 processors this has been reduced to 8.3× slower.

The time for a propagation step and the parallel speedup is slightly different to that presented in Ref. [35], as a newer version of code compiled with an Intel rather than GNU compiler was used. The conclusions drawn above are broadly the same, however the code benefits from an approximate 4× speedup overall when compiled with an Intel compiler and run on Intel hardware, compared to when compiled with a GNU compiler and run on Intel hardware. A calculation to determine the numerical efficiency of CCS with $K = 2000$ was also carried out, as 2L-CCS with $K = 2000$ and $J = 1$ uses slightly different routines in the program code for the propagation despite being numerically equivalent. However, the calculation times were virtually the same therefore it has not been included.

The OpenMP shared memory construct was used to parallelise the code, requiring limited modification to the serial version. This did limit the number of threads to a maximum of 16, as computational hardware with 16 processors was used for the calculations and the general rule of thumb of 1 processor per thread was obeyed. More than 1 thread per processor could have been used, however this can lead to increased overhead that may

slow down the program, and large matrices could run into memory trouble. For larger and more complicated calculations, Message Passing Interface (MPI) parallelisation could be implemented, although this may require significant restructuring of the serial code. Further details of the code and parallelisation may be found in Sec. A.2.

3.4 Conclusions

In this chapter a 2-layer coupled coherent states scheme has been developed, drawing inspiration from the multilayer extension of MCTDH and the 2-layer extension of G-MCTDH. The working equations have been derived and presented, with different dynamical descriptions employed in each layer for different subsystems of a quantum mechanical problem. The outer layer is represented by a sum over K coherent state basis functions that are guided by Ehrenfest trajectories and describe more "classical" degrees of freedom, albeit in a fully quantum manner. The inner layer is represented by coherent state basis functions that are guided by CCS trajectories and are summed over K, as well as an additional sum over J. This provides a factor of J more basis functions for a more "quantum" degree or degrees of freedom that may require an increased mathematical description.

The 2L-CCS method has been applied to the system-bath asymmetric double well tunnelling problem studied in Chapter 2, where a benchmark calculation was provided for it. The simplest case treated by the benchmark calculation of 19-dimensional bath coupled to 1-dimensional tunnelling mode with system bath coupling $\lambda = 0.1$ was attempted by 2L-CCS. It should be noted that whilst this was the simplest parameter set treated by the benchmark calculation, it is still a challenging problem as evidenced by previous methods of studying it achieving varying degrees of success [39,46,138,140]. The 2L-CCS wavefunction representation is particularly suited to a system-bath Hamiltonian such as this, as it is split into inner and outer layers. The system tunnelling mode was represented by the inner layer, providing improved description to take into account delocalisation, whilst the bath was represented by the outer layer.

The 2L-CCS calculation was observed to compare well to the benchmark and other methods for the first 25 a.u. of the calculation, and thereafter showed divergence that is apparent in all the other methods of studying the problem. 2L-CCS was shown to converge appropriately with respect to K and J, as the calculation improved relative to the benchmark in both the short and long time regimes upon increasing these parameters. However, in the long time regime increasing K had a more profound effect than increasing J.

As well as an improved description for a subsystem of a quantum mechanical problem, one of the primary motivations for the multilayer formalism is the improved numerical efficiency of the method. The essential idea behind this is that solving K linear systems of size $J \times J$ and one linear system of size $K \times K$ is more efficient than solving a single $[J \times K] \times [J \times K]$ linear system, as long as J and K are adequately balanced. This was demonstrated by the calculations of size $K = 2000$, $J = 1$ and $K = 500$, $J = 4$, where the latter was over 1.5× as fast for a single propagation step on 1 processor, and around 2× as fast for a single propagation step on 16 processors. Improved parallel efficiency of the method as J is increased was also demonstrated with the calculations of size $K = 2000$, $J = 4$ and $K = 2000$, $J = 1$. On 1 processor a propagation step is 11.5× slower for the former compared to the latter, whilst for 16 processors this has been reduced to 8.3×

slower.

Both of these effects are expected to be enhanced for a problem where J and K can be more evenly balanced. In particular, the method may be utilised to study the phenomenon of high harmonic generation that has previously been studied by CCS [78], and was briefly reviewed in Sec. 1.3.4. It was noted that modelling the electron ionisation and recombination responsible for high harmonic generation required trajectories that occupy extremely large regions of phase space. Therefore, 2L-CCS may be a suitable candidate to model the process, with its inner layer able to provide an improved description of this highly delocalised electron. As 2L-CCS is most accurate for short timescales, it will also be particularly suited to the attosecond regime over which high harmonic generation occurs. Future work where an increased value of J will be used can also investigate the behaviour of the $\mathbf{z}^{(\mathrm{q})}$ trajectories with respect to J, to ensure they remain stable.

The above avenues of research are left to future work however, and in the following chapter a further development of the CCS method is presented: to indistinguishable bosons. As the present chapter built upon a previous CCS treatment of the double well tunnelling problem via improved bath sampling and an increased treatment of the tunnelling mode but still left some room for improvement, a different method of tackling the problem with CCS will be presented. Drawing inspiration from the benchmark calculation, where the permutational symmetry and effective indistinguishability of the bath modes was exploited, a similar approach is derived for CCS in the second quantisation picture. The ultimate aim for the method is to be used to model Bose-Einstein condensates, and this will be put into context in the following chapter.

Chapter 4

Coupled Coherent States for Indistinguishable Bosons (CCSB)

4.1 Introduction

In the past two decades there has been significant interest in systems of indistinguishable bosons, due to experimental generation of Bose-Einstein condensates of ultracold alkali metal atoms [157–159]. These condensates, first posited by the eponymous Bose and Einstein in 1924–25, have permitted macroscopic observations of quantum phenomena and lead to a wealth of experimental research in areas such as atomic interferometry [160], bosonic Josephson junctions [161, 162] and quantum vortices [163, 164].

From the theoretician's point of view, the Gross-Pitaevskii equation (GPE) [165, 166] has been the predominant method used to study Bose-Einstein condensates [149, 167–173]. However the GPE is a mean-field theory and as such cannot describe many-body effects in condensates. It also assumes that all bosons occupy a single state at all times, and therefore cannot describe fragmentation. In recent years, the multiconfigurational time-dependent Hartree method for bosons (MCTDHB) [121, 122], and its extension to multilayer formalism (ML-MCTDHB) [127] have been used to treat indistinguishable bosons from the standpoint of exact quantum mechanics (see Refs. [174–183] and [184–187] for applications of MCTDHB and ML-MCTDHB respectively).

In this chapter the CCS method is extended to the study of indistinguishable bosons, as MCTDH and ML-MCTDH have been, and the new formalism is named CCS for indistinguishable bosons (CCSB). Due to the use of coherent states in CCS and their relation to the creation and annihilation operators of second quantisation, it is expected that the method will be particularly suited to this problem. Initially, indistinguishable particles and second quantisation are introduced briefly in Sec. 4.2, before the CCSB method is presented in Sec. 4.3, then it is applied to the double well tunnelling problem with second quantised bath modes in Sec. 4.4, and a model Bose-Einstien condensate problem in Sec. 4.5. In the latter application, a brief overview of the Gross-Pitaevskii equation and MCTDHB method is given first. Conclusions and potential future applications of the method are discussed in Sec. 4.6.

4.2 Indistinguishable Particles and Second Quantisation

When two particles possess the same physical properties such as mass, charge, and spin, they may be referred to as identical. Classically, if two particles are identical it is still possible to distinguish them due to differing positions or momenta. However, in the quantum regime the positions and momenta are delocalised in the wavefunction representation, as it describes probabilities of finding particles at certain positions and momenta. It is therefore impossible to assign measurements of positions and momenta to specific particles, and the particles are said to be indistinguishable.

The wavefunction for indistinguishable particles is subject to exchange symmetry, which describes what happens to the sign of the wavefunction if particles are swapped. The Pauli principle states that the wavefunction is antisymmetric with respect to exchange of identical fermions, and symmetric with respect to exchange of identical bosons. Considering a two state system $|\alpha\rangle$ and $|\beta\rangle$ occupied by two particles r' and r'' with single particle wavefunctions $\psi^{(\alpha)}$ and $\psi^{(\beta)}$, there is the following wavefunction representation if the particles are fermions

$$\Psi_{\mathrm{f}}^{(\alpha,\beta)}(r',r'') = \frac{1}{\sqrt{2}}\left(\psi^{(\alpha)}(r')\psi^{(\beta)}(r'') - \psi^{(\alpha)}(r'')\psi^{(\beta)}(r')\right), \tag{4.2.1}$$

and the following wavefunction representations if the particles are bosons

$$\Psi_{\mathrm{b1}}^{(\alpha,\beta)}(r',r'') = \frac{1}{\sqrt{2}}\left(\psi^{(\alpha)}(r')\psi^{(\beta)}(r'') + \psi^{(\alpha)}(r'')\psi^{(\beta)}(r')\right) \tag{4.2.2a}$$

$$\Psi_{\mathrm{b2}}^{(\alpha,\beta)}(r',r'') = \psi^{(\alpha)}(r')\psi^{(\alpha)}(r'') \tag{4.2.2b}$$

$$\Psi_{\mathrm{b3}}^{(\alpha,\beta)}(r',r'') = \psi^{(\beta)}(r')\psi^{(\beta)}(r''). \tag{4.2.2c}$$

It can be seen that if r' and r'' are switched in the above then $\Psi_{\mathrm{f}}^{(\alpha,\beta)}(r',r'') = -\Psi_{\mathrm{f}}^{(\alpha,\beta)}(r'',r')$ for the fermionic state, and $\Psi_{\mathrm{b}}^{(\alpha,\beta)}(r',r'') = \Psi_{\mathrm{b}}^{(\alpha,\beta)}(r'',r')$ for the bosonic states. A further consequence of the above is the Pauli exclusion principle, which states that no two fermions may occupy the same quantum state. On the other hand, multiple bosons may occupy the same quantum state. These statistical properties are known as Fermi-Dirac statistics for fermions, and Bose-Einstein statistics for bosons.

For multiparticle states, second quantisation may be used to keep track of the occupation of quantum states. In the "first" quantisation representation shown above, the properly symmetrised wavefunctions are described by assigning specific particles to specific states. In the "second" quantisation representation, the states are instead given an occupation number that describes the number of particles belonging to that state, rather than assigning specific particles to specific states. This can be represented as

$$|\mathbf{n}\rangle = |n^{(\alpha)}, n^{(\beta)}, \ldots, n^{(\Omega)}\rangle \tag{4.2.3}$$

where $n^{(\alpha)}$ is the occupation number of state $|\alpha\rangle$, i.e. there are $n^{(\alpha)}$ particles in state $|\alpha\rangle$. The set of occupation number states $|\mathbf{n}\rangle$ is known as a Fock state, and the sum of the

occupation numbers is equal to the total number of particles. Fermions can take values of 0 or 1 for each occupation number, whilst bosons can take any value. The Fock state with all occupation numbers equal to zero is known as the vacuum state

$$|0\rangle = |0^{(\alpha)}, 0^{(\beta)}, \ldots, 0^{(\Omega)}\rangle \,. \tag{4.2.4}$$

A Fock state with a single non-zero occupation in state $|\alpha\rangle$ is known as a single mode Fock state

$$|n^{(\alpha)}\rangle = |n^{(\alpha)}, 0^{(\beta)}, \ldots, 0^{(\Omega)}\rangle \,. \tag{4.2.5}$$

To build multimode Fock states, or alter the occupation number of an existing Fock state, creation and annihilation operators must be used. These operators were presented in Sec. 1.3.1, and the coherent states $|z\rangle$ used as basis functions for the CCS method were shown to be eigenfunctions of them, with eigenvalues z^* and z, respectively. In the context of first quantisation, it was mentioned that they are also known as raising or lowering operators of the quantum harmonic oscillator, where they act on eigenfunctions of its Hamiltonian to generate another eigenfunction with eigenvalue 1 larger or smaller, respectively. In second quantisation, the creation and annihilation operators act on Fock states to populate or depopulate them. They have slightly different effects on bosonic and fermionic Fock states to maintain the occupation rules and proper symmetry. The effect of the creation and annihilation operators on bosonic Fock states is

$$\hat{a}_{\mathrm{b}}^{(\Omega)\dagger} |n^{(\alpha)}, n^{(\beta)}, \ldots, n^{(\Omega)}\rangle = \sqrt{n^{(\Omega)} + 1}\, |n^{(\alpha)}, n^{(\beta)}, \ldots, n^{(\Omega)} + 1\rangle \tag{4.2.6a}$$

$$\hat{a}_{\mathrm{b}}^{(\Omega)} |n^{(\alpha)}, n^{(\beta)}, \ldots, n^{(\Omega)}\rangle = \sqrt{n^{(\Omega)}}\, |n^{(\alpha)}, n^{(\beta)}, \ldots, n^{(\Omega)} - 1\rangle \,, \tag{4.2.6b}$$

whilst the effect on fermionic Fock states is

$$\hat{a}_{\mathrm{f}}^{(\Omega)\dagger} |n^{(\alpha)}, n^{(\beta)}, \ldots, n^{(\chi)}, n^{(\Omega)}\rangle = (-1)^{\sum_{\chi<\Omega} n^{(\chi)}} (1 - n^{(\Omega)}) \, |n^{(\alpha)}, n^{(\beta)}, \ldots, n^{(\chi)}, 1 - n^{(\Omega)}\rangle \tag{4.2.7a}$$

$$\hat{a}_{\mathrm{f}}^{(\Omega)} |n^{(\alpha)}, n^{(\beta)}, \ldots, n^{(\chi)}, n^{(\Omega)}\rangle = (-1)^{\sum_{\chi<\Omega} n^{(\chi)}} n^{(\Omega)} \, |n^{(\alpha)}, n^{(\beta)}, \ldots, n^{(\chi)}, 1 - n^{(\Omega)}\rangle \,. \tag{4.2.7b}$$

The term $(-1)^{\sum_{\chi<\Omega} n^{(\chi)}}$ in the above for fermions is known as the Jordan-Wigner string, and maintains proper symmetry of the fermionic Fock state. It involves a sum over the preceding fermion occupation numbers to obtain the parity of the state.

The creation and annihilation operators in the above have both acted on state $|\Omega\rangle$ to populate or depopulate it by a single particle, respectively. For bosons, multiparticle states can be formed by repeated application of the creation operator on the vacuum state to populate it with an arbitrary number of particles

$$|n^{(\alpha)}, n^{(\beta)}, \ldots, n^{(\Omega)}\rangle = \frac{\left(\hat{a}_{\mathrm{b}}^{(\alpha)\dagger}\right)^{n^{(\alpha)}}}{\sqrt{n^{(\alpha)}!}} \frac{\left(\hat{a}_{\mathrm{b}}^{(\beta)\dagger}\right)^{n^{(\beta)}}}{\sqrt{n^{(\beta)}!}} \cdots \frac{\left(\hat{a}_{\mathrm{b}}^{(\Omega)\dagger}\right)^{n^{(\Omega)}}}{\sqrt{n^{(\Omega)}!}} |0^{(\alpha)}, 0^{(\beta)}, \ldots, 0^{(\Omega)}\rangle \,. \tag{4.2.8}$$

The converse, the annihilation operator acting on the vacuum state will equal zero for both bosons and fermions. Also for fermions, action of the creation operator on a singly occupied state will equal zero.

The bosonic and fermionic creation and annihilation operators obey the following commutation and anticommutation rules

$$[\hat{a}_{\mathrm{b}}^{(\alpha)\dagger}, \hat{a}_{\mathrm{b}}^{(\beta)\dagger}] = \hat{a}_{\mathrm{b}}^{(\alpha)\dagger}\hat{a}_{\mathrm{b}}^{(\beta)\dagger} - \hat{a}_{\mathrm{b}}^{(\beta)\dagger}\hat{a}_{\mathrm{b}}^{(\alpha)\dagger} = 0 \tag{4.2.9a}$$

$$[\hat{a}_{\mathrm{b}}^{(\alpha)}, \hat{a}_{\mathrm{b}}^{(\beta)}] = \hat{a}_{\mathrm{b}}^{(\alpha)}\hat{a}_{\mathrm{b}}^{(\beta)} - \hat{a}_{\mathrm{b}}^{(\beta)}\hat{a}_{\mathrm{b}}^{(\alpha)} = 0 \tag{4.2.9b}$$

$$[\hat{a}_{\mathrm{b}}^{(\alpha)}, \hat{a}_{\mathrm{b}}^{(\beta)\dagger}] = \hat{a}_{\mathrm{b}}^{(\alpha)}\hat{a}_{\mathrm{b}}^{(\beta)\dagger} - \hat{a}_{\mathrm{b}}^{(\beta)\dagger}\hat{a}_{\mathrm{b}}^{(\alpha)} = \delta_{\alpha\beta} \tag{4.2.9c}$$

$$\{\hat{a}_{\mathrm{f}}^{(\alpha)\dagger}, \hat{a}_{\mathrm{f}}^{(\beta)\dagger}\} = \hat{a}_{\mathrm{f}}^{(\alpha)\dagger}\hat{a}_{\mathrm{f}}^{(\beta)\dagger} + \hat{a}_{\mathrm{f}}^{(\beta)\dagger}\hat{a}_{\mathrm{f}}^{(\alpha)\dagger} = 0 \tag{4.2.10a}$$

$$\{\hat{a}_{\mathrm{f}}^{(\alpha)}, \hat{a}_{\mathrm{f}}^{(\beta)}\} = \hat{a}_{\mathrm{f}}^{(\alpha)}\hat{a}_{\mathrm{f}}^{(\beta)} + \hat{a}_{\mathrm{f}}^{(\beta)}\hat{a}_{\mathrm{f}}^{(\alpha)} = 0 \tag{4.2.10b}$$

$$\{\hat{a}_{\mathrm{f}}^{(\alpha)}, \hat{a}_{\mathrm{f}}^{(\beta)\dagger}\} = \hat{a}_{\mathrm{f}}^{(\alpha)}\hat{a}_{\mathrm{f}}^{(\beta)\dagger} + \hat{a}_{\mathrm{f}}^{(\beta)\dagger}\hat{a}_{\mathrm{f}}^{(\alpha)} = \delta_{\alpha\beta}, \tag{4.2.10c}$$

where $\delta_{\alpha\beta}$ is the Kronecker delta. From the latter commutation and anticommutation relationship in the above, the number operator may be defined as

$$\hat{N} = \sum_{\alpha} \hat{a}^{(\alpha)\dagger}\hat{a}^{(\alpha)}. \tag{4.2.11}$$

This counts the total number of particles via a sum over all quantum states, and is applicable for both bosons and fermions.

A connection between position space $\vec{r}$ and the creation and annihilation operators can be offered by their generalisation to creation and annihilation quantum field operators $\hat{\Psi}^{\dagger}(\vec{r})$ and $\hat{\Psi}(\vec{r})$. The transformation is given by

$$\hat{\Psi}^{\dagger}(\vec{r}) = \sum_{\alpha} \psi^{(\alpha)*}(\vec{r})\hat{a}^{(\alpha)\dagger} \tag{4.2.12a}$$

$$\hat{\Psi}(\vec{r}) = \sum_{\alpha} \psi^{(\alpha)}(\vec{r})\hat{a}^{(\alpha)}, \tag{4.2.12b}$$

where $\psi^{(\alpha)}(\vec{r})$ is the single particle wavefunction for a particle at $\vec{r}$ in state $|\alpha\rangle$. The quantum field operators create and annihilate a particle at position $\vec{r}$, and obey similar commutator and anticommutator relationships for bosons and fermions as $\hat{a}^{\dagger}$ and $\hat{a}$

$$[\hat{\Psi}_{\mathrm{b}}(\vec{r}'), \hat{\Psi}_{\mathrm{b}}^{\dagger}(\vec{r}'')] = \delta(\vec{r}' - \vec{r}'') \tag{4.2.13a}$$

$$\{\hat{\Psi}_{\mathrm{f}}(\vec{r}'), \hat{\Psi}_{\mathrm{f}}^{\dagger}(\vec{r}'')\} = \delta(\vec{r}' - \vec{r}''), \tag{4.2.13b}$$

where $\delta(\vec{r}' - \vec{r}'')$ is the delta function as opposed to the Kronecker delta used previously, as $\vec{r}$ is a continuous variable. In the quantum field representation, the number operator is given by

$$\hat{N} = \int \hat{\Psi}^{\dagger}(\vec{r})\hat{\Psi}(\vec{r})\,\mathrm{d}\vec{r} = \int \hat{\rho}(\vec{r})\,\mathrm{d}\vec{r}, \tag{4.2.14}$$

where $\hat{\rho}(\vec{r})$ is known as the density operator.

This completes the brief introduction to indistinguishable particles and second quantisation, and in the following a CCS method will be developed that is capable of treating systems of indistinguishable bosons. The "b" symbol will therefore be omitted wherever creation and annihilation operators appear, as bosons are exclusively treated from this point onwards. Fermions were merely included in the above discussion for comparison and completeness.

4.3 Numerical Details

In standard CCS, the coherent state basis vector $|\mathbf{z}\rangle$ is the product of M 1-dimensional coherent state basis functions for each particle, as shown in Eq. (1.3.11). When dealing with indistinguishable bosons it is not possible to keep track of them individually, therefore it does not make sense for the coherent state basis functions to represent individual bosons. Instead a different interpretation is provided, using the coherent state basis functions for a basis set expansion of Fock states

$$|\mathbf{n}\rangle = \sum_{k=1}^{K} D_k \mathrm{e}^{iS_k/\hbar} |\mathbf{z}_k\rangle \tag{4.3.1}$$

where

$$|\mathbf{z}_k\rangle = \prod_{\alpha=0}^{\Omega} |z^{(\alpha)}\rangle \,. \tag{4.3.2}$$

The multidimensional coherent state $|\mathbf{z}\rangle$ is now a product of coherent states that describe occupations of each quantum state $|\alpha\rangle$. As the representation of Fock states by CCSB is the same as the wavefunction representation in standard CCS, the dynamical equations are also the same, with the time-dependence of the coherent state centers z given by Eq. (1.3.14), amplitudes D by Eq. (1.3.31) and action S by Eq. (1.3.20). The only difference, other than the representation of the multidimensional coherent state, is that any Hamiltonian used must be second quantised before appearing in the dynamical equations. The approach used to second quantise a Hamiltonian is well known [188], and it may be written in terms of 1-body $\hat{h}(\mathbf{Q})$ and 2-body $\hat{W}(\mathbf{Q}, \mathbf{Q}')$ operators as

$$\hat{H} = \sum_{\alpha,\beta} \langle\alpha|\hat{h}|\beta\rangle \, \hat{a}^{(\alpha)\dagger}\hat{a}^{(\beta)} + \frac{1}{2} \sum_{\alpha,\beta,\gamma,\zeta} \langle\alpha,\beta|\hat{W}|\gamma,\zeta\rangle \, \hat{a}^{(\alpha)\dagger}\hat{a}^{(\beta)\dagger}\hat{a}^{(\zeta)}\hat{a}^{(\gamma)}, \tag{4.3.3}$$

where $|\alpha\rangle$, $|\beta\rangle$, $|\gamma\rangle$, and $|\zeta\rangle$ are quantum states. This conveniently gives a second quantised Hamiltonian in normal ordered form, which is required in CCSB to evaluate matrix elements, as with standard CCS. This procedure is employed to second quantise specific Hamiltonians in the following sections where CCSB is applied to two test problems.

4.4 Application 1: Double Well Tunnelling Problem

The first application of CCSB is to the double well tunnelling problem studied in the previous two chapters, where the benchmark calculation for it was produced in Chapter 2 and the newly developed 2L-CCS method was applied to it in Chapter 3. In the benchmark calculation, permutational symmetry of the Hamiltonian and effective indistinguishability of the bath modes was exploited to reduce the expense of the calculation. In the present application the same idea is applied, with the bath modes treated as indistinguishable oscillators, and the bath part of the Hamiltonian is second quantised for use with CCSB. As the tunnelling mode is not part of this indistinguishable system, the portion of the Hamiltonian that describes it will not be second quantised. However, this will not pose a problem as the dynamical equations are identical for CCS and CCSB, the only subtlety is the interpretation of the coherent state basis vectors $|\mathbf{z}\rangle$ as will be discussed below.

4.4.1 Second Quantisation and Normal Ordering of Hamiltonian

The starting point for the second quantisation of the bath part of Hamiltonian is the distinguishable representation in Eq. (2.2.1), where it is given in terms of 1-body operators $(\hat{\mathbf{Q}}, \hat{\mathbf{P}})$. Using the definition of a second quantised Hamiltonian in Eq. (4.3.3), and the fact that there are no 2-body operators in Eq. (2.2.1), it may be written as

$$\begin{aligned}
\hat{H} &= \frac{\hat{p}^{(m=1)^2}}{2} - \frac{\hat{q}^{(m=1)^2}}{2} + \frac{\hat{q}^{(m=1)^4}}{16\eta} + \left[\sum_{\alpha,\beta=0}^{\Omega} \langle\alpha| \frac{\hat{\mathbf{P}}^2}{2} + \frac{\hat{\mathbf{Q}}^2}{2} |\beta\rangle \, \hat{a}^{(\alpha)\dagger}\hat{a}^{(\beta)}\right] \\
&\quad + \frac{\lambda\hat{q}^{(m=1)}}{2}\left[\sum_{\alpha,\beta=0}^{\Omega} \langle\alpha|\hat{\mathbf{Q}}^2|\beta\rangle \, \hat{a}^{(\alpha)\dagger}\hat{a}^{(\beta)}\right] \\
&= \frac{\hat{p}^{(m=1)^2}}{2} - \frac{\hat{q}^{(m=1)^2}}{2} + \frac{\hat{q}^{(m=1)^4}}{16\eta} + \left[\sum_{\alpha=0}^{\Omega} \langle\alpha| \frac{\hat{\mathbf{P}}^2}{2} + \frac{\hat{\mathbf{Q}}^2}{2} |\alpha\rangle \, \hat{a}^{(\alpha)\dagger}\hat{a}^{(\alpha)}\right] \\
&\quad + \frac{\lambda\hat{q}^{(m=1)}}{2}\left[\sum_{\alpha,\beta=0}^{\Omega} Q^{(\alpha,\beta)^2} \hat{a}^{(\alpha)\dagger}\hat{a}^{(\beta)}\right] \\
&= \frac{\hat{p}^{(m=1)^2}}{2} - \frac{\hat{q}^{(m=1)^2}}{2} + \frac{\hat{q}^{(m=1)^4}}{16\eta} + \left[\sum_{\alpha=0}^{\Omega} \epsilon^{(\alpha)} \hat{a}^{(\alpha)\dagger}\hat{a}^{(\alpha)}\right] \\
&\quad + \frac{\lambda\hat{q}^{(m=1)}}{2}\left[\sum_{\alpha,\beta=0}^{\Omega} Q^{(\alpha,\beta)^2} \hat{a}^{(\alpha)\dagger}\hat{a}^{(\beta)}\right].
\end{aligned} \tag{4.4.1}$$

The quantum states $|\alpha\rangle$ and $|\beta\rangle$ are those of the harmonic oscillator with α and β numbers of quanta, and the equality on the second line for $\langle\alpha|\frac{\hat{\mathbf{P}}^2}{2} + \frac{\hat{\mathbf{Q}}^2}{2}|\beta\rangle$ follows because this is non-zero with eigenvalue $\epsilon^{(\alpha)}$ only when $\alpha = \beta$. The sums are from the ground level $\alpha = 0$, to some upper level Ω. In principle, one should choose $\Omega = \infty$ for a complete description of the bath, however in practice additional oscillator levels may simply be added on until a converged result is achieved. The degenerate vibrational excitations in the benchmark calculation, illustrated in Eq. (2.2.6), are taken into account automatically in the second quantisation representation for a particular harmonic oscillator level, and do not need to

be explicitly written.

The position and momentum operators of the tunnelling mode have explicitly been labelled with $(m = 1)$ to distinguish them from the α labelling scheme of the second quantised bath modes. The matrix $Q^{(\alpha,\beta)^2}$ is evaluated in a similar manner to the benchmark calculation, Eq. (2.2.12), however the normalisation factors that appear due to the bath basis functions in the benchmark are not necessary here

$$\langle\alpha|\hat{\mathbf{Q}}^2|\beta\rangle = \begin{cases} \frac{1}{2}\sqrt{(\alpha+2)(\alpha+1)} & \text{if } \alpha = \beta - 2 \\ \frac{1}{2}\sqrt{\alpha(\alpha-1)} & \text{if } \alpha = \beta + 2 \\ \epsilon^{(\alpha)} & \text{if } \alpha = \beta \\ 0 & \text{otherwise.} \end{cases} \tag{4.4.2}$$

As this matrix is non-zero only for quanta $\alpha = \beta$ and $\alpha = \beta \pm 2$, and all bath modes are initially in the ground state, only harmonic oscillator levels with even numbers of quanta will be included. Using this fact and the definition of the normal ordered Hamiltonian matrix elements for the tunnelling mode in Eq. (3.3.1), Eq. (4.4.1) can be written in normal ordered matrix element form as

$$\begin{aligned} H^{\text{ord}}(\mathbf{z}_k^*, \mathbf{z}_l) = &-\frac{1}{2}\left(z_k^{(m=1)*^2} + z_l^{(m=1)^2}\right) \\ &+ \frac{1}{64\eta}\left(z_k^{(m=1)*^4} + z_l^{(m=1)^4} + 4z_k^{(m=1)*^3} z_l^{(m=1)} + 4z_k^{(m=1)*} z_l^{(m=1)^3}\right. \\ &\left.+6z_k^{(m=1)*^2} z_l^{(m=1)^2} + 12 z_k^{(m=1)*} z_l^{(m=1)} + 6z_k^{(m=1)*^2} + 6z_l^{(m=1)^2} + 3\right) \\ &+ \sum_{\alpha=0}^{\Omega} z_k^{(2\alpha)*} z_l^{(2\alpha)} \epsilon^{(2\alpha)} + \frac{\lambda}{2}\left(\sum_{\alpha,\beta=0}^{\Omega} z_k^{(2\alpha)*} z_l^{(2\beta)} Q^{(2\alpha,2\beta)^2}\right) \\ &\times \left(z_k^{(m=1)*} + z_l^{(m=1)}\right). \end{aligned} \tag{4.4.3}$$

The multidimensional coherent state basis vector $|\mathbf{z}\rangle$ is therefore represented as

$$|\mathbf{z}\rangle = |z^{(m=1)}\rangle \times \prod_{\alpha=0}^{\Omega} |z^{(2\alpha)}\rangle \tag{4.4.4}$$

where $|z^{(m=1)}\rangle$ is a basis function for the tunnelling mode and $|z^{(2\alpha)}\rangle$ is a basis function for the second quantised bath modes.

4.4.2 Initial Conditions

Sampling the initial coherent state basis functions for the tunnelling mode proceeds in the same way as Chapter 3, from a Gaussian distribution centered around the initial tunnelling mode coordinates and momenta. Sampling the initial coherent states for the bath can be performed by obtaining a probability distribution from the square of the coherent state

M	λ	K	Ω	$\sigma^{(2\alpha=0)}$	$\sigma^{(2\alpha>0)}$	$\sigma^{(\mathrm{s})}$	$\mathrm{d}t$ (a.u.)
20	0.1	4000	5	1.0	100	1.0	0.1
20	0.2	12000	9	1.0	2000	1.0	0.05
40	0.1	7000	8	1.0	20000	1.0	0.05
80	0.1	12000	9	1.0	1000000	0.5	0.025

Table 4.1: Sampling parameters for the CCSB calculations: number of degrees of freedom in distinguishable representation M, system-bath coupling constant λ, number of configurations K, number of harmonic oscillator levels in bath basis Ω, compression parameter for ground harmonic oscillator state distribution $\sigma^{(2\alpha=0)}$, compression parameter for excited harmonic oscillator state distributions $\sigma^{(2\alpha>0)}$, compression parameter for system tunnelling mode distribution $\sigma^{(\mathrm{s})}$, and timestep $\mathrm{d}t$.

representation of the initial bath Fock state. The initial bath Fock state is equal to

$$|\mathbf{n}\rangle = \prod_{\alpha=0}^{\Omega} |n^{(2\alpha)}\rangle = |n^{(2\alpha=0)}, n^{(2\alpha=2)}, \ldots, n^{(2\alpha=2\Omega)}\rangle = |(M-1), 0, \ldots, 0\rangle\,, \tag{4.4.5}$$

where there are $M-1$ bath oscillators all in the ground harmonic oscillator state. Using the representation of a coherent state in a basis of Fock states

$$|z\rangle = \mathrm{e}^{-\frac{|z|^2}{2}} \sum_{\alpha} \frac{z^{n^{(\alpha)}}}{\sqrt{n^{(\alpha)}!)}} |n^{(\alpha)}\rangle \tag{4.4.6}$$

the following may be obtained

$$|\,\langle z^{(2\alpha)}|n^{(2\alpha)}\rangle\,|^2 = \frac{\mathrm{e}^{-|z^{(2\alpha)}|^2} \left(|z^{(2\alpha)}|^2\right)^{n^{(2\alpha)}}}{\pi n^{(2\alpha)}!}, \tag{4.4.7}$$

where the value of π has appeared to enforce normalisation. This resembles a Poissonian distribution, however $|z^{(2\alpha)}|^2$ is continuous so a gamma distribution is used instead

$$f(|z^{(2\alpha)}|^2) \propto \frac{1}{\Gamma(n^{(2\alpha)}+1)\left(\sigma^{(2\alpha)}\right)^{n^{(2\alpha)}+1}} \left(|z^{(2\alpha)}|^2\right)^{n^{(2\alpha)}} \mathrm{e}^{\frac{-|z^{(2\alpha)}|^2}{\sigma^{(2\alpha)}}}, \tag{4.4.8}$$

where $\sigma^{(2\alpha)}$ is a compression parameter controlling the width of the distribution, and Γ is the gamma function that is calculated using $n^{(2\alpha)}+1$ because $\Gamma(n) = (n-1)!$.

The gamma distribution will be centred around $\sigma^{(2\alpha)} n^{(2\alpha)}$, however $|\,\langle z^{(2\alpha)}|n^{(2\alpha)}\rangle\,|^2$ should be centred around $|z^{(2\alpha)}|^2 = n^{(2\alpha)}$ as its maximum is found by

$$\begin{aligned}\frac{\mathrm{d}|\,\langle z^{(2\alpha)}|n^{(2\alpha)}\rangle\,|^2}{\mathrm{d}|z^{(2\alpha)}|^2} &= \frac{1}{\pi n^{(2\alpha)}!}\left(-\mathrm{e}^{-|z^{(2\alpha)}|^2}\left(|z^{(2\alpha)}|^2\right)^{n^{(2\alpha)}} + n^{(2\alpha)}\mathrm{e}^{-|z^{(2\alpha)}|^2}\left(|z^{(2\alpha)}|^2\right)^{n^{(2\alpha)}-1}\right) \\ &= 0.\end{aligned} \tag{4.4.9}$$

Fortunately, for all the calculations in this work this is not an issue, as when $n^{(2\alpha)} = 0$ the distribution will be centred around 0 irrespective of the compression parameter, and

for $n^{(2\alpha=0)} = M-1$ a compression parameter of $\sigma^{(2\alpha=0)} = 1.0$ is used. Full details of the compression parameters and other calculation parameters used in this application may be found in Table 4.1

The initial amplitudes are calculated by projection of the initial basis onto the initial wavefunction with the action set to zero

$$\langle \mathbf{z}_k(0)|\Psi(0)\rangle = \sum_{l=1}^{K} D_l(0)\,\langle \mathbf{z}_k(0)|\mathbf{z}_l(0)\rangle\,. \tag{4.4.10}$$

The overlap of the initial coherent state basis with the initial wavefunction can be decomposed to

$$\langle \mathbf{z}_k(0)|\Psi(0)\rangle = \langle z_k^{(m=1)}(0)|\Psi^{(\mathrm{s})}(0)\rangle\,\langle \prod_{\alpha=0}^{\Omega} z_k^{(2\alpha)}(0)|\mathbf{n}\rangle\,. \tag{4.4.11}$$

The coherent state overlap with initial tunnelling mode wavefunction $\langle z_k^{(m=1)}(0)|\Psi^{(\mathrm{s})}(0)\rangle$ can be calculated via a Gaussian overlap, Eq. (1.3.7), similar to 2L-CCS. The coherent state overlap with initial bath Fock state can be calculated by once more using the coherent state representation in a basis of Fock states, Eq. (4.4.6). The overlap with the unoccupied states will be equal to 1, therefore only the ground harmonic oscillator state with occupation $n^{(2\alpha=0)} = M-1$ will contribute

$$\begin{aligned}\langle \prod_{\alpha=0}^{\Omega} z_k^{(2\alpha)}(0)|\mathbf{n}\rangle &= \langle z_k^{(2\alpha=0)}(0)|n^{(2\alpha=0)}\rangle \\ &= \mathrm{e}^{-\frac{|z_k^{(2\alpha=0)}(0)|^2}{2}}\frac{(z_k^{(2\alpha=0)*}(0))^{M-1}}{\sqrt{(M-1)!}}.\end{aligned} \tag{4.4.12}$$

The coherent state width parameter is set to $\gamma = m\omega/\hbar = 1$.

4.4.3 Results

As with the previous chapters, the quantities of interest are the CCF between the wavefunction at time t and the mirror image of the initial wavepacket, and the FT of the real part of the CCF. The CCF is calculated via the overlap of Gaussians for the tunnelling mode like Eq. (3.3.4), and the overlap of coherent states with bath Fock state like Eq. (4.4.12), alongside the D amplitude and phase factor $\mathrm{e}^{iS/\hbar}$. This gives

$$\begin{aligned}\langle \bar{\Psi}(0)|\Psi(t)\rangle &= \sum_{k=1}^{K} D_k(t)\mathrm{e}^{iS_k(t)/\hbar}\,\langle \bar{\Psi}^{(\mathrm{s})}(0)|z_k^{(m=1)}(t)\rangle\,\langle \prod_{\alpha=0}^{\Omega} z_k^{(2\alpha)}(t)|\mathbf{n}\rangle \\ &= \sum_{k=1}^{K} D_k(t)\mathrm{e}^{iS_k(t)/\hbar}\exp\Bigg[\frac{1}{\sqrt{2}}\left(\bar{q}^{(m=1)}(0) - i\bar{p}^{(m=1)}(0)\right)z_{ik}^{(m=1)}(t) \\ &\quad - \frac{1}{2}\Bigg(\frac{1}{2}\left(\bar{q}^{(m=1)}(0) - i\bar{p}^{(m=1)}(0)\right)\left(\bar{q}^{(m=1)}(0) + i\bar{p}^{(m=1)}(0)\right) \\ &\quad + z_{ik}^{(m=1)*}(t)z_{ik}^{(m=1)}(t)\Bigg)\Bigg]\mathrm{e}^{-\frac{|z_k^{(2\alpha=0)}(0)|^2}{2}}\frac{(z_k^{(2\alpha=0)}(0))^{M-1}}{\sqrt{(M-1)!}}.\end{aligned} \tag{4.4.13}$$

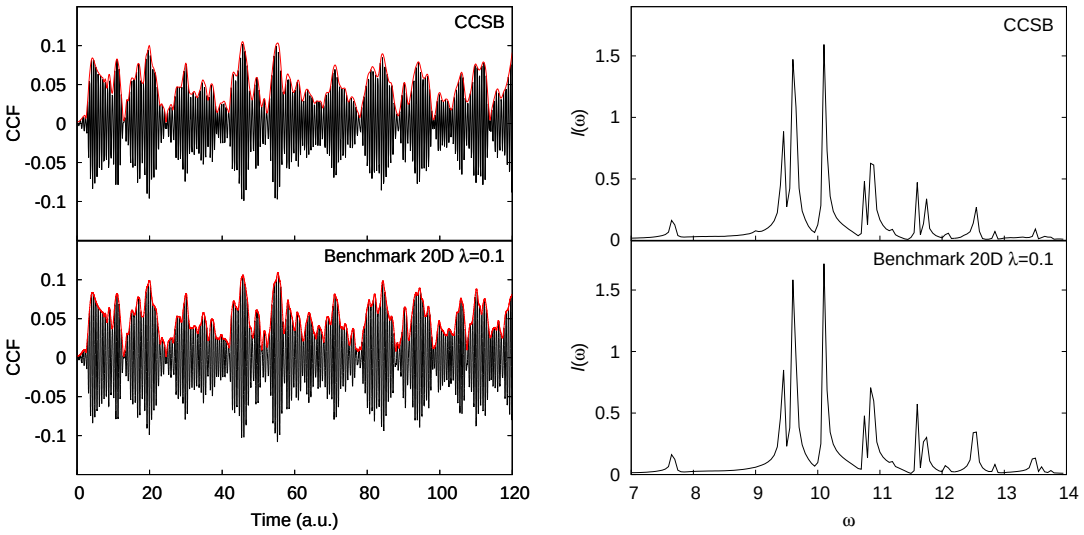

Figure 4.1: Comparison of the cross-correlation functions (left, real parts in black and absolute values in red) and Fourier transforms of the real part (right) for the CCSB calculation and benchmark, with $M = 20$ and $\lambda = 0.1$. The CCSB calculation uses $K = 4000$ and $\Omega = 5$.

Initially the same parameter set as the 2L-CCS calculations will be used, with $M = 20$ and $\lambda = 0.1$.

4.4.3.1 20D $\lambda = 0.1$

The results of the CCSB calculation compared to only the benchmark (as the other methods of studying the problem have been compared thoroughly in previous chapters) is shown in Fig. 4.1. The CCSB calculation uses $K = 4000$ configurations and $\Omega = 5$ even harmonic oscillator levels in the bath basis. This corresponds to including even harmonic oscillator levels up to a total quanta of 10, as opposed to the benchmark calculation in Sec. 2.3.1.1 that included even harmonic oscillator levels up to a total quanta of 8. This was necessary to ensure a stable propagation at the compression parameter $\sigma^{(2\alpha>0)}$ used for the excited levels. A smaller value of Ω required a smaller value of $\sigma^{(2\alpha>0)}$, and this resulted in the coherent state basis functions spreading too quickly and the CCF rapidly losing amplitude. Despite the increase in the number of harmonic oscillator levels used in the basis compared to the benchmark, the dimensionality of the problem has been reduced from 20 to only 6. Larger values of Ω also do not significantly increase the cost of the calculation, as none of the CCS working equations depend explicitly on dimensionality. The only additional overhead is calculation of extra Hamiltonian matrix elements, however this is not a large expense.

As can be seen from the CCF and the FT spectrum in Fig. 4.1, the CCSB results compare extremely favourably to the benchmark with the CCF being virtually identical for the duration of the calculation, and all peaks with splitting reproduced in the FT spectrum. Therefore, for this problem it appears taking account of the symmetry of the Hamiltonian is tantamount to achieving a good quality propagation. Due to the success of this calculation the more challenging cases put forward by the benchmark of $M = 40$ and

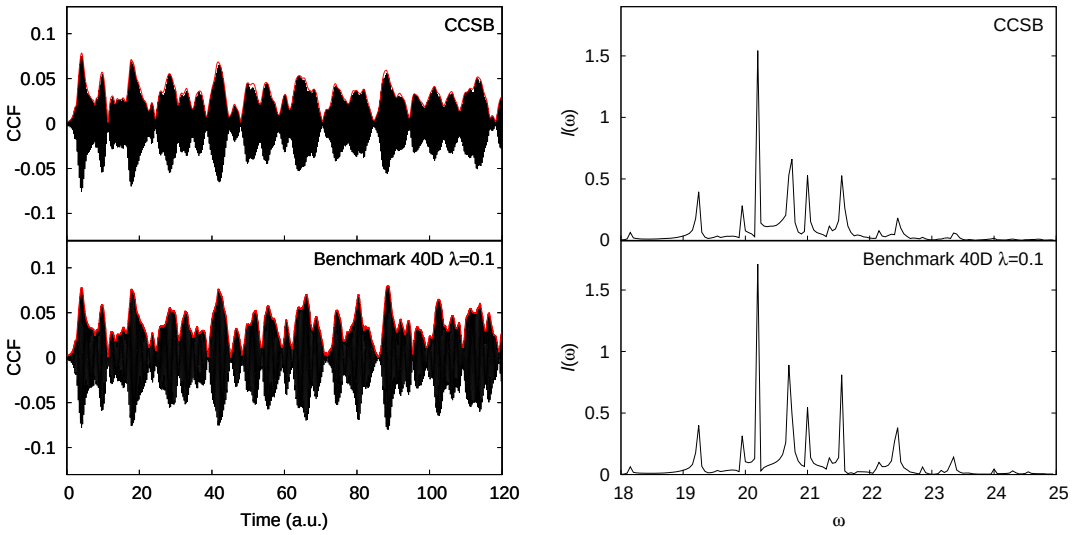

Figure 4.2: Comparison of the cross-correlation functions (left, real parts in black and absolute values in red) and Fourier transforms of the real part (right) for the CCSB calculation and benchmark, with $M = 40$ and $\lambda = 0.1$. The CCSB calculation uses $K = 7000$ and $\Omega = 8$.

$M = 80$ with $\lambda = 0.1$, and $M = 20$ with $\lambda = 0.2$ have been considered, and are presented in the following.

4.4.3.2 40D $\lambda = 0.1$

The results of the CCSB calculation compared to the benchmark for $M = 40$ is shown in Fig. 4.2, where the CCSB calculation uses $K = 7000$ configurations and $\Omega = 8$ even harmonic oscillator levels for the bath. This corresponds to including even harmonic oscillator levels up to a total quanta of 16, as opposed to 12 for the benchmark calculation in Sec. 2.3.2. As with the $M = 20$, $\lambda = 0.1$ case, this was to enable the use of a large $\sigma^{(2\alpha>0)}$ compression parameter on the distribution for the excited levels. The $\sigma^{(2\alpha>0)}$ parameter is larger than the $M = 20$, $\lambda = 0.1$ case, as the basis for the excited levels spreads rapidly, and so needs to be highly compressed initially to ensure the basis functions do not become uncoupled. The dimensionality of this problem has been reduced from 40 to 9, an even greater reduction than the $M = 20$ case, albeit with additional configurations required in the basis. More configurations are required because the occupation number of the $\alpha = 0$ level is greater initially, therefore representation of it with coherent state basis functions occupies a greater region of phase space. Furthermore, as the tunnelling mode is coupled to more bath modes, it will also require more basis functions to represent accurately.

It can be seen that the CCSB calculation compares very well to the benchmark calculation once more, with the CCF remaining accurate for the duration of the calculation, although there is some loss of structure and amplitude at $t > 45$ a.u. The peaks of FT spectrum also match those of the benchmark, with only minor differences in the intensities of the high frequency peaks.

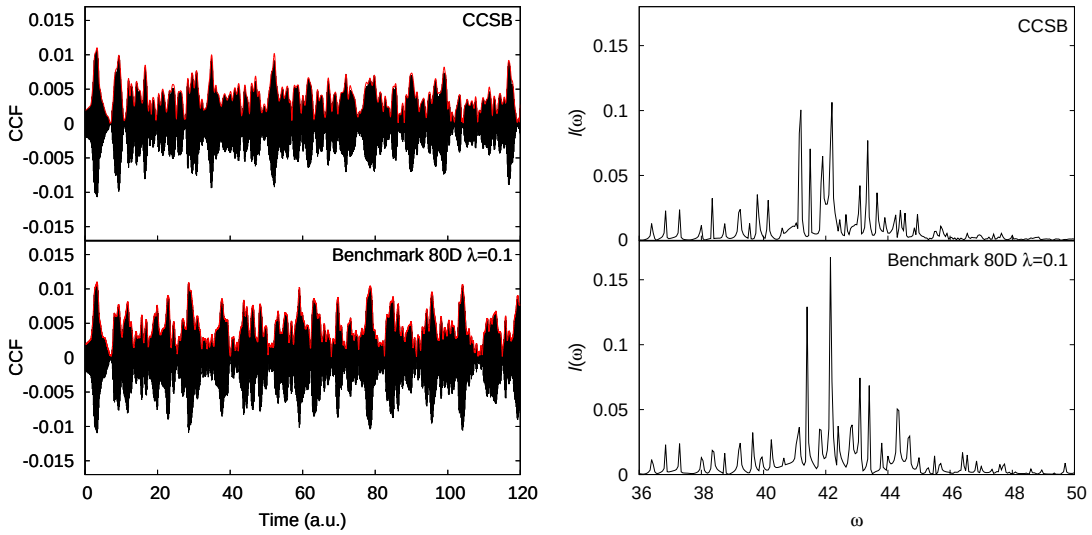

Figure 4.3: Comparison of the cross-correlation functions (left, real parts in black and absolute values in red) and Fourier transforms of the real part (right) for the CCSB calculation and benchmark, with $M = 80$ and $\lambda = 0.1$. The CCSB calculation uses $K = 12000$ and $\Omega = 9$.

4.4.3.3 80D $\lambda = 0.1$

The results of the CCSB calculation compared to the benchmark for $M = 80$ is shown in Fig. 4.3, where the CCSB calculation uses $K = 12000$ configurations and $\Omega = 9$ harmonic oscillator levels for the bath. This corresponds to including even excited levels up to a total quanta of 18, as opposed to 14 for the benchmark calculation in Sec. 2.3.2. As shown in Table 4.1, a value of $\sigma^{(s)} = 0.5$ was found to be necessary for the compression parameter on the distribution for sampling the tunnelling mode, as opposed to $\sigma^{(s)} = 1.0$ for the $M = 20$ and $M = 40$, $\lambda = 0.1$ cases. A very large value of $\sigma^{(2\alpha>0)}$ was necessary, as the basis for the excited levels spread even more rapidly than for the $M = 40$, $\lambda = 0.1$ case.

The CCF and FT spectrum are much more challenging to reproduce than the previous $M = 20$ and $M = 40$ cases due to the higher frequency oscillations of the CCF, increase in the number of peaks in the FT spectrum, and decrease in tunnelling amplitude due to larger separation of the two wells in the double well potential. This can be seen in Fig. 4.3, as the CCSB calculation does not reproduce the benchmark calculation as accurately as the prior cases, with the CCF only following the benchmark result for the first 10 a.u. Despite not reproducing the benchmark result exactly, the FT spectrum does however display a number of similar peaks, in particular the low frequency peaks in the region $\omega = 36$–37, and the main peak at $\omega = 42$, albeit without the same intensity.

As a large contribution to the accuracy of a CCS calculation depends on the initial conditions chosen, a number of different input parameters and techniques were attempted to try and improve the accuracy of the result. These included: an increased number of configurations K and harmonic oscillator levels in the basis Ω; altering the $\sigma^{(2\alpha>0)}$ and $\sigma^{(s)}$ compression parameters; using variable compression parameters for excited levels in the bath, with smaller compression parameters for lower levels as they are more likely

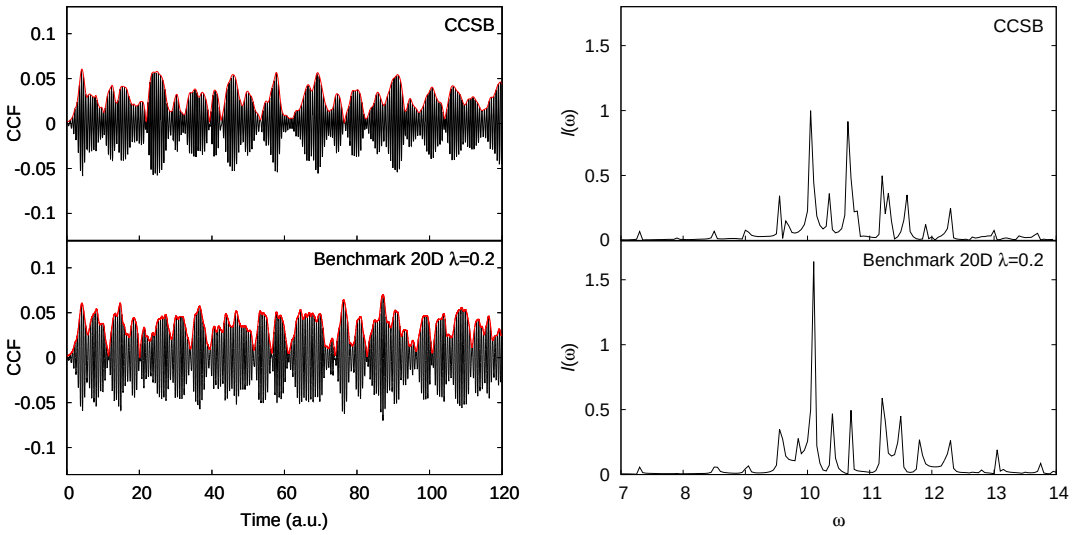

Figure 4.4: Comparison of the cross-correlation functions (left, real parts in black and absolute values in red) and Fourier transforms of the real part (right) for the CCSB calculation and benchmark, with $M = 20$ and $\lambda = 0.2$. The CCSB calculation uses $K = 12000$ and $\Omega = 9$.

to be occupied; and placing basis functions for the tunnelling mode in the upper part of the well to compensate for any trajectories that may not effectively take the basis there over the course of the calculation. However, none of these modifications lead to significant improvements over the present calculation, and it can be concluded that the $M = 80$ parameter set is a limiting case for CCSB applied to this problem. The additional calculations performed are shown in Appendix B.

4.4.3.4 20D $\lambda = 0.2$

The results of the CCSB calculation compared to the benchmark for $M = 20$, $\lambda = 0.2$ is shown in Fig. 4.4, where the CCSB calculation uses $K = 12000$ configurations and $\Omega = 9$ harmonic oscillator levels for the bath. This corresponds to including even excited levels up to a total quanta of 18, as opposed to 14 for the benchmark calculation in Sec. 2.3.1.2. Like the $M = 80$ case, it was expected that this problem would be difficult to treat, due to the higher level calculation required for the benchmark. Furthermore, due to the larger coupling constant, any deficiencies in treating either the bath or tunnelling mode are likely to be compounded through it. It can be seen from Fig. 4.4 that, like the $M = 80$ case, the CCF only matches the benchmark for the first 10 a.u. of the calculation. The peaks in the FT spectrum are mainly of the same frequency as the benchmark result, however the intensity and splittings of most are not well matched. The low frequency peaks in the FT spectrum are well reproduced however, like in the $M = 80$ case, which for $M = 20$, $\lambda = 0.2$ amount to the $\omega = 7$–9 region. The same modifications to the input parameters as the $M = 80$ case were attempted to try and improve the accuracy of the calculation, however, again this did not lead to any significant improvement over the present case. These additional calculations are shown in Appendix B.

Despite the CCSB calculations not getting the last two cases to agree with the bench-

mark perfectly, the first two show promise, and the latter two are significantly more challenging and would pose problems for any quantum dynamical method. Success at treating first two cases provides impetus to use the method on Bose-Einstein condensates, and this is attempted with a model problem in the following application.

4.5 Application 2: Indistinguishable Bosons in a Displaced Harmonic Trap

The second application of CCSB is to a system composed purely of indistinguishable bosons, with M weakly interacting bosons placed in a harmonic trap displaced from the origin. The oscillations in the density are calculated and compared to an MCTDHB result that is equivalent to the Gross-Pitaevskii equation. It should be noted that this is a relatively straightforward problem, however it serves as an introductory challenge for CCSB in the realm of pure Bose-Einstein condensates, and establishes how to calculate matrix elements of 2-body operators due to the weakly interacting nature of the bosonic cloud. Initially, the Gross-Pitaevskii equation and MCTDHB will be reviewed briefly to provide background to the methods, before discussing the Hamiltonian, how the matrix elements are obtained, and the results.

4.5.1 Gross-Pitaevskii Equation and MCTDHB

4.5.1.1 Gross-Pitaevskii Equation

The Gross-Pitaevskii equation is a mean field nonlinear Schrödinger equation, assuming that all bosons reside in the ground state. It is given in time-dependent form by

$$i\hbar\frac{\partial\Psi(\mathbf{q},t)}{\partial t} = \left(-\frac{\hbar^2}{2m}\nabla^2 + V(\mathbf{q}) + \frac{4\pi\hbar^2 a_s}{m}|\Psi(\mathbf{q},t)|^2\right)\Psi(\mathbf{q},t), \tag{4.5.1}$$

where a_s is a scattering length that is positive for a repulsive interaction between bosons, and negative for an attractive interaction. The ground state solution to this equation is usually determined variationally [169], and the wavefunction represented as a symmetrised Hartree product of single particle states. It has been applied to a number of theoretical studies on Bose-Einstein condensates [149, 167–173], however it cannot describe fragmentation of condensates and many body effects, and an improved description can be provided by MCTDHB.

4.5.1.2 MCTDHB

In MCTDHB the wavefunction for M bosons is represented as

$$\Psi(q^{(1)},q^{(2)},\ldots,q^{(M)},t) = \sum_{\mathbf{n}} C_{\mathbf{n}}(t)\Phi_{\mathbf{n}}(q^{(1)},q^{(2)},\ldots,q^{(M)},t) \tag{4.5.2}$$

where the $\Phi_{\mathbf{n}}$ are properly symmetrised Hartree products (permanents) constructed of $\theta = 1,\ldots,\Theta$ orthonormal time-dependent orbitals $\{\phi^{(\theta)}(\mathbf{q},t)\}$. The summation is over all possible occupations $\mathbf{n} = n^{(1)},n^{(2)},\ldots,n^{(\Theta)}$ such that $\sum_\theta n^{(\theta)} = M$. The time-dependence of the orbitals and coefficients $C_{\mathbf{n}}$ are found variationally, and allow the wavefunction to be propagated. In second quantisation representation, the wavefunction ansatz can be

written as

$$|\Psi(t)\rangle = \sum_{\mathbf{n}} C_{\mathbf{n}}(t)\,|\mathbf{n};t\rangle \tag{4.5.3}$$

where the Fock state $|\mathbf{n};t\rangle$ is assembled from

$$\begin{aligned}|\mathbf{n};t\rangle &= |n^{(1)},n^{(2)},\ldots,n^{(\Theta)}\rangle \\ &= \frac{1}{\sqrt{n^{(1)}!n^{(2)}!\ldots n^{(\Theta)}!}}\left[\hat{a}^{(1)\dagger}(t)\right]^{n^{(1)}}\left[\hat{a}^{(2)\dagger}(t)\right]^{n^{(2)}}\ldots\left[\hat{a}^{(\Theta)\dagger}(t)\right]^{n^{(\Theta)}}|0^{(1)},0^{(2)},\ldots,0^{(\Theta)}\rangle\,.\end{aligned} \tag{4.5.4}$$

The $\hat{a}^{(\theta)\dagger}$ are creation operators, and they are related to the orbitals via the field creation operator

$$\hat{a}^{(\theta)\dagger}(t) = \int \phi^{(\theta)*}(\mathbf{q},t)\hat{\Psi}^{\dagger}(\mathbf{q})\,\mathrm{d}\mathbf{q}. \tag{4.5.5}$$

Note the difference between the use of Fock states and creation and annihilation operators in MCTDHB compared to CCSB. In CCSB, the Fock states represent the occupation of quantum states, for example harmonic oscillator states, and the creation and annihilation operators add or remove bosons from these quantum states. In MCTDHB, the Fock states represent the occupation of orbitals, and the creation and annihilation operators add or remove bosons from these orbitals. The orbitals are time-dependent, and may be represented as a basis set expansion of primitive functions, such as harmonic oscillator basis functions. Therefore the orbitals incorporate a description of different quantum states, but do not relate to their occupation directly. MCTDHB with multiple orbitals can describe fragmented condensates, and it is expected that CCSB should be able to provide a similar description, but in a Monte Carlo fashion. This is left to future work however, and in this introductory example CCSB is compared to MCTDHB with 1 orbital, such that it is equivalent to the Gross-Pitaevskii equation. It should be noted that for this problem increasing the number of orbitals for MCTDHB does not change the result obtained for the density oscillations.

4.5.2 Hamiltonian

The Hamiltonian (in dimensionless units and distinguishable representation) for this problem consists of a shifted harmonic potential and a 2-body interaction term

$$\hat{H} = \frac{\hat{\mathbf{P}}^2}{2} + \frac{(\hat{\mathbf{Q}}-\xi)^2}{2} + \hat{W}(\mathbf{Q},\mathbf{Q}'). \tag{4.5.6}$$

where $\hat{\mathbf{Q}}$ and $\hat{\mathbf{P}}$ are the position and momentum operators of the M bosons, $\xi = 2.1$ is a parameter that shifts the harmonic potential from the origin, and $\hat{W}$ is the 2-body interaction, given by the contact interaction

$$\hat{W}(\mathbf{Q},\mathbf{Q}') = \lambda_0\delta(\mathbf{Q}-\mathbf{Q}'). \tag{4.5.7}$$

The constant $\lambda_0 = 0.001$ which indicates weak interactions and accounts for the mean-field effects in MCTDHB with 1 orbital (demonstrated in Ref. [189]), whilst $\delta(\mathbf{Q} - \mathbf{Q}')$ is the Dirac delta function. As with the previous application to the double well problem, the Hamiltonian must be second quantised and normal-ordered before it can be used with CCSB. Once more, the definition for a second quantised Hamiltonian in Eq. (4.3.3) may be utilised, and this time the 2-body elements are included to obtain

$$\begin{aligned}
\hat{H} &= \sum_{\alpha,\beta=0}^{\Omega} \langle\alpha|\frac{\hat{\mathbf{P}}^2}{2} + \frac{\hat{\mathbf{Q}}^2}{2}|\beta\rangle\, \hat{a}^{(\alpha)\dagger}\hat{a}^{(\beta)} - \sum_{\alpha,\beta=0}^{\Omega} \langle\alpha|2.1\hat{\mathbf{Q}}|\beta\rangle\, \hat{a}^{(\alpha)\dagger}\hat{a}^{(\beta)} \\
&\quad + \sum_{\alpha,\beta=0}^{\Omega} \langle\alpha|2.205|\beta\rangle\, \hat{a}^{(\alpha)\dagger}\hat{a}^{(\beta)} + \frac{1}{2}\sum_{\alpha,\beta,\gamma,\zeta=0}^{\Omega} \langle\alpha,\beta|\lambda_0\delta(\mathbf{Q}-\mathbf{Q}')|\gamma,\zeta\rangle\, \hat{a}^{(\alpha)\dagger}\hat{a}^{(\beta)\dagger}\hat{a}^{(\zeta)}\hat{a}^{(\gamma)} \\
&= \sum_{\alpha=0}^{\Omega} \langle\alpha|\frac{\hat{\mathbf{P}}^2}{2} + \frac{\hat{\mathbf{Q}}^2}{2}|\alpha\rangle\, \hat{a}^{(\alpha)\dagger}\hat{a}^{(\alpha)} - \sum_{\alpha,\beta=0}^{\Omega} \langle\alpha|2.1\hat{\mathbf{Q}}|\beta\rangle\, \hat{a}^{(\alpha)\dagger}\hat{a}^{(\beta)} \\
&\quad + \sum_{\alpha=0}^{\Omega} \langle\alpha|2.205|\alpha\rangle\, \hat{a}^{(\alpha)\dagger}\hat{a}^{(\alpha)} + \frac{1}{2}\sum_{\alpha,\beta,\gamma,\zeta=0}^{\Omega} \langle\alpha,\beta|\lambda_0\delta(\mathbf{Q}-\mathbf{Q}')|\gamma,\zeta\rangle\, \hat{a}^{(\alpha)\dagger}\hat{a}^{(\beta)\dagger}\hat{a}^{(\zeta)}\hat{a}^{(\gamma)} \\
&= \sum_{\alpha=0}^{\Omega} \epsilon^{(\alpha)}\hat{a}^{(\alpha)\dagger}\hat{a}^{(\alpha)} - \sum_{\alpha,\beta=0}^{\Omega} 2.1Q^{(\alpha,\beta)}\hat{a}^{(\alpha)\dagger}\hat{a}^{(\beta)} + \sum_{\alpha=0}^{\Omega} 2.205\hat{a}^{(\alpha)\dagger}\hat{a}^{(\alpha)} \\
&\quad + \frac{1}{2}\sum_{\alpha,\beta,\gamma,\zeta=0}^{\Omega} \lambda_0\delta^{(\alpha,\beta,\gamma,\zeta)}\hat{a}^{(\alpha)\dagger}\hat{a}^{(\beta)\dagger}\hat{a}^{(\zeta)}\hat{a}^{(\gamma)}.
\end{aligned} \tag{4.5.8}$$

In the above, $\epsilon^{(\alpha)}$ is the eigenvalue of the harmonic oscillator for state $|\alpha\rangle$, like in Eq. (4.4.1), and $Q^{(\alpha,\beta)}$ is a matrix given by

$$Q^{(\alpha,\beta)} = \langle\alpha|\hat{\mathbf{Q}}|\beta\rangle = \begin{cases} \sqrt{\frac{\alpha}{2}} & \alpha = \beta + 1 \\ \sqrt{\frac{\beta}{2}} & \beta = \alpha + 1 \\ 0 & \text{otherwise.} \end{cases}. \tag{4.5.9}$$

Evaluation of the $\delta^{(\alpha,\beta,\gamma,\zeta)}$ matrix is slightly more involved, as it is required to solve the integral

$$\begin{aligned}
\delta^{(\alpha,\beta,\gamma,\zeta)} &= \langle\alpha,\beta|\delta(\mathbf{Q}-\mathbf{Q}')|\gamma,\zeta\rangle \\
&= \int_{-\infty}^{+\infty}\int_{-\infty}^{+\infty} \frac{1}{\sqrt{2^\alpha\alpha!}}\left(\frac{1}{\pi}\right)^{1/4} \mathrm{e}^{-\mathbf{Q}^2/2} He^{(\alpha)}(\mathbf{Q}) \frac{1}{\sqrt{2^\beta\beta!}}\left(\frac{1}{\pi}\right)^{1/4} \mathrm{e}^{-\mathbf{Q}'^2/2} He^{(\beta)}(\mathbf{Q}') \\
&\quad \times \delta(\mathbf{Q}-\mathbf{Q}') \frac{1}{\sqrt{2^\gamma\gamma!}}\left(\frac{1}{\pi}\right)^{1/4} \mathrm{e}^{-\mathbf{Q}^2/2} He^{(\gamma)}(\mathbf{Q}) \frac{1}{\sqrt{2^\zeta\zeta!}}\left(\frac{1}{\pi}\right)^{1/4} \mathrm{e}^{-\mathbf{Q}'^2/2} He^{(\zeta)}(\mathbf{Q}') \\
&\quad \mathrm{d}\mathbf{Q}\,\mathrm{d}\mathbf{Q}'
\end{aligned} \tag{4.5.10}$$

where $He^{(\alpha)}(\mathbf{Q})$ is a Hermite polynomial of order α. However, an analytic solution is possible, and the above may be simplified using the relationship

$$\int_{-\infty}^{+\infty} f(x')\delta(x-x')\,\mathrm{d}x' = f(x), \tag{4.5.11}$$

and like terms collated to obtain

$$\delta^{(\alpha,\beta,\gamma,\zeta)} = \frac{1}{\pi\sqrt{2^{(\alpha+\beta+\gamma+\zeta)}\alpha!\beta!\gamma!\zeta!}} \int_{-\infty}^{+\infty} \mathrm{e}^{-2\mathbf{Q}^2} He^{(\alpha)}(\mathbf{Q}) He^{(\beta)}(\mathbf{Q}) He^{(\gamma)}(\mathbf{Q}) He^{(\zeta)}(\mathbf{Q})\,\mathrm{d}\mathbf{Q}. \tag{4.5.12}$$

This will only be non-zero if the integrand is an even function, so the product of Hermite polynomials can only have even powers of $\mathbf{Q}$

$$\delta^{(\alpha,\beta,\gamma,\zeta)} = \frac{1}{\pi\sqrt{2^{\alpha+\beta+\gamma+\zeta}\alpha!\beta!\gamma!\zeta!}} \int_{-\infty}^{+\infty} \mathrm{e}^{-2\mathbf{Q}^2} \sum_{\tau=0}^{(\alpha+\beta+\gamma+\zeta)/2} c_{2\tau}\mathbf{Q}^{2\tau}\,\mathrm{d}\mathbf{Q} \tag{4.5.13}$$

where $c_{2\tau}$ is a constant obtained from the product of Hermite polynomial coefficients. Using the following identity

$$\int_{-\infty}^{+\infty} x^{2n}\mathrm{e}^{-\frac{1}{2}ax^2} = \sqrt{\frac{2\pi}{a}}\frac{1}{a^n}(2n-1)!! \quad \text{for } n>0 \tag{4.5.14}$$

combined with a Gaussian integral for $\tau = 0$, Eq. (4.5.13) can be evaluated as

$$\delta^{(\alpha,\beta,\gamma,\zeta)} = \frac{1}{\pi\sqrt{2^{\alpha+\beta+\gamma+\zeta}\alpha!\beta!\gamma!\zeta!}} \left[\sqrt{\frac{\pi}{2}}c_0 + \sum_{\tau=1}^{(\alpha+\beta+\gamma+\zeta)/2} c_{2\tau}\sqrt{\frac{\pi}{2}}\frac{1}{4^\tau}(2\tau-1)!!\right]. \tag{4.5.15}$$

4.5.3 Results

4.5.3.1 Initial Conditions

For this problem $M = 100$ bosons in the trap are used, where all reside in the ground harmonic oscillator state initially

$$|\mathbf{n}\rangle = \prod_{\alpha=0}^{\Omega} |n^{(\alpha)}\rangle = |n^{(0)}, n^{(1)}, \ldots, n^{(\Omega)}\rangle = |100, 0, \ldots, 0\rangle\,. \tag{4.5.16}$$

As with the double well problem, the coherent states are sampled via a gamma distribution like in Eq. (4.4.8). The ground state with occupation $n^{(\alpha=0)} = 100$ is sampled with compression parameter $\sigma^{(\alpha=0)} = 1.0$, whilst the excited states with occupation $n^{(\alpha>0)} = 0$ are sampled with compression parameter $\sigma^{(\alpha>0)} = 10000$. The large compression parameter for the latter is necessary to ensure the coherent states do not become uncoupled over the course of the calculation.

Initial amplitudes are calculated by projecting the basis onto this initial Fock state

$$\langle \mathbf{z}_k(0)|\mathbf{n}\rangle = \sum_{l=1}^{K} D_l(0)\,\langle \mathbf{z}_k(0)|\mathbf{z}_l(0)\rangle\,, \tag{4.5.17}$$

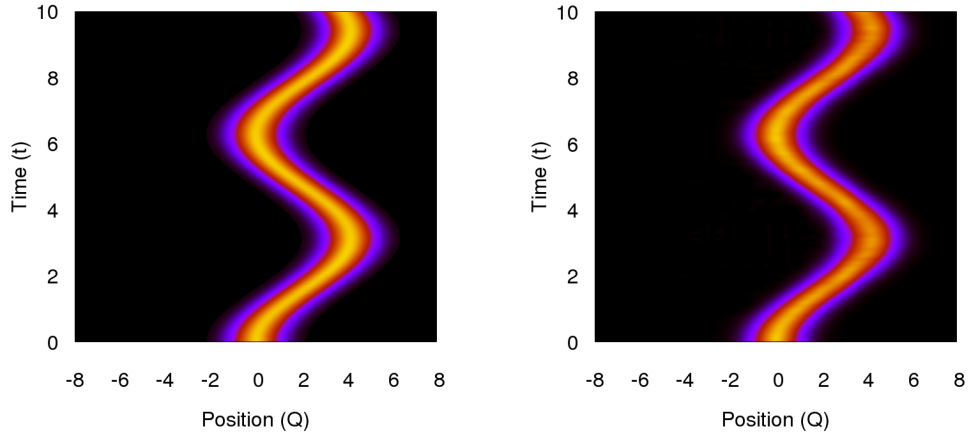

Figure 4.5: Space-time representation of the evolution of the 1-body density for MCTDHB (left) and CCSB with $K = 250$ configurations and $\Omega = 25$ harmonic oscillator levels in the basis (right).

where

$$\begin{aligned}\langle \mathbf{z}_k(0)|\mathbf{n}\rangle &= \langle \prod_{\alpha=0}^{\Omega} z_k^{(\alpha)}(0)|\mathbf{n}\rangle\rangle \\ &= \langle z_k^{(\alpha=0)}(0)|n^{(\alpha=0)}\rangle \\ &= \mathrm{e}^{-\frac{|z_k^{(\alpha=0)}(0)|^2}{2}} \frac{(z_k^{(\alpha=0)*}(0))^{100}}{\sqrt{100!}}.\end{aligned} \tag{4.5.18}$$

The coherent state width parameter is set to $\gamma = m\omega/\hbar = 1$.

4.5.3.2 Dynamics

The dynamics are followed by observing the evolution of the density matrix over the course of the calculation, which in CCSB can be evaluated as

$$\rho^{(\alpha,\beta)} = \langle \Psi|\hat{a}^{(\alpha)\dagger}\hat{a}^{(\beta)}|\Psi\rangle = \sum_{k,l}^{K} D_k^* D_l \mathrm{e}^{i(S_k - S_l)} \langle \mathbf{z}_k|\mathbf{z}_l\rangle z_k^{(\alpha)*} z_l^{(\beta)}. \tag{4.5.19}$$

As the creation and annihilation operators have different interpretations in CCSB and MCTDHB (acting on quantum states vs orbitals), the density matrix in this form also has a different interpretation. Therefore, to compare the two methods on the same footing, the 1-body density is evaluated as a function of position, which for CCSB can be calculated by the following

$$\begin{aligned}\rho(\mathbf{Q}) &= \langle \alpha|\rho^{(\alpha,\beta)}|\beta\rangle \\ &= \sum_{\alpha,\beta=0}^{\Omega} \frac{1}{\sqrt{2^\alpha \alpha!}} \left(\frac{1}{\pi}\right)^{1/4} \mathrm{e}^{-\mathbf{Q}^2/2} He_\alpha(\mathbf{Q}) \rho^{(\alpha,\beta)} \frac{1}{\sqrt{2^\beta \beta!}} \left(\frac{1}{\pi}\right)^{1/4} \mathrm{e}^{-\mathbf{Q}^2/2} He_\beta(\mathbf{Q}).\end{aligned} \tag{4.5.20}$$

The 1-body density can also be calculated by MCTDHB, and this allows a direct comparison between the methods to be made as shown in Fig. 4.5. The CCS calculation uses $K = 250$ configurations and $\Omega = 25$ harmonic oscillator levels in the basis. It can be seen from the figures that CCSB compares well with the MCTDHB calculation, reproducing the oscillation in the 1-body density of the bosonic cloud due to the displacement of the potential from the origin. This brief initial application to a Bose-Einstein condensate system provides impetus for investigation of further problems in this vein with CCSB.

4.6 Conclusions

In this chapter CCS has been extended to investigate systems of indistinguishable bosons, as MCTDH and ML-MCTDH have been. The modification to the method is relatively small, and more of an interpretive one rather than reformative. Instead of the coherent state basis functions being used to represent individual degrees of freedom like in the standard distinguishable representation of CCS, in CCSB they are used as a basis for Fock states that represent all degrees of freedom, and their occupation of quantum states, simultaneously. CCSB therefore treats problems involving indistinguishable bosons in second quantisation representation, and any Hamiltonians studied by the method must be in this form, and subsequently normal-ordered like in standard CCS.

Two example model Hamiltonians have been studied in this chapter, illustrating how the second quantisation and normal ordering may be carried out. In the first example, CCSB was applied to the system-bath asymmetric double well tunnelling problem studied in Chapters 2 and 3. As the bath is comprised of oscillators of the same frequency, they were treated as indistinguishable and the bath portion of the Hamiltonian second quantised. The system tunnelling portion of the Hamiltonian was kept in distinguishable representation, therefore this first application was a hybrid of standard CCS and CCSB. This does not pose a problem however, as the wavefunction representation and working equations for trajectories and time-dependence of amplitudes are the same in each. The previously studied 20D, system-bath coupling $\lambda = 0.1$ case was investigated initially. The second quantised bath required $\Omega = 5$ harmonic oscillator levels in the basis for the converged result, thus the dimensionality of the problem was reduced from 20 to 6. The CCSB calculation was in excellent agreement with the benchmark result, illustrating the accuracy of the method and providing incentive to study the more difficult cases put forward by the benchmark in Chapter 2. For the 40D, $\lambda = 0.1$ problem CCSB also performed well, producing a result that was in very good agreement with the benchmark calculation, and reducing the dimensionality of the problem from 40 to 9. The 80D, $\lambda = 0.1$, and 20D, $\lambda = 0.2$ cases were not as successful, however these are much more challenging problems and the fact that CCSB was successful in treating the first two cases is promising. In particular, no previous quantum dynamics method that has studied the Hamiltonian [39, 46, 138, 140] has produced a result as accurate as CCSB for the 20D, $\lambda = 0.1$ case.

In the second example, a model Hamiltonian for a system of 100 bosons in a shifted harmonic trap was studied, and oscillations in the 1-body density calculated. This is a system composed entirely of indistinguishable bosons, and provided an introductory test for CCSB in the realm of Bose-Einstein condensates. Ultimately, the method is aimed for use in studying such systems. Matrix elements of 2-body operators had to be calculated, as is common for interacting condensates, and it was demonstrated that these could be computed analytically by CCSB. The density oscillations were compared to a MCTDHB calculation that was equivalent to using the Gross-Pitaevskii equation, which

are two of the main methods used for studying condensates theoretically. The CCSB result compared well to that of MCTDHB/GPE, and provides motivation for further study on more challenging Bose-Einstein condensate systems.

This chapter concludes the portion of this thesis concerning developing extensions to the CCS family of methods. In the following chapter there is a change of tack, with the existing AIMC method used to study the nonadiabatic dynamics of 2-ethylpyrrole, and compare to pyrrole.

Chapter 5

Ultrafast Dynamics of 2-Ethylpyrrole

5.1 Introduction

A number of fundamental processes in chemistry and biology involve ultrafast excited state dynamics following photo-absorption, including light harvesting in plants and natural fluorescence. Nitrogen containing aromatic heterocycles are found in molecules responsible for the above processes, and in particular pyrrole is a component of chlorophyll as well as being present in chromophores of other important natural compounds such as: vitamin B12; heme; bilirubin; biliverdin; and tryptophan. Due to this prevalence, in recent years there has been significant interest in its excited state dynamics both experimentally [110, 190–205] and theoretically [109, 204–224].

Whilst a large component of effort has been directed to understanding the excited state dynamics of pyrrole, much less well studied are its derivatives. This is also an important area to explore how modification alters its function. Recently, 2-ethylpyrrole (2-EP) has been studied experimentally by H (Rydberg) atom photofragment translational spectroscopy (HRA-PTS) [222], time-resolved velocity map imaging (TR-VMI) and time-resolved ion yield (TR-IY) mass spectrometry [225] to examine the effects of ring-substitution on pyrrole. The only theoretical investigations on 2-EP have consisted of electronic structure calculations [222], therefore in the present chapter nonadiabatic quantum dynamics calculations are performed on the molecule via the *ab initio* multiple cloning (AIMC) method [34], to offer insight to experiment [225]. The effect of selective deuteration at the N-H bond has also been studied experimentally [225], so this is modelled as well to illustrate the capability of AIMC to reproduce experimental kinetic isotope effects. Pyrrole has been studied previously by AIMC [223, 224], and these results are presented with additional analysis, as well as unpublished deuterated pyrrole calculations performed by D. Makhov, and comparison to experiment [203].

A description of the AIMC method, including the diabatic to adiabatic modification of the MCE working equations from Sec. 1.4.2.2 to allow on-the-fly dynamics will be presented in Sec. 5.2. Following this, a brief overview of the experiments [203, 225] that the AIMC

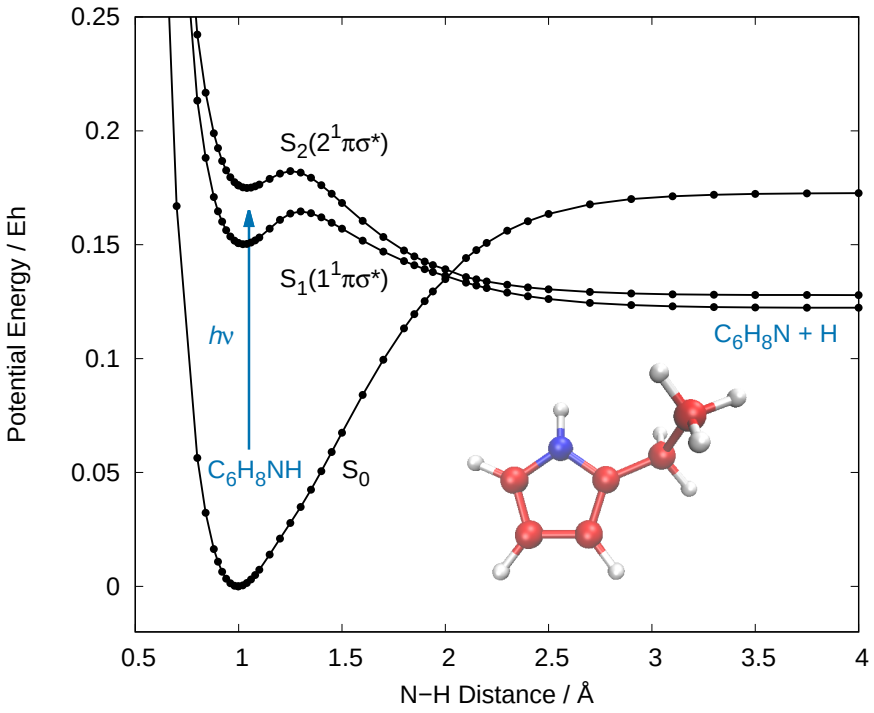

Figure 5.1: Potential energy curve for the ground and two lowest lying $\pi\sigma^*$ singlet states of 2-EP calculated at the SA3-CAS(8,7) level of theory, overlaid with a brief schematic of the photoexcitation process, and image of the 2-EP molecule.

calculations are being compared to will be given in Sec. 5.3. The computational details for the AIMC calculations will then be shown in Sec. 5.4, and subsequently the results of these and comparison to experiment will be given in Sec. 5.5, with 2-EP in Sec. 5.5.1 and pyrrole in Sec. 5.5.2. Finally, conclusions drawn from these results and possible future molecules of photochemical interest to be studied will be presented in Sec. 5.6. Initially however, it is worthwhile to briefly summarise the current understanding of the ultrafast excited state dynamics of pyrrole, and to contrast and compare to 2-EP.

Early electronic structure work on pyrrole [206–209] helped to characterise the lowest energy excited states, with the seminal work by Sobolewski *et al.* [207, 208] identifying the importance of the low lying $\pi\sigma^*$ states. These states are dissociative along the N-H stretch coordinate, and provide an ultrafast radiationless transfer route through a conical intersection with the ground state, deactivating potentially reactive excited species. There are two low lying $\pi\sigma^*$ states in pyrrole that have spin symmetry labels 1^1A_2 and 1^1B_1 due to its C_{2v} molecular symmetry. Transitions from the X^1A_1 ground state to the lower energy of these two, the $1^1A_2(\pi\sigma^*)$ state, are formally electric dipole forbidden. However, it can become directly populated through vibronic mixing with nearby higher lying $\pi\pi^*$ states 1^1A_1 and 1^1B_2 (albeit with low transition cross-sections), or indirectly via internal conversion from the $1^1B_2(\pi\pi^*)$ state at shorter wavelengths. Electronic structure calculations for 2-EP revealed an increase in oscillator strength for the ground to first excited $\pi\sigma^*$ state transition compared to pyrrole [222], which is to be expected due to the reduction in molecular symmetry to C_s in the *anti* conformation and C_1 in the lowest energy *gauche* conformer. Fig. 5.1 shows a potential energy curve along the N-H stretch

coordinate for the ground and two lowest lying singlet $\pi\sigma^*$ states for 2-EP, calculated at the SA3-CAS(8,7) level of theory (further details of this are in Sec. 5.4). The curves are labelled by their adiabatic electronic states, and are overlaid with a brief schematic of the photoexcitation process, and image of the 2-EP molecule.

Early experimental studies on pyrrole observed two H atom dissociation channels: one with a sharp high kinetic energy distribution of H atoms emitted perpendicular to the transition dipole moment; and one with a broader lower kinetic energy distribution, and a more isotropic emission [110, 190–194]. It was posited that the former high kinetic energy dissociation channel was due to rapid N-H dissociation along the $1^1A_2(\pi\sigma^*)$ state, followed by conical intersection with the ground state to produce a pyrrolyl radical in the 1^2A_2 state. The latter lower kinetic energy dissociation channel was thought to be due to internal conversion to a "hot" ground state, followed by statistical dissociation. The high kinetic energy channel is believed to be dominant at longer pump wavelengths, with Wei *et al.* [191] observing approximately 76% following this route at $\lambda = 243.1$ nm via the integration of the kinetic energy spectrum. At shorter pump wavelengths ($\lambda < 218$ nm) the lower kinetic energy channel is dominant [110], with $1^1B_2(\pi\pi^*)$ populated initially before passing through conical intersections to reach the ground state of the radical (either sequentially via $1^1B_2(\pi\pi^*) \rightarrow 1^1A_2(\pi\sigma^*) \rightarrow 1^2A_2$, or by some other mechanism). The addition of a σ donating ethyl group in 2-EP causes the onset of H atom dissociation to appear at longer wavelengths: 267 nm in 2-EP [222] vs 254 nm in pyrrole [110]. Excitation in the range $248 \leq \lambda \leq 263$ nm leads to a single high kinetic energy peak in the H atom total kinetic energy release (TKER) spectrum due to dissociation from the lowest energy $\pi\sigma^*$ state [222].

Time-resolved studies on pyrrole provided quantitative measures of the H atom appearance lifetimes in each of these dissociation channels [200–205]. Lippert *et al.* [200] conducted the first of these studies by using TR-IY to obtain time-constants of $\tau_1 = 110 \pm 80$ fs for the high kinetic energy channel and $\tau_2 = 1.1 \pm 0.5$ ps for the lower kinetic energy channel at $\lambda = 250$ nm. Subsequently, Roberts *et al.* used both TR-VMI and TR-IY to observe a single time constant of 126 ± 28 fs for the high kinetic energy channel at $\lambda = 250$ nm [203]. It was postulated that tunnelling out of the quasi-bound region of the $1^1A_2(\pi\sigma^*)$ state played a role at this excitation wavelength, as a time constant of 1.4 ± 0.3 ps for selectively deuterated pyrrole-d_1 dissociation gave a kinetic isotope effect (KIE) of ~ 11. Further pump wavelengths were used by Roberts *et al.* in this study, with excitation at $\lambda = 238$ nm yielding a time constant of 46 ± 22 fs for undeuterated pyrrole, and 136 ± 38 fs for pyrrole-d_1. Due to the smaller KIE (~ 3), this was therefore attributed to faster, over the barrier dissociation with negligible contribution from tunnelling. Finally, at $\lambda = 200$ nm a time constant of 52 ± 12 fs was observed, attributed to initial population of the $1^1B_2(\pi\pi^*)$ state and subsequent rapid internal conversion to the $1^1A_2(\pi\sigma^*)$ state and dissociation. A low kinetic energy feature was observed at this wavelength, however it had a time-constant of 1.0 ± 0.4 ns rather than the picosecond timescale observed by Lippert *et al.* [200] It was suggested that the nanosecond time-constant was

due to C-H statistical dissociation, that N-H statistical dissociation may have an even longer timescale, and the picosecond timescale observed by Lippert *et al.* could be due to undesired multiphoton dissociative ionisation events [203]. The TR-VMI study by Roberts *et al.* at pump wavelength $\lambda = 238$ nm is used for comparison to AIMC calculations on pyrrole in Sec. 5.5.2, and the experimental details will be discussed further in Sec. 5.3.

TR-VMI and TR-IY studies on 2-EP in the $248 \leq \lambda \leq 265$ nm range found high kinetic energy H atom appearance lifetimes on the order of 50–80 fs, similar to the over the barrier dissociation times for pyrrole [225]. Selectively deuterated 2-EP-d_1 at $\lambda = 257$ nm had an appearance lifetime of 140 ± 20 fs giving a KIE of ~ 2, further suggesting that tunnelling is not involved in the dissociation mechanism. At excitation wavelengths shorter than 248 nm, an additional low kinetic energy feature appeared in the H atom TKER spectrum, similar to pyrrole. However, the appearance lifetime was ∼1.5 ps, intimating it was not due to statistical dissociation [225]. The same experimental methodology and kinetic fits were used as Roberts *et al.* with pyrrole [203], suggesting undesired multiphoton dissociative ionisation events were not the cause. Furthermore, the same low kinetic energy feature was observed with 2-EP-d_1 at $\lambda = 238$ nm, implying this feature is due to fission of the N-H/N-D bond. Involvement of higher lying excited states (such as $\pi\pi^*$) and slow migration from them was proposed, with coupling to a number of vibrational modes. The TR-VMI studies by Cole-Filipiak *et al.* in this work are used for comparison to AIMC calculations on 2-EP in Sec. 5.5.1, and the experimental details will be discussed further in Sec. 5.3.

Previous quantum dynamics calculations on pyrrole have used reduced dimensionality potential energy surfaces [210–212], surface hopping [214–218], and MCTDH with parameterised potential energy surfaces [204, 205, 219–221]. The AI-MCE [100] and AIMC [34] methods have also previously been used for dynamics studies on pyrrole [109, 223, 224]. In the former, using the AI-MCE method, conical intersections of the 1^2A_2 and 1^2B_1 radical states following H dissociation were observed, helping to explain the lack of experimentally observed pyrrolyl radicals in the 1^2B_1 state [109]. In the latter, using the AIMC method, it was suggested that some low kinetic energy H atoms are formed in an ultrafast manner as a result of dissociation where the radical does not transfer to the ground state immediately [223, 224]. These AIMC results are re-analysed in this chapter and compared to the 2-EP calculations, as well as the newly calculated deuterated pyrrole results performed by D. Makhov. Before this however, the AIMC method is described in the following section.

The results from this chapter have been written into a manuscript that is in preparation to be published [226].

5.2 Ab Initio Multiple Cloning (AIMC)

The AIMC scheme is based on the second version of the MCE method described in Sec. 1.4.2.2, and its subsequent interface with electronic structure software to produce AI-MCE mentioned in Sec. 1.4.3. A deficiency of the MCE and AI-MCE methods that AIMC seeks to address is the poor convergence at long times, due to the mean-field Ehrenfest trajectories producing unphysical dynamics when they have significant components on multiple electronic states. AIMC achieves this by expanding the basis set, or "cloning", when a trajectory has significant amplitude on more than one electronic state, and the forces on these electronic states are considerably different. In this case, the Ehrenfest dynamics would be a poor description as they contain an average over all the states. This cloning procedure typically occurs following a nonadiabatic transition, or in regions of strong nonadiabatic coupling. It splits the affected basis function into two new basis functions, one with amplitude on only one electronic state, and another with amplitude on all the remaining states (although usually one state is dominant). This is analogous to the spawning procedure in AIMS, reviewed in Sec. 1.5.2.

5.2.1 Working Equations

The wavefunction ansatz for AIMC is that of MCE v2, given in Eq. (1.4.18). The working equations describing the trajectories and amplitudes are given in Sec. 1.4.2.2 in diabatic representation. However, electronic structure programs calculate adiabatic electronic states, so the matrix element $\hat{H}_{ij} = 0 \,\forall\, i \neq j$. Therefore, the working equations of MCE v2 need to be modified to allow the interface with electronic structure software for on-the-fly calculations.

Rather than the off diagonal elements of the Hamiltonian, electronic structure software can calculate the nonadiabatic coupling vector $\mathbf{d}_{ij}(\mathbf{q}_k)$ at the coordinate centre of the kth basis function $|\mathbf{z}_k\rangle$, which couples the ith and jth electronic states in the adiabatic representation via the gradient ∇_q

$$\mathbf{d}_{ij}(\mathbf{q}_k) = \langle \phi_i | \nabla_q | \phi_j \rangle \,. \tag{5.2.1}$$

The equations of motion for the trajectories can then be given in adiabatic representation, with the time-dependence of the phase space centres $(\mathbf{q}_k, \mathbf{p}_k)$ of the coherent states given as

$$\dot{\mathbf{q}}_k = \mathbf{p}_k \mathbf{m}^{-1} \tag{5.2.2a}$$

$$\dot{\mathbf{p}}_k = \mathbf{F}_k \tag{5.2.2b}$$

$$\begin{aligned} \mathbf{F}_k = &\sum_{i=1}^{J} a_{ik}^* a_{ik} \nabla_q V_i(\mathbf{q}_k) \\ &+ \sum_{i=1}^{J} \sum_{j \neq i} a_{ik}^* a_{jk} \mathbf{d}_{ij}(\mathbf{q}_k) \left[V_i(\mathbf{q}_k) - V_j(\mathbf{q}_k) \right] . \end{aligned} \tag{5.2.2c}$$

In the above, $\mathbf{m}$ is a vector of atomic masses, $\mathbf{F}_k$ is the Ehrenfest force, $V_i(\mathbf{q}_k)$ is the adiabatic electronic energy of the ith electronic state, and a_{ik} is the electronic state amplitude, given by $a_{ik} = d_{ik}\mathrm{e}^{is_{ik}}$. Comparison of the above with the trajectories for AIMS in Eq. (1.5.7) reveals the main difference between the two methods — AIMC uses Ehrenfest trajectories that incorporate effects from multiple electronic states, whereas AIMS uses classical trajectories that evolve only on the potential energy surface the trajectory finds itself on. This has two advantages: firstly, the Ehrenfest trajectories take into account nonadiabatic effects at all times, whereas nonadiabatic effects are only incorporated in the region of conical intersections in AIMS; secondly, Ehrenfest trajectories do not separate as quickly as classical ones, which can aid convergence in the short time period.

The time-dependence of the electronic state amplitudes a_{ik} is given by

$$\dot{a}_{ik} = -\frac{i}{\hbar}\sum_{j=1}^{J} H_{ij}^{\mathrm{el}}(\mathbf{z}_k)a_{jk}, \tag{5.2.3}$$

where the elements of the electronic Hamiltonian $H_{ij}^{\mathrm{el}}(\mathbf{z}_k)$, evaluated at the phase space centres of $\mathbf{z}_k$, are

$$H_{ij}^{\mathrm{el}}(\mathbf{z}_k) = \begin{cases} V_i(\mathbf{q}_k) & i = j \\ -i\hbar\mathbf{p}_k\mathbf{d}_{ij}(\mathbf{q}_k)\mathbf{m}^{-1} & i \neq j \end{cases}. \tag{5.2.4}$$

The time-dependence of the multiconfigurational amplitudes D_k is given by

$$\sum_{l=1}^{K}\langle\varphi_k|\varphi_l\rangle\,\dot{D}_l = -\frac{i}{\hbar}\sum_{l=1}^{K}\left[\langle\varphi_k|\hat{H}|\varphi_l\rangle - i\hbar\,\langle\varphi_k|\dot{\varphi}_l\rangle\right]D_l. \tag{5.2.5}$$

In the above, the overlap $\langle\varphi_k|\varphi_l\rangle$ is given by Eq. (1.4.21) in MCE v2, whilst the right-hand time-derivative of this overlap $\langle\varphi_k|\dot{\varphi}_l\rangle$, which accounts for the time-dependence of the basis functions, is given by

$$\langle\varphi_k|\dot{\varphi}_l\rangle = \langle\mathbf{z}_k|\dot{\mathbf{z}}_l\rangle\left[\sum_{i=1}^{J}a_{ik}^{*}a_{il}\right] + \langle\mathbf{z}_k|\mathbf{z}_l\rangle\left[\sum_{i=1}^{J}a_{ik}^{*}\dot{a}_{il}\right]. \tag{5.2.6}$$

The entire Hamiltonian matrix elements $\langle\varphi_k|\hat{H}|\varphi_l\rangle$ are the sum of kinetic energy and potential energy components, as well as a nonadiabatic coupling term

$$\begin{aligned}\langle\varphi_k|\hat{H}|\varphi_l\rangle &= \sum_{i,j=1}^{J}a_{ik}^{*}a_{jl}\,\langle\mathbf{z}_k\phi_i|\hat{H}|\phi_j\mathbf{z}_l\rangle \\ &= \sum_{i,j=1}^{J}a_{ik}^{*}a_{jl}\left[\delta_{ij}\,\langle\mathbf{z}_k|\hat{T}|\mathbf{z}_l\rangle + \delta_{ij}\,\langle\mathbf{z}_k|V_i(\mathbf{q})|\mathbf{z}_l\rangle - \hbar^2\,\langle\mathbf{z}_k|\mathbf{d}_{ij}(\mathbf{q})\dot{\mathbf{q}}|\mathbf{z}_l\rangle\right].\end{aligned} \tag{5.2.7}$$

The kinetic energy component may be calculated analytically using the usual normal ordering

$$\langle\mathbf{z}_k|\hat{T}|\mathbf{z}_l\rangle = \langle\mathbf{z}_k|\mathbf{z}_l\rangle\,\frac{\hbar^2\gamma}{4}(\mathbf{z}_k^{*}\mathbf{z}_k^{*} + \mathbf{z}_l\mathbf{z}_l - 2\mathbf{z}_k^{*}\mathbf{z}_l), \tag{5.2.8}$$

where γ is a vector of widths for the multidimensional coherent state $\mathbf{z}_k$, which will have

different values for the different atoms the basis is representing. The potential energy and nonadiabatic coupling matrix elements (NACMEs) must be calculated approximately, and a bra-ket averaged Taylor (BAT) expansion is utilised that takes the average of two Taylor expansions centred around the maximum of one of the basis functions involved in the matrix element. For the potential energy term, expansion to first order gives

$$\begin{aligned}\langle \mathbf{z}_k|V_i(\mathbf{q})|\mathbf{z}_l\rangle \approx \langle \mathbf{z}_k|\mathbf{z}_l\rangle \left(\frac{V_i(\mathbf{q}_k)+V_i(\mathbf{q}_l)}{2}\right) \\ + \left(\frac{\langle \mathbf{z}_k|(\mathbf{q}-\mathbf{q}_k)|\mathbf{z}_l\rangle \nabla_q V_i(\mathbf{q}_k) + \langle \mathbf{z}_k|(\mathbf{q}-\mathbf{q}_l)|\mathbf{z}_l\rangle \nabla_q V_i(\mathbf{q}_l)}{2}\right).\end{aligned} \tag{5.2.9}$$

The potential energy and its derivative has already been evaluated at coordinates $\mathbf{q}_k$ and $\mathbf{q}_l$ for the trajectories in Eq. (5.2.2), therefore no additional electronic structure calculations are required to evaluate the potential energy matrix element. A zeroth order expansion has been used previously in AI-MCE [100, 109], however this first order expansion is no more expensive and should be more accurate. Going to second order is possible, but would be more expensive as second derivatives of the potential energy surfaces would be required.

The NACME is approximated by a zeroth order BAT expansion to give

$$\langle \mathbf{z}_k|\mathbf{d}_{ij}(\mathbf{q})\dot{\mathbf{q}}|\mathbf{z}_l\rangle \approx \frac{i}{2\hbar}\langle \mathbf{z}_k|\mathbf{z}_l\rangle \left(\dot{\mathbf{q}}_k \mathbf{d}_{ij}(\mathbf{q}_k) + \dot{\mathbf{q}}_l \mathbf{d}_{ij}(\mathbf{q}_l)\right). \tag{5.2.10}$$

As with the potential energy matrix element, the NACME requires no extra electronic structure calculations to evaluate the BAT expansion. Each trajectory may also be propagated individually and then combined via the time-dependence of the multiconfigurational amplitudes D after the calculations have taken place, provided that the electronic structure information is saved at each time step.

5.2.2 Cloning Procedure

The previous section described the working equations and matrix element evaluation for the AIMC method, and this present section describes the cloning procedure that expands the basis to address the mean-field deficiency of the Ehrenfest trajectories, and take into account wavepacket splitting. The cloning procedure is applied when a trajectory $|\varphi_k\rangle$ has significant population, or equivalently significant amplitude, on multiple electronic states with differing forces. In this circumstance, the Ehrenfest force guiding the trajectory would be an unphysical average of the different forces and lead to a poor reproduction of the dynamics occurring. The difference between the force on the ith state and the Ehrenfest average force is given by

$$\Delta\mathbf{F}_{ik} = \nabla_q V_i(\mathbf{q}) - \sum_{j=1}^{J} a_{jk}^* a_{jk} \nabla_q V_j(\mathbf{q}). \tag{5.2.11}$$

The "breaking force" that triggers cloning is then defined as

$$\mathbf{F}_{ik}^{\mathrm{br}} = a_{ik}^* a_{ik} \Delta\mathbf{F}_{ik}. \tag{5.2.12}$$

When $|\mathbf{F}_{ik}^{\mathrm{br}}\mathbf{m}^{-1}| > \xi_{\mathrm{clon}}$ and the nonadiabatic coupling vector is small $|\mathbf{d}_{ij}(\mathbf{q}_k)| < \xi_{\mathrm{nac}}$ cloning occurs. The thresholds ξ_{clon} and ξ_{nac} are determined empirically. For the former, ξ_{clon} needs to be large enough to limit the rate of basis set expansion so that it does not rise exponentially, but small enough to allow cloning to take place at all. The latter threshold ξ_{nac} is utilised to ensure that cloning does not take place in regions of large population transfer, again to limit the size of the basis expansion. Furthermore, when there is large population transfer cloning should not need to be applied since the state the population is transferred to will be dominant in the dynamics.

When the cloning procedure is applied, one trajectory $|\varphi_k\rangle$ becomes two: $|\varphi_k'\rangle$ and $|\varphi_k''\rangle$. The amplitudes of the electronic states are adjusted to ensure that one trajectory has population on the ith electronic state with zero on the rest, whilst the other is the opposite — zero population on the ith electronic state, and non-zero on the rest

$$|\varphi_k'\rangle = \left(\frac{a_{ik}}{|a_{ik}|}|\phi_i\rangle + \sum_{j\neq i} 0 \times |\phi_j\rangle\right)|\mathbf{z}_k\rangle \tag{5.2.13a}$$

$$|\varphi_k''\rangle = \left(0 \times |\phi_i\rangle + \frac{1}{\sqrt{1-|a_{ik}|^2}}\sum_{j\neq i} a_{jk}|\phi_j\rangle\right)|\mathbf{z}_k\rangle\,. \tag{5.2.13b}$$

The multiconfigurational amplitudes are then adjusted to ensure that the wavefunction remains unchanged as a result of the cloning procedure

$$D_k' = D_k|a_{ik}| \tag{5.2.14a}$$

$$D_k'' = D_k\sqrt{1-|a_{ik}|^2}. \tag{5.2.14b}$$

5.3 Experimental Details

A brief overview of the experiments conducted by Cole-Filipiak *et al.* [225] and Roberts *et al.* [203] on 2-EP and pyrrole, respectively, and their selectively deuterated forms will be presented herein, to provide some background to the results AIMC is aiming to add insight to. Both sets of experiments use TR-VMI apparatus with temporally delayed femtosecond "pump" and "probe" laser pulses to provide ultrafast time-resolved photochemical measurements. The pump pulse initiates the photochemistry, whilst the probe ionises the resulting photoproducts. The ionised photoproducts are accelerated down a time-of-flight tube, and impact an imaging stack that is gated to allow exclusive detection of H^+ (or D^+). This detector projects the 3-dimensional photofragment velocity distribution onto a 2-dimensional image to produce a VMI, and the VMI may then be transformed into a TKER spectrum. Multiple TKER spectra may be recorded at various time delays to produce H/D transients, which are used to obtain their appearance lifetimes.

The pump and probe laser pulses are both generated from an 800 nm laser pulse produced by a Ti:sapphire oscillator with temporal width at half maximum of $\sim$ 40 fs. This laser pulse is split and used to pump two optical parametric amplifiers that produce the pump laser pulse in the wavelength range $238 \leq \lambda_{\text{pump}} \leq 265$ nm for 2-EP, and $238 \leq \lambda_{\text{pump}} \leq 250$ nm for pyrrole; and the probe laser pulse at wavelength $\lambda_{\text{probe}} = 243.1$ nm. The pump laser pulse at $\lambda_{\text{pump}} = 200$ nm for pyrrole is produced in a different manner via frequency doubling, however this result is not included for comparison, and only the over the barrier dissociation at $\lambda_{\text{pump}} = 238$ nm is considered. The probe pulse is produced at $\lambda_{\text{probe}} = 243.1$ nm to facilitate the 2+1 resonance enhanced multiphoton ionisation (REMPI) of H/D atom photofragments via the two photon allowed 2s$\leftarrow$1s transition, and subsequent one photon ionisation. A Gaussian instrument response function $G_{\text{IRF}}(t)$ may be obtained via the convolution or cross-correlation of the pump and probe laser pulses, and fitting to a Gaussian distribution. The temporal width at half maximum for $G_{\text{IRF}}(t)$ was found to be $\sim$ 90 fs for 2-EP [225], and $\sim$ 120 fs for pyrrole [203].

5.4 Computational Details

As with previous AIMC studies [34, 223, 224], dynamics were simulated using a modified version of AIMS-MOLPRO [101, 102, 104] that incorporates Ehrenfest trajectories. Electronic structure calculations were performed using the complete active space self-consistent field (CASSCF) method. The electronic basis set used was Dunning's cc-PVDZ set [227], with one additional additional diffuse s function, one additional set of p functions, and one additional set of d functions added to the nitrogen atom attached to the dissociative hydrogen atom; as well as one additional diffuse s function, and one additional set of p functions added to the dissociative hydrogen atom, for both 2-EP and pyrrole. The active space used for both 2-EP and pyrrole has 8 electrons in 7 orbitals: three ring π orbitals and two corresponding π^* orbitals, and the N-H σ and corresponding σ^* orbital. State averaging was performed over three states for 2-EP and four states for pyrrole, and dynamics were performed on three states: the ground and two lowest excited singlet states. The active space and the electronic configurations for the lowest three electronic states of 2-EP are illustrated in Fig. 5.2 at equilibrium and extended N-H bond length. The width of the Gaussian basis functions γ was taken to be 4.7 Bohr^{-2} for hydrogen, 6.6 Bohr^{-2} for deuterium, 22.7 Bohr^{-2} for carbon, and 19.0 Bohr^{-2} for nitrogen, as suggested previously [228].

Initial positions and momenta for the nuclei were sampled from the ground state vibrational Wigner distribution in the harmonic approximation using vibrational frequencies and normal modes calculated at the same level of CASSCF theory as above. As in previous AIMC works [34, 223, 224], excitation from ground to excited state is approximated by simply placing the trajectory on the excited electronic state surface. It is noted that the

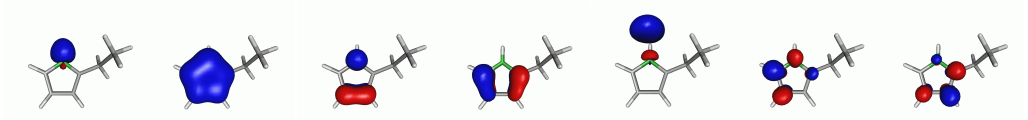

	σ	π	π	π	σ^*	π^*	π^*
S_0	2	2	2	2	0	0	0
S_1	2	2	2	1	1	0	0
S_2	2	2	1	2	1	0	0

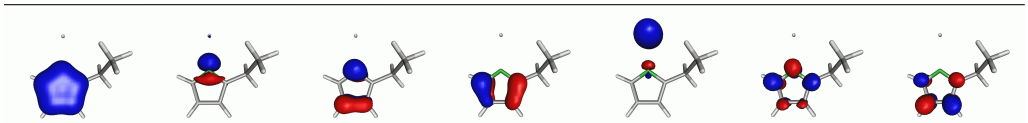

	π	σ	π	π	σ^*	π^*	π^*
S_0	2	2	2	1	1	0	0
S_1	2	2	1	2	1	0	0
S_2	2	1	2	2	1	0	0

Figure 5.2: Active space orbitals and electronic configurations at the SA3-CAS(8,7)-SCF level of theory for the lowest three electronic states of 2-EP at equilibrium N-H bond length (top), and an N-H bond length of 2.5 Å (bottom).

Molecule Label	Initial Trajectories	Starting Adiabatic Electronic State	Cloning Events
2-EP(S_1)	600	S_1	142
2-EP(S_2)	600	S_2	51
2-EP-d_1(S_1)	600	S_1	18
pyrrole	900	S_1	250
pyrrole-d_1	900	S_1	39

Table 5.1: Molecule labels, initial number of trajectories, starting electronic state and number of cloning events for each AIMC calculation carried out in this chapter.

finer details of initial photoexcitation are not accounted for completely by this approximation, and there may be some small energetic sampling deficiencies that are discussed in the following section. The temporal widths of the pump and probe laser pulses from the photoexcitation are taken into account when calculating time-constants for H dissociation however, the details of which shall also be explained in the following section.

The initial number of trajectories, starting adiabatic electronic state, and number of cloning events for each calculation carried out in this work are shown in Table 5.1. The pyrrole and deuterated pyrrole and 2-EP calculations all start their dynamics on the S_1 state, whilst undeuterated 2-EP calculations are performed starting on the S_1 and S_2 states. Hereafter, the 2-EP calculations are referred to with the starting adiabatic electronic state in parenthesis afterwards. The thresholds for cloning were set to $\xi_{\text{clon}} = 5 \times 10^{-6}$ a.u. and $\xi_{\text{nac}} = 2 \times 10^{-3}$ a.u. The number of cloning events per branch was restricted to three, to limit the rate of basis set expansion. The smaller number of cloning events for 2-EP(S_2) compared to 2-EP(S_1) is due to more complete population transfer at conical intersections. The smaller number of cloning events for 2-EP-d_1(S_1) and pyrrole-d_1 compared to 2-EP(S_1) and pyrrole, respectively, is due to the lower frequency of the N-D vibration compared to N-H, meaning fewer conical intersections are encountered along this coordinate. Furthermore, the cloning procedure models wavepacket splitting, and this is less likely to occur for D than H as it is heavier. Calculations were run for 350 fs for 2-EP and 200 fs for pyrrole, both using a timestep of ∼0.6 fs (2.5 a.u.), or until the N-H bond exceeded 4 Å, which was defined as the point of dissociation.

5.5 Results

In the following section, calculated H/D atom TKER spectra are presented for 2-EP and pyrrole and compared to experiment. The dissociation energies obtained from calculation are smoothed with Gaussian functions (σ = 200 cm^{-1}) to create a curve for the TKER spectrum, as opposed to a stick spectrum of delta functions. This allows better comparison to experiment, and this procedure has been used before to obtain simulated TKER spectra [223, 224].

Calculated dissociation times are also presented, in terms of raw dissociation times from the trajectory data, and following a smoothing procedure to take into account experimental laser pump and probe temporal widths. This smoothing procedure is applied to obtain dissociation time constants that are comparable to experiment, as the simulation has well defined start and end points, however, experimentally these points are "blurred" by the laser pump and probe temporal widths. The process for this smoothing procedure is as follows: the pump and probe laser pulses are assumed to be Gaussian in shape, with widths obtained from experimental cross-correlation measurements. These widths are used to convert the raw dissociation times from the trajectory data into Gaussian probability distributions, centred around each raw dissociation time, with width parameters σ_{pump} and σ_{probe}. These Gaussian distributions are summed up for each trajectory with associated weights from calculated amplitudes, enabling a smoothed transient to be produced that can be compared to experimental data. The σ_{pump} and σ_{probe} parameters used are defined in the relevant section for 2-EP and pyrrole. This smoothed transient is then fitted to the kinetic model employed in experiment [203, 225] to obtain time constants, and these fits are analysed relative to the raw dissociation times to better understand the kinetic model and add insight to experimental results. The kinetic model is given by an exponential rise with time constant τ and time zero correction t_0, convoluted with a Gaussian instrument response function $G_{\text{IRF}}(t)$ (with width parameter σ_{XC}, obtained from the cross-correlation/convolution of pump and probe pulses), multiplied by amplitude A and Heaviside unit step function $\Theta(t)$

$$S(t) = A \cdot G_{\text{IRF}}(t) * \left[\left(1 - \mathrm{e}^{-(t-t_0)/\tau}\right)\Theta(t)\right]. \tag{5.5.1}$$

Calculated velocity distributions of ejected H atoms are also produced relative to the molecular axes for 2-EP(S_1), rather than experimental velocity map images (VMIs) that are relative to the electric component of the laser field.

5.5.1 2-Ethylpyrrole (2-EP)

Calculated TKER spectra for 2-EP are shown in Fig. 5.3, with experimental TKER spectra shown on the insets [225]. The theoretical spectra show good qualitative agreement with those obtained by experiment, with one main peak and some smaller features at lower kinetic energies. Comparing the spectra from S_1 and S_2 dynamics in Fig. 5.3a, a broader profile of the main peak from 2-EP(S_2) than 2-EP(S_1) is observed. This is also seen

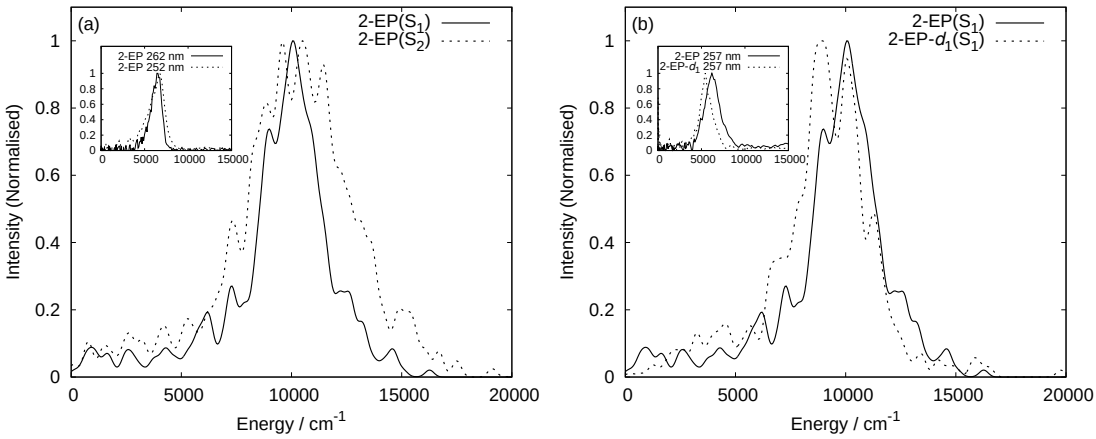

Figure 5.3: (a) Calculated H atom TKER spectrum for 2-EP(S_1) and 2-EP(S_2), with experimental results at a pump wavelengths of $\lambda_{\text{pump}} = 262$ nm and $\lambda_{\text{pump}} = 252$ nm on inset [225]. (b) Calculated H atom TKER spectrum for 2-EP-d_1(S_1) overlaid with that of 2-EP(S_1), and experimental results at a pump wavelength of $\lambda_{\text{pump}} = 257$ nm on inset [225].

experimentally upon decreasing the pump wavelength, where the effect of going from a 262 to 252 nm pump pulse is illustrated on the inset. This indicates that excitation at shorter wavelengths may involve some population of the S_2 state initially, rather than just the S_1 state. Quantitatively, the energy of the main peak is roughly 1.5 times larger from simulation than experiment, due to inaccuracies in the CASSCF potential energy surface. A similar effect has been noted previously with pyrrole [109, 223]. There are also slightly larger shoulders on the high energy side than experiment that can be ascribed to the sampling procedure producing some artificially high energy trajectories. This issue may be remedied by a new sampling procedure, currently in development, that simulates the initial photoexcitation by taking into account the laser pump wavelength and pulse shape. Preliminary results using this procedure appear to confirm this hypothesis [229].

The TKER spectrum for 2-EP-d_1(S_1) is shown in Fig. 5.3b, with the 2-EP(S_1) TKER spectrum overlaid for comparison. An experimental spectrum for 2-EP-d_1 at a pump wavelength of 257 nm is shown on the inset, with undeuterated 2-EP at the same pump wavelength overlaid [225]. It can be seen that AIMC correctly reproduces the shift of the main peak to lower kinetic energies, due to the difference in zero point energies of the deuterated and undeuterated forms of 2-EP. Both parts of Fig. 5.3 therefore demonstrate the ability of AIMC to reproduce spectral features observed experimentally.

Turning to the kinetics of dissociation, a cumulative sum of raw dissociation times, alongside smoothed H/D atom appearance transients with associated fits, and experimental data are presented in Fig. 5.4 for 2-EP(S_1), 2-EP(S_2), and 2-EP-d_1(S_1). The proportion of trajectories that are dissociated by the end of each calculation is shown by a bar chart on the insets. The smoothing procedure is performed as outlined in the introduction to this section, taking into account the temporal widths of the pump and probe laser pulses. As discussed in Sec. 5.3, the pump and probe laser pulses are both produced in the same manner, so it is expected that their temporal widths will be similar. However, as the

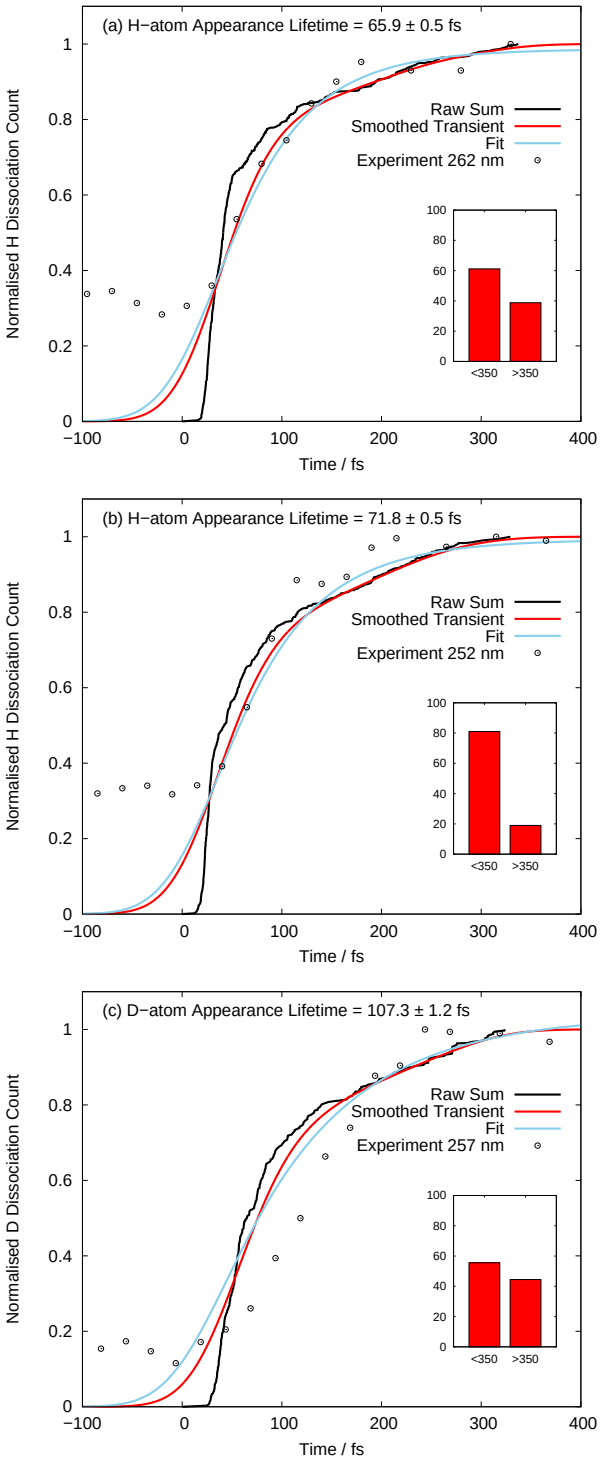

Figure 5.4: Raw cumulative sum of dissociation times from trajectories, alongside smoothed H atom appearance transients with associated fits and experimental data for (a) 2-EP(S_1) with experimental data at a pump wavelength of $\lambda_{\text{pump}} = 262$ nm, (b) 2-EP(S_2) with experimental data at a pump wavelength of $\lambda_{\text{pump}} = 252$ nm, (c) 2-EP-d_1(S_1) with experimental data at a pump wavelength of $\lambda_{\text{pump}} = 257$ nm. Proportion of trajectories that are dissociated by the end of the calculations are shown on the insets of each.

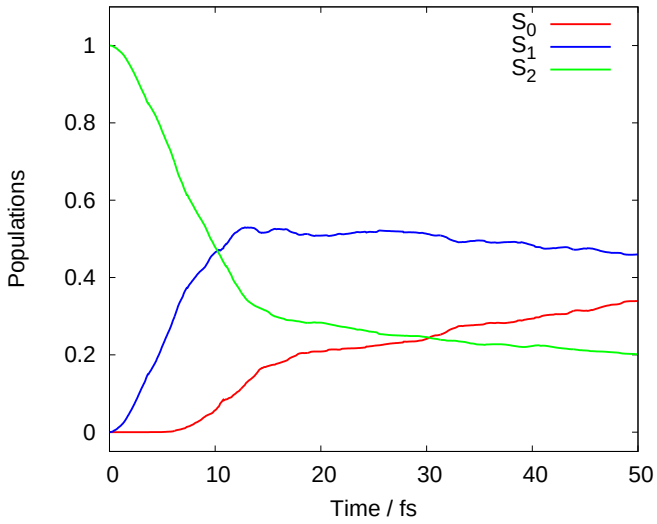

Figure 5.5: Averaged electronic state populations for 2-EP(S_2) trajectories.

probe consists of a 2+1 REMPI of H atom photofragments, this simultaneous absorption of 3 photons will reduce the width of the Gaussian probability distribution that models the probe pulse by a factor of $\sqrt{3}$, such that $\sigma_{\text{probe}} = \sigma_{\text{pump}}/\sqrt{3}$. Using the experimentally obtained cross-correlation width of the pump and probe pulses $\sigma_{\text{XC}} = 38$ fs [225], (which gives a temporal width at half maximum of ~ 90 fs), the Gaussian probability distribution widths are $\sigma_{\text{pump}} = 31$ fs and $\sigma_{\text{probe}} = 31/\sqrt{3} = 18$ fs. Fitting the smoothed transients obtained from these trajectory dissociation time probability distributions to the kinetic model of Eq. (5.5.1) then uses σ_{XC} for the width of $G_{\text{IRF}}(t)$. The time zero correction is applied to the experimental data as determined in Ref. [225], whilst it is not necessary ($t_0 = 0$) for the AIMC data. The experimental data shows a non-zero baseline at negative times due to "reverse dynamics". In these reverse dynamics, the probe pulse acts as a pump to photoexcite 2-EP, and then subsequently provides two photons in the 2+1' REMPI scheme for the dissociated H atom, whilst the third photon is provided by the "pump" pulse. This phenomenon has been explained previously in Refs. [200] and [203].

Visually, it can be seen that the smoothed transients compare well to experimental data, albeit with a slight time shift for 2-EP-$d_1(S_1)$. The lifetimes obtained of 65.9 ± 0.5 fs, 71.8 ± 0.5 fs, and 107.3 ± 1.2 fs for 2-EP(S_1), 2-EP(S_2), and 2-EP-$d_1(S_1)$, respectively, also compare well to the experimentally obtained 55 ± 13 fs and 70 ± 20 fs at $\lambda_{\text{pump}} = 262$ nm and 252 nm for 2-EP, and 140 ± 20 fs at $\lambda_{\text{pump}} = 257$ nm for 2-EP-d_1. The KIE from simulation of ~ 1.6 is slightly less than the experimentally obtained KIE of ~ 2, however if the calculation was extended for a longer period of time so that more trajectories dissociate it is expected that this value will increase.

From the lifetimes obtained from the fit, it would appear that the kinetics of dissociation are similar from the S_1 and S_2 surfaces. However, when considering the proportion of total trajectories that are dissociated by 350 fs (shown on the insets of Figs. 5.4a and 5.4b) it is observed that a greater proportion have dissociated from the S_2 surface (81 %) than the S_1 surface (61 %). The reason for both of these effects may be seen from the aver-

aged electronic state populations for 2-EP(S_2) trajectories in the first 50 fs, illustrated in Fig. 5.5. This figure shows that there is an immediate and significant transfer of population from S_2 to S_1 as the calculation begins, indicating that the S_2 state is unstable with respect to S_1. Around 10 fs later some trajectories reach the S_1–S_0 conical intersection, there is steady population transfer, and trajectories begin to dissociate. The immediate S_2 to S_1 transfer produces trajectories in the S_1 state with high energy, and is the reason why a larger percentage of 2-EP(S_2) trajectories dissociate compared to 2-EP(S_1). Furthermore, this may also explain the broader profile of the main peak in the 2-EP(S_2) TKER spectrum compared to 2-EP(S_1) in Fig. 5.3a, as the higher energy trajectories result in a broader distribution of kinetic energies for the emitted H atoms.

Returning to the transients in Fig. 5.4, further insight into the dissociation kinetics may be obtained by considering the raw cumulative sum of dissociation times from the trajectories. Examining these a few things may be noticed, particularly in the sub 50 fs regime, that are masked by the temporal widths of the laser pulses experimentally. Firstly, no trajectories dissociate until 14.6 fs for 2-EP(S_1), 12.3 fs for 2-EP(S_2), and 24.8 fs for 2-EP-d_1(S_1). This is merely a consequence of defining the point of dissociation as 4 Å, with the delay the time taken for the N-H/D bond to stretch to this distance. Experimentally this will also occur, as the N-H bond extends over the $\pi\sigma^*$ surface following the pump laser pulse. However, lack of temporal resolution does not permit this to be observed in the experimental transient, and the exact point of dissociation is less easy to define. The longer time for 2-EP-d_1(S_1) trajectories to begin to dissociate compared to 2-EP(S_1) is due to the lower vibrational frequency of the N-D bond compared to N-H.

More interestingly, from the initial dissociation point onwards for the next ∼40 fs a rapid increase in the number of trajectories dissociating is observed, as those prepared in geometries with the correct orientation and sufficient energy to dissociate over the barrier do so immediately. The majority of trajectories that dissociate within the calculation time do so by this mechanism in the first 50 fs for 2-EP(S_1) and 2-EP(S_2), and in the first 70 fs for 2-EP-d_1(S_1). This rapid increase of dissociating molecules is not seen to the same extent experimentally, instead there is a much smoother rise due to the "blurring" effect of the laser pulses. Following this initial rapid rise, the rate of dissociation slows for the rest of the calculations as the remaining trajectories do not have enough energy to immediately dissociate, and must first sample more of the potential energy surface to find a way around the barrier.

A calculated velocity distribution of the spread of ejected H atoms relative to the molecular axes is shown in Fig. 5.6 for 2-EP(S_1), with the x component of the velocity versus the projection on the yz plane in panel (a), and the y component of the velocity versus the projection on the xz plane in panel (b). The definitions of the molecular axes are shown at the top of the figure. It can be seen that the H atoms are ejected predominantly in the direction of the N-H stretching coordinate, however there is some small preference for the negative x and y directions, i.e. away from the ethyl group. Also, low velocity (and hence low kinetic energy) dissociated H atoms appear to be emitted in a relatively

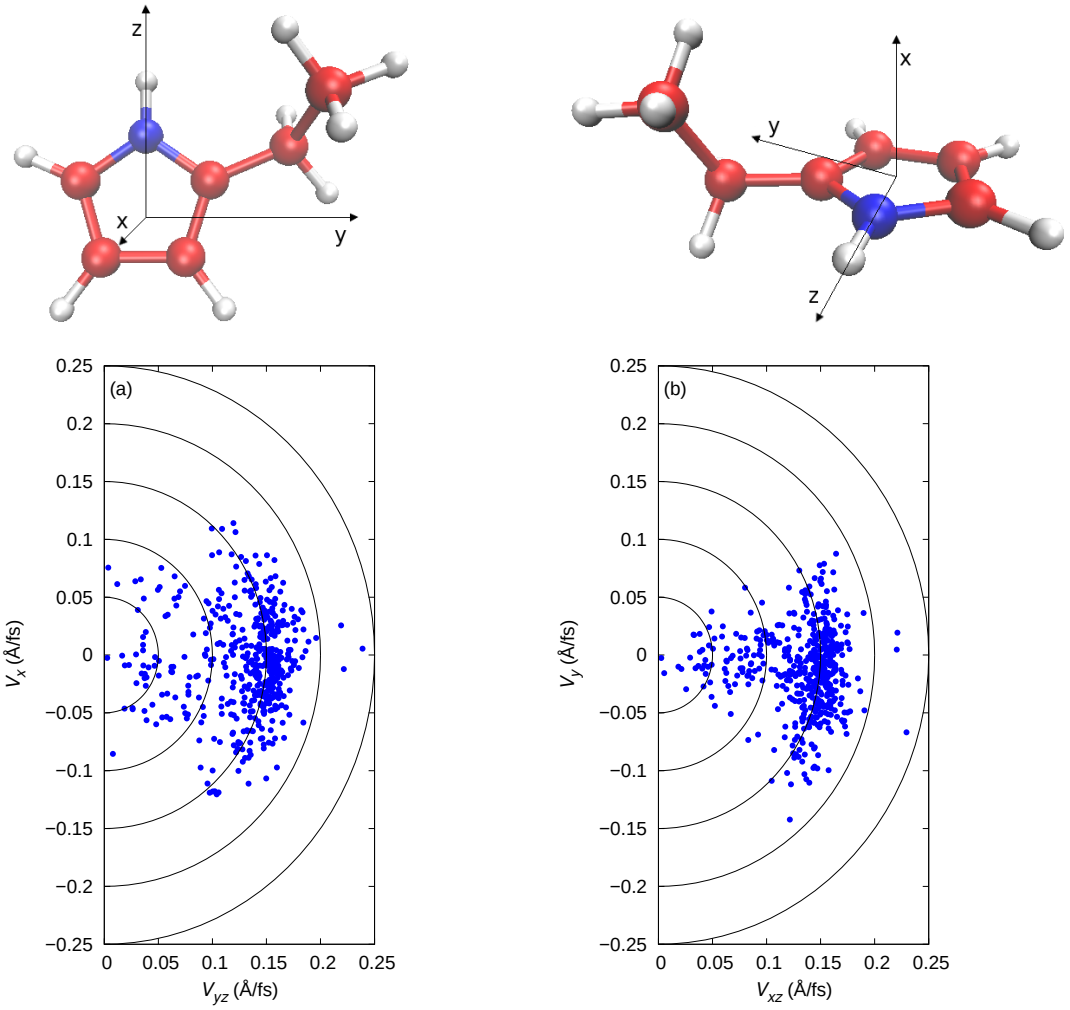

Figure 5.6: Calculated velocities of the ejected H atom with respect to the orientation of 2-EP, for dynamics starting on the S_1 state. Panel (a) shows the x component of the velocity versus the projection on the yz plane, and panel (b) shows the y component of the velocity versus the projection on the xz plane.

isotropic manner in the x axis and yz plane, as shown in Fig. 5.6a. These isotropically emitted low kinetic energy H atoms are primarily due to trajectories that undergo cloning events and retain some character on the excited states as dissociation occurs. This effect has also been noted to be responsible for the similar weak intensity low kinetic energy portion of the pyrrole TKER spectrum [223].

Isotropic emission with low kinetic energy H atoms is also seen experimentally, albeit with a more intense feature in the TKER spectrum. This is due to a second N-H dissociation channel that appears at $\lambda_{\text{pump}} < 248$ nm, with a longer (~ 1.5 ps) time constant [225]. This feature begins to appear predominantly in the TKER spectrum after 200 fs, and is the main source of ejected H atoms at $\lambda_{\text{pump}} = 238$ nm. The calculations showed no large increase in the low kinetic energy feature in the 200–350 fs range, and is unlikely to appear if the calculations were continued beyond 350 fs, as the majority of trajectories have dissociated by this point. This, combined with the fact that the absorption edge of the higher lying $\pi\pi^*$ states begins to appear at $\lambda_{\text{pump}} < 248$ nm, suggests that initial excitation to

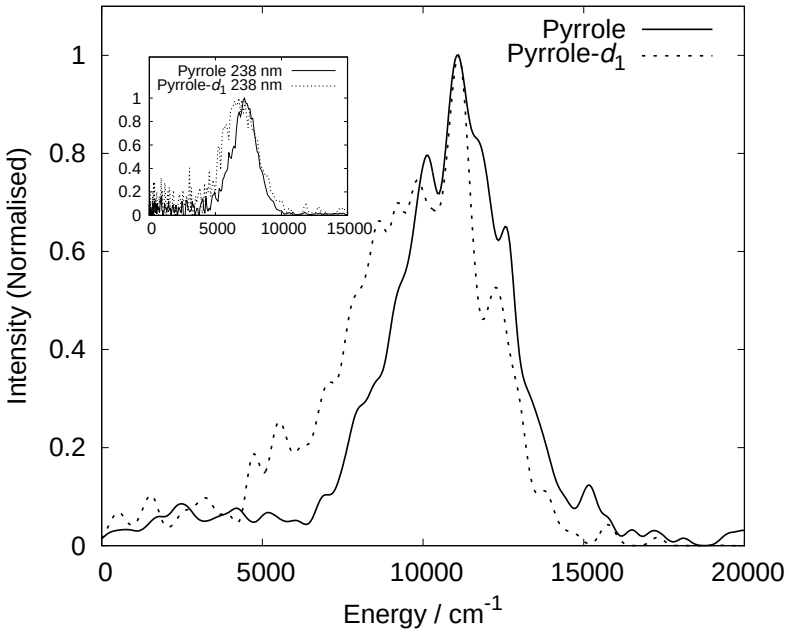

Figure 5.7: Calculated H atom TKER spectrum for pyrrole-d_1, overlaid with that of undeuterated pyrrole, with experimental results at a pump wavelength of $\lambda_{\text{pump}} = 238$ nm on the inset [203].

the S_3 or S_4 $\pi\pi^*$ states occurs at these pump wavelengths rather than S_1 (or S_2). From that point, the mechanism of the low kinetic energy H dissociation is unclear, as currently dynamics calculations involving additional excited states (hence greater active space for the CASSCF calculation) are prohibitively expensive. However, it is possible that it will involve 2-EP molecules that retain some $\pi\pi^*$ excited state character as they dissociate, similar to the much less intense low kinetic energy feature seen in 2-EP(S_1) dynamics, where the trajectories retain some $\pi\sigma^*$ excited state character.

5.5.2 Pyrrole

The calculated TKER spectrum for pyrrole-d_1 is shown in Fig. 5.7, overlaid with the pyrrole spectrum calculated previously [224], and with experimental spectra at a pump wavelength of 238 nm shown on the inset [203]. The pump wavelength of 238 nm was chosen for comparison as the simulated dynamics show over the barrier dissociation, rather than tunnelling. Similar to 2-EP, for pyrrole AIMC correctly reproduces the shift of the main peak to lower energies as a result of the lower zero point energy of the N-D bond compared to N-H. Furthermore, comparing the spectra of pyrrole and 2-EP(S_1) directly, a shift of the main peak to higher energy is observed (~ 11000 cm^{-1} for pyrrole and ~ 10000 cm^{-1} for 2-EP(S_1)). This is also seen experimentally (~ 7200 cm^{-1} for pyrrole and ~ 6600 cm^{-1} for 2-EP), where the overestimation of the simulated peaks is due to inaccuracies of the CASSCF potential energy surface as noted in the previous section.

Turning to the kinetics of dissociation, a cumulative sum of raw dissociation times, alongside smoothed H/D atom appearance transients with associated fits and experimental data is presented in Fig. 5.8 for pyrrole and pyrrole-d_1. The proportion of trajectories that are dissociated by the end of the calculation is shown via bar charts on the insets. The

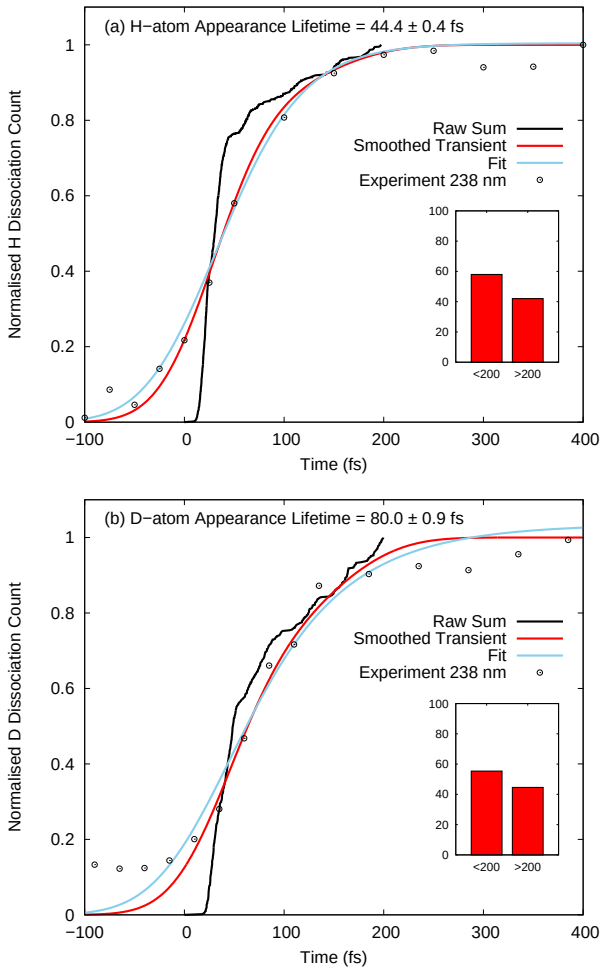

Figure 5.8: Raw cumulative sum of dissociation times from trajectories, alongside smoothed H atom appearance transients with associated fits and experimental data for (a) pyrrole and (b) pyrrole-d_1 with experimental data at a pump wavelength of $\lambda_{\text{pump}} = 238$ nm [203]. Proportion of trajectories that are dissociated by the end of the calculations are shown on the insets of each.

smoothing procedure is performed in the same manner as for 2-EP, with the experimental pump and probe pulses produced from the same source and the probe consisting of a 2+1 REMPI mechanism as discussed in Sec. 5.3. The only difference with pyrrole compared to 2-EP is that the experimental cross-correlation $\sigma_{\text{XC}} = 52$ fs (which gives a temporal width at half maximum of ~ 120 fs) as opposed to $\sigma_{\text{XC}} = 38$ fs for 2-EP. This yields $\sigma_{\text{pump}} = 37$ fs and $\sigma_{\text{probe}} = 37/\sqrt{3} = 21$ fs for the widths of the Gaussian probability distributions modelling the smoothed trajectory dissociation times. The smoothed transients obtained from these probability distributions were then fitted to the kinetic model in Eq. (5.5.1), which uses σ_{XC} for the width of $G_{\text{IRF}}(t)$. An arbitrary time zero correction was applied to the experimental data in Fig. 5.8, as the true t_0 could not be established. Due to this arbitrary correction, visually the experimental transients compare extremely well to those obtained from simulation. The lifetime obtained of 44.4 ± 0.4 fs for pyrrole also compares extremely well to the experimentally obtained 46 ± 22 fs, and the arbitrary t_0 correction is not a factor for this comparison as it was known at the time of publication. For pyrrole-d_1 the calculated lifetime of 80.0 ± 0.9 fs gives a KIE of ~ 1.8, which is slightly

smaller than the experimentally obtained 136 ± 38 fs with KIE ~ 3. However, as with 2-EP, if the calculation was extended for a longer period of time so that more trajectories dissociate it is expected that this value will increase. Furthermore, the pyrrole calculation correctly produces a larger KIE than for 2-EP, despite a shorter calculation time. The raw cumulative sum of dissociation times displays a similar profile to that of 2-EP, with an initial delay for the first trajectory to dissociate, followed by a steep rise as the trajectories prepared in such a geometry to immediately dissociate do so, and a final slower rise time from the trajectories that need to sample more of the potential energy surface before finding a way around the barrier.

5.6 Conclusions

AIMC has been used to simulate the ultrafast photodissociation of 2-EP with dynamics starting on the S_1 and S_2 $\pi\sigma^*$ states, and deuterated 2-EP with dynamics starting on the S_1 state. Calculations have also been performed by D. Makhov for deuterated pyrrole with dynamics starting on the S_1 state, and further analysis has been performed on previous calculations involving undeuterated pyrrole with dynamics started on the S_1 state [223, 224]. TKER spectra and H/D atom appearance lifetimes from the N-H/D dissociation have been obtained and compared to experimental results for 2-EP [225] and pyrrole [203]. The TKER spectra are qualitatively accurate with respect to the experimental results, reproducing the structure of the main peak and less intense low kinetic energy features in each. Comparative features observed experimentally have also been reproduced in each of the spectra, such as the shift of the main peak to lower energies due to deuteration, the lower energy of the peak for pyrrole compared to 2-EP, and the broadening of the peak due to shorter pump wavelengths for 2-EP. The latter effect was observed in the 2-EP(S_2) calculations compared to 2-EP(S_1), and was explained by considering the averaged electronic state populations of 2-EP(S_2) trajectories. These populations demonstrated that the S_2 state is unstable with respect to S_1, leading to rapid transfer from S_2 to S_1 that produced trajectories in a high energy S_1 state, and led to a broad distribution of kinetic energies for the dissociated H atoms.

The H/D atom appearance lifetimes were obtained by applying a smoothing procedure to the raw dissociation times obtained from calculation. This smoothing procedure took into account the experimental pump and probe laser pulse temporal widths to allow a direct comparison between simulation and experiment. Visually, these smoothed transients compared well to the experimental results, and the time constants obtained from fitting to the kinetic model used in the experiments were also in close agreement. Insight into the kinetic model and sub-50 fs dynamics was achieved by considering the raw dissociation time data, and how it compared to the smoothed transients and experimental data. The raw dissociation time data showed that the dissociation was essentially a two-step process: firstly, 2-EP/pyrrole molecules with the correct geometry to dissociate over the barrier do so immediately; and secondly, this is followed by a slower rate of dissociation for the 2-EP/pyrrole molecules that must sample more of the potential energy surface before finding a way around the barrier. This two-step process is "blurred" by the temporal width of the pump and probe laser pulses, leading to a single lifetime for the smoothed transients and experimental data.

Velocity distributions were also calculated for 2-EP(S_1), illustrating predominant dissociation in the direction of the N-H bond, but with a slight preference for the H atom to be ejected away from the ethyl group. Furthermore, a somewhat isotropic distribution of low kinetic energy H atoms was observed, primarily due to trajectories that retain $\pi\sigma^*$ excited state character upon dissociation. This low kinetic energy emission of H atoms is a small feature of the dynamics on the S_1 state, and the intense isotropic low kinetic

energy emission of H atoms observed experimentally at $\lambda_{\text{pump}} < 248$ nm were not seen in these calculations. However, it was posited that a similar mechanism for their production may occur, but with coupling to the $\pi\pi^*$ states rather than $\pi\sigma^*$ states.

The ability of AIMC to reproduce experimental quantities and add insight into them makes it a very useful theoretical technique, with further calculations into molecules of photochemical interest either currently underway or planned; including pyrazole, imidazole, and aniline.

Chapter 6

Conclusions and Outlook

In this thesis two new numerical extensions to the coupled coherent states (CCS) family of multidimensional quantum dynamics methods have been developed and tested, alongside an application of the existing *ab initio* multiple cloning (AIMC) extension to nonadiabatic dynamics. The two new numerical extensions to CCS were both tested on the same model Hamiltonian, consisting of a 1-dimensional system tunnelling mode governed by an asymmetric double well potential, coupled to a bath of $M-1$ oscillators. The model Hamiltonian has been utilised by CCS and other quantum dynamics methods previously with $M = 20$ [39, 46, 138, 140], however it had never been converged properly, and as such no standard benchmark result had been proposed. Therefore, in Chapter 2 for the first time a properly converged result was obtained, providing this benchmark result. The calculation exploited the permutational symmetry of the Hamiltonian to produce a basis set expansion of the wavefunction that required no approximation, as the symmetry of the problem permitted a reduction in the cost of the calculation. The fully converged result allowed comparison to the previous quantum dynamics methods, and provided a reference result for the CCS extensions developed in this thesis. Benchmark results for higher dimensional cases of $M = 40$ and $M = 80$ were also obtained, as well as an $M = 20$ case with stronger system bath coupling constant. These provide more challenging reference results for any future method that wishes to use the model Hamiltonian.

In Chapter 3 the first of the two numerical extensions to CCS was developed, a 2-layer version of CCS (2L-CCS). The motivation behind this approach was the multilayer extension of MCTDH to ML-MCTDH, and the 2-layer extension of G-MCTDH. The aim for this method was to provide a more flexible wavefunction representation than standard CCS, increased numerical treatment of a degree or degrees of freedom in a quantum mechanical problem where necessary, and to give improved numerical and scalability properties. The working equations were derived and presented, and the method tested on the model Hamiltonian with the same parameter set as the previous methods of studying it. The additional numerical treatment provided by the inner layer of 2L-CCS was used for the tunnelling mode. 2L-CCS was found to converge appropriately in the short and long time regimes by increasing the number of basis functions in both the inner and outer layers. The final result obtained was in closer agreement to the benchmark than the previous

CCS calculation, although this was determined to be primarily due to improved sampling of the bath, rather than the increased treatment of the tunnelling mode.

The numerical performance and parallel scalability of 2L-CCS was demonstrated, with improvements of each upon increasing the number of inner layer basis functions. It was posited that this will be an extremely attractive feature when dealing with problems where a large number of inner layer basis functions are required, such as if the method is applied to studying high harmonic generation. High harmonic generation has been studied by standard CCS previously [78], and the dynamics of the phenomenon involves a highly delocalised electron that requires extensive phase space sampling to model. This highly delocalised electron could be treated by the inner layer of 2L-CCS to provide increased phase space sampling. The method could also be paired with electronic structure theory for on-the-fly dynamics. The effect of increasing the number of inner layer basis functions may also be used to investigate the behaviour of the trajectories, to ensure they remain stable.

In Chapter 4 the second of the two numerical extensions to CCS was developed, coupled coherent states for indistinguishable bosons (CCSB). The modification required compared to standard CCS was relatively small, changing the interpretation of the coherent states to be basis functions for Fock states that represent all particles and their occupation of quantum states, rather than basis functions for individual particles. The wavefunction ansatz remained the same as standard CCS, and the working equations for trajectories and amplitudes also remained the same. However, as the Fock basis is in second quantisation representation, any Hamiltonians studied by CCSB must be second quantised. The procedure for doing this was demonstrated as CCSB was applied to two example problems.

In the first example problem, the model Hamiltonian studied in the prior two chapters was used. The bath portion of this Hamiltonian could be second quantised as it is comprised of oscillators of the same frequency, hence they could be treated as indistinguishable. This was a similar approach to that used in Chapter 2, where the permutational symmetry of the bath part of the Hamiltonian was exploited. The parameter set previously studied was tested initially, the results were found to be almost identical to the benchmark. The dimensionality of the problem was also reduced from 20 to 6. The more challenging cases put forward by the benchmark were then tested, with the $M = 40$ case also showing very good agreement with the benchmark, and the dimensionality was reduced from 40 to 9. The $M = 80$ case and $M = 20$ case with stronger coupling were not as successful, demonstrating accuracy with respect to the benchmark for only the first 10 a.u. of the calculation. However, these are much more challenging problems, and would be difficult for any quantum dynamical method.

The second example problem was a model Hamiltonian consisting of a system of 100 bosons in a shifted harmonic trap, where oscillations in the 1-body density were calculated. The aim for this example was to provide an introductory test for CCSB in the realm of Bose-Einstein condensates, as ultimately the method is aimed for use in studying such systems. 2-body matrix elements were required to be calculated, a prominent feature for

interacting condensates, and it was demonstrated that these could be computed analytically by CCSB. The results were compared to a MCTDHB calculation that was equivalent to the Gross-Pitaevskii equation, the two main time-dependent approaches for studying condensates, and CCSB was shown to compare favourably. Future avenues of research for CCSB include more complicated Bose-Einstein condensate problems, such as that in Ref. [122] of a condensate in a double well trap, and the combination of the method with one to treat identical fermions.

In Chapter 5 there was a change of tack, with the existing extension of CCS to nonadiabatic dynamics in AIMC used to study the ultrafast photodissociation of 2-ethylpyrrole (2-EP), and compare to calculations on pyrrole and experimental results. Total kinetic energy release spectra were produced and shown to be qualitatively accurate with respect to experiment, reproducing the structure of the main peak and less intense low kinetic energy features. Other features seen experimentally were also shown to be reproduced by AIMC, such as the shift of the main peak to lower energies due to deuteration, the lower energy of the peak for pyrrole compared to 2-EP, and the broadening of the peak due to shorter pump wavelengths for 2-EP.

The dissociation time constants from experiment were also reproduced, using a smoothing process on the raw calculated dissociation times to produce a H/D atom appearance transient that could be directly compared to the experimental transient. The smoothing process took into account the experimental pump and probe laser pulse temporal widths to model the uncertainty in the start and finish points in the experimental photochemistry. Novel insight into the dissociation mechanism was also obtained by comparing raw calculated dissociation times to these smoothed dissociation times, and experimental data. The raw dissociation time data showed that the dissociation was essentially a two-step process: firstly, 2-EP/pyrrole molecules with the correct geometry to dissociate over the barrier do so immediately; and secondly, this is followed by a slower rate of dissociation for the 2-EP/pyrrole molecules that must sample more of the potential energy surface before finding a way around the barrier. This two-step process is "blurred" by the temporal width of the pump and probe laser pulses, leading to a single lifetime for the smoothed transients and experimental data. The ability of AIMC to reproduce experimental quantities and add novel insight into them was therefore demonstrated by this chapter, providing further motivation to study molecules of photochemical interest, such as pyrazole, imidazole and aniline. Further work on the AIMC method may also be to incorporate GPU accelerated electronic structure theory to permit studies of larger molecules, for longer times, or to be able to include more excited states in the calculation. This could permit simulation of 2-EP up to the picosecond timescale, including the $\pi\pi^*$ states in the active space of the CASSCF electronic structure theory, allowing the dynamics of the low kinetic energy hydrogen dissociation channel to be observed. The recently developed modelling of the initial pump laser pulse [229] should also be investigated, to compare with the sampling of initial conditions from the Wigner distribution that was used in the present study.

Bibliography

1. Dror, R.O., Dirks, R.M., Grossman, J., Xu, H. and Shaw, D.E., Biomolecular Simulation: A Computational Microscope for Molecular Biology. *Annual Review of Biophysics*, 2012, **41**(1), pp. 429–452.

2. Feit, M.D., Fleck, J.A. and Steiger, A., Solution of the Schrödinger Equation by a Spectral Method. *Journal of Computational Physics*, 1982, **47**(3), pp. 412–433.

3. Feit, M.D. and Fleck, J.A., Solution of the Schrödinger Equation by a Spectral Method II: Vibrational Energy Levels of Triatomic Molecules. *Journal of Chemical Physics*, 1983, **78**(1), pp. 301–308.

4. Tal-Ezer, H. and Kosloff, R., An Accurate and Efficient Scheme for Propagating the Time Dependent Schrödinger Equation. *Journal of Chemical Physics*, 1984, **81**(9), pp. 3967–3971.

5. Park, T.J. and Light, J.C., Unitary Quantum Time Evolution by Iterative Lanczos Reduction. *Journal of Chemical Physics*, 1986, **85**(10), pp. 5870–5876.

6. Heller, E.J., Timedependent Approach to Semiclassical Dynamics. *Journal of Chemical Physics*, 1975, **62**, pp. 1544–1555.

7. Heller, E.J., Frozen Gaussians: A Very Simple Semiclassical Approximation. *Journal of Chemical Physics*, 1981, **75**, pp. 2923–2931.

8. Herman, M.F. and Kluk, E., A Semiclasical Justification for the Use of Non-spreading Wavepackets in Dynamics Calculations. *Chemical Physics*, 1984, **91**(1), pp. 27–34.

9. Kluk, E., Herman, M.F. and Davis, H.L., Comparison of the Propagation of Semiclassical Frozen Gaussian Wave Functions with Quantum Propagation for a Highly Excited Anharmonic Oscillator. *Journal of Chemical Physics*, 1986, **84**, pp. 326–334.

10. Miller, W.H., Semiclassical Theory of Atom-Diatom Collisions: Path Integrals and the Classical S Matrix. *Journal of Chemical Physics*, 1970, **53**(5), pp. 1949–1959.

11. Miller, W.H., Classical S Matrix: Numerical Application to Inelastic Collisions. *Journal of Chemical Physics*, 1970, **53**(9), pp. 3578–3587.

12. Miller, W.H. and George, T.F., Analytic Continuation of Classical Mechanics for Classically Forbidden Collision Processes. *Journal of Chemical Physics*, 1972, **56**(11), pp. 5668–5681.

13. Miller, W.H., Classical-Limit Quantum Mechanics and the Theory of Molecular Collisions. *Advances in Chemical Physics*, 1974, **25**, pp. 69–177.

14. Marcus, R.A., Theory of Semiclassical Transition Probabilities (S Matrix) for Inelastic and Reactive Collisions. *Journal of Chemical Physics*, 1971, **54**(9), pp. 3965–3979.

15. Van Vleck, J.H., The Correspondence Principle in the Statistical Interpretation of Quantum Mechanics. *Proceedings of the National Academy of Sciences of the United States of America*, 1928, **14**(2), pp. 178–188.

16. Gutzwiller, M.C., Phase-Integral Approximation in Momentum Space and the Bound States of an Atom. *Journal of Mathematical Physics*, 1967, **8**(10), pp. 1979–2000.

17. Meyer, H.D., Manthe, U. and Cederbaum, L., The Multi-Configurational Time-Dependent Hartree Approach. *Chemical Physics Letters*, 1990, **165**(1), pp. 73–78.

18. Beck, M.H., Jäckle, A., Worth, G.A. and Meyer, H.D., The Multiconfiguration Time-Dependent Hartree (MCTDH) Method: a Highly Efficient Algorithm for Propagating Wavepackets. *Physics Reports*, 2000, **324**(1), pp. 1–105.

19. Meyer, H.D., Studying Molecular Quantum Dynamics with the Multiconfiguration Time-Dependent Hartree Method. *WIREs Computational Molecular Science*, 2012, **2**(2), pp. 351–374.

20. Raab, A., Worth, G.A., Meyer, H.D. and Cederbaum, L.S., Molecular Dynamics of Pyrazine After Excitation to the S_2 Electronic State Using a Realistic 24-Mode Model Hamiltonian. *Journal of Chemical Physics*, 1999, **110**(2), pp. 936–946.

21. Wang, H., Basis Set Approach to the Quantum Dissipative Dynamics: Application of the Multiconfiguration Time-Dependent Hartree Method to the Spin-Boson Problem. *Journal of Chemical Physics*, 2000, **113**(22), pp. 9948–9956.

22. Nest, M. and Meyer, H.D., Benchmark Calculations on High-Dimensional Henon-Heiles Potentials with the Multi-Configuration Time Dependent Hartree (MCTDH) Method. *Journal of Chemical Physics*, 2002, **117**(23), pp. 10499–10505.

23. Nest, M. and Meyer, H.D., Dissipative Quantum Dynamics of Anharmonic Oscillators with the Multiconfiguration Time-Dependent Hartree Method. *Journal of Chemical Physics*, 2003, **119**(1), pp. 24–33.

24. Burghardt, I., Meyer, H.D. and Cederbaum, L.S., Approaches to the Approximate Treatment of Complex Molecular Systems by the Multiconfiguration Time-Dependent Hartree Method. *Journal of Chemical Physics*, 1999, **111**(7), pp. 2927–2939.

25. Worth, G.A. and Burghardt, I., Full Quantum Mechanical Molecular Dynamics Using Gaussian Wavepackets. *Chemical Physics Letters*, 2003, **368**(3-4), pp. 502–508.

26. Ronto, M. and Shalashilin, D.V., Numerical Implementation and Test of the Modified Variational Multiconfigurational Gaussian Method for High-Dimensional Quantum Dynamics. *Journal of Physical Chemistry A*, 2013, **117**(32), pp. 6948–6959.

27. Martínez, T.J., Ben-Nun, M. and Levine, R.D., Multi-Electronic-State Molecular Dynamics: A Wave Function Approach with Applications. *Journal of Physical Chemistry*, 1996, **100**(19), pp. 7884–7895.

28. Wu, Y. and Batista, V.S., Matching-Pursuit for Simulations of Quantum Processes. *Journal of Chemical Physics*, 2003, **118**(15), pp. 6720–6724.

29. Shalashilin, D.V. and Child, M.S., Time Dependent Quantum Propagation in Phase Space. *Journal of Chemical Physics*, 2000, **113**(22), pp. 10028–10036.

30. Shalashilin, D.V. and Child, M.S., The Phase Space CCS Approach to Quantum and Semiclassical Molecular Dynamics for High-Dimensional Systems. *Chemical Physics*, 2004, **304**(1-2), pp. 103–120.

31. Shalashilin, D.V., Quantum Mechanics with the Basis Set Guided by Ehrenfest Trajectories: Theory and Application to Spin-Boson Model. *Journal of Chemical Physics*, 2009, **130**(24), 244101.

32. Shalashilin, D.V., Nonadiabatic Dynamics with the Help of Multiconfigurational Ehrenfest Method: Improved Theory and Fully Quantum 24d Simulation of Pyrazine. *Journal of Chemical Physics*, 2010, **132**(24), 244111.

33. Shalashilin, D.V., Multiconfigurational Ehrenfest Approach to Quantum Coherent Dynamics in Large Molecular Systems. *Faraday Discussions*, 2011, **153**, pp. 105–116.

34. Makhov, D.V., Glover, W.J., Martínez, T.J. and Shalashilin, D.V., Ab Initio Multiple Cloning Algorithm for Quantum Nonadiabatic Molecular Dynamics. *Journal of Chemical Physics*, 2014, **141**(5), 054110.

35. Green, J.A., Grigolo, A., Ronto, M. and Shalashilin, D.V., A Two-Layer Approach to the Coupled Coherent States Method. *Journal of Chemical Physics*, 2016, **144**(2), 024111.

36. Burghardt, I., Nest, M. and Worth, G.A., Multiconfigurational System-Bath Dynamics Using Gaussian Wave Packets: Energy Relaxation and Decoherence Induced by a Finite-Dimensional Bath. *Journal of Chemical Physics*, 2003, **119**(11), pp. 5364–5378.

37. Burghardt, I., Giri, K. and Worth, G.A., Multimode Quantum Dynamics Using Gaussian Wavepackets: the Gaussian-Based Multiconfiguration Time-Dependent Hartree (G-MCTDH) Method Applied to the Absorption Spectrum of Pyrazine. *Journal of Chemical Physics*, 2008, **129**(17), 174104.

38. Ben-Nun, M. and Martínez, T.J., A Multiple Spawning Approach to Tunneling Dynamics. *Journal of Chemical Physics*, 2000, **112**(14), pp. 6113–6121.

39. Wu, Y. and Batista, V.S., Quantum Tunneling Dynamics in Multidimensional Systems: a Matching-Pursuit Description. *Journal of Chemical Physics*, 2004, **121**(4), pp. 1676–1680.

40. Wu, Y. and Batista, V.S., Matching-Pursuit Split-Operator Fourier-Transform Simulations of Excited-State Intramolecular Proton Transfer in 2-(2'-Hydroxyphenyl)-Oxazole. *Journal of Chemical Physics*, 2006, **124**(22), 224305.

41. Chen, X. and Batista, V.S., Matching-Pursuit/Split-Operator-Fourier-Transform Simulations of Excited-State Nonadiabatic Quantum Dynamics in Pyrazine. *Journal of Chemical Physics*, 2006, **125**(12), 124313.

42. Shalashilin, D.V. and Child, M.S., Multidimensional Quantum Propagation with the Help of Coupled Coherent States. *Journal of Chemical Physics*, 2001, **115**(12), pp. 5367–5375.

43. Shalashilin, D.V. and Child, M.S., Nine-Dimensional Quantum Molecular Dynamics Simulation of Intramolecular Vibrational Energy Redistribution in the CHD_3 Molecule with the Help of Coupled Coherent States. *Journal of Chemical Physics*, 2003, **119**(4), pp. 1961–1969.

44. Shalashilin, D.V., Child, M.S. and Clary, D.C., Quantum Initial Value Representation Simulation of Water Trimer Far Infrared Absorption Spectrum. *Journal of Chemical Physics*, 2004, **120**(12), pp. 5608–5615.

45. Shalashilin, D.V. and Child, M.S., Real Time Quantum Propagation on a Monte Carlo Trajectory Guided Grids of Coupled Coherent States: 26D Simulation of Pyrazine Absorption Spectrum. *Journal of Chemical Physics*, 2004, **121**(8), pp. 3563–3568.

46. Sherratt, P.A.J., Shalashilin, D.V. and Child, M.S., Description of Multidimensional Tunnelling with the Help of Coupled Coherent States Guided by Classical Hamiltonians with Quantum Corrections. *Chemical Physics*, 2006, **322**(1-2), pp. 127–134.

47. Glowacki, D.R., Reed, S.K., Pilling, M.J., Shalashilin, D.V. and Martinez-Nunez, E., Classical, Quantum and Statistical Simulations of Vibrationally Excited HOSO2: IVR, Dissociation, and Implications for OH + SO2 Kinetics at High Pressures. *Physical Chemistry Chemical Physics*, 2009, **11**, pp. 963–974.

48. Reed, S.K., Glowacki, D.R. and Shalashilin, D.V., Quantum Dynamics Simulations of Energy Redistribution in HO-SO2. *Chemical Physics*, 2010, **370**, pp. 223–231.

49. Reed, S.K., González-Martínez, M.L., Rubayo-Soneira, J. and Shalashilin, D.V., Cartesian Coupled Coherent States Simulations: Ne_nBr_2 Dissociation as a Test Case. *Journal of Chemical Physics*, 2011, **134**(5), 054110.

50. Feynman, R.P. and Hibbs, A.R., *Quantum Mechanics and Path Integrals*. 1st ed., McGraw-Hill, 1965.

51. Levit, S. and Smilansky, U., A New Approach to Gaussian Path Integrals and the Evaluation of the Semiclassical Propagator. *Annals of Physics*, 1977, **103**(1), pp. 198–207.

52. Levit, S. and Smilansky, U., A Theorem on Infinite Products of Eigenvalues of Sturm-Liouville Type Operators. *Proceedings of the American Mathematical Society*, 1977, **65**(2), pp. 299–302.

53. Tannor, D.J., *Introduction to Quantum Mechanics - A Time-Dependent Perspective*. University Science Books, 2007.

54. Kay, K.G., Integral Expressions for the Semiclassical Time-Dependent Propagator. *Journal of Chemical Physics*, 1994, **100**(6), pp. 4377–4392.

55. Kay, K.G., Numerical Study of Semiclassical Initial Value Methods for Dynamics. *Journal of Chemical Physics*, 1994, **100**(6), pp. 4432–4445.

56. Kay, K.G., Semiclassical Propagation for Multidimensional Systems by an Initial Value Method. *Journal of Chemical Physics*, 1994, **101**(3), pp. 2250–2260.

57. Heller, E.J., Cellular Dynamics: a New Semiclassical Approach to Time-Dependent Quantum Mechanics. *Journal of Chemical Physics*, 1991, **94**(4), pp. 2723–2729.

58. Heller, E.J., Reply to Comment On: Semiclassical Time Evolution Without Root Searches: Comments and Perspective. *Journal of Chemical Physics*, 1991, **95**(12), pp. 9431–9432.

59. Miller, W.H., Comment On: Semiclassical Time Evolution Without Root Searches. *Journal of Chemical Physics*, 1991, **95**(12), pp. 9428–9430.

60. Herman, M.F., Dynamics by Semiclassical Methods. *Annual Review of Physical Chemistry*, 1994, **45**(1), pp. 83–111.

61. Miller, W.H., The Semiclassical Initial Value Representation: A Potentially Practical Way for Adding Quantum Effects to Classical Molecular Dynamics Simulations. *Journal of Physical Chemistry A*, 2001, **105**(13), pp. 2942–2955.

62. Thoss, M. and Wang, H., Semiclassical Description of Molecular Dynamics Based on Inital-Value Representation Methods. *Annual Review of Physical Chemistry*, 2004, **55**(1), pp. 299–332.

63. Kay, K.G., Semiclassical Initial Value Treatments of Atoms and Molecules. *Annual Review of Physical Chemistry*, 2005, **56**, pp. 255–280.

64. Heller, E.J., Classical S-Matrix Limit of Wave Packet Dynamics. *Journal of Chemical Physics*, 1976, **65**(11), pp. 4979–4989.

65. Huber, D. and Heller, E.J., Generalized Gaussian Wave Packet Dynamics. *Journal of Chemical Physics*, 1987, **87**(9), pp. 5302–5311.

66. Dirac, P.A.M., *The Principles of Quantum Mechanics*. 4th ed., Oxford University Press, 1958.

67. Schrödinger, E., Der Stetige Übergang Von Der Mikro- Zur Makromechanik. *Naturwissenschaften*, 1926, **14**(28), pp. 664–666.

68. Glauber, R.J., The Quantum Theory of Optical Coherence. *Physical Review*, 1963, **130**, pp. 2529–2539.

69. Glauber, R.J., Coherent and Incoherent States of the Radiation Field. *Physical Review*, 1963, **131**, pp. 2766–2788.

70. Glauber, R.J., Photon Correlations. *Physical Review Letters*, 1963, **10**, pp. 84–86.

71. Tannor, D.J. and Garashchuk, S., Semiclassical Calculation of Chemical Reaction Dynamics via Wavepacket Correlation Functions. *Annual Review of Physical Chemistry*, 2000, **51**, pp. 553–600.

72. Sawada, S.I., Heather, R., Jackson, B. and Metiu, H., A Strategy for Time Dependent Quantum Mechanical Calculations Using a Gaussian Wave Packet Representation of the Wave Function. *Journal of Chemical Physics*, 1985, **83**(6), pp. 3009–3027.

73. Sawada, S.I. and Metiu, H., A Multiple Trajectory Theory for Curve Crossing Problems Obtained by Using a Gaussian Wave Packet Representation of the Nuclear Motion. *Journal of Chemical Physics*, 1986, **84**(1), pp. 227–238.

74. Shalashilin, D.V. and Jackson, B., Guiding Paths and Time-Dependent Basis Sets for Wavefunction Propagation. *Chemical Physics Letters*, 2000, **318**(4-5), pp. 305–313.

75. Shalashilin, D.V. and Child, M.S., Description of Tunneling with the Help of Coupled Frozen Gaussians. *Journal of Chemical Physics*, 2001, **114**(21), pp. 9296–9304.

76. Shalashilin, D.V. and Child, M.S., Basis Set Sampling in the Method of Coupled Coherent States: Coherent State Swarms, Trains, and Pancakes. *Journal of Chemical Physics*, 2008, **128**(5), 054102.

77. Miller, W.H., On the Relation Between the Semiclassical Initial Value Representation and an Exact Quantum Expansion in Time-Dependent Coherent States. *Journal of Physical Chemistry B*, 2002, **106**(33), pp. 8132–8135.

78. Symonds, C., Wu, J., Ronto, M., Zagoya, C., Figueira de Morisson Faria, C. and Shalashilin, D.V., Coupled-Coherent-States Approach for High-Order Harmonic Generation. *Physical Review A*, 2015, **91**, 023427.

79. Mandelshtam, V.A. and Ovchinnikov, M., Extraction of Tunneling Splittings from a Real Time Semiclassical Propagation. *Journal of Chemical Physics*, 1998, **108**(22), pp. 9206–9209.

80. Brewer, M.L., On the Scaling of Semiclassical Initial Value Methods. *Journal of Chemical Physics*, 1999, **111**(14), pp. 6168–6170.

81. Child, M.S. and Shalashilin, D.V., Locally Coupled Coherent States and Herman-Kluk Dynamics. *Journal of Chemical Physics*, 2003, **118**(5), pp. 2061–2071.

82. Worth, G.A., Meyer, H.D. and Cederbaum, L.S., Relaxation of a System with a Conical Intersection Coupled to a Bath: a Benchmark 24-Dimensional Wave Packet Study Treating the Environment Explicitly. *Journal of Chemical Physics*, 1998, **109**(9), pp. 3518–3529.

83. Coletti, C. and Billing, G., Quantum Dressed Classical Mechanics: Application to the Photo-Absorption of Pyrazine. *Chemical Physics Letters*, 2003, **368**(3-4), pp. 289–298.

84. Thoss, M., Miller, W.H. and Stock, G., Semiclassical Description of Nonadiabatic Quantum Dynamics: Application to the S_1-S_2 Conical Intersection in Pyrazine. *Journal of Chemical Physics*, 2000, **112**(23), pp. 10282–10292.

85. Thoss, M. and Stock, G., Mapping Approach to the Semiclassical Description of Nonadiabatic Quantum Dynamics. *Physical Review A*, 1999, **59**, pp. 64–79.

86. Yamazaki, I., Murao, T., Yamanaka, T. and Yoshihara, K., Intramolecular Electronic Relaxation and Photoisomerization Processes in the Isolated Azabenzene Molecules Pyridine, Pyrazine and Pyrimidine. *Faraday Discussions of the Chemical Society*, 1983, **75**, pp. 395–405.

87. Shalashilin, D.V. and Child, M.S., Electronic Energy Levels with the Help of Trajectory-Guided Random Grid of Coupled Wave Packets. I. Six-Dimensional Simulation of H_2. *Journal of Chemical Physics*, 2005, **122**(22), 224108.

88. Shalashilin, D.V. and Child, M.S., A Version of Diffusion Monte Carlo Method Based on Random Grids of Coherent States. II. Six-Dimensional Simulation of Electronic States of H_2. *Journal of Chemical Physics*, 2005, **122**(22), 224109.

89. Shalashilin, D.V., Child, M.S. and Kirrander, A., Mechanisms of Double Ionization in Strong Laser Field from Simulation with Coupled Coherent States: Beyond Reduced Dimensionality Models. *Chemical Physics*, 2008, **347**(1-3), pp. 257–262.

90. Kirrander, A. and Shalashilin, D.V., Quantum Dynamics with Fermion Coupled Coherent States: Theory and Application to Electron Dynamics in Laser Fields. *Physical Review A*, 2011, **84**(3), 033406.

91. Eidi, M., Vafaee, M., Niknam, A.R. and Morshedian, N., A New Version of Fermion Coupled Coherent States Method: Theory and Applications in Simulation of Two-Electron Systems. *Chemical Physics Letters*, 2016, **653**, pp. 60–66.

92. Zagoya, C., Wu, J., Ronto, M., Shalashilin, D.V. and de Morisson Faria, C.F., Quantum and Semiclassical Phase-Space Dynamics of a Wave Packet in Strong Fields Using Initial-Value Representations. *New Journal of Physics*, 2014, **16**(10), 103040.

93. Arbelo-González, W., González-Martínez, M.L., Reed, S.K., Rubayo-Soneira, J. and Shalashilin, D.V., Quasi-Classical Trajectories Study of Ne2Br2(B) Vibrational Predissociation: Kinetics and Product Distributions. *Journal of Chemical Physics*, 2012, **136**(14), 144303.

94. Meyer, H.D. and Miller, W.H., A Classical Analog for Electronic Degrees of Freedom in Nonadiabatic Collision Processes. *Journal of Chemical Physics*, 1979, **70**(7), pp. 3214–3223.

95. Billing, G.D., On the Use of Ehrenfest's Theorem in Molecular Scattering. *Chemical Physics Letters*, 1983, **100**(6), pp. 535–539.

96. Kramer, P. and Saraceno, M., *Geometry of the Time-Dependent Variational Principle in Quantum Mechanics*, vol. 140 of *Lecture Notes in Physics*. Springer, 1981.

97. Wang, H. and Thoss, M., Multilayer Formulation of the Multiconfiguration Time-Dependent Hartree Theory. *Journal of Chemical Physics*, 2003, **119**(3), pp. 1289–1299.

98. Wang, H. and Thoss, M., From Coherent Motion to Localization: Dynamics of the Spin-Boson Model at Zero Temperature. *New Journal of Physics*, 2008, **10**(11), 115005.

99. Ye, S.Y., Shalashilin, D.V. and Serafini, A., Modeling of Quantum-Information Processing with Ehrenfest Guided Trajectories: a Case Study with Spin-Boson-Like Couplings. *Physical Review A*, 2012, **86**(3), 032312.

100. Saita, K. and Shalashilin, D.V., On-The-Fly Ab Initio Molecular Dynamics with Multiconfigurational Ehrenfest Method. *Journal of Chemical Physics*, 2012, **137**(22), 22A506.

101. Werner, H.J., Knowles, P.J., Knizia, G., Manby, F.R., Schütz, M. et al., Molpro, Version 2010.1, a Package of Ab Initio Programs. 2010, see http://www.molpro.net.

102. Werner, H.J., Knowles, P.J., Knizia, G., Manby, F.R. and Schütz, M., Molpro: a General-Purpose Quantum Chemistry Program Package. *WIREs Computational Molecular Science*, 2012, **2**, pp. 242–253.

103. Ben-Nun, M. and Martínez, T.J., Photodynamics of Ethylene: Ab Initio Studies of Conical Intersections. *Chemical Physics*, 2000, **259**(2-3), pp. 237–248.

104. Levine, B.G., Coe, J.D., Virshup, A.M. and Martínez, T.J., Implementation of Ab Initio Multiple Spawning in the MolPro Quantum Chemistry Package. *Chemical Physics*, 2008, **347**(1-3), pp. 3–16.

105. Ben-Nun, M. and Martínez, T.J., Ab Initio Quantum Molecular Dynamics. *Advances in Chemical Physics*, 2002, **121**, pp. 439–512.

106. Kirrander, A., Saita, K. and Shalashilin, D.V., Ultrafast X-Ray Scattering from Molecules. *Journal of Chemical Theory and Computation*, 2016, **12**(3), pp. 957–967.

107. Minitti, M.P., Budarz, J.M., Kirrander, A., Robinson, J.S., Ratner, D., Lane, T.J., Zhu, D., Glownia, J.M., Kozina, M., Lemke, H.T., Sikorski, M., Feng, Y., Nelson, S., Saita, K., Stankus, B., Northey, T., Hastings, J.B. and Weber, P.M., Imaging Molecular Motion: Femtosecond X-Ray Scattering of an Electrocyclic Chemical Reaction. *Physical Review Letters*, 2015, **114**, 255501.

108. Stefanou, M., Saita, K., Shalashilin, D.V. and Kirrander, A., Comparison of Ultrafast Electron and X-Ray Diffraction - A Computational Study. *Chemical Physics Letters*, 2017, **683**, pp. 300–305.

109. Saita, K., Nix, M.G.D. and Shalashilin, D.V., Simulation of Ultrafast Photodynamics of Pyrrole with a Multiconfigurational Ehrenfest Method. *Physical Chemistry Chemical Physics*, 2013, **15**, pp. 16227–16235.

110. Cronin, B., Nix, M.G.D., Qadiri, R.H. and Ashfold, M.N.R., High Resolution Photofragment Translational Spectroscopy Studies of the near Ultraviolet Photolysis of Pyrrole. *Physical Chemistry Chemical Physics*, 2004, **6**, pp. 5031–5041.

111. Humeniuk, A. and Mitrić, R., Non-Adiabatic Dynamics Around a Conical Intersection with Surface-Hopping Coupled Coherent States. *Journal of Chemical Physics*, 2016, **144**(23), 234108.

112. Fernandez-Alberti, S., Makhov, D.V., Tretiak, S. and Shalashilin, D.V., Non-Adiabatic Excited State Molecular Dynamics of Phenylene Ethynylene Dendrimer Using a Multiconfigurational Ehrenfest Approach. *Physical Chemistry Chemical Physics*, 2016, **18**, pp. 10028–10040.

113. Tully, J.C. and Preston, R.K., Trajectory Surface Hopping Approach to Nonadiabatic Molecular Collisions: the Reaction of H+ with D2. *Journal of Chemical Physics*, 1971, **55**(2), pp. 562–572.

114. Tully, J.C., Molecular Dynamics with Electronic Transitions. *Journal of Chemical Physics*, 1990, **93**(2), pp. 1061–1071.

115. Makhov, D.V., Symonds, C., Fernandez-Alberti, S. and Shalashilin, D.V., Ab Initio Quantum Direct Dynamics Simulations of Ultrafast Photochemistry With Multiconfigurational Ehrenfest Approach. *Chemical Physics*, 2017, **493**, pp. 200–218.

116. Dirac, P.A.M., Note on Exchange Phenomena in the Thomas Atom. *Mathematical Proceedings of the Cambridge Philosophical Society*, 1930, **26**(3), pp. 376–385.

117. McLachlan, A., A Variational Solution of the Time-Dependent Schrodinger Equation. *Molecular Physics*, 1964, **8**(1), pp. 39–44.

118. Broeckhove, J., Lathouwers, L., Kesteloot, E. and Leuven, P.V., On the Equivalence of Time-Dependent Variational Principles. *Chemical Physics Letters*, 1988, **149**(5-6), pp. 547–550.

119. Manthe, U., A Multilayer Multiconfigurational Time-Dependent Hartree Approach for Quantum Dynamics on General Potential Energy Surfaces. *Journal of Chemical Physics*, 2008, **128**(16), 164116.

120. Vendrell, O. and Meyer, H.D., Multilayer Multiconfiguration Time-Dependent Hartree Method: Implementation and Applications to a Henon-Heiles Hamiltonian and to Pyrazine. *Journal of Chemical Physics*, 2011, **134**(4), 044135.

121. Streltsov, A.I., Alon, O.E. and Cederbaum, L.S., Role of Excited States in the Splitting of a Trapped Interacting Bose-Einstein Condensate by a Time-Dependent Barrier. *Physical Review Letters*, 2007, **99**, 030402.

122. Alon, O.E., Streltsov, A.I. and Cederbaum, L.S., Multiconfigurational Time-Dependent Hartree Method for Bosons: Many-Body Dynamics of Bosonic Systems. *Physical Review A*, 2008, **77**, 033613.

123. Zanghellini, J., Kitzler, M., Fabian, C., Brabec, T. and Scrinzi, A., An MCTDHF Approach to Multi-Electron Dynamics in Laser Fields. *Laser Physics*, 2003, **13**, pp. 1064–1068.

124. Kato, T. and Kono, H., Time-Dependent Multiconfiguration Theory for Electronic Dynamics of Molecules in an Intense Laser Field. *Chemical Physics Letters*, 2004, **392**(4), pp. 533–540.

125. Nest, M., Klamroth, T. and Saalfrank, P., The Multiconfiguration Time-Dependent Hartree-Fock Method for Quantum Chemical Calculations. *Journal of Chemical Physics*, 2005, **122**(12), 124102.

126. Alon, O.E., Streltsov, A.I. and Cederbaum, L.S., Unified View on Multiconfigurational Time Propagation for Systems Consisting of Identical Particles. *Journal of Chemical Physics*, 2007, **127**(15), 154103.

127. Wang, H. and Thoss, M., Numerically Exact Quantum Dynamics for Indistinguishable Particles: the Multilayer Multiconfiguration Time-Dependent Hartree Theory in Second Quantization Representation. *Journal of Chemical Physics*, 2009, **131**(2), 024114.

128. Worth, G.A., Robb, M.A. and Burghardt, I., A Novel Algorithm for Non-Adiabatic Direct Dynamics Using Variational Gaussian Wavepackets. *Faraday Discussions*, 2004, **127**, pp. 307–323.

129. Ben-Nun, M., Quenneville, J. and Martínez, T.J., Ab Initio Multiple Spawning: Photochemistry from First Principles Quantum Molecular Dynamics. *Journal of Physical Chemistry A*, 2000, **104**(22), pp. 5161–5175.

130. Ufimtsev, I.S. and Martínez, T.J., Graphical Processing Units for Quantum Chemistry. *Computing in Science & Engineering*, 2008, **10**(6), pp. 26–34.

131. Ufimtsev, I.S. and Martínez, T.J., Quantum Chemistry on Graphical Processing Units. 1. Strategies for Two-Electron Integral Evaluation. *Journal of Chemical Theory and Computation*, 2008, **4**(2), pp. 222–231.

132. Ufimtsev, I.S. and Martínez, T.J., Quantum Chemistry on Graphical Processing Units. 2. Direct Self-Consistent-Field Implementation. *Journal of Chemical Theory and Computation*, 2009, **5**(4), pp. 1004–1015.

133. Ufimtsev, I.S. and Martínez, T.J., Quantum Chemistry on Graphical Processing Units. 3. Analytical Energy Gradients, Geometry Optimization, and First Principles Molecular Dynamics. *Journal of Chemical Theory and Computation*, 2009, **5**(10), pp. 2619–2628.

134. Snyder, J.W., Curchod, B.F.E. and Martínez, T.J., GPU-Accelerated State-Averaged Complete Active Space Self-Consistent Field Interfaced with Ab Initio Multiple Spawning Unravels the Photodynamics of Provitamin D3. *Journal of Physical Chemistry Letters*, 2016, **7**(13), pp. 2444–2449.

135. Curchod, B.F.E., Sisto, A. and Martínez, T.J., Ab Initio Multiple Spawning Photochemical Dynamics of DMABN Using GPUs. *Journal of Physical Chemistry A*, 2017, **121**(1), pp. 265–276.

136. Wu, Y., Herman, M.F. and Batista, V.S., Matching-Pursuit/Split-Operator Fourier-Transform Simulations of Nonadiabatic Quantum Dynamics. *Journal of Chemical Physics*, 2005, **122**(11), 114114.

137. Chen, X. and Batista, V.S., The MP/SOFT Methodology for Simulations of Quantum Dynamics: Model Study of the Photoisomerization of the Retinyl Chromophore in Visual Rhodopsin. *Journal of Photochemistry and Photobiology A*, 2007, **190**(2), pp. 274–282.

138. Habershon, S., Trajectory-Guided Configuration Interaction Simulations of Multidimensional Quantum Dynamics. *Journal of Chemical Physics*, 2012, **136**(5), 054109.

139. Saller, M.A.C. and Habershon, S., Basis Set Generation for Quantum Dynamics Simulations Using Simple Trajectory-Based Methods. *Journal of Chemical Theory and Computation*, 2015, **11**(1), pp. 8–16.

140. Saller, M.A.C. and Habershon, S., Quantum Dynamics with Short-Time Trajectories and Minimal Adaptive Basis Sets. *Journal of Chemical Theory and Computation*, 2017, **13**(7), pp. 3085–3096.

141. Worth, G., Robb, M. and Lasorne, B., Solving the Time-Dependent Schrödinger Equation for Nuclear Motion in One Step: Direct Dynamics of Non-Adiabatic Systems. *Molecular Physics*, 2008, **106**(16-18), pp. 2077–2091.

142. Crespo-Otero, R. and Barbatti, M., Recent Advances and Perspectives on Nonadiabatic Mixed Quantum-Classical Dynamics. *Chemical Reviews*, 2018, article ASAP (On Web) DOI: 10.1021/acs.chemrev.7b00577.

143. Curchod, B.F.E. and Martínez, T.J., Ab Initio Nonadiabatic Quantum Molecular Dynamics. *Chemical Reviews*, 2018, **118**(7), pp. 3305–3336.

144. Cha, Y., Murray, C. and Klinman, J., Hydrogen Tunneling in Enzyme Reactions. *Science*, 1989, **243**(4896), pp. 1325–1330.

145. Bahnson, B.J. and Klinman, J.P., Hydrogen Tunneling in Enzyme Catalysis. In D.L. Purich, ed., *Enzyme Kinetics and Mechanism Part D: Developments in Enzyme Dynamics*, vol. 249 of *Methods in Enzymology*, Academic Press, 1995, pp. 373 – 397.

146. Kohen, A., Cannio, R., Bartolucci, S. and Klinman, J.P., Enzyme Dynamics and Hydrogen Tunnelling in a Thermophilic Alcohol Dehydrogenase. *Nature*, 1999, **399**, pp. 496–499.

147. Topaler, M. and Makri, N., Quantum Rates for a Double Well Coupled to a Dissipative Bath: Accurate Path Integral Results and Comparison with Approximate Theories. *Journal of Chemical Physics*, 1994, **101**(9), pp. 7500–7519.

148. Milburn, G.J., Corney, J., Wright, E.M. and Walls, D.F., Quantum Dynamics of an Atomic Bose-Einstein Condensate in a Double-Well Potential. *Physical Review A*, 1997, **55**, pp. 4318–4324.

149. Smerzi, A., Fantoni, S., Giovanazzi, S. and Shenoy, S.R., Quantum Coherent Atomic Tunneling Between Two Trapped Bose-Einstein Condensates. *Physical Review Letters*, 1997, **79**, pp. 4950–4953.

150. Caldeira, A.O. and Leggett, A.J., Influence of Dissipation on Quantum Tunneling in Macroscopic Systems. *Physical Review Letters*, 1981, **46**, pp. 211–214.

151. Caldeira, A.O. and Leggett, A.J., Quantum Tunnelling in a Dissipative System. *Annals of Physics*, 1983, **149**(2), pp. 374–456.

152. Makhlin, Y., Schön, G. and Shnirman, A., Quantum-State Engineering with Josephson-Junction Devices. *Reviews of Modern Physics*, 2001, **73**, pp. 357–400.

153. Makri, N. and Miller, W.H., Basis Set Methods for Describing the Quantum Mechanics of a "System" Interacting with a Harmonic Bath. *Journal of Chemical Physics*, 1987, **86**(3), pp. 1451–1457.

154. Green, J.A. and Shalashilin, D.V., Benchmark Calculation for Tunnelling Through a Multidimensional Asymmetric Double Well Potential. *Chemical Physics Letters*, 2015, **641**, pp. 173–180.

155. Atkinson, K.E., *An Introduction to Numerical Analysis*. 2nd ed., Wiley, 1988.

156. Römer, S., Ruckenbauer, M. and Burghardt, I., Gaussian-Based Multiconfiguration Time-Dependent Hartree: a Two-Layer Approach. I. Theory. *Journal of Chemical Physics*, 2013, **138**(6), 064106.

157. Anderson, M.H., Ensher, J.R., Matthews, M.R., Wieman, C.E. and Cornell, E.A., Observation of Bose-Einstein Condensation in a Dilute Atomic Vapor. *Science*, 1995, **269**(5221), pp. 198–201.

158. Bradley, C.C., Sackett, C.A., Tollett, J.J. and Hulet, R.G., Evidence of Bose-Einstein Condensation in an Atomic Gas with Attractive Interactions. *Physical Review Letters*, 1995, **75**, pp. 1687–1690.

159. Davis, K.B., Mewes, M.O., Andrews, M.R., van Druten, N.J., Durfee, D.S., Kurn, D.M. and Ketterle, W., Bose-Einstein Condensation in a Gas of Sodium Atoms. *Physical Review Letters*, 1995, **75**, pp. 3969–3973.

160. Orzel, C., Tuchman, A.K., Fenselau, M.L., Yasuda, M. and Kasevich, M.A., Squeezed States in a Bose-Einstein Condensate. *Science*, 2001, **291**(5512), pp. 2386–2389.

161. Albiez, M., Gati, R., Fölling, J., Hunsmann, S., Cristiani, M. and Oberthaler, M.K., Direct Observation of Tunneling and Nonlinear Self-Trapping in a Single Bosonic Josephson Junction. *Physical Review Letters*, 2005, **95**, 010402.

162. Levy, S., Lahoud, E., Shomroni, I. and Steinhauer, J., The A.C. and D.C. Josephson Effects in a Bose-Einstein Condensate. *Nature*, 2007, **449**, pp. 579–583.

163. Matthews, M.R., Anderson, B.P., Haljan, P.C., Hall, D.S., Wieman, C.E. and Cornell, E.A., Vortices in a Bose-Einstein Condensate. *Physical Review Letters*, 1999, **83**, pp. 2498–2501.

164. Madison, K.W., Chevy, F., Wohlleben, W. and Dalibard, J., Vortex Formation in a Stirred Bose-Einstein Condensate. *Physical Review Letters*, 2000, **84**, pp. 806–809.

165. Gross, E.P., Structure of a Quantized Vortex in Boson Systems. *Nuovo Cimento*, 1961, **20**(3), pp. 454–477.

166. Pitaevskii, L.P., Vortex Lines in an Imperfect Bose Gas. *Soviet Physics JETP-USSR*, 1961, **13**(2), pp. 451–454.

167. Pérez-García, V.M., Michinel, H., Cirac, J.I., Lewenstein, M. and Zoller, P., Dynamics of Bose-Einstein Condensates: Variational Solutions of the Gross-Pitaevskii Equations. *Physical Review A*, 1997, **56**, pp. 1424–1432.

168. Raghavan, S., Smerzi, A., Fantoni, S. and Shenoy, S.R., Coherent Oscillations Between Two Weakly Coupled Bose-Einstein Condensates: Josephson Effects, π Oscillations, and Macroscopic Quantum Self-Trapping. *Physical Review A*, 1999, **59**, pp. 620–633.

169. Bao, W., Jaksch, D. and Markowich, P.A., Numerical Solution of the Gross-Pitaevskii Equation for Bose-Einstein Condensation. *Journal of Computational Physics*, 2003, **187**(1), pp. 318–342.

170. Liang, Z.X., Zhang, Z.D. and Liu, W.M., Dynamics of a Bright Soliton in Bose-Einstein Condensates with Time-Dependent Atomic Scattering Length in an Expulsive Parabolic Potential. *Physical Review Letters*, 2005, **94**, 050402.

171. Ananikian, D. and Bergeman, T., Gross-Pitaevskii Equation for Bose Particles in a Double-Well Potential: Two-Mode Models and Beyond. *Physical Review A*, 2006, **73**, 013604.

172. Leggett, A.J., Bose-Einstein Condensation in the Alkali Gases: Some Fundamental Concepts. *Reviews of Modern Physics*, 2001, **73**, pp. 307–356.

173. Minguzzi, A., Succi, S., Toschi, F., Tosi, M. and Vignolo, P., Numerical Methods for Atomic Quantum Gases with Applications to Bose-Einstein Condensates and to Ultracold Fermions. *Physics Reports*, 2004, **395**(4-5), pp. 223–355.

174. Streltsov, A.I., Alon, O.E. and Cederbaum, L.S., Formation and Dynamics of Many-Boson Fragmented States in One-Dimensional Attractive Ultracold Gases. *Physical Review Letters*, 2008, **100**, 130401.

175. Streltsov, A.I., Alon, O.E. and Cederbaum, L.S., Scattering of an Attractive Bose-Einstein Condensate from a Barrier: Formation of Quantum Superposition States. *Physical Review A*, 2009, **80**, 043616.

176. Streltsov, A.I., Alon, O.E. and Cederbaum, L.S., Efficient Generation and Properties of Mesoscopic Quantum Superposition States in an Attractive Bose-Einstein Condensate Threaded by a Potential Barrier. *Journal of Physics B*, 2009, **42**(9), 091004.

177. Lode, A.U.J., Streltsov, A.I., Alon, O.E., Meyer, H.D. and Cederbaum, L.S., Exact Decay and Tunnelling Dynamics of Interacting Few-Boson Systems. *Journal of Physics B*, 2009, **42**(4), 044018.

178. Sakmann, K., Streltsov, A.I., Alon, O.E. and Cederbaum, L.S., Exact Quantum Dynamics of a Bosonic Josephson Junction. *Physical Review Letters*, 2009, **103**, 220601.

179. Sakmann, K., Streltsov, A.I., Alon, O.E. and Cederbaum, L.S., Quantum Dynamics of Attractive Versus Repulsive Bosonic Josephson Junctions: Bose-Hubbard and Full-Hamiltonian Results. *Physical Review A*, 2010, **82**, 013620.

180. Streltsov, A.I., Alon, O.E. and Cederbaum, L.S., Swift Loss of Coherence of Soliton Trains in Attractive Bose-Einstein Condensates. *Physical Review Letters*, 2011, **106**, 240401.

181. Streltsov, A.I., Sakmann, K., Alon, O.E. and Cederbaum, L.S., Accurate Multi-Boson Long-Time Dynamics in Triple-Well Periodic Traps. *Physical Review A*, 2011, **83**, 043604.

182. Lode, A.U.J., Sakmann, K., Alon, O.E., Cederbaum, L.S. and Streltsov, A.I., Numerically Exact Quantum Dynamics of Bosons with Time-Dependent Interactions of Harmonic Type. *Physical Review A*, 2012, **86**, 063606.

183. Streltsov, A.I., Quantum Systems of Ultracold Bosons with Customized Interparticle Interactions. *Physical Review A*, 2013, **88**, 041602.

184. Cao, L., Krönke, S., Vendrell, O. and Schmelcher, P., The Multi-Layer Multi-Configuration Time-Dependent Hartree Method for Bosons: Theory, Implementation, and Applications. *Journal of Chemical Physics*, 2013, **139**(13), 134103.

185. Schmitz, R., Krönke, S., Cao, L. and Schmelcher, P., Quantum Breathing Dynamics of Ultracold Bosons in One-Dimensional Harmonic Traps: Unraveling the Pathway from Few- to Many-Body Systems. *Physical Review A*, 2013, **88**, 043601.

186. Krönke, S., Cao, L., Vendrell, O. and Schmelcher, P., Non-Equilibrium Quantum Dynamics of Ultra-Cold Atomic Mixtures: the Multi-Layer Multi-Configuration Time-Dependent Hartree Method for Bosons. *New Journal of Physics*, 2013, **15**(6), 063018.

187. Wang, H., Multilayer Multiconfiguration Time-Dependent Hartree Theory. *Journal of Physical Chemistry A*, 2015, **119**(29), pp. 7951–7965.

188. Sakurai, J.J. and Napolitano, J., *Modern Quantum Mechanics*. 2nd ed., Addison-Wesley, 1994.

189. Sakmann, K., Streltsov, A.I., Alon, O.E. and Cederbaum, L.S., Universality of Fragmentation in the Schrödinger Dynamics of Bosonic Josephson Junctions. *Physical Review A*, 2014, **89**, 063606.

190. Blank, D.A., North, S.W. and Lee, Y.T., The Ultraviolet Photodissociation Dynamics of Pyrrole. *Chemical Physics*, 1994, **187**(1), pp. 35–47.

191. Wei, J., Kuczmann, A., Riedel, J., Renth, F. and Temps, F., Photofragment Velocity Map Imaging of H Atom Elimination in the First Excited State of Pyrrole. *Physical Chemistry Chemical Physics*, 2003, **5**, pp. 315–320.

192. Wei, J., Riedel, J., Kuczmann, A., Renth, F. and Temps, F., Photodissociation Dynamics of Pyrrole: Evidence for Mode Specific Dynamics from Conical Intersections. *Faraday Discussions*, 2004, **127**, pp. 267–282.

193. Cronin, B., Devine, A.L., Nix, M.G.D. and Ashfold, M.N.R., Near Ultraviolet Photolysis of Deuterated Pyrrole. *Physical Chemistry Chemical Physics*, 2006, **8**, pp. 3440–3445.

194. Rubio-Lago, L., Zaouris, D., Sakellariou, Y., Sofikitis, D., Kitsopoulos, T.N., Wang, F., Yang, X., Cronin, B., Devine, A.L., King, G.A., Nix, M.G.D., Ashfold, M.N.R. and Xantheas, S.S., Photofragment Slice Imaging Studies of Pyrrole and the Xe$\cdots$Pyrrole Cluster. *Journal of Chemical Physics*, 2007, **127**(6), 064306.

195. Ashfold, M.N.R., Cronin, B., Devine, A.L., Dixon, R.N. and Nix, M.G.D., The Role of $\pi\sigma^*$ Excited States in the Photodissociation of Heteroaromatic Molecules. *Science*, 2006, **312**(5780), pp. 1637–1640.

196. Ashfold, M.N.R., King, G.A., Murdock, D., Nix, M.G.D., Oliver, T.A.A. and Sage, A.G., $\pi\sigma^*$ Excited States in Molecular Photochemistry. *Physical Chemistry Chemical Physics*, 2010, **12**, pp. 1218–1238.

197. Roberts, G.M. and Stavros, V.G., The Role of $\pi\sigma^*$ States in the Photochemistry of Heteroaromatic Biomolecules and Their Subunits: Insights from Gas-Phase Femtosecond Spectroscopy. *Chemical Science*, 2014, **5**, pp. 1698–1722.

198. Crane, S.W., Zawadzki, M.M., Thompson, J.O.F., Kotsina, N., Ghafur, O. and Townsend, D., Caveats in the Interpretation of Time-Resolved Photoionization Measurements: a Photoelectron Imaging Study of Pyrrole. *Journal of Chemical Physics*, 2016, **145**(23), 234304.

199. Horton, S.L., Liu, Y., Chakraborty, P., Matsika, S. and Weinacht, T., Ultrafast Internal Conversion Dynamics of Highly Excited Pyrrole Studied with VUV/UV Pump Probe Spectroscopy. *Journal of Chemical Physics*, 2017, **146**(6), 064306.

200. Lippert, H., Ritze, H.H., Hertel, I.V. and Radloff, W., Femtosecond Time-Resolved Hydrogen-Atom Elimination from Photoexcited Pyrrole Molecules. *ChemPhysChem*, 2004, **5**(9), pp. 1423–1427.

201. Montero, R., Álvaro Peralta Conde, Ovejas, V., Fernández-Fernández, M., Castano, F., de Aldana, J.R.V. and Longarte, A., Femtosecond Evolution of the Pyrrole Molecule Excited in the near Part of Its UV Spectrum. *Journal of Chemical Physics*, 2012, **137**(6), 064317.

202. Montero, R., Ovejas, V., Fernández-Fernández, M., Álvaro Peralta Conde and Longarte, A., Revisiting the Relaxation Dynamics of Isolated Pyrrole. *Journal of Chemical Physics*, 2014, **141**(1), 014303.

203. Roberts, G.M., Williams, C.A., Yu, H., Chatterley, A.S., Young, J.D., Ullrich, S. and Stavros, V.G., Probing Ultrafast Dynamics in Photoexcited Pyrrole: Timescales for $1\pi\sigma^*$ Mediated H-Atom Elimination. *Faraday Discussions*, 2013, **163**, pp. 95–116.

204. Wu, G., Neville, S.P., Schalk, O., Sekikawa, T., Ashfold, M.N.R., Worth, G.A. and Stolow, A., Excited State Non-Adiabatic Dynamics of Pyrrole: a Time-Resolved Photoelectron Spectroscopy and Quantum Dynamics Study. *Journal of Chemical Physics*, 2015, **142**(7), 074302.

205. Kirkby, O.M., Parkes, M.A., Neville, S.P., Worth, G.A. and Fielding, H.H., Non-Radiative Relaxation Dynamics of Pyrrole Following Excitation in the Range 249.5-200 nm. *Chemical Physics Letters*, 2017, **683**, pp. 179–185.

206. Palmer, M.H., Walker, I.C. and Guest, M.F., The Electronic States of Pyrrole Studied by Optical (VUV) Absorption, Near-Threshold Electron Energy-Loss (EEL) Spectroscopy and Ab Initio Multi-Reference Configuration Interaction Calculations. *Chemical Physics*, 1998, **238**(2), pp. 179–199.

207. Sobolewski, A.L. and Domcke, W., Conical Intersections Induced by Repulsive $1\pi\sigma^*$ States in Planar Organic Molecules: Malonaldehyde, Pyrrole and Chlorobenzene as Photochemical Model Systems. *Chemical Physics*, 2000, **259**(2), pp. 181–191.

208. Sobolewski, A.L., Domcke, W., Dedonder-Lardeux, C. and Jouvet, C., Excited-State Hydrogen Detachment and Hydrogen Transfer Driven by Repulsive $1\pi\sigma^*$ States: a New Paradigm for Nonradiative Decay in Aromatic Biomolecules. *Physical Chemistry Chemical Physics*, 2002, **4**, pp. 1093–1100.

209. Roos, B.O., Åke Malmqvist, P., Molina, V., Serrano-Andrés, L. and Merchán, M., Theoretical Characterization of the Lowest-Energy Absorption Band of Pyrrole. *Journal of Chemical Physics*, 2002, **116**(17), pp. 7526–7536.

210. Vallet, V., Lan, Z., Mahapatra, S., Sobolewski, A.L. and Domcke, W., Time-Dependent Quantum Wave-Packet Description of the $1\pi\sigma^*$ Photochemistry of Pyrrole. *Faraday Discussions*, 2004, **127**, pp. 283–293.

211. Vallet, V., Lan, Z., Mahapatra, S., Sobolewski, A.L. and Domcke, W., Photochemistry of Pyrrole: Time-Dependent Quantum Wave-Packet Description of the Dynamics at the $1\pi\sigma^*$-S_0 Conical Intersections. *Journal of Chemical Physics*, 2005, **123**(14), 144307.

212. Lan, Z., Dupays, A., Vallet, V., Mahapatra, S. and Domcke, W., Photoinduced Multi-Mode Quantum Dynamics of Pyrrole at the $1\pi\sigma^*$-S_0 Conical Intersections. *Journal of Photochemistry and Photobiology A*, 2007, **190**(2), pp. 177–189.

213. Barbatti, M., Vazdar, M., Aquino, A.J.A., Eckert-Maksić, M. and Lischka, H., The Nonadiabatic Deactivation Paths of Pyrrole. *Journal of Chemical Physics*, 2006, **125**(16), 164323.

214. Vazdar, M., Eckert-Maksić, M., Barbatti, M. and Lischka, H., Excited-State Non-Adiabatic Dynamics Simulations of Pyrrole. *Molecular Physics*, 2009, **107**(8-12), pp. 845–854.

215. Sellner, B., Barbatti, M. and Lischka, H., Dynamics Starting at a Conical Intersection: Application to the Photochemistry of Pyrrole. *Journal of Chemical Physics*, 2009, **131**(2), 024312.

216. Barbatti, M., Pittner, J., Pederzoli, M., Werner, U., Mitrić, R., Bonačić-Koutecký, V. and Lischka, H., Non-adiabatic Dynamics of Pyrrole: Dependence of Deactivation Mechanisms on the Excitation Energy. *Chemical Physics*, 2010, **375**(1), pp. 26–34.

217. Barbatti, M. and Sen, K., Effects of Different Initial Condition Samplings on Photodynamics and Spectrum of Pyrrole. *International Journal of Quantum Chemistry*, 2016, **116**(10), pp. 762–771.

218. Sapunar, M., Ponzi, A., Chaiwongwattana, S., Malis, M., Prlj, A., Decleva, P. and Doslic, N., Timescales of N-H Bond Dissociation in Pyrrole: a Nonadiabatic Dynamics Study. *Physical Chemistry Chemical Physics*, 2015, **17**, pp. 19012–19020.

219. Neville, S.P. and Worth, G.A., A Reinterpretation of the Electronic Spectrum of Pyrrole: a Quantum Dynamics Study. *Journal of Chemical Physics*, 2014, **140**(3), 034317.

220. Köppel, H., Gromov, E. and Trofimov, A., Multi-Mode-Multi-State Quantum Dynamics of Key Five-Membered Heterocycles: Spectroscopy and Ultrafast Internal Conversion. *Chemical Physics*, 2004, **304**(1), pp. 35–49.

221. Faraji, S., Vazdar, M., Reddy, V.S., Eckert-Maksic, M., Lischka, H. and Köppel, H., Ab Initio Quantum Dynamical Study of the Multi-State Nonadiabatic Photodissociation of Pyrrole. *Journal of Chemical Physics*, 2011, **135**(15), 154310.

222. Karsili, T.N.V., Marchetti, B., Moca, R. and Ashfold, M.N.R., UV Photodissociation of Pyrroles: Symmetry and Substituent Effects. *Journal of Physical Chemistry A*, 2013, **117**(46), pp. 12067–12074.

223. Makhov, D.V., Saita, K., Martínez, T.J. and Shalashilin, D.V., Ab Initio Multiple Cloning Simulations of Pyrrole Photodissociation: TKER Spectra and Velocity Map Imaging. *Physical Chemistry Chemical Physics*, 2015, **17**, pp. 3316–3325.

224. Makhov, D.V., Martínez, T.J. and Shalashilin, D.V., Toward Fully Quantum Modelling of Ultrafast Photodissociation Imaging Experiments. Treating Tunnelling in the Ab Initio Multiple Cloning Approach. *Faraday Discussions*, 2016, **194**, pp. 81–94.

225. Cole-Filipiak, N.C., Staniforth, M., d. N. Rodrigues, N., Peperstraete, Y. and Stavros, V.G., Ultrafast Dissociation Dynamics of 2-Ethylpyrrole. *Journal of Physical Chemistry A*, 2017, **121**(5), pp. 969–976.

226. Green, J.A., Makhov, D.V., Cole-Filipiak, N.C., Stavros, V.G. and Shalashilin, D.V., Ultrafast Photodissociation Dynamics of Pyrroles: Adding Insight to Experiment With Ab Initio Multiple Cloning., 2018, (In Preparation).

227. Dunning Jr., T.H., Gaussian Basis Sets for Use in Correlated Molecular Calculations. I. the Atoms Boron Through Neon and Hydrogen. *Journal of Chemical Physics*, 1989, **90**(2), pp. 1007–1023.

228. Thompson, A.L., Punwong, C. and Martínez, T.J., Optimization of Width Parameters for Quantum Dynamics with Frozen Gaussian Basis Sets. *Chemical Physics*, 2010, **370**(1), pp. 70–77.

229. Makhov, D.V. and Shalashilin, D.V., Modelling of Electronic Excitation as a Part of Multiple Cloning Dynamics, 2018, (In Preparation).

230. Anderson, E., Bai, Z., Bischof, C., Blackford, S., Demmel, J., Dongarra, J., Du Croz, J., Greenbaum, A., Hammarling, S., McKenney, A. and Sorensen, D., *LAPACK Users' Guide*. 3rd ed., Philadelphia, PA: Society for Industrial and Applied Mathematics, 1999.

231. Intel Fortran Compiler 15.0. 2015.

232. Intel Math Kernel Library (Intel MKL). 2017.

Appendix A

Programming Details

A.1 Benchmark Calculation

The program code described herein was used to perform the calculations in Chapter 2 for the benchmark calculation on the system-bath asymmetric double well tunnelling Hamiltonian of Eq. (2.2.1). The code was designed in modular form as follows:

- **Main program:** controls program flow.
- **Constants module:** stores global variables that are used by various subroutines, such as the parameters read from input file, propagation time and timestep, Hamiltonian parameters, and physical constants.
- **Initialisation module:** reads parameters from input file, initialises arrays, and sets initial amplitudes according to Eq. (2.2.16).
- **Hamiltonian module:** sets the matrix elements of Hamiltonian Eq. (2.2.1).
- **Propagation module:** propagates the amplitudes according to Eq. (2.2.3).
- **Auxiliary module:** performs the composite Simpsons numerical integration for matrix elements and initial amplitudes, Eqs. (2.2.9) and (2.2.17).
- **Output module:** calculates CCF and FT and puts them in output files.

The layout of the program is shown in the flow chart in Fig. A.1.

A.1.1 Program Overview

The code is written in Fortran90, with separate files for each of the modules listed above. The names of these files and their dependencies are shown in Table A.1. The code is compiled via a compile.sh file that creates a run_as2.exe executable to conduct the calculation.

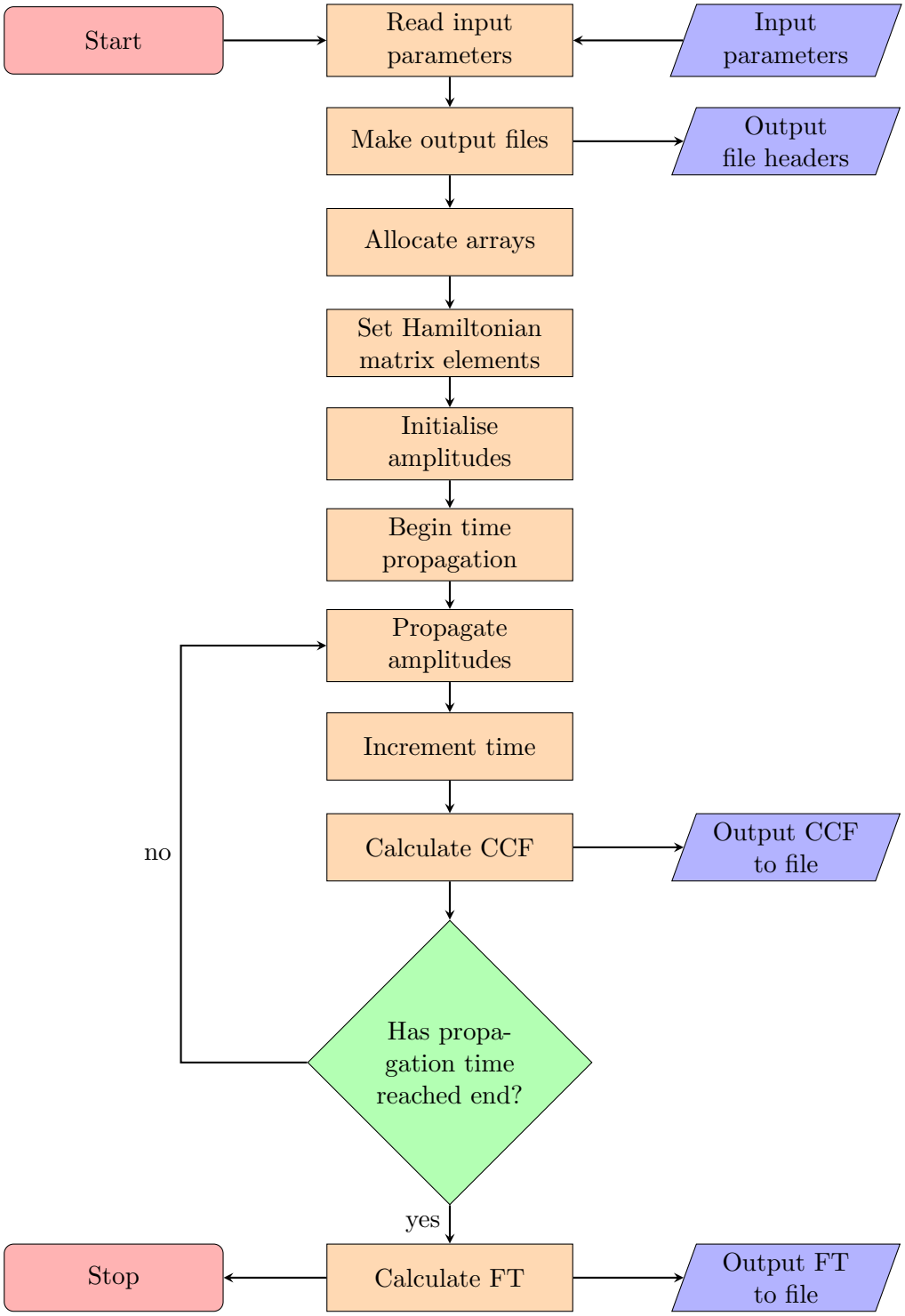

Figure A.1: Flow chart showing the layout of the program used to generate the results for the benchmark calculation of the asymmetric double well model in Chapter 2.

File Name	Module Name	Module Purpose	Dependencies
const.f90	`constants`	Contains parameters read from input file, propagation time and timestep, Hamiltonian parameters, and physical constants.	none
aux.f90	`auxiliary`	Performs the composite Simpsons numerical integration for matrix elements and initial amplitudes	`constants`
init.f90	`initialise`	Reads parameters from input file, initialises arrays and sets initial amplitudes	`constants` `auxiliary`
ham.f90	`hamiltonian`	Computes matrix elements of the Hamiltonian	`constants` `auxiliary`
prop.f90	`propagation`	Finds time derivative of amplitudes and propagates them via a Runge-Kutta 4 scheme	`constants`
out.f90	`outputs`	Calculates CCF and FT and puts them in output files	`constants` `auxiliary`
Main.f90	`main`	Controls program flow	`constants` `initialise` `hamiltonian` `propagation` `outputs`

Table A.1: Source code files/modules for the benchmark calculation program.

A.1.2 Input Parameters

The input parameters for the calculation are found in the input.dat file and are shown in Table A.2. Variables of the same name as these parameters are found in the const.f90 file, to be used by various routines in the program. The const.f90 also contains other parameters and constants that are set as default and used by the program, but can be changed and the code recompiled. These additional parameters are shown in Table A.3.

A.1.3 Output

The program outputs two files:

- **ccf.out**: The cross-correlation function, with data given in 4 columns as: time, Re(CCF), Im(CCF) and Abs(CCF). A header with the calculation input parameters is also displayed.
- **ft.out**: The Fourier transform of the real part of the cross-correlation function. Data is given in two columns as: ω and $I(\omega)$. A header with the calculation input parameters is also displayed.

Parameter	Value	Description
`nbf`	<integer>	Number of system basis functions N_{sys}
`nbth`	<integer>	Number of bath basis functions N_{bth}
`L`	<real number>	Size of box for system basis functions L
`q0`	<real number>	Lower coordinate of box q_{box}
`lambda`	<real number>	System-bath coupling constant λ
`dim_bth`	<integer>	Dimensionality of bath $M-1$
`omega_start`	<real number>	Starting frequency for Fourier transform
`omega_end`	<real number>	End frequency for Fourier transform

Table A.2: Parameters in input.dat file for benchmark calculation program.

Parameter	Value	Description
`q_init`	-2.5	Initial position for system wavefunction
`Pi`	$4\arctan(1)$	Value of constant π
`eta`	1.3544	Well depth parameter η
`time_end`	120	End propagation time
`dt`	0.001	Propagation timestep
`dft`	0.05	Stepsize for discrete Fourier transform
`im`	i	Imaginary number

Table A.3: Additional parameters and constants found in the const.f90 file for benchmark calculation program.

A.2 CCS Program

The program designed to perform CCS, 2L-CCS and CCSB calculations is described in this section. As with the benchmark calculation program, it is designed in modular form as follows:

- **Main program:** controls program flow.
- **Initialisation module:** reads parameters from input file (including if a prior basis set is read in), initialises arrays, and generates seed for random number generators.
- **Constants module:** stores global variables that are used by various subroutines, such as the parameters read from input file, various Hamiltonian parameters, and physical constants.
- **Basis module:** generates the initial coherent state basis distribution and sets initial amplitudes.
- **Hamiltonian module:** sets the normal ordered z matrix elements for various Hamiltonians, as well as their z derivatives.
- **Propagation module:** propagates the trajectories, action, and amplitudes.
- **Auxiliary module:** calculates coherent state overlap, norm, CCF, 1-body density, and performs linear equation handling for the initialisation and propagation of amplitudes equations.
- **Output module:** creates output files for calculated quantities and basis, and writes data to them.

The layout of the program is shown via flow charts for the basis set generation portion in Fig. A.2, and basis set propagation in Fig. A.3.

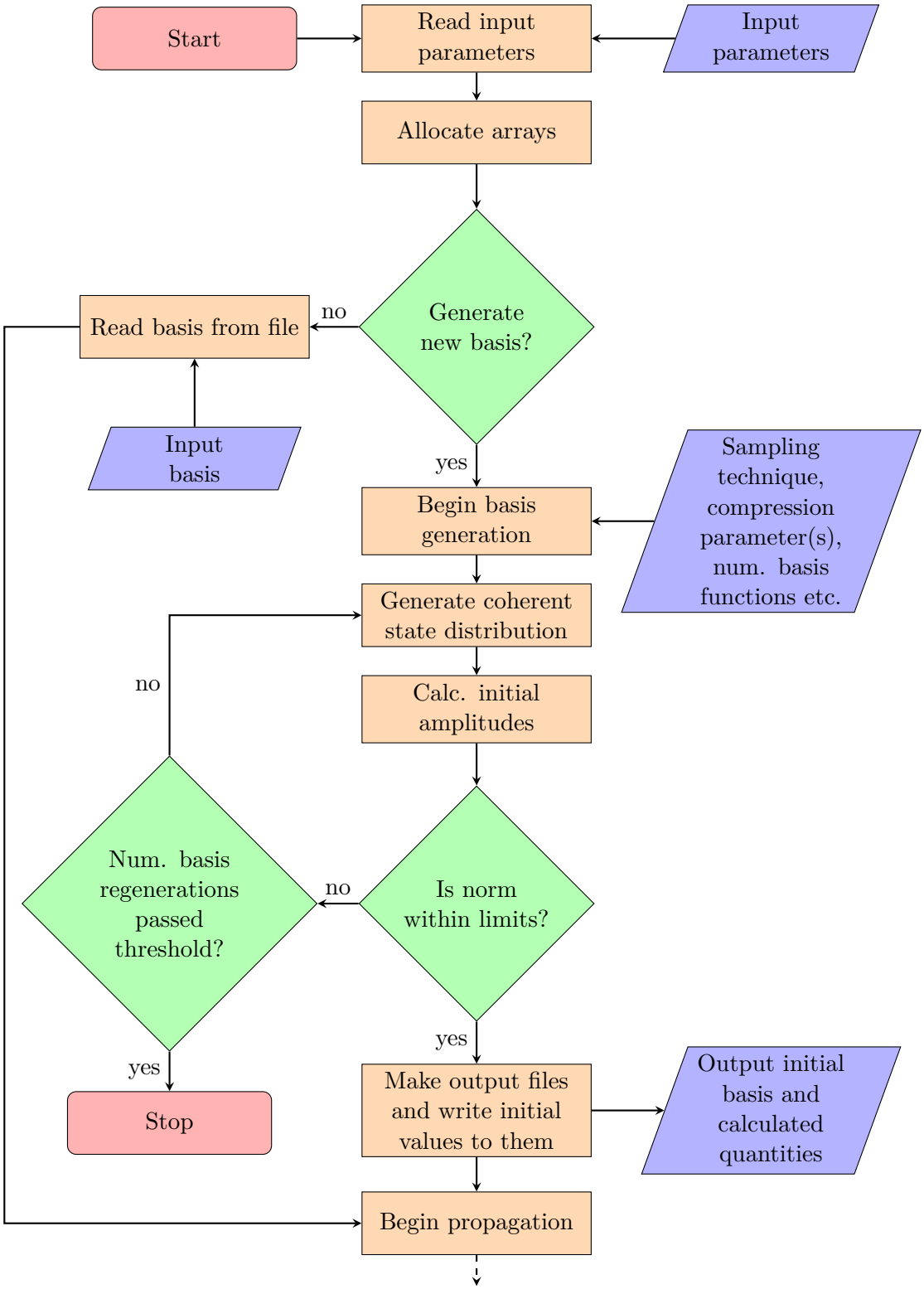

Figure A.2: Flow chart showing the layout of the basis set generation portion of the program used for the 2L-CCS and CCSB calculations in Chapters 3 and 4.

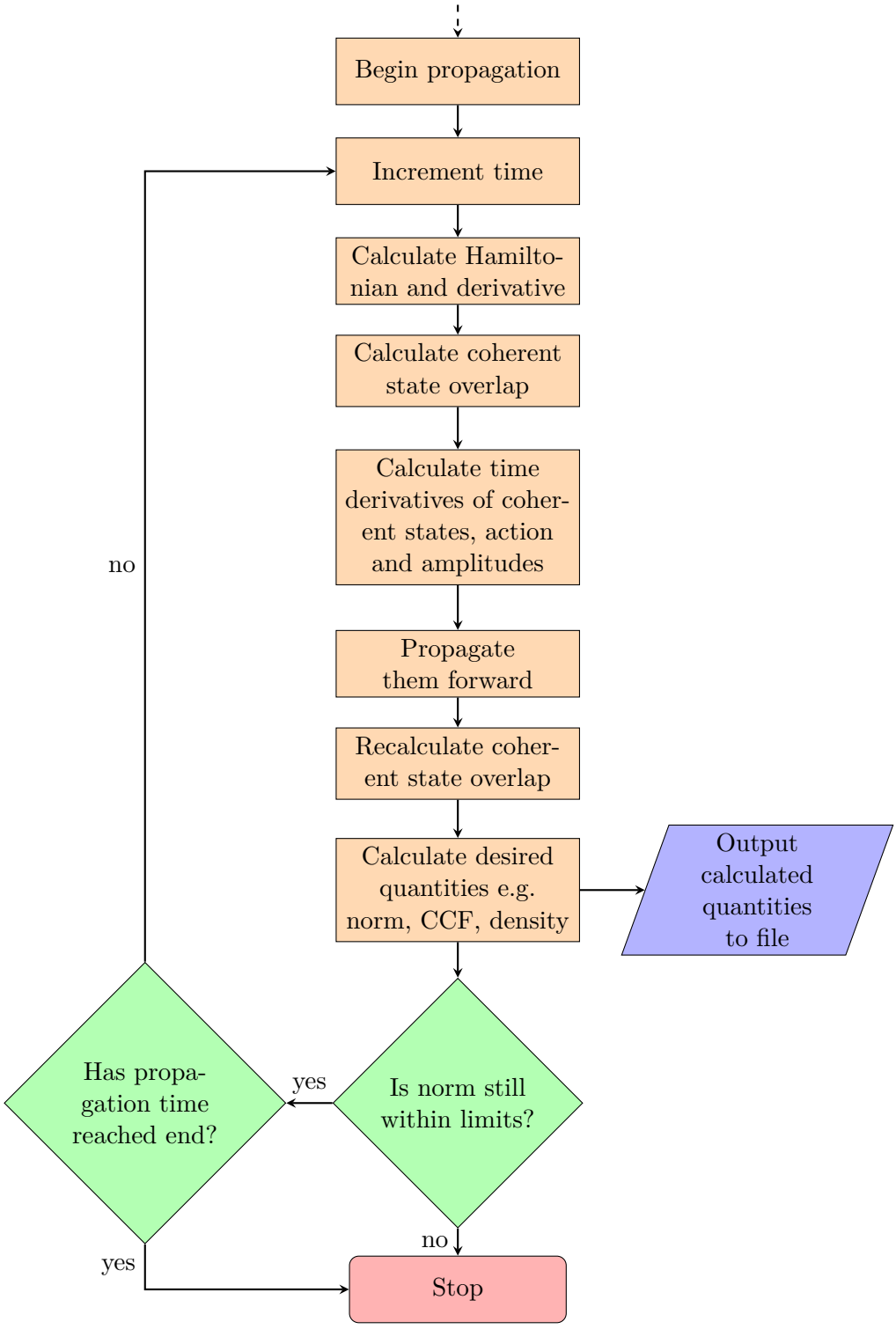

Figure A.3: Flow chart showing the layout of the basis set propagation portion of the program used for the 2L-CCS and CCSB calculations in Chapters 3 and 4.

File Name	Module Name	Module Purpose	Dependencies
const.f90	`constants`	Contains parameters read from input file, Hamiltonian parameters, and physical constants	none
init.f90	`initialise`	Reads parameters from input file, initialises arrays and generates random seed	`constants`
aux.f90	`auxiliary`	Calculates coherent state overlap, norm, CCF, 1-body density, and performs linear equation handling	`constants`
ham.f90	`hamiltonian`	Computes z matrix elements of the Hamiltonian and z derivatives	`constants`
basis.f90	`basis`	Generates initial coherent state distribution and sets initial amplitudes	`constants` `auxiliary`
prop.f90	`propagation`	Propagates the trajectories, action, and amplitudes via a Runge-Kutta 4 scheme	`constants` `auxiliary` `hamiltonian`
out.f90	`outputs`	Creates output files for calculated quantities and basis, and writes data	`constants`
main.f90	`main`	Controls program flow	`constants` `initialise` `auxiliary` `basis` `hamiltonian` `propagation` `outputs`

Table A.4: Source code files/modules for the CCS, 2L-CCS and CCSB calculation program.

A.2.1 Program Overview

The code is written in Fortran90 with separate files for each of the modules listed above. The names of these files and their dependencies are shown in Table A.4. The source code, executables, input files, output files and object files are split into a folder structure as follows: src/, bin/, in/, out/, and obj/. The code is compiled via a compile.sh file in the bin/ directory to create a run_QD.exe executable.

Parameter	Value	Description
`dof`	<integer>	Number of degrees of freedom M in basis for CCS/2L-CCS Number of excited states Ω in basis for CCSB
`sys_dof`	<integer>	Number of degrees of freedom for "inner layer" in 2L-CCS Default 1 for CCS and CCSB
`nbv`	<integer>	Number of "inner layer" basis functions J in 2L-CCS Default 1 for CCS and CCSB
`nconf`	<integer>	Number of configurations K
`dt`	<real number>	Timestep for propagation
`time_end`	<real number>	End time for propagation
`cmprss`	<real number>	Compression parameter for basis set sampling $\sigma^{(\mathrm{b})}$, $\sigma^{(2\alpha>0)}$, and $\sigma^{(\alpha>0)}$
`sys_cmprss`	<real number>	Compression parameter for tunnelling mode basis functions in double well calculations $\sigma^{(\mathrm{s})}$
`method`	CCS 2LCCS	Flag for method used: CCS(B) or 2L-CCS
`qsystem`	 FP HP MP AS 2Q BC	Flag for system studied: free particle harmonic potential Morse potential asymmetric double well second quantised asymmetric double well model Bose-Einstein condensate
`sampling`	SWARM PANCAKE	Type of sampling used for coherent states
`as_upper_well_dim`	<integer>	Used to put basis functions in upper well of asymmetric double well potential Default 0
`bsout`	Y/N	Output the basis to file for calculations that need to be stopped and restarted
`readbs`	Y/N	Read basis from previous output file to restart calculation
`reporting`	Y/N	Dump trajectories and amplitudes at all times (for error reporting)
`n_prtcls`	<integer>	For CCSB, number of particles in ground state

Table A.5: Parameters in input.dat file for CCS, 2L-CCS and CCSB calculation program.

Parameter	Value	Description
fp_max_norm	1.001	Max. value of the norm of the wavefunction for free particle Hamiltonian
fp_min_norm	0.999	Min. value of the norm of the wavefunction for free particle Hamiltonian
hp_max_norm	1.001	Max. value of the norm of the wavefunction for harmonic potential Hamiltonian
hp_min_norm	0.999	Min. value of the norm of the wavefunction for harmonic potential Hamiltonian
mp_max_norm	1.001	Max. value of the norm of the wavefunction for Morse potential Hamiltonian
mp_min_norm	0.999	Min. value of the norm of the wavefunction for Morse potential Hamiltonian
mp_diss_en	10.25	Dissociation energy for Morse potential
mp_well_param	0.2209	Well width parameter for Morse potential
as_max_norm	1.01	Max. value of the norm of the wavefunction for asymmetric double well Hamiltonian
as_min_norm	0.99	Min. value of the norm of the wavefunction for asymmetric double well Hamiltonian
as_eta	1.3544	Well depth parameter for asymmetric double well Hamiltonian
as_lambda	0.1 (Default)	System-bath coupling parameter for asymmetric double well Hamiltonian
bc_max_norm	1.001	Max. value of the norm of the wavefunction for model Bose-Einstein condensate Hamiltonian
bc_min_norm	0.999	Min. value of the norm of the wavefunction for model Bose-Einstein condensate Hamiltonian
bc_lambda	0.001 (Default)	Strength of 2-body interaction for model Bose-Einstein condensate Hamiltonian
bc_W_mnop	<empty>	Dirac delta function matrix elements for model Bose-Einstein condensate Hamiltonian. Array size (dof,dof,dof,dof). Calculated at runtime.
hermite_coeff	<empty>	Coefficients for Hermite polynomials. Array size (dof,dof). First array index is the power of the variable, second array index is the order of the Hermite polynomial. Calculated at runtime.
sigq	$1/\sqrt{2}$	Conversion factor between q and real z
sigp	$1/\sqrt{2}$	Conversion factor between p and imag. z
im	i	Imaginary number
acf_ccf_flag	1 or 2	Flag for autocorrelation function (1) or cross-correlation function (2)
Pi	$4\arctan(1)$	Value of constant π
n_prtcls_fact	<real number>	Factorial of n_prtcles. Assigned at runtime.
filename	<string>	Name appended to output files. Assigned at runtime.

Table A.6: Additional parameters and constants found in the const.f90 file for CCS, 2LCCS and CCSB calculation program.

A.2.2 Input Parameters

The input parameters for the calculation are found in the input.dat file in the in/ directory and are shown in Table A.5. Variables of the same name as these parameters are found in the const.f90 file, to be used by various routines in the program. The const.f90 also contains other parameters and constants that are set as default and used by the program, but can be changed and the code recompiled. It also contains global variables that are used by various modules. These additional parameters and variables are shown in Table A.6, and examples of the parameters that may be changed include `as_lambda` and `bc_lambda`. The free particle, harmonic potential and Morse potential Hamiltonians were included to ensure the code was working correctly when first written.

A.2.3 Output

The program produces output files in the out/ directory, with three data output files generated by default: the initial coherent state basis, final coherent state basis, and cross-correlation function file. For the Bose-Einstein condensate problem, an additional 1-body density output file is generated. Files to automatically plot these quantities with gnuplot are also generated, one for the CCF, one for the FT (whose data is generated by a separate standalone program, discussed below), and two for the 1-body density: a space-time map as shown in Fig. 4.5, and an animated GIF of the density oscillations, for inspection. If the `bsout` flag is set to "Y", an output file for the basis during the propagation is produced to restart the calculation if it is stopped. A list of these files and their descriptions are shown in Table A.7, a number are appended with the `filename` parameter.

If the `reporting` flag is set to "Y", an additional output file is generated in the out/-dump/<`filename`> directory for the values of the trajectories, action and amplitudes at all times, alongside gnuplot files to plot them. A list of these files and their descriptions are shown in Table A.8.

File	Description
ccf_<filename>.out	Propagation time, real, imaginary and absolute values of the cross correlation function, and norm of the wavefunction
ft_<filename>.out	Fourier transform of the real part of the cross-correlation function, generated by separate standalone program
density_<filename>.out	1-body density for Bose-Einstein condensate Hamiltonian
basis_<filename>.out	Initial distribution of coherent state basis functions
final_basis_<filename>.out	Final distribution of coherent state basis functions
plotccf.gnu	Gnuplot plotting file to generate an .eps image of the cross-correlation function
plotft.gnu	Gnuplot plotting file to generate an .eps image of the Fourier transform spectrum
plot_density_map.gnu	Gnuplot plotting file to generate an .eps image of the space-time map of the 1-body density for the Bose-Einstein condensate Hamiltonian
plot_density_gif.gnu	Gnuplot plotting file to generate an animated .gif image of the 1-body density for the Bose-Einstein condensate Hamiltonian
outbs.out	If the `bsout` flag is set to "Y", output of the basis to enable the calculation to be restarted if it is stopped

Table A.7: Output files generated by the CCS, 2LCCS and CCSB calculation program

File	Description
var_dump.out	If `reporting` is set to "Y", output of trajectories, action and amplitudes throughout propagation in dump/<filename> directory
plot_traj_dof$m$.gnu	If `reporting` is set to "Y", gnuplot plotting file to plot evolution of trajectory m in dump/<filename> directory
plot_action.gnu	If `reporting` is set to "Y", gnuplot plotting file to plot evolution of action in dump/<filename> directory
plot_d_amps.gnu	If `reporting` is set to "Y", gnuplot plotting file to plot evolution of real vs imaginary d in dump/<filename> directory
plot_abs_d_amps.gnu	If `reporting` is set to "Y", gnuplot plotting file to plot evolution of $\|d\|$ in dump/<filename> directory
plot_bigD_amps.gnu	If `reporting` is set to "Y", gnuplot plotting file to plot evolution of real vs imaginary D in dump/<filename> directory
plot_abs_bigD_amps.gnu	If `reporting` is set to "Y", gnuplot plotting file to plot evolution of $\|D\|$ in dump/<filename> directory

Table A.8: Output files generated by the CCS, 2LCCS and CCSB calculation program if `reporting` is set to "Y".

Variable	Description
`z(dof,nbv,nconf)`	Coherent state basis function array $z_{ik}^{(m)}$ for 2L-CCS, and $z_k^{(m)}$ for CCS(B) with `nbv`=1
`d(nbv,nconf)`	2L-CCS amplitude array for d_{ik} For CCS(B) all elements are set to 1
`bigD(nconf)`	2L-CCS and CCS(B) amplitude vector D_k
`s(nbv,nconf)`	Classical action array s_{ik} for 2L-CCS, and S_k for CCS(B) with `nbv`=1
`H(nbv,nbv,nconf,nconf)`	Normal ordered Hamiltonian array $H^{\mathrm{ord}}(\mathbf{z}_{ik}^*, \mathbf{z}_{jl})$ for 2L-CCS, and $H^{\mathrm{ord}}(\mathbf{z}_k^*, \mathbf{z}_l)$ for CCS(B) with `nbv`=1
`ovrlp(nbv,nbv,nconf,nconf)`	Coherent states overlap array $\langle \mathbf{z}_{ik} \vert \mathbf{z}_{jl} \rangle$ for 2L-CCS, and $\langle \mathbf{z}_k \vert \mathbf{z}_l \rangle$ for CCS(B) with `nbv`=1
`density_fock(dof,dof)`	Density matrix array for CCSB $\rho^{(\alpha,\beta)}$ Unused for 2L-CCS
`psi0(dof)`	Initial wavepacket vector $\Psi(0)$
`t`	Propagation time
`norm`	Norm of wavefunction representation
`acf_ccf`	ACF or CCF depending on `acf_ccf_flag`
`restart`	Basis set regeneration flag (1=regenerate basis, 0=basis has been generated correctly)
`norm_fail_counter`	Counter for number of basis regenerations Terminates program when exceeds threshold

Table A.9: Variables and arrays used by the main.f90 file in the CCS, 2LCCS and CCSB calculation program.

A.2.4 Program Implementation

As the program written to conduct the 2L-CCS and CCSB calculations is significantly more complicated than that for the benchmark calculation, it is worthwhile to explain in further detail how various tasks are carried out in the source code.

A.2.4.1 Variables and Arrays

The key variables and arrays used by the program for the basis, Hamiltonian, and calculated quantities are defined in the main.f90 file. These are then passed to other modules and subroutines that perform various operations. These variables and arrays (with dimensions in terms of input parameters) are shown in Table A.9

```
subroutine gen_basis(z,d,bigD,ovrlp,psi0)

  implicit none

  complex(kind=8),intent(inout)::z(:,:,:) !coherent state array (dof,nbv,nconf)
  complex(kind=8),intent(inout)::d(:,:) !single config amplitude (nbv,nconf)
  complex(kind=8),intent(inout)::bigD(:) !multi config amplitude (nconf)
  complex(kind=8),intent(inout)::ovrlp(:,:,:,:) !Overlap <z1|z2> (nbv,nbv,nconf,
    nconf)
  complex(kind=8),intent(inout)::psi0(:) !Initial wavepacket (dof)

    select case (trim(sampling))
      case ("SWARM")
        call gen_z_swarm(z,psi0)
      case ("PANCAKE")
        call gen_z_pancake(z,psi0)
    end select

  call calc_ovrlp(ovrlp,z)

  call gen_d(d,z,ovrlp,psi0)
  call gen_bigD(bigD,z,d,ovrlp,psi0)

  return

end subroutine gen_basis
```

Listing A.1: Code for the `gen_basis` subroutine of the `basis` module

A.2.4.2 Basis Set Generation

Basis set generation is carried out in the `basis` module, with the process initiated from the `main` module with a call to the `gen_basis` subroutine shown in Listing A.1. This subroutine in turn calls subroutines for the generation of the coherent state basis and initial amplitudes.

The "PANCAKE" sampling type for coherent state generation is used for the asymmetric double well tunnelling problem in both 2L-CCS and CCSB, as there are two types of modes that are sampled via different distributions (tunnelling mode and bath modes). For both methods, the tunnelling mode is sampled from a Gaussian distribution centered around the initial tunnelling mode coordinates and momenta with compression parameter `sys_cmprss` ($\sigma^{(\mathrm{s})}$ in the main text). The `ZBQLNOR` external routine, part of LAPACK (Linear Algebra Package), [230] was used for this Gaussian distribution. The code snippet of its use is shown in Listing A.2, with the additional options of placing basis functions in the upper well of the double well potential, and using multiple degrees of freedom for the inner layer in 2L-CCS (neither of these options are exercised in the calculations presented in the main text, although the former is used in Appendix B).

For 2L-CCS, a random two bath modes per configuration are sampled from a Gaussian distribution with compression parameter `cmprss` ($\sigma^{(\mathrm{b})}$ in the main text), whilst all others remain at the origin, which is equivalent to sampling from a Gaussian distribution with infinite compression parameter. The code snippet for this process is shown in Listing A.3. For CCSB, the bath modes are sampled from separate gamma distributions for the ground and excited states respectively. The `ZBQLGAM` external routine, part of LAPACK, was used for this with compression parameter `cmprss` utilised for the excited states ($\sigma^{(2\alpha>0)}$ in the main text), whilst the compression parameter for the ground state is set to 1. The code

```
if (trim(method).eq."2LCCS") then !System part
  do m=1,sys_dof
    if ((m.eq.1).and.(as_upper_well_dim.ne.0).and.(uw_counter.lt.as_upper_well_dim)
    ) then !For upper well basis function sampling
      z(m,i,k) = cmplx((ZBQLNOR(real(-psi0(m)),sigq/sys_cmprss)),(ZBQLNOR(imag(-
    psi0(m)),sigp/sys_cmprss)),kind=8)
      uw_counter=uw_counter+1
    else
      z(m,i,k) = cmplx((ZBQLNOR(real(psi0(m)),sigq/sys_cmprss)),(ZBQLNOR(imag(psi0(
    m)),sigp/sys_cmprss)),kind=8)
    end if
  end do
else
  if ((as_upper_well_dim.ne.0).and.(uw_counter.lt.as_upper_well_dim)) then !For
    upper well basis function sampling
    z(1,1,k) = cmplx((ZBQLNOR(real(-psi0(1)),sigq/sys_cmprss)),(ZBQLNOR(imag(-psi0
    (1)),sigp/sys_cmprss)),kind=8)
    uw_counter=uw_counter+1
  else
    z(1,1,k) = cmplx((ZBQLNOR(real(psi0(1)),sigq/sys_cmprss)),(ZBQLNOR(imag(psi0(1)
    ),sigp/sys_cmprss)),kind=8)
  end if
end if
```

Listing A.2: Code for the Gaussian distribution of tunnelling mode coherent states in the asymmetric double well tunnelling problem for 2L-CCS and CCSB

```
m=1 !Define m=1 to loop over bath_sampling bath modes

do while (m.le.bath_sampling) !loop bath_sampling number of bath modes to be
    decompressed
  call random_number(rand_num)
  rand_mode = int(rand_num*(dof-1))+2
  if (z(rand_mode,i,k).ne.(0.d0,0.d0)) then
    cycle !if the random number is the same as previous (z already occupied) then
    cycle the loop to find another
  else
    z(rand_mode,:,k) = cmplx((ZBQLNOR(real(psi0(rand_mode)),sigq/(cmprss))),&
                             (ZBQLNOR(imag(psi0(rand_mode)),sigp/(cmprss))),kind=8)
    m=m+1
  end if
end do
```

Listing A.3: Code for the Gaussian distribution of bath mode coherent states in the asymmetric double well tunnelling problem for 2L-CCS

snippet for this is shown in Listing A.4.

The "SWARM" sampling type is used for the CCSB calculation of the model Bose-Einstein condensate problem, as well as the free particle, harmonic oscillator and Morse potential test examples in the code. The CCSB calculation uses separate gamma distributions for the ground and excited state levels, as with the second quantised asymmetric double well problem. The code for this is shown in Listing A.5, with compression parameter `cmprss` utilised for the excited states ($\sigma^{(\alpha>0)}$ in the main text), whilst the compression parameter for the ground state is set to 1.

The initial amplitudes are calculated according to Eqs. (3.3.2) and (3.3.3) for 2L-CCS applied to the asymmetric double well tunnelling problem, and Eqs. (4.4.10) and (4.5.17) for CCSB applied to the asymmetric double well tunnelling problem and model Bose-Einstein condensate problem, respectively. The code for the `gen_d` subroutine that calculates initial d amplitudes in 2L-CCS is shown in Listing A.6, where the routine sets them to 1 for CCS(B) calculations. The code for the `gen_bigD` subroutine that calculates initial

```
1 if (m.eq.2) then
2   call random_number(phase_fact)
3   z_abs = ZBQLGAM(n_prtcls+1.d0,1.d0)
4   z(m,:,k) = cmplx(sqrt(abs(z_abs))*cos(phase_fact*2.d0*Pi),sqrt(abs(z_abs))*sin(
      phase_fact*2.d0*Pi),kind=8)
5 else
6   call random_number(phase_fact)
7   z_abs = ZBQLGAM(1.d0,cmprss)
8   z(m,:,k) = cmplx(sqrt(abs(z_abs))*cos(phase_fact*2.d0*Pi),sqrt(abs(z_abs))*sin(
      phase_fact*2.d0*Pi),kind=8)
9 end if
```

Listing A.4: Code for the gamma distributions of bath mode coherent states in the asymmetric double well tunnelling problem for CCSB

```
1 call random_number(phase_fact)
2 if (m.eq.1) z_abs = ZBQLGAM(sys_cmprss*(n_prtcls+1.d0),sys_cmprss)
3 if (m.ne.1) z_abs = ZBQLGAM(1.d0,cmprss)
4 z(m,i,k) = cmplx(sqrt(abs(z_abs))*cos(phase_fact*2.d0*Pi),sqrt(abs(z_abs))*sin(
    phase_fact*2.d0*Pi),kind=8)
```

Listing A.5: Code for the gamma distributions of coherent states in the model Bose-Einstein condensate problem for CCSB

D amplitudes in 2L-CCS and CCSB is shown in Listing A.7, with different options for the different methods and systems studied. Both subroutines feature a call to `lineq`, which is in the `auxiliary` module and handles linear equation solving. This routine is shown in Listing A.8, it uses the `zgesv` external routine from LAPACK that computes the solution to a complex set of linear equations via LU decomposition.

```
subroutine gen_d(d,z,ovrlp,psi0)

  implicit none

  complex(kind=8),intent(inout)::d(:,:) !single config amplitude (nbv,nconf)
  complex(kind=8),intent(in)::z(:,:,:) !coherent state array (dof,nbv,nconf)
  complex(kind=8),intent(inout)::ovrlp(:,:,:,:) !Overlap <z1|z2> (nbv,nbv,nconf,
    nconf)
  complex(kind=8),intent(in)::psi0(:) !Initial wavefunction
  complex(kind=8),allocatable::c(:) !<z^q|Psi^q(0)> overlap for 2LCCS (nbv)
  integer::i,k

  if (trim(method).eq."CCS") then
    d(1,:) = (1.d0,0.d0)
  else if (trim(method).eq."2LCCS") then
    allocate(c(nbv))
    do k=1,size(d,2) !nconf
      do i=1,size(d,1) !nbv
        c(i) = exp(sum(conjg(z(1:sys_dof,i,k))*psi0(1:sys_dof)-0.5d0*(conjg(z(1:
    sys_dof,i,k))*z(1:sys_dof,i,k)&
              +conjg(psi0(1:sys_dof))*psi0(1:sys_dof))))
      end do
      call lineq(ovrlp(:,:,k,k),c,d(:,k))
    end do
    deallocate(c)
  end if

  return

end subroutine gen_d
```

Listing A.6: Code for the calculation of initial d amplitudes

```
subroutine gen_bigD(bigD,z,d,ovrlp,psi0)

  implicit none

  complex(kind=8),intent(inout)::bigD(:) !multi config amplitude (nconf)
  complex(kind=8),intent(in)::z(:,:,:) !coherent state array (dof,nbv,nconf)
  complex(kind=8),intent(in)::d(:,:) !single config amplitude (nbv,nconf)
  complex(kind=8),intent(in)::ovrlp(:,:,:,:) !Overlap <z1|z2> (nbv,nbv,nconf,nconf)
  complex(kind=8),intent(in)::psi0(:) !Initial wavepacket (dof)
  complex(kind=8),allocatable::C(:) !<z|Psi(0)> overlap (nconf)
  complex(kind=8),allocatable::LHS_bigD(:,:) !Overlap*d (nconf,nconf)
  integer::i,j,k,l

  allocate(C(size(bigD)),LHS_bigD(size(bigD),size(bigD)))
  C(:) = (0.d0,0.d0)
  LHS_bigD(:,:) = (0.d0,0.d0)

  do k=1,size(bigD) !nconf
    do i=1,size(z,2) !nbv(=1 for CCS)
      if (qsystem.eq.'2Q') then
        C(k) = C(k) + exp(sum(conjg(z(:,i,k))*psi0(:) - 0.5d0*(conjg(z(:,i,k))*z(:,
    i,k)+conjg(psi0(:))*psi0(:))))&
                    *conjg(z(2,i,k))**real(n_prtcls)/sqrt(n_prtcls_fact)
      else if (qsystem.eq.'BC') then
        C(k) = C(k) + exp(sum(-0.5d0*(conjg(z(:,i,k))*z(:,i,k))))&
```

```
25                      *conjg(z(1,i,k))**real(n_prtcls)/sqrt(n_prtcls_fact)
26        else
27          C(k) = C(k) + exp(sum(conjg(z(:,i,k))*psi0(:) - 0.5d0*(conjg(z(:,i,k))*z(:,
      i,k)+conjg(psi0(:))*psi0(:))))
28        end if
29      end do
30    end do
31
32    do l=1,size(ovrlp,4) !nconf
33      do k=1,size(ovrlp,3) !nconf
34        do j=1,size(ovrlp,2) !nbv (=1 for CCS)
35          do i=1,size(ovrlp,1) !nbv (=1 for CCS)
36            LHS_bigD(k,l) = LHS_bigD(k,l) + d(j,l)*ovrlp(i,j,k,l)
37          end do
38        end do
39      end do
40    end do
41
42    call lineq(LHS_bigD,C,bigD)
43
44    deallocate(C,LHS_bigD)
45
46    return
47
48  end subroutine gen_bigD
```

Listing A.7: Code for the calculation of initial D amplitudes

```
1   subroutine lineq(LHS,RHS,D) !Linear equation : LHS*D=RHS
2
3     implicit none
4
5     complex(kind=8),intent(in)::LHS(:,:) !left hand side of linear equation, usually
        coherent state overlap (nbv,nbv for d; nconf,nconf for D)
6     complex(kind=8),intent(inout)::RHS(:) !RHS of linear equation to calc amplitudes
        (nbv for d; nconf for D)
7     complex(kind=8),intent(inout)::D(:) !amplitude (nconf/nbv)
8     integer::N,NRHS,INFO !Parameters for zgesv routine
9     integer,allocatable::IPIV(:)
10    complex(kind=8),allocatable::LHS_temp(:,:) !Temp placeholder for LHS, as zgesv
        will overwrite its contents
11
12    N=size(RHS)
13    NRHS=1
14    INFO=0
15    allocate(IPIV(N),LHS_temp(size(LHS,1),size(LHS,2)))
16    LHS_temp(:,:)=LHS(:,:)
17
18    call zgesv(N,NRHS,LHS_temp,N,IPIV,RHS,N,INFO)
19
20    D=RHS      !zgesv routine assigns the answer, D to the RHS input array
21
22    deallocate(IPIV,LHS_temp)
23
24    return
25
26  end subroutine lineq
```

Listing A.8: Code for the subroutine that handles linear equation solving

A.2.4.3 Basis Set Propagation

Propagation of the trajectories, action, and amplitudes in the basis is achieved via the Runge-Kutta 4th order (RK4) method of numerical integration. For a function y, where its initial value and time-dependence is known, $y(t_n) = y_n$ and $\dot{y} = f(y,t)$, the RK4 method propagates it to find $y(t_n + \mathrm{d}t) = y(t_{n+1}) = y_{n+1}$ via

$$y_{n+1} = y_n + \frac{\mathrm{d}t}{6}(k_1 + 2k_2 + 2k_3 + k_4) \tag{A1.2.1}$$

where

$$k_1 = f(y_n, t_n) \tag{A1.2.2a}$$
$$k_2 = f\left(y_n + k_1\frac{\mathrm{d}t}{2}, t_n + \frac{\mathrm{d}t}{2}\right) \tag{A1.2.2b}$$
$$k_3 = f\left(y_n + k_2\frac{\mathrm{d}t}{2}, t_n + \frac{\mathrm{d}t}{2}\right) \tag{A1.2.2c}$$
$$k_4 = f(y_n + \mathrm{d}t k_3, t_n + \mathrm{d}t). \tag{A1.2.2d}$$

This is conducted in the program via a call to the `rk4_prop` subroutine in the `propagation` module from the `main` module. This subroutine is shown in Listing A.9 and features calls to the `derivs` subroutine in the `propagation` module, shown in Listing A.10. This `derivs` subroutine in turn calls the subroutines for calculation of Hamiltonian matrix elements; Hamiltonian coherent state derivative; overlap of coherent states; and time-derivatives of trajectories, action, and amplitudes. For the latter, the calculation of the time-derivatives of amplitudes features a call to the `lineq` subroutine shown in Listing A.8 that solves the linear systems in Eqs. (1.3.31), (3.2.6) and (3.2.8). The time-derivatives subroutines are contained within the `propagation` module, the coherent state overlap is calculated in the `auxiliary` module, and the matrix elements of the Hamiltonian and the coherent state derivatives of the Hamiltonian are calculated within the `hamiltonian` module. The source code for the majority of these routines is relatively straightforward, and therefore will not be presented for brevity. However, the calculation of the Dirac delta matrix elements `bc_W_mnop` in the Bose-Einstein condensate Hamiltonian given by Eq. (4.5.15) is slightly more involved, so this will be discussed below.

```
subroutine rk4_prop(z,d,bigD,s,ovrlp,H)

  implicit none

  complex(kind=8),intent(inout)::z(:,:,:) !coherent state array (dof,nbv,nconf)
  complex(kind=8),intent(inout)::d(:,:) !single config amplitude (nbv,nconf)
  complex(kind=8),intent(inout)::bigD(:) !multi config amplitude (nconf)
  real(kind=8),intent(inout)::s(:,:) !action (nvb,nconf)
  complex(kind=8),intent(inout)::ovrlp(:,:,:,:) !Overlap <z1|z2> (nbv,nbv,nconf,
    nconf)
  complex(kind=8),intent(inout)::H(:,:,:,:) !Hamiltonian (nbv,nbv,nconf,nconf)
  complex(kind=8),allocatable::dHdz(:,:,:,:) !Hamiltonian derivative (dof,nbv,nbv,
    nconf)
  complex(kind=8),allocatable::dzdt(:,:,:) !Time derivative of z (dof,nbv,nconf)
  complex(kind=8),allocatable::dddt(:,:) !Time derivative of d (nbv,nconf)
  complex(kind=8),allocatable::dbigDdt(:) !Time derivateive of bigD (nconf)
  real(kind=8),allocatable::dsdt(:,:) !Time derivative of s (nbv,nconf)
  complex(kind=8),allocatable::k_z(:,:,:,:) !Runge-Kutta increments of z (dof,nbv,
    nconf,inc) where inc is k1, k2 etc
  complex(kind=8),allocatable::k_d(:,:,:) !Runge-Kutta increments of d (nbv,nconf,
    inc) where inc is k1, k2 etc
  complex(kind=8),allocatable::k_bigD(:,:) !Runge-Kutta increments of bigD (nconf,
    inc) where inc is k1, k2 etc
  real(kind=8),allocatable::k_s(:,:,:) !Runge-Kutta increments of s (nbv,nconf,inc)
     where inc is k1, k2 etc
  complex(kind=8),allocatable::z_new(:,:,:) !Runge-Kutta temp variable for coherent
     state array (dof,nbv,nconf)
  complex(kind=8),allocatable::d_new(:,:) !Runge-Kutta temp variable for factored
    single config amplitude (nbv,nconf)
  complex(kind=8),allocatable::bigD_new(:) !Runge-Kutta temp variable for multi
    config amplitude (nconf)
  real(kind=8),allocatable::s_new(:,:) !Runge-Kutta temp variable for action (nvb,
    nconf)

  allocate(dHdz(size(z,1),size(z,2),size(z,2),size(z,3)))
  allocate(dzdt(size(z,1),size(z,2),size(z,3)),dddt(size(d,1),size(d,2)),dbigDdt(
    size(bigD)),dsdt(size(s,1),size(s,2)))
  allocate(k_z(size(z,1),size(z,2),size(z,3),4),k_d(size(d,1),size(d,2),4),k_bigD(
    size(bigD),4),k_s(size(s,1),size(s,2),4))
  allocate(z_new(size(z,1),size(z,2),size(z,3)),d_new(size(d,1),size(d,2)),bigD_new
    (size(bigD)),s_new(size(s,1),size(s,2)))

  z_new(:,:,:) = z(:,:,:)
  d_new(:,:) = d(:,:)
  s_new(:,:) = s(:,:)
  bigD_new(:) = bigD(:)

  call derivs(z_new,d_new,bigD_new,s_new,dzdt,dddt,dbigDdt,dsdt,ovrlp,H,dHdz)

  k_z(:,:,:,1) = dzdt(:,:,:)
  k_d(:,:,1) = dddt(:,:)
  k_s(:,:,1) = dsdt(:,:)
  k_bigD(:,1) = dbigDdt(:)

  z_new(:,:,:) = z(:,:,:) + dt/2.d0*k_z(:,:,:,1)
  d_new(:,:) = d(:,:) + dt/2.d0*k_d(:,:,1)
  s_new(:,:) = s(:,:) + dt/2.d0*k_s(:,:,1)
  bigD_new(:) = bigD(:) + dt/2.d0*k_bigD(:,1)
```

```
46
47    call derivs(z_new,d_new,bigD_new,s_new,dzdt,dddt,dbigDdt,dsdt,ovrlp,H,dHdz)
48
49    k_z(:,:,:,2) = dzdt(:,:,:)
50    k_d(:,:,2) = dddt(:,:)
51    k_bigD(:,2) = dbigDdt(:)
52    k_s(:,:,2) = dsdt(:,:)
53
54    z_new(:,:,:) = z(:,:,:) + dt/2.d0*k_z(:,:,:,2)
55    d_new(:,:) = d(:,:) + dt/2.d0*k_d(:,:,2)
56    s_new(:,:) = s(:,:) + dt/2.d0*k_s(:,:,2)
57    bigD_new(:) = bigD(:) + dt/2.d0*k_bigD(:,2)
58
59    call derivs(z_new,d_new,bigD_new,s_new,dzdt,dddt,dbigDdt,dsdt,ovrlp,H,dHdz)
60
61    k_z(:,:,:,3) = dzdt(:,:,:)
62    k_d(:,:,3) = dddt(:,:)
63    k_bigD(:,3) = dbigDdt(:)
64    k_s(:,:,3) = dsdt(:,:)
65
66    z_new(:,:,:) = z(:,:,:) + dt*k_z(:,:,:,3)
67    d_new(:,:) = d(:,:) + dt*k_d(:,:,3)
68    s_new(:,:) = s(:,:) + dt*k_s(:,:,3)
69    bigD_new(:) = bigD(:) + dt*k_bigD(:,3)
70
71    call derivs(z_new,d_new,bigD_new,s_new,dzdt,dddt,dbigDdt,dsdt,ovrlp,H,dHdz)
72
73    k_z(:,:,:,4) = dzdt(:,:,:)
74    k_d(:,:,4) = dddt(:,:)
75    k_bigD(:,4) = dbigDdt(:)
76    k_s(:,:,4) = dsdt(:,:)
77
78    z(:,:,:) = z(:,:,:) + dt/6.d0*(k_z(:,:,:,1)+2.d0*k_z(:,:,:,2)+2.d0*k_z(:,:,:,3)+
        k_z(:,:,:,4))
79    d(:,:) = d(:,:) + dt/6.d0*(k_d(:,:,1)+2.d0*k_d(:,:,2)+2.d0*k_d(:,:,3)+k_d(:,:,4))
80    s(:,:) = s(:,:) + dt/6.d0*(k_s(:,:,1)+2.d0*k_s(:,:,2)+2.d0*k_s(:,:,3)+k_s(:,:,4))
81    bigD(:) = bigD(:) + dt/6.d0*(k_bigD(:,1)+2.d0*k_bigD(:,2)+2.d0*k_bigD(:,3)+k_bigD
        (:,4))
82
83    deallocate(dzdt,dddt,dsdt,dbigDdt,k_z,k_d,k_s,k_bigD,z_new,d_new,s_new,bigD_new,
        dHdz)
84
85    return
86
87  end subroutine rk4_prop
```

Listing A.9: Code for the subroutine that conducts the RK4 numerical integration to propagate the wavefunction

```
subroutine derivs(z,d,bigD,s,dzdt,dddt,dbigDdt,dsdt,ovrlp,H,dHdz)

  implicit none

  complex(kind=8),intent(inout)::z(:,:,:) !coherent state array (dof,nbv,nconf)
  complex(kind=8),intent(inout)::d(:,:) !single config amplitude (nbv,nconf)
  complex(kind=8),intent(inout)::bigD(:) !multi config amplitude (nconf)
  real(kind=8),intent(inout)::s(:,:) !action (nvb,nconf)
  complex(kind=8),intent(inout)::dzdt(:,:,:) !Time derivative of z (dof,nbv,nconf)
  complex(kind=8),intent(inout)::dddt(:,:) !Time derivative of d (nbv,nconf)
  complex(kind=8),intent(inout)::dbigDdt(:) !Time derivateive of bigD (nconf)
  real(kind=8),intent(inout)::dsdt(:,:) !Time derivative of s (nbv,nconf)
  complex(kind=8),intent(inout)::ovrlp(:,:,:,:) !Overlap <z1|z2> (nbv,nbv,nconf,
    nconf)
  complex(kind=8),intent(inout)::H(:,:,:,:) !Hamiltonian (nbv,nbv,nconf,nconf)
  complex(kind=8),intent(inout)::dHdz(:,:,:,:) !Hamiltonian derivative (dof,nbv,nbv
    ,nconf)

  call calc_H(H,z)

  call calc_dHdz(dHdz,z)

  call calc_ovrlp(ovrlp,z)

  call calc_dzdt(dzdt,d,s,dHdz,ovrlp)

  call calc_dddt(dddt,dzdt,z,d,s,ovrlp,H)

  call calc_dsdt(dsdt,dzdt,z,H)

  call calc_dbigDdt(dbigDdt,dzdt,dddt,z,d,bigD,s,ovrlp,H)

  return

end subroutine derivs
```

Listing A.10: Code for the subroutine that handles calculation of the time-derivatives of basis set elements

The `bc_W_mnop` matrix is set via a call to the `calc_bc_W_mnop` subroutine in the `auxiliary` module, shown in Listing A.11. This is conducted after reading the initial parameters in the `main` module, as the size of the array depends on the `dof` parameter. After `bc_W_mnop` is initially set, it remains unchanged for the duration of the calculation. The `calc_hermite_int` function that the `calc_bc_W_mnop` subroutine uses calculates the integral of the product of 4 Hermite polynomials, shown in the parenthesis of Eq. (4.5.15). The code for this function is shown in Listing A.12.

The coefficients for the Hermite polynomials, stored in the `hermite_coeff` array, are calculated via a prior call from the `main` module to the `calc_hermite_coeff` subroutine in the `auxiliary` module. The code for this is shown in Listing A.13. The code uses the fact that for a Hermite polynomial $He^{(\alpha)}(\mathbf{Q})$ of order α, the coefficient for the highest power of the variable $\mathbf{Q}$ will be 2^{α}. Then the following recurrence relationship is used to generate the coefficients a_n for the preceding powers of $\mathbf{Q}$

$$a_n = \frac{(n+2)(n+1)}{2(n-\alpha)} a_{n+2} \tag{A1.2.3}$$

where $n = 1, 3, \ldots, (\alpha - 2)$ if α is odd, and $n = 0, 2, \ldots, (\alpha - 2)$ if α is even.

```
subroutine calc_bc_W_mnop

  implicit none

  integer::m,n,o,p

  bc_W_mnop(:,:,:,:) = 0.d0

  do p=1,size(bc_W_mnop,4) !dof
    do o=1,size(bc_W_mnop,3) !dof
      do n=1,size(bc_W_mnop,2) !dof
        do m=1,size(bc_W_mnop,1) !dof
          if (mod(((p-1)+(o-1)+(n-1)+(m-1)),2).eq.0) then !Only even overall
    functions will integrate out to nonzero matrix elements
            bc_W_mnop(m,n,o,p) = 1/Pi&
            *1/sqrt(real(2.d0**(m-1),kind=8)*calc_factorial(m-1))&
            *1/sqrt(real(2.d0**(n-1),kind=8)*calc_factorial(n-1))&
            *1/sqrt(real(2.d0**(o-1),kind=8)*calc_factorial(o-1))&
            *1/sqrt(real(2.d0**(p-1),kind=8)*calc_factorial(p-1))&
            *calc_hermite_int(m,n,o,p)
          end if
        end do
      end do
    end do
  end do

  return

end subroutine calc_bc_W_mnop
```

Listing A.11: Code for the subroutine that calculates the Dirac delta matrix elements

```
function calc_hermite_int(m,n,o,p)

  integer,intent(in)::m,n,o,p !Order of the Hermite polynomials
  real(kind=8)::calc_hermite_int !Function to calculate the integral of the product
     of Hermites
  real(kind=8),allocatable::hermite_prod_coeff(:) !Array for product of 4 Hermite
    polynomial coefficients (power of x)
  integer::pow_x_m,pow_x_n,pow_x_o,pow_x_p
  integer::high_pow_x,pow_x

  high_pow_x = (m-1)+(n-1)+(o-1)+(p-1)+1 !Highest power of x (+1) for this
    combination of Hermite polynomials (+-1 involved as array index = power+1)

  allocate(hermite_prod_coeff(high_pow_x)) !Allocate the array for the coefficients
     of the product of 4 Hermite polynomials to be the largest power of x possible
    for that combination

  hermite_prod_coeff(:) = 0.d0

  calc_hermite_int = 0.d0

  do pow_x_p=1,p
    do pow_x_o=1,o
      do pow_x_n=1,n
        do pow_x_m=1,m
          hermite_prod_coeff((pow_x_m-1)+(pow_x_n-1)+(pow_x_o-1)+(pow_x_p-1)+1)=&
```

```
22          hermite_prod_coeff((pow_x_m-1)+(pow_x_n-1)+(pow_x_o-1)+(pow_x_p-1)+1)+
    hermite_coeff(pow_x_m,m)*hermite_coeff(pow_x_n,n)&
23          *hermite_coeff(pow_x_o,o)*hermite_coeff(pow_x_p,p)
24        end do
25      end do
26    end do
27  end do
28
29  calc_hermite_int = hermite_prod_coeff(1)*sqrt(Pi/2.d0) !0 state
30
31  do pow_x = (high_pow_x-1)/2,1,-1 !pow_x is actual power of x in product of
    hermite polynomials, not array index
32    calc_hermite_int = calc_hermite_int+sqrt(Pi/2.d0)/(real(4.d0**pow_x,kind=8))*
    calc_factorial(2*pow_x)&
33    /real(2.d0**pow_x,kind=8)/calc_factorial(pow_x)& !relationship between double
    factorial and single
34    *hermite_prod_coeff(2*pow_x+1) !plus 1 because array starts at 1
35  end do
36
37  deallocate(hermite_prod_coeff)
38
39  return
40
41 end function calc_hermite_int
```

Listing A.12: Code for the function that calculates the integral of the product of 4 Hermite polynomials

```
1  subroutine calc_hermite_coeff !To calculate array of hermite coefficients
2
3    implicit none
4
5    integer::m,pow_x
6
7    hermite_coeff(:,:) = 0.d0 !Set array initally to zero, then only change non-zero
     elements
8
9    do m=1,size(hermite_coeff,2) !order of Hermite
10     do pow_x=m,1,-2 !Loop counter -2 as hermite function powers will either be all
       even or all odd
11       if (pow_x.eq.m) then
12         hermite_coeff(pow_x,m) = real(2.d0**(pow_x-1),kind=8) !coefficient for
       largest power is 2^Hermite_order. Minus 1 because array index is one greater
       than power of x (can't have array index 0)
13       else
14         hermite_coeff(pow_x,m) = (pow_x+1.d0)*pow_x/(2.d0*(pow_x-m))*hermite_coeff(
       pow_x+2,m) !Recurrance relation for generating hermite polynomial coefficients
       from the largest power
15       end if
16     end do
17   end do
18
19   return
20
21 end subroutine calc_hermite_coeff
```

Listing A.13: Code to calculate the array that stores the coefficients of Hermite polynomials

```
1  subroutine gen_filename()
2
3    implicit none
4
5    character(len=10)::nconf_char,nbv_char,dof_char,cmprss_char,plot_low_char,
       plot_high_char,ndof_char
6    character(len=100)::cmprss_char_tmp
7
8    write(nconf_char,"(i0)")nconf
9    write(nbv_char,"(i0)")nbv
10   write(ndof_char,"(i0)")dof
11   write(cmprss_char_tmp,"(ES100.10E2)")real(cmprss,kind=4)
12
13   cmprss_char = cmprss_char_tmp((101-len(trim(adjustl(cmprss_char_tmp)))):(104-len(
       trim(adjustl(cmprss_char_tmp)))))&
14                                 //cmprss_char_tmp(97:100)
15
16   filename = trim(method)//"_"//trim(qsystem)//"_"//trim(ndof_char)//"dof_"//trim(
       nconf_char)//"conf_"&
17             //trim(nbv_char)//"bv_"//trim(cmprss_char)//"cmprss"
18
19   return
20
21 end subroutine gen_filename
```

Listing A.14: Code for the subroutine that generates the `filename` parameter to label output files

A.2.4.4 Output Generation

The output files documented in Tables A.7 and A.8 are generated in the `outputs` module. The `filename` parameter appended to a number of them is generated with the `gen_filename` subroutine, shown in Listing A.14. It labels the output files with various calculation parameters to identify them.

The data for the output files, namely the CCF for the double well tunnelling problem, and 1-body reduced density for the Bose-Einstein condensate problem, is generated in the `auxiliary` module. For the former, the CCF is calculated via the `calc_acf_ccf` function shown in Listing A.15 and stored in the `acf_ccf` variable in the `main` module. This variable is passed to the `outputs` module to be written to file. For the latter, the 1-body reduced density is calculated via a call from the `outputs` module to the `calc_density_1_body` function, shown in Listing A.16. This function takes position `x` as an input, and there is a loop over a range of values for `x` in the `outputs` module. The `calc_density_1_body` function converts from the density matrix in the Fock basis to the position basis according to Eq. (4.5.20). The density matrix in the Fock basis is calculated according to Eq. (4.5.19), and in the program it is obtained via a call to the `calc_density_fock` subroutine from the `main` module, and stored in the `density_fock` array. The `calc_density_1_body` function also features a call to the `hermite` function, that evaluates a Hermite polynomial of a given order at position `x`, and utilises the Hermite coefficients calculated in Listing A.13 and stored in the `hermite_coeff` array.

For the asymmetric double well problem, the FT spectrum is calculated via a separate standalone program fourier.exe in the bin/ directory that performs a discrete Fourier transform on the real part of the CCF. The code for this program is shown in Listing A.17. It takes the starting frequency and end frequency of the spectrum as input, as well as the

propagation time, timestep and name of the CCF output file, and outputs the FT to file as detailed in Table A.7.

```
function calc_acf_ccf(z,d,bigD,s,ovrlp,psi0)

  implicit none

  complex(kind=8),intent(in)::z(:,:,:) !coherent state array (dof,nbv,nconf)
  complex(kind=8),intent(in)::d(:,:) !single config amplitude (nbv,nconf)
  complex(kind=8),intent(in)::bigD(:) !multi config amplitude (nconf)
  real(kind=8),intent(in)::s(:,:) !action (nvb,nconf)
  complex(kind=8),intent(in)::ovrlp(:,:,:,:) !Overlap <z1|z2> (nbv,nbv,nconf,nconf)
  complex(kind=8),intent(in)::psi0(:) !Initial wavepacket (dof)
  complex(kind=8),allocatable::temp_psi0(:) !Temp variable for psi0 so it doesn't
    get changed
  complex(kind=8)::calc_acf_ccf
  integer::i,k

  allocate(temp_psi0(size(psi0)))

  calc_acf_ccf=(0.d0,0.d0)

  temp_psi0(:) = psi0(:)

  if (acf_ccf_flag.eq.2) temp_psi0(:)=-psi0(:) !If CCF, make initial wavepacket its
     mirror image

  do k=1,size(z,3) !nconf
    do i=1,size(z,2) !nbv (=1 for CCS)
      if (qsystem.eq.'2Q') then
        calc_acf_ccf = calc_acf_ccf + exp(sum(conjg(temp_psi0(:))*z(:,i,k)-0.5d0*(
    conjg(temp_psi0(:))*temp_psi0(:)&
                                    +conjg(z(:,i,k))*z(:,i,k))))*d(i,k)*exp(im*s(i
    ,k))*bigD(k)&
                                    *z(2,i,k)**real(n_prtcls)/sqrt(n_prtcls_fact)
    !Extra bit due to second quantisation
      else
        calc_acf_ccf = calc_acf_ccf + exp(sum(conjg(temp_psi0(:))*z(:,i,k)-0.5d0*(
    conjg(temp_psi0(:))*temp_psi0(:)&
                                   + conjg(z(:,i,k))*z(:,i,k))))*d(i,k)*exp(im*s(i
    ,k))*bigD(k)
      end if
    end do
  end do

  deallocate(temp_psi0)

  return

end function calc_acf_ccf
```

Listing A.15: Code for the function used to calculate the cross-correlation function in the asymmetric double well problem

```
function calc_density_1_body(x,density_fock)

  implicit none

  real(kind=8),intent(inout)::x !x coordinate for the 1 body density element you are calculating
  complex(kind=8),intent(in)::density_fock(:,:) !Density indexed in terms of HO levels = <Psi | a* a |Psi>
  complex(kind=8)::calc_density_1_body !1 body density, in terms of coordinate
  integer::m,n

  calc_density_1_body = cmplx(0.d0,0.d0)

  do n=1,size(density_fock,2)
    do m=1,size(density_fock,1)
      calc_density_1_body = calc_density_1_body + 1/sqrt(2**(m-1)*calc_factorial(m-1))*(1/sqrt(Pi))**0.25d0*exp(-(x**2.d0)/2.d0)&
                            *hermite(m-1,x)*density_fock(m,n)&
                            *1/sqrt(2**(n-1)*calc_factorial(n-1))*(1/sqrt(Pi))**0.25d0*exp(-(x**2.d0)/2.d0)*hermite(n-1,x)
    end do
  end do

  return

end function calc_density_1_body
```

Listing A.16: Code to calculate the 1-body density for the Bose-Einstein condensate problem

```
program fourier


  implicit none
  real(kind=8)::reCCF,t,omega,dt,dft,omega_end,time_end
  complex(kind=8)::im,fourier_sum
  character(len=10)::omega_start_char,omega_end_char,time_end_char,dt_char
  character(len=100)::filename
  integer::r

  if (IARGC().ne.5) then
     print*, "Arguments should be starting frequency, end frequency, time, timestep and filename"
     stop
  end if

  call getarg(1,omega_start_char)
  call getarg(2,omega_end_char)
  call getarg(3,time_end_char)
  call getarg(4,dt_char)
  call getarg(5,filename)

  read(omega_start_char,*)omega
  read(omega_end_char,*)omega_end
  read(time_end_char,*)time_end
  read(dt_char,*)dt

  open(410,file="../out/"//trim(filename))
```

```
28
29    open(411,file="../out/ft"//trim(filename(4:)))
30
31    dft=0.05d0
32    im=cmplx(0.d0,1.d0)
33
34    do while(omega.le.omega_end)
35      fourier_sum=cmplx(0.d0,0.d0)
36      read(410,*)
37      read(410,*)
38      read(410,*)
39      do r=1,int(time_end/dt+1)
40        read(410,*)t,reCCF
41        fourier_sum = fourier_sum + cdexp(-im*omega*t) * reCCF * dt
42      end do
43
44      rewind(410)
45      write(411,*)omega,real(fourier_sum)
46
47      omega=omega+dft
48
49    end do
50
51    close(410)
52    close(411)
53
54    stop
55
56  end program fourier
```

Listing A.17: Code for the standalone Fourier transform program that computes the FT spectra for the asymmetric double well tunnelling problem

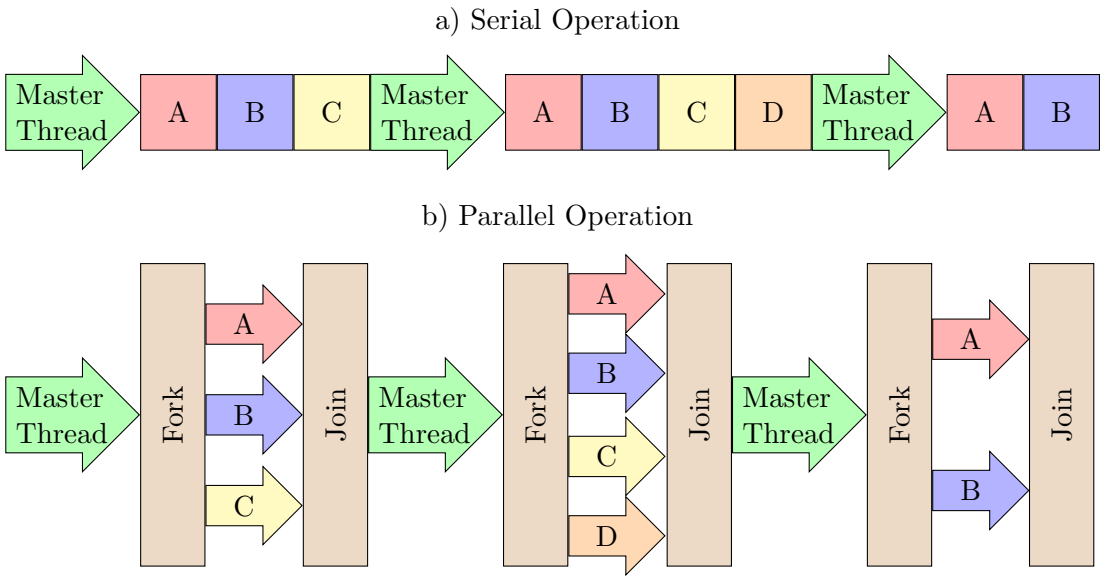

Figure A.4: Illustration of the difference between an a) serial process and b) parallel process that uses the fork-join model.

A.2.4.5 Parallelisation

Parallel computing consists of the execution of multiple calculations simultaneously on multiple processing threads. There are two main methods of achieving this: using a shared memory architecture, such as OpenMP (Open Multi-Processing); and using a distributed memory architecture, such as MPI (Message Passing Interface). In the shared memory architecture, all threads involved in the parallelisation have access to the same data stored in memory. This means that independent processes may be carried out concurrently without messages being passed between them. In the distributed memory architecture, the data is spread out amongst many memory locations, and messages must be passed between separate threads to transfer data from one thread to another. Generally, the shared memory architecture is capable of fewer parallel processes than the distributed memory architecture. In a high performance computing environment, there are interconnected nodes of processors each with their own memory store. The shared memory architecture will be possible on only one of these nodes, whilst the distributed memory architecture will be possible between nodes. The shared memory architecture is generally easier to implement than the distributed memory architecture as it requires minimal alteration to the serial code, so OpenMP was chosen to parallelise the 2L-CCS/CCS(B) program.

The OpenMP scheme consists of a "fork–join" model, where a master thread runs a controlling serial process, before approaching a region where parallel calculations are possible. At this parallel region multiple threads fork off from the master thread and then rejoin the master thread when the parallel region is complete. This is illustrated in Fig. A.4. In OpenMP the directives `!$omp parallel` and `!$omp end parallel` are used to initiate and terminate this fork-join process, and they appear above and below the region in the serial code that is being parallelised, respectively. Within the parallel region variables may be declared as `shared` if they are able to be viewed and modified by

```
!$omp parallel shared(temp_psi0,z,d,s,bigD) private(i,k) reduction(+:calc_acf_ccf)
!$omp do collapse(2)
do k=1,size(z,3) !nconf
  do i=1,size(z,2) !nbv (=1 for CCS)
    if (qsystem.eq.'2Q') then
      calc_acf_ccf = calc_acf_ccf + exp(sum(conjg(temp_psi0(:))*z(:,i,k)-0.5d0*(
    conjg(temp_psi0(:))*temp_psi0(:)&
                                     +conjg(z(:,i,k))*z(:,i,k))))*d(i,k)*exp(im*s(i,k
    ))*bigD(k)&
                                     *z(2,i,k)**real(n_prtcls)/sqrt(n_prtcls_fact)
     !Extra bit due to second quantisation
    else
      calc_acf_ccf = calc_acf_ccf + exp(sum(conjg(temp_psi0(:))*z(:,i,k)-0.5d0*(
    conjg(temp_psi0(:))*temp_psi0(:)&
                                    + conjg(z(:,i,k))*z(:,i,k))))*d(i,k)*exp(im*s(i,k
    ))*bigD(k)
    end if
  end do
end do
!$omp end do
!$omp end parallel
```

Listing A.18: Code for the parallelisation of the function used to calculate the cross-correlation function in the asymmetric double well problem

all threads, or `private` if every thread should have its own copy of the variable.

All of the parallel regions in the 2L-CCS/CCS(B) code feature a `do` loop, which is parallelised by the `!$omp do` and `!$omp end do` directives. Perfectly nested loops may be parallelised via the `collapse(n)` directive, where `n` is the number of nested loops that should be included. When a loop is performing an associative operation on a variable, such as an addition, the `reduction` directive may be applied to that variable to collate all values obtained by individual threads once the parallel region is complete. An example of all these directives is shown in Listing A.18, as they have been applied to the serial code for the `calc_acf_ccf` function shown in Listing A.15.

As well as the implementation of OpenMP directives in the code, parallelised LAPACK routines were used courtesy of the Intel Math Kernel Library. [231,232] All of these parallel modifications lead to near perfect speedup of the code, demonstrated in Sec. 3.3.2.3. MPI parallelisation may be considered in future applications that require further speedup.

Appendix B

Additional CCSB Calculations for the Double Well Tunnelling Problem

As discussed in Sec. 4.4, the $M = 80$, $\lambda = 0.1$ and $M = 20$, $\lambda = 0.2$ calculations for the second quantised double well tunnelling problem were not as well matched to the benchmark result as the $M = 20$, $\lambda = 0.1$ and $M = 40$, $\lambda = 0.1$ cases. Additional calculations were performed to attempt to converge these problematic cases with limited success. It was mentioned in the section that a large contribution to the accuracy of a CCS calculation depends upon the initial conditions chosen, therefore a number of different input parameters were selected to attempt to improve the accuracy. These included: an increased number of configurations K and harmonic oscillator excited levels in the basis Ω; altering the $\sigma^{(2\alpha>0)}$ and $\sigma^{(\mathrm{s})}$ compression parameters; using variable compression parameters for excited levels in the bath, with smaller compression parameters for lower levels as they are more likely to be occupied; and placing basis functions for the tunnelling mode in the upper well of the double well potential to compensate for any trajectories that may not effectively take the basis there over the course of the calculation. When one parameter was altered, the rest were kept fixed at the value used in Sec. 4.4 unless otherwise stated. The results from these with brief comment are shown below.

B.1 80D $\lambda = 0.1$

B.1.1 Altering the Number of Configurations in the Basis

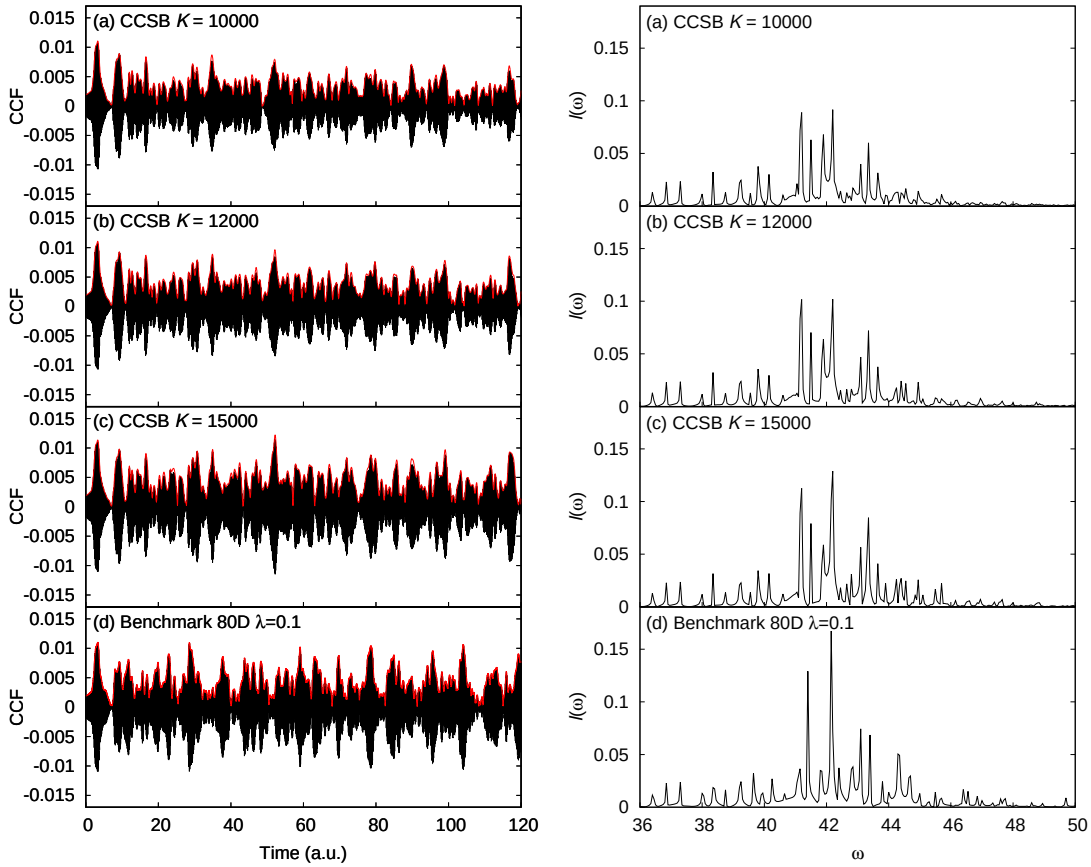

Figure B.1: Comparison to the benchmark of the cross-correlation functions (left, real parts in black and absolute values in red) and Fourier transforms of the real part (right) for $M = 80$ and $\lambda = 0.1$ CCSB calculations with different numbers of configurations K.

The effect of changing the number of configurations K for $M = 80$, $\lambda = 0.1$ CCSB calculations is illustrated in Fig. B.1. The $K = 12000$ calculation in panel (b) was presented in Sec. 4.4.3.3. It can be seen that the amplitude of the CCF in the $K = 10000$ case in panel (a) decays slightly quicker than the $K = 12000$ case, resulting in a slightly less intense FT spectrum. The amplitude of the CCF in the $K = 15000$ case in panel (c) decays more slowly than the $K = 12000$ case, however the oscillations are not more closely matched to the benchmark. This slower decay of the CCF results in a FT spectrum that is slightly more intense, in particular the main peak at $\omega = 42$. However, there is limited other difference despite being a much more expensive calculation.

B.1.2 Altering the Number of Excited Levels in the Basis

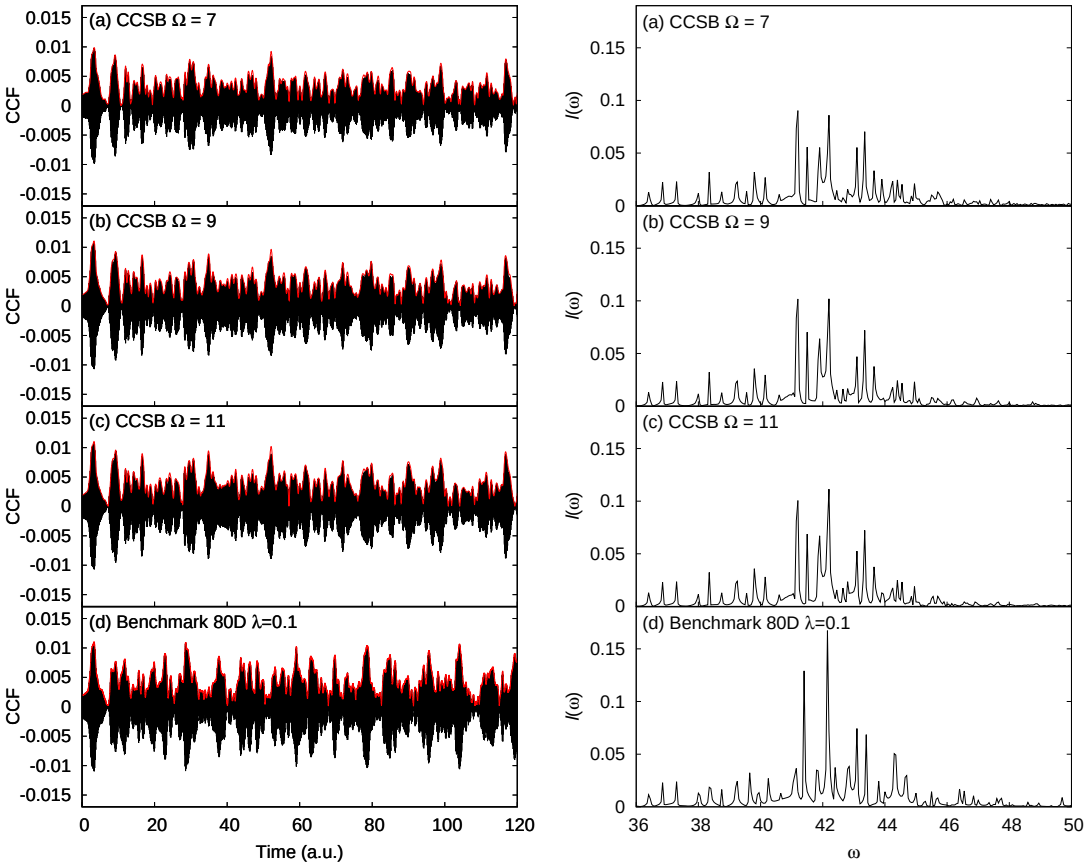

Figure B.2: Comparison to the benchmark of the cross-correlation functions (left, real parts in black and absolute values in red) and Fourier transforms of the real part (right) for $M = 80$ and $\lambda = 0.1$ CCSB calculations with different numbers of excited levels Ω.

The effect of changing the number of excited levels Ω for $M = 80$, $\lambda = 0.1$ CCSB calculations is illustrated in Fig. B.2. The $\Omega = 9$ calculation in panel (b) was presented in Sec. 4.4.3.3. It can be seen that when $\Omega = 7$ in panel (a) the amplitude of the CCF decays slightly quicker than when $\Omega = 9$, resulting in a slightly less intense FT spectrum. When $\Omega = 11$ in panel (c) there is virtually no difference to when $\Omega = 9$, so it can be concluded that increases in the number of excited levels in the basis beyond $\Omega = 9$ will lead to no improvement in the calculation.

B.1.3 Altering the Excited Level Sampling Compression Parameter

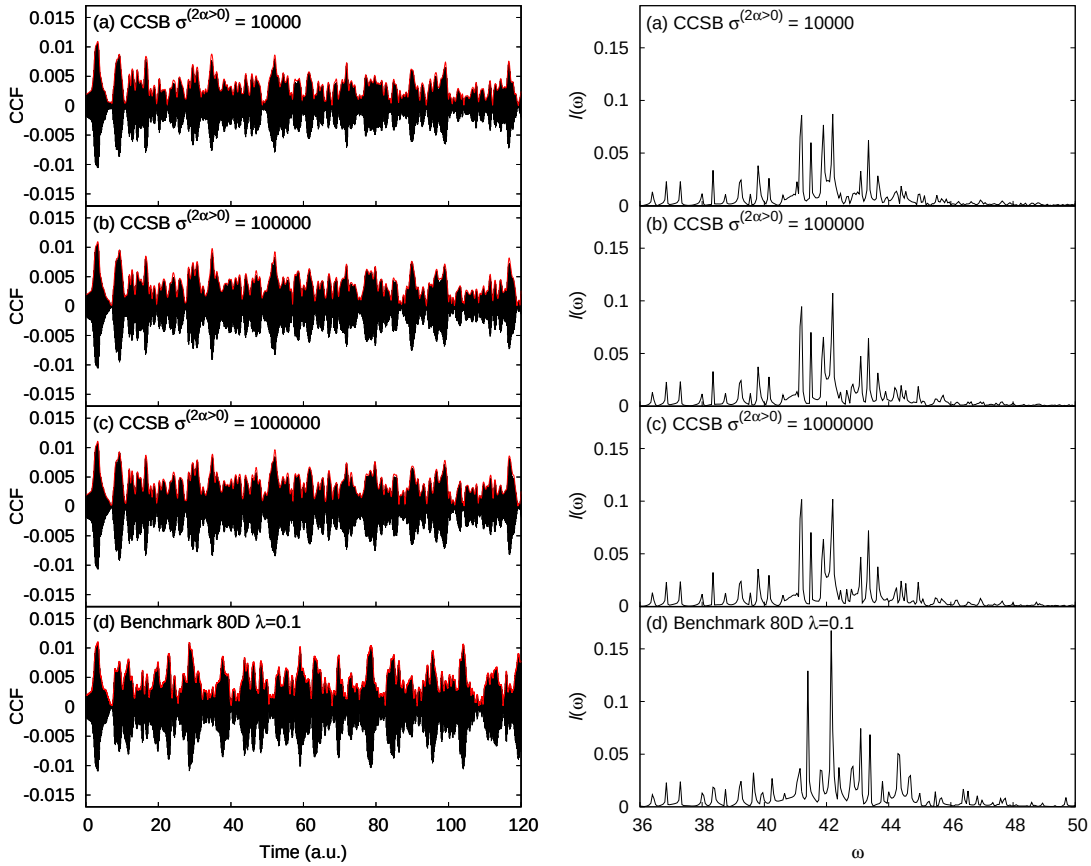

Figure B.3: Comparison to the benchmark of the cross-correlation functions (left, real parts in black and absolute values in red) and Fourier transforms of the real part (right) for $M = 80$ and $\lambda = 0.1$ CCSB calculations with different compression parameters on the distribution for sampling the excited levels $\sigma^{(2\alpha>0)}$.

The effect of changing the compression parameter on the distribution for sampling the excited levels $\sigma^{(2\alpha>0)}$, for $M = 80$, $\lambda = 0.1$ CCSB calculations is illustrated in Fig. B.3. The $\sigma^{(2\alpha>0)} = 1000000$ calculation in panel (c) was presented in Sec. 4.4.3.3. It can be seen that when $\sigma^{(2\alpha>0)} = 10000$ in panel (a), the amplitude of the CCF decays faster than when $\sigma^{(2\alpha>0)} = 100000$ and $\sigma^{(2\alpha>0)} = 1000000$ in panels (b) and (c), resulting in a slightly less intense FT spectrum. It can be concluded that the excited levels need a large compression parameter on their sampling distribution because, as mentioned in Sec. 4.4.3.3, the trajectories for these basis functions cause them to rapidly spread in phase space.

B.1.4 Altering the Tunnelling Mode Sampling Compression Parameter

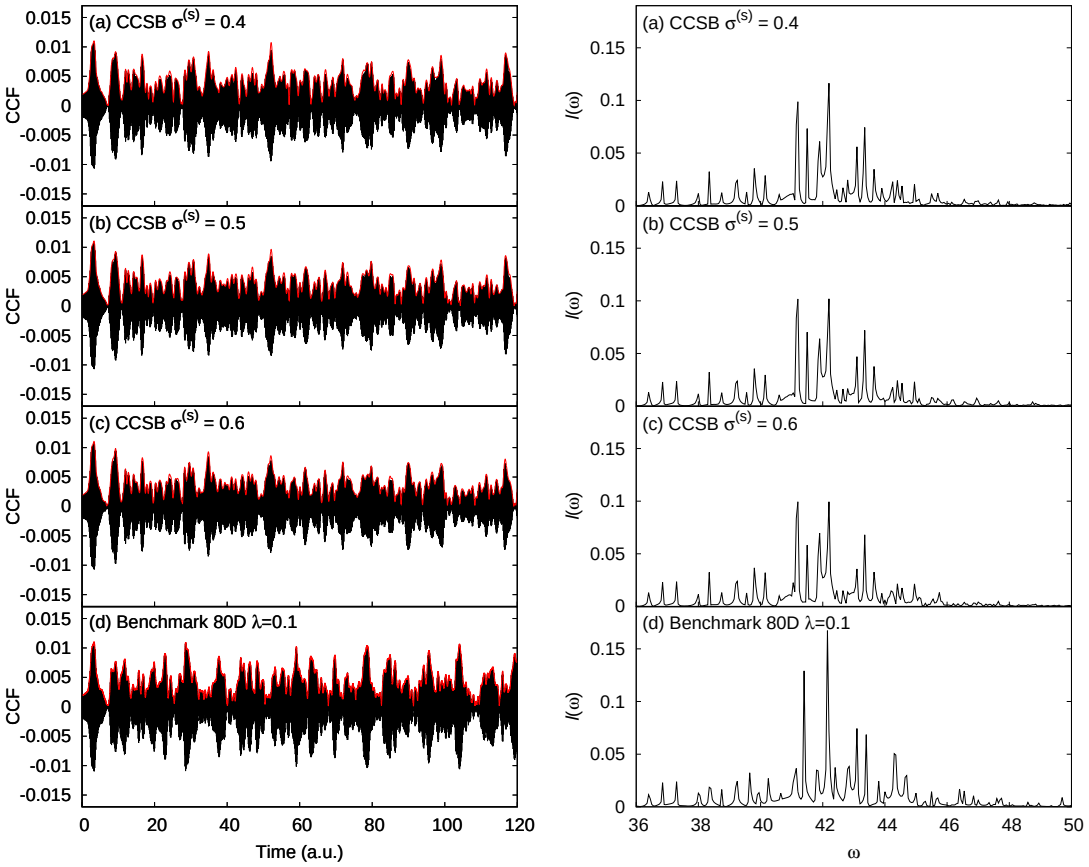

Figure B.4: Comparison to the benchmark of the cross-correlation functions (left, real parts in black and absolute values in red) and Fourier transforms of the real part (right) for $M = 80$ and $\lambda = 0.1$ CCSB calculations with different compression parameters on the distribution for sampling the tunnelling mode $\sigma^{(s)}$.

The effect of changing the compression parameter on the distribution for sampling the tunnelling mode $\sigma^{(s)}$ for $M = 80$, $\lambda = 0.1$ CCSB calculations is illustrated in Fig. B.4. The $\sigma^{(s)} = 0.5$ calculation in panel (b) was presented in Sec. 4.4.3.3. A smaller value for this parameter than the $M = 20$ and $M = 40$ cases was found to be necessary as a broader distribution was required for the tunnelling mode. It can be seen in panel (c) that increasing the value to $\sigma^{(s)} = 0.6$ causes a slight decay in the amplitude of the CCF, and a slight decrease in the intensity of the FT spectrum. This effect is exacerbated upon further increases of $\sigma^{(s)}$ (not shown here). Decreasing the value of this parameter in panel (a) caused a slight increase in the intensity of the peak at $\omega = 42$, however there was limited other effect, and decreasing the value further than $\sigma^{(s)} = 0.4$ led to a basis being unable to be formed, as the basis functions were not sufficiently coupled.

B.1.5 Placing Tunnelling Mode Basis Functions in the Upper Well

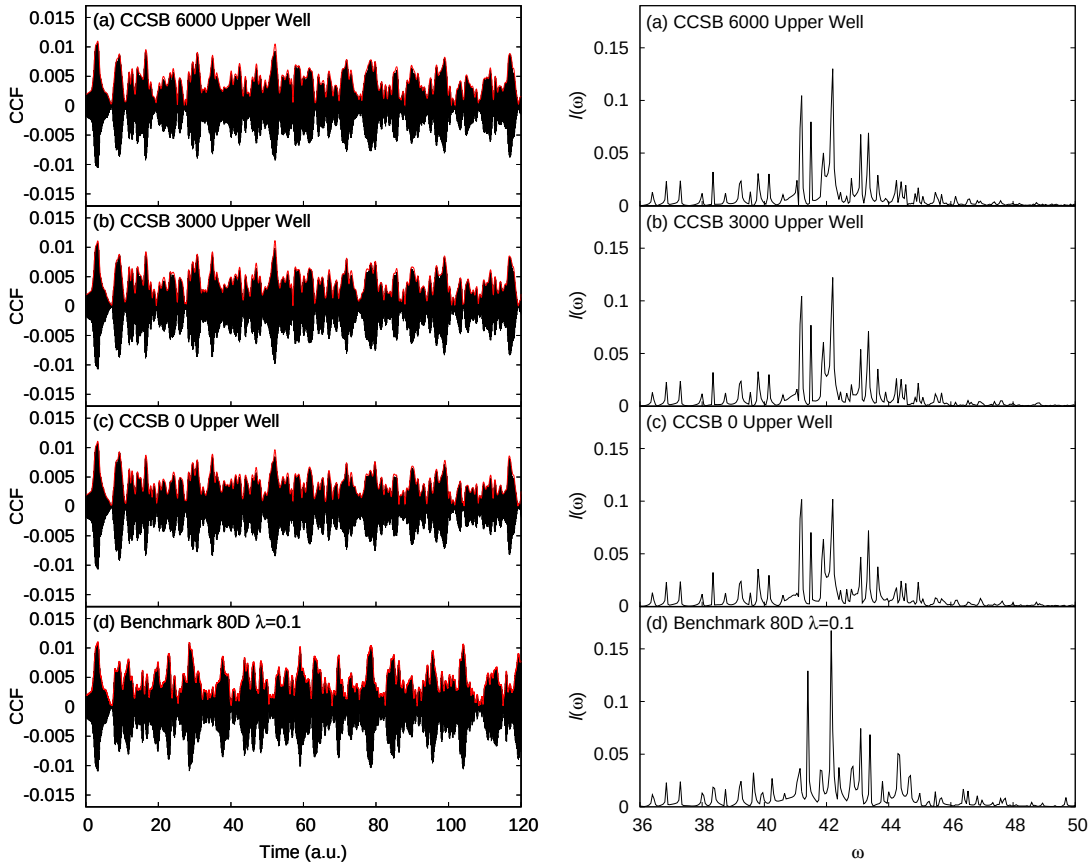

Figure B.5: Comparison to the benchmark of the cross-correlation functions (left, real parts in black and absolute values in red) and Fourier transforms of the real part (right) for $M = 80$ and $\lambda = 0.1$ CCSB calculations with tunnelling mode basis functions placed in the upper well of the potential.

The effect of initially placing a number of tunnelling mode basis functions in the upper well of the asymmetric double well potential for $M = 80$, $\lambda = 0.1$ CCSB calculations is illustrated in Fig. B.5. No tunnelling mode basis functions were placed in the upper well in the calculation presented in Sec. 4.4.3.3, and this is shown in panel (c). The number of basis functions placed in the upper well are noted in each of the panels of the figure, and they are centered around the mirror image coordinates $\bar{q}^{(1)}(0) = +2.5$. Visually, it appears that there is limited change to the CCF as a result of initially placing tunnelling mode basis functions in the upper well, however the peaks in the FT spectrum at $\omega > 42$ become better resolved, and match the benchmark calculation more closely. In particular, the splitting and intensity of the main peak at $\omega = 42$ more closely resembles the benchmark when placing 6000 of the 12000 tunnelling mode basis functions in the upper well in panel (a). Despite these small improvements, the CCSB calculation is still not as closely matched to the benchmark as the $M = 20$ and $M = 40$, $\lambda = 0.1$ cases.

B.1.6 Variable Excited Level Sampling Compression Parameter

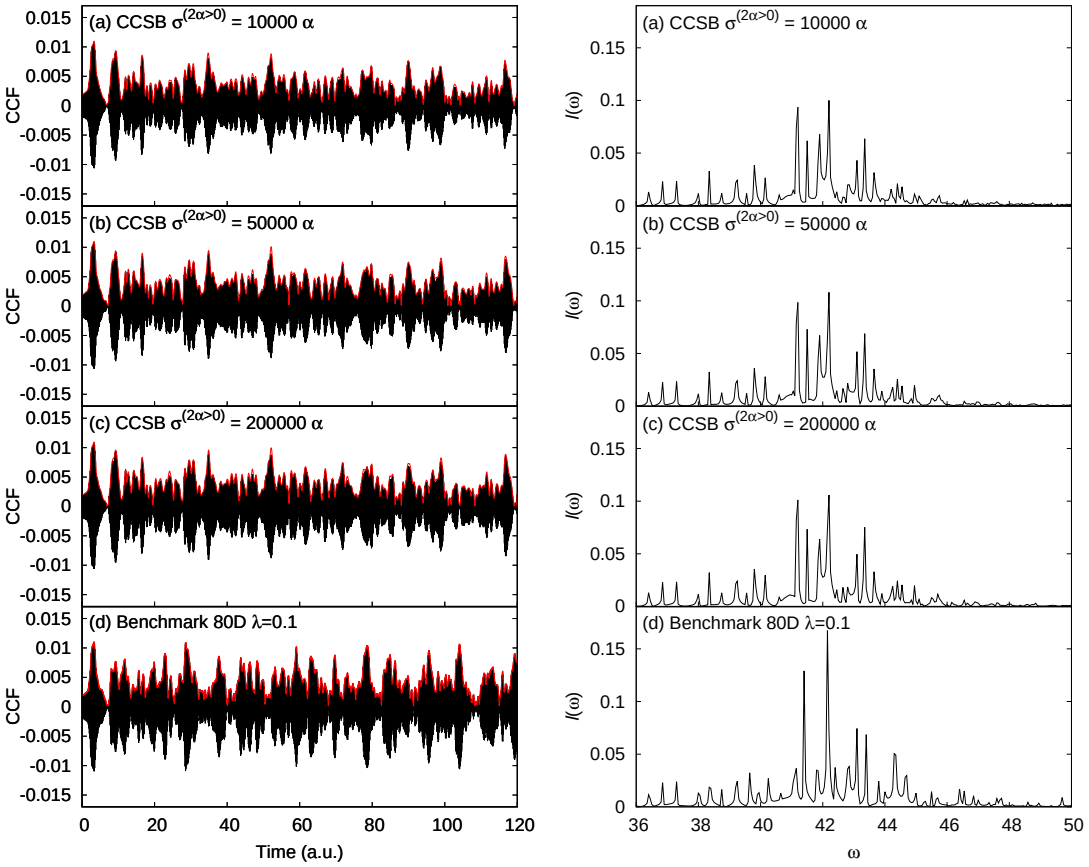

Figure B.6: Comparison to the benchmark of the cross-correlation functions (left, real parts in black and absolute values in red) and Fourier transforms of the real part (right) for $M = 80$ and $\lambda = 0.1$ CCSB calculations with variable compression parameter for sampling excited levels.

The effect of having a variable compression parameter for sampling excited levels in the basis for $M = 80$, $\lambda = 0.1$ CCSB calculations is illustrated in Fig. B.6. A simple linear scaling on the compression parameter is used, with the value of $\sigma^{(2\alpha>0)} = N\alpha$, where $N = 10000$, 50000 and 200000 in panels (a), (b) and (c), respectively. Lower excited levels have a smaller compression parameter, as they are more likely to be occupied so their basis should occupy a greater region of phase space. It can be seen that this has a limited effect in comparison to previous calculations with a constant $\sigma^{(2\alpha>0)} = 1000000$ parameter, and all values of the variable compression parameter produce similar results. The $\sigma^{(2\alpha>0)} = 10000\alpha$ case in panel (a) is an improvement over the constant $\sigma^{(2\alpha>0)} = 10000$ case in panel (a) of Fig. B.3 however, indicating that the higher compression parameters on the levels $\alpha > 1$ are beneficial. Other variable compression parameter schemes were tested, such as quadratic scaling with excited level, however these also had limited effect.

B.2 20D $\lambda = 0.2$

B.2.1 Altering the Number of Configurations in the Basis

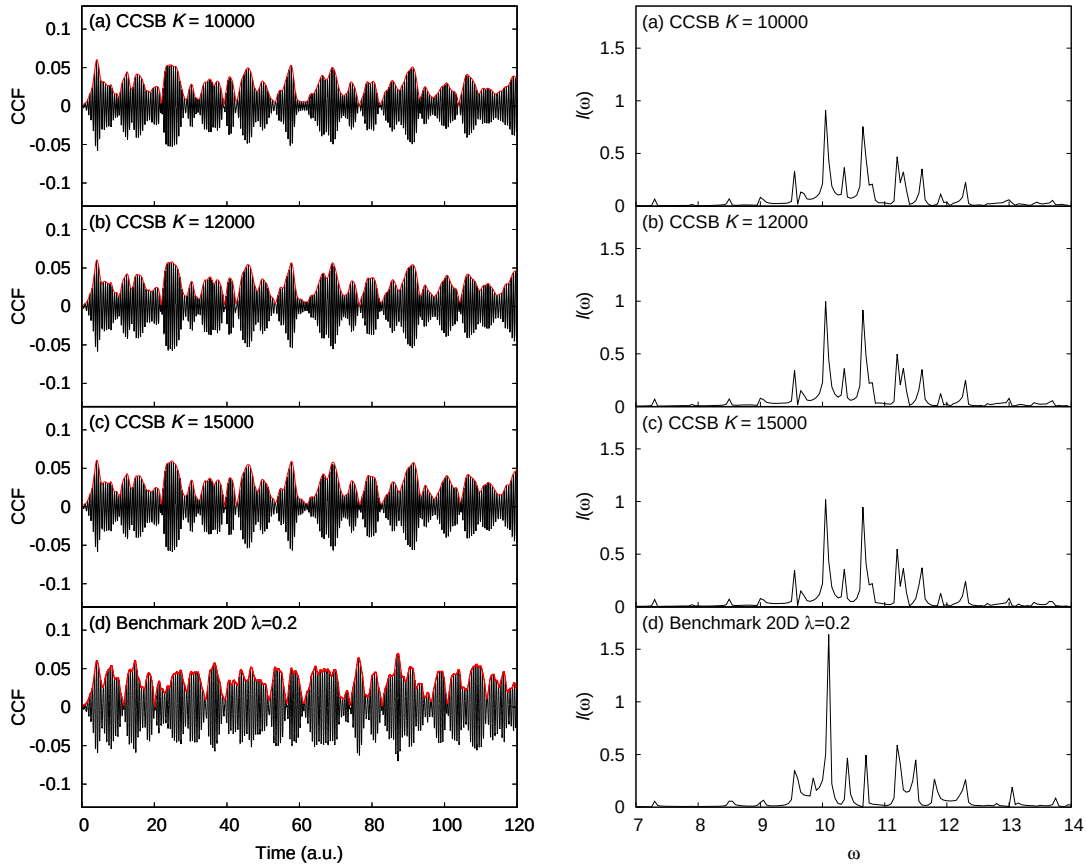

Figure B.7: Comparison to the benchmark of the cross-correlation functions (left, real parts in black and absolute values in red) and Fourier transforms of the real part (right) for $M = 20$ and $\lambda = 0.2$ CCSB calculations with different numbers of configurations K.

The effect of changing the number of configurations K for $M = 20$, $\lambda = 0.2$ CCSB calculations is illustrated in Fig. B.7. The $K = 12000$ calculation in panel (b) was presented in Sec. 4.4.3.4. The $K = 15000$ calculation required a smaller compression parameter for sampling the excited states than the $K = 12000$ and $K = 10000$ cases to preserve norm conservation. A value of $\sigma^{(2\alpha>0)} = 1000$ was used as opposed to $\sigma^{(2\alpha>0)} = 2000$. It can be seen that the amplitude of the CCF in the $K = 10000$ case decays slightly quicker than the $K = 12000$ case, resulting in a slightly less intense FT spectrum. The $K = 15000$ case exhibits virtually no difference to the $K = 12000$ despite being a more expensive calculation.

B.2.2 Altering the Number of Excited Levels in the Basis

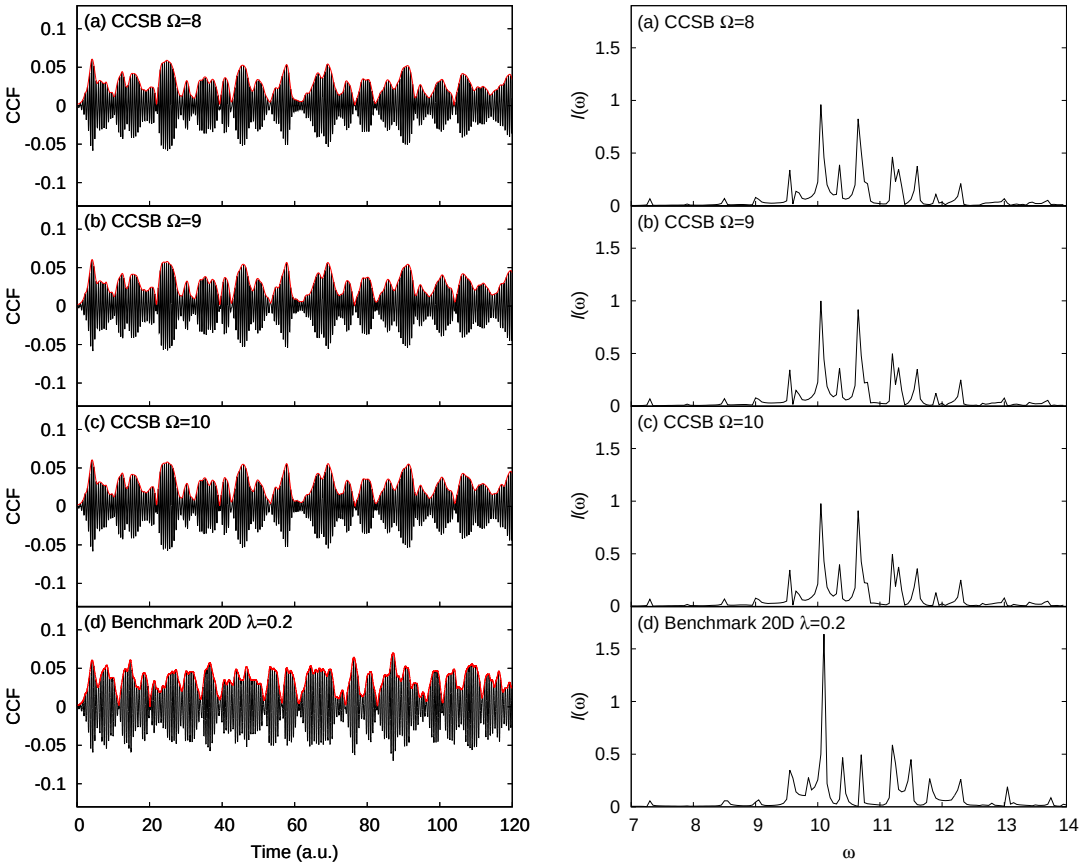

Figure B.8: Comparison to the benchmark of the cross-correlation functions (left, real parts in black and absolute values in red) and Fourier transforms of the real part (right) for $M = 20$ and $\lambda = 0.2$ CCSB calculations with different numbers of excited levels Ω.

The effect of changing the number of excited levels Ω for $M = 20$, $\lambda = 0.2$ CCSB calculations is illustrated in Fig. B.8. The $\Omega = 9$ calculation in panel (b) was presented in Sec. 4.4.3.4. The $\Omega = 8$ calculation required a smaller compression parameter for sampling the excited states than the $\Omega = 9$ and $\Omega = 10$ cases to preserve norm conservation. A value of $\sigma^{(2\alpha>0)} = 1000$ was used as opposed to $\sigma^{(2\alpha>0)} = 2000$. The amplitude of the CCF in the $\Omega = 8$ case decays slightly quicker than the $\Omega = 9$ case, resulting in a slightly less intense FT spectrum. The $\Omega = 10$ case exhibits virtually no difference to the $\Omega = 9$ case, so it can be concluded that increases in the number of excited levels in the basis beyond $\Omega = 9$ will lead to no improvement in the calculation.

B.2.3 Altering the Excited Level Sampling Compression Parameter

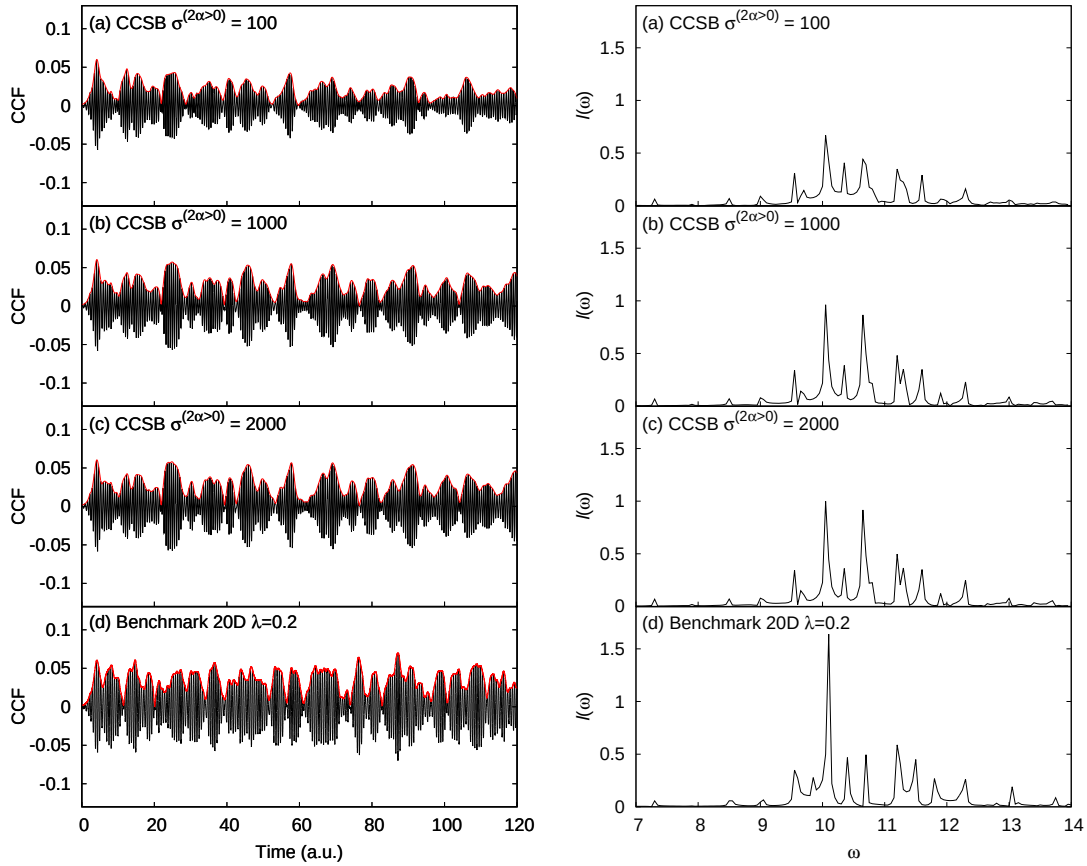

Figure B.9: Comparison to the benchmark of the cross-correlation functions (left, real parts in black and absolute values in red) and Fourier transforms of the real part (right) for $M = 20$ and $\lambda = 0.2$ CCSB calculations with different compression parameters on the distribution for sampling the excited levels $\sigma^{(2\alpha>0)}$.

The effect of changing the compression parameter on the distribution for sampling the excited levels $\sigma^{(2\alpha>0)}$ for $M = 20$, $\lambda = 0.2$ CCSB calculations is illustrated in Fig. B.9. The $\sigma^{(2\alpha>0)} = 2000$ calculation in panel (c) was presented in Sec. 4.4.3.4. The compression parameter $\sigma^{(2\alpha>0)} = 100$ in panel (a) results in basis functions for the excited levels being sampled from too broad a distribution. The CCF rapidly loses amplitude, resulting in a low intensity FT spectrum as the trajectories guiding the basis functions cause them to separate too quickly. Increasing the compression parameter in panels (b) and (c) remedies this issue, although increasing it further than $\sigma^{(2\alpha>0)} = 2000$ causes the calculation to become unstable with respect to norm conservation. However, there is limited difference between panels (b) and (c), and it can be concluded that further increases on the compression parameter would have limited effect on the calculation.

B.2.4 Altering the Tunnelling Mode Sampling Compression Parameter

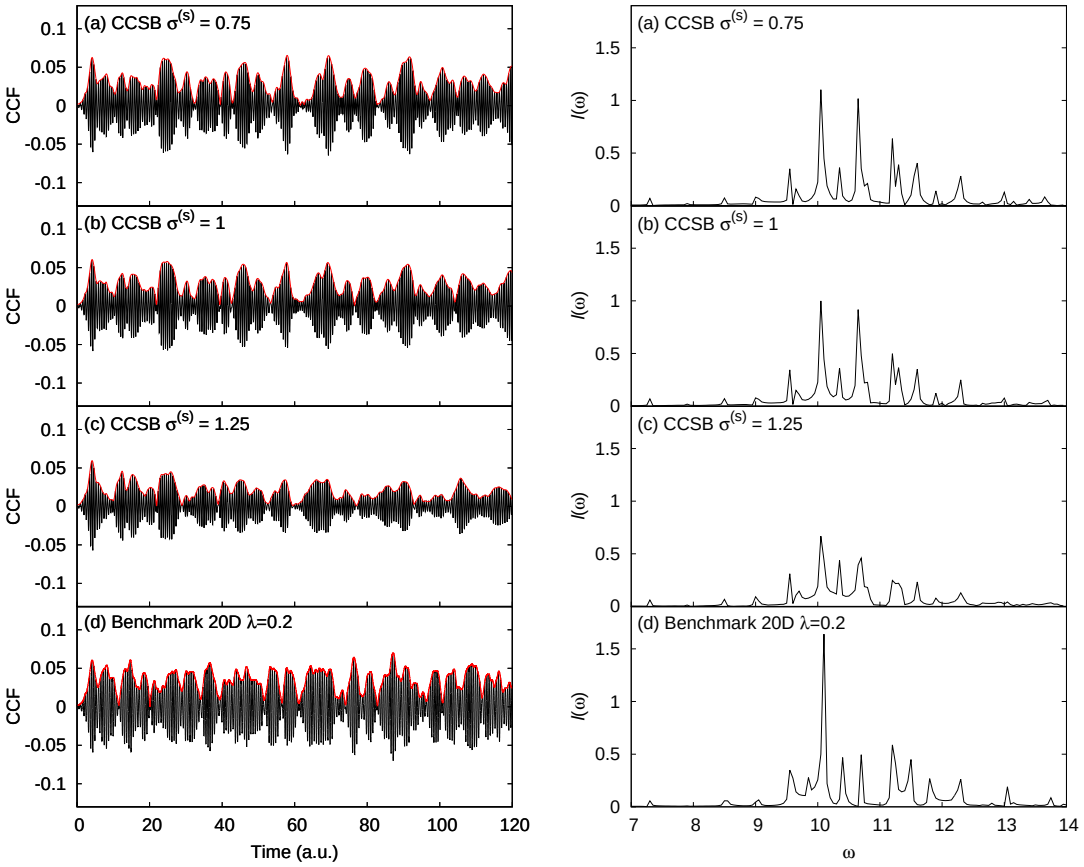

Figure B.10: Comparison to the benchmark of the cross-correlation functions (left, real parts in black and absolute values in red) and Fourier transforms of the real part (right) for $M = 20$ and $\lambda = 0.2$ CCSB calculations with different compression parameters on the distribution for sampling the tunnelling mode $\sigma^{(s)}$.

The effect of changing the compression parameter on the distribution for sampling the tunnelling mode $\sigma^{(s)}$ for $M = 20$, $\lambda = 0.2$ CCSB calculations is illustrated in Fig. B.10. The $\sigma^{(s)} = 1$ calculation in panel (b) was presented in Sec. 4.4.3.4. Sampling from a broader distribution with $\sigma^{(s)} = 0.75$ in panel (a) has limited effect on the calculation, whilst sampling from a narrower distribution with $\sigma^{(s)} = 1.25$ in panel (c) has a significantly detrimental effect on the calculation. It can be concluded that sampling the tunnelling mode from a broader distribution is not necessary, whilst sampling it from a narrower distribution results in the basis not spreading quickly enough.

B.2.5 Placing Tunnelling Mode Basis Functions in the Upper Well

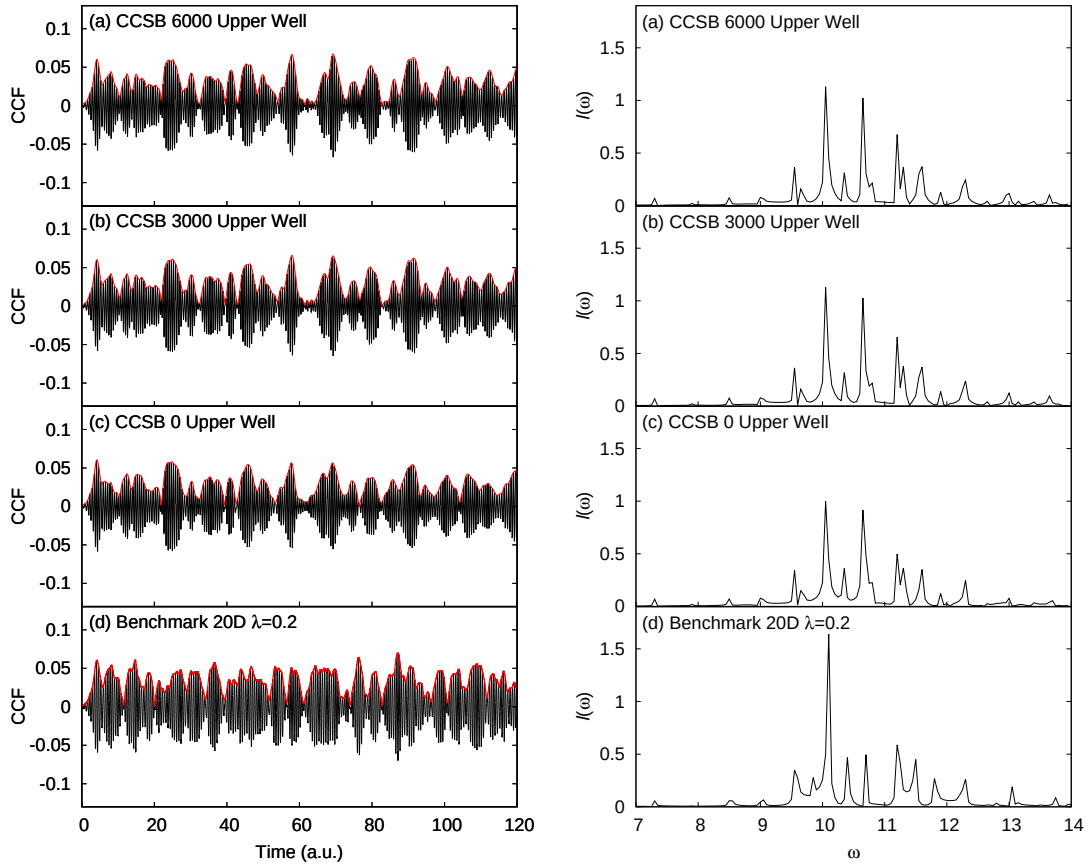

Figure B.11: Comparison to the benchmark of the cross-correlation functions (left, real parts in black and absolute values in red) and Fourier transforms of the real part (right) for $M = 20$ and $\lambda = 0.2$ CCSB calculations with tunnelling mode basis functions placed in the upper well of the potential.

The effect of initially placing a number of tunnelling mode basis functions in the upper well of the asymmetric double well potential for $M = 20$, $\lambda = 0.2$ CCSB calculations is illustrated in Fig. B.11. No tunnelling mode basis functions were placed in the upper well for the calculation presented in Sec. 4.4.3.4, and this is shown in panel (c). The number of basis functions placed in the upper well are noted in each of the panels of the figure, and they are centered around the mirror image coordinates $\bar{q}^{(1)}(0) = +2.5$. It can be seen that there is some improvement to the CCF at $t = 5$ a.u. by placing basis functions in the upper well, however the effect is relatively small. The higher frequency peaks in the FT spectra are also slightly better better resolved, however again this effect is relatively small, and these calculations are not significantly more accurate with respect to the benchmark.

B.2.6 Variable Excited Level Sampling Compression Parameter

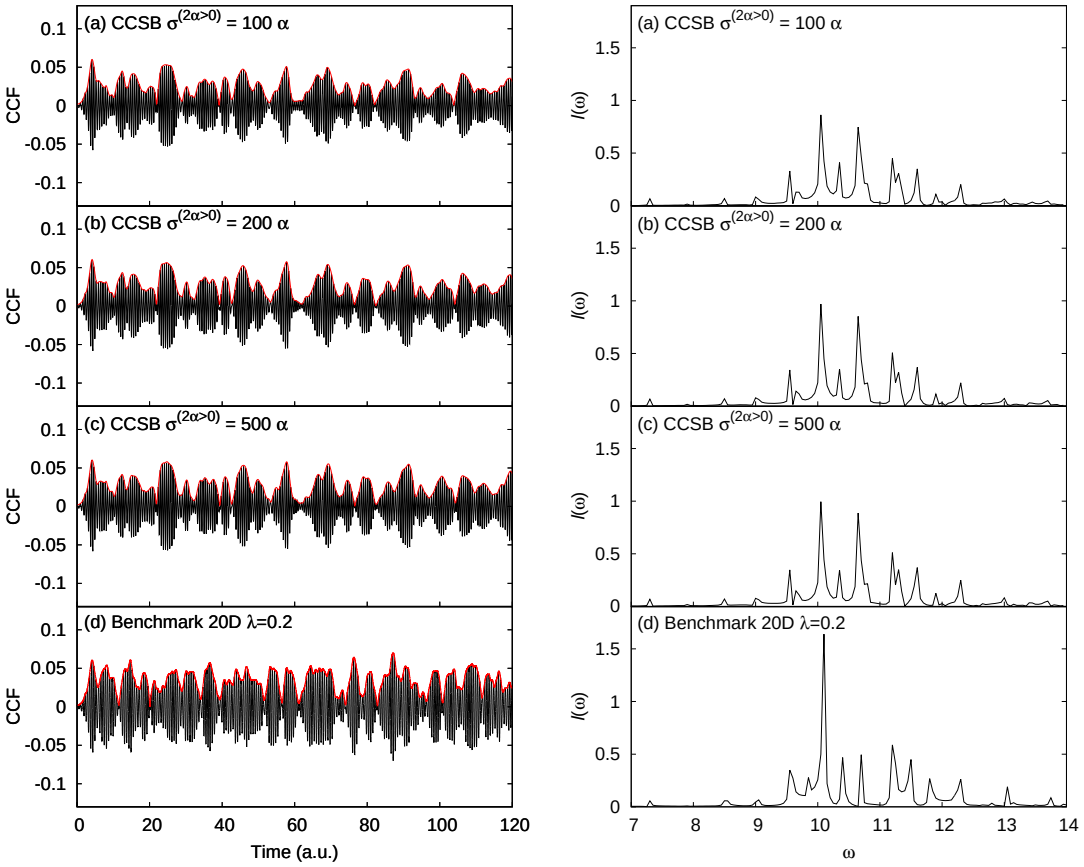

Figure B.12: Comparison to the benchmark of the cross-correlation functions (left, real parts in black and absolute values in red) and Fourier transforms of the real part (right) for $M = 20$ and $\lambda = 0.2$ CCSB calculations with variable compression parameter for sampling excited levels.

The effect of having a variable compression parameter for sampling excited levels in the basis for $M = 20$, $\lambda = 0.2$ CCSB calculations is illustrated in Fig. B.12. A simple linear scaling on the compression parameter is used, like in the $M = 80$, $\lambda = 0.1$ calculation, with the value of $\sigma^{(2\alpha>0)} = N\alpha$, where $N = 100$, 200 and 500 in panels (a), (b) and (c), respectively. Lower excited levels have a smaller compression parameter, as they are more likely to be occupied so their basis should occupy a greater region of phase space. It can be seen that this has a limited effect in comparison to previous calculations with a constant $\sigma^{(2\alpha>0)} = 2000$ parameter, only the $\sigma^{(2\alpha>0)} = 100\alpha$ case shows any difference with a decrease in amplitude of the CCF and intensity of the FT spectrum, as the excited levels are too decompressed and separate too rapidly. However, like in the $M = 80$, $\lambda = 0.1$ calculations in Fig. B.6, this is an improvement over the constant $\sigma^{(2\alpha>0)} = 100$ calculation in panel (a) of Fig. B.9.